Quantum simulation of the dipolar XY model using arrays of Rydberg atoms

Simulation quantique du modèle XY dipolaire en utilisant des matrices d'atomes de Rydberg

Thèse de doctorat de l'université Paris-Saclay

École doctorale n° 572, Ondes et Matière (EDOM)
Spécialité de doctorat : Physique
Graduate School : Physique
Référent : Institut d'Optique

Thèse préparée dans l'unité de recherche **Laboratoire Charles Fabry** (IOGS, Université Paris-Saclay, CNRS), sous la direction de **Antoine BROWAEYS** et le co-encadrement de **Thierry LAHAYE**.

Thèse soutenue à Paris-Saclay, le 27 septembre 2024, par

Guillaume BORNET

Composition du jury

Mark-Oliver GOERBIG	Président
Chargé de recherche, CNRS-LPS	
Clément SAYRIN	Rapporteur
Maître de conférences, LKB	
Monika AIDELSBURGER	Examinatrice
Professor, MPQ-LMU	
Martin ROBERT DE SAINT VINCENT	Examinateur
Chargé de recherche, CNRS-LPL	

Direction de la thèse

Antoine Browaeys	Directeur
Directeur de recherche, CNRS-LCF	
Thierry Lahaye	Codirecteur
Directeur de recherche, CNRS-LCF	

Acknowledgements

au labo. J'ai été admiratif de ton calme olympien face à des situations de stress ou de crise, et j'ai beaucoup appris en travaillant avec toi.

Pascal, je te remercie tout particulièrement pour l'année que nous avons passée ensemble au sous-sol de l'institut et pour tous les bons moments qui l'accompagnent. Il est impressionnant de travailler avec toi et de constater ta vivacité d'esprit ainsi que la fulgurance de tes idées. Chaque jour à travailler à tes côtés est à la fois un véritable défi pour rester au niveau, mais aussi une incroyable opportunité de donner le meilleur de soi-même et d'en apprendre davantage. En plus des souvenirs de moments mémorables passés ensemble, ce que je garde précieusement est "l'esprit de CHADOQ" (comme tu aimes l'appeler) que tu as réussi, je pense, à m'inculquer: un savant mélange d'ingéniosité, de débrouillardise, de résilience, de ténacité et d'esprit de compétition nécessaires pour travailler sur la manip. Pour tout cela, je te remercie.

Après cette première année, une nouvelle équipe s'est constituée. J'ai eu la chance de passer la plus grande partie de ma thèse en trinôme avec deux personnes d'exception: Gabriel Emperauger (co-thésard) et Cheng Chen (postdoc). Rétrospectivement, malgré tous les obstacles et difficultés que nous avons dû affronter, et alors que les chefs considéraient déjà l'idée d'arrêter la manip pour en construire une nouvelle, je pense que nous pouvons être fiers de tout ce que nous avons réussi à faire ensemble.

Gabriel, je pense sincèrement que tu es le meilleur co-thésard que l'on puisse avoir. Tu es brillant, toujours à l'écoute et partant pour de nouvelles idées (même parfois un peu loufoques). Tu as une intégrité et une honnêteté scientifiques sans faille, ainsi qu'une capacité exceptionnelle de compréhension des phénomènes physiques. Comme tu nous l'as démontré plusieurs fois, tu es même capable de comprendre certains concepts théoriques complexes plus vite que les théoriciens eux-mêmes! Toutes ces qualités scientifiques s'allient à de grandes qualités humaines : une bienveillance et une gentillesse naturelles, doublées d'un enthousiasme contagieux. J'ai passé des moments formidables avec toi, que ce soit en travaillant jusqu'à quatre heures du matin au labo avec Daniel, en préparant un live Twitch sur Arte, ou en se faisant courser par Agnes Seckler dans le parking de l'institut. Un grand merci pour tous ces moments passés ensemble.

Cheng, you are the best! Tu es un travailleur inépuisable, plein de ressources et de détermination. On ne compte plus le nombre de fois où ta persévérance et ton talent nous ont permis de résoudre des problèmes critiques sur la manip, sans lesquels le projet en cours n'aurait jamais pu aboutir. Ce qui m'a le plus impressionné dans ta

façon de travailler, c'est ta force mentale. Quel que soit l'état dans lequel se trouvait la manip, tu gardais cet indéfectible enthousiasme, optimisme et entrain à aller de l'avant, et c'était quelque chose sur lequel nous pouvions tous compter. Travailler avec toi a été une expérience très enrichissante et j'ai appris enormément à tes côtés. 丞,这些年来，非常感谢你。与你合作真是荣幸和愉快。我会想念你的。我期待下次会议再次见到你。祝你未来的职业生涯一切顺利。

Merci à vous deux pour ces super moments et pour cette aventure extraordinaire! Vous allez me manquez, j'espère que l'on se revera très vite.

Passons maintenant au postdoc le plus célèbre de l'institut: Daniel Barredo. Durant ma thèse, Daniel a passé la moitié de son temps en Espagne à commencer son propre groupe, et l'autre moitié en France à nous aider. Je pense qu'il n'est pas exagéré de dire que la recherche mondiale sur les simulateurs/ordinateurs quantiques avec des atomes de Rydberg aurait été significativement différente si tu n'avais pas été là. Cette affirmation résume à elle seule l'excellence scientifique et l'esprit pionnier qui te caractérisent si bien. Tu as la capacité de spontanément faire ressortir le meilleur de nous-mêmes pour repousser les limites. Tantôt tu joues le rôle de Daniel-le-technicien, qui nous aide à réparer ou à améliorer CHADOQ, tantôt tu es le postdoc exigeant qui nous pousse à donner le meilleur de nous-mêmes, et tantôt tu es le grand frère qui réconforte les thésards après une très dure journée. Tu t'impliques toujours au maximum dans les projets, et nous pouvons toujours compter sur toi. Si les chefs peuvent être considérés comme le cerveau de la manip et l'équipe de thésards/postdocs comme son cœur, alors tu en es définitivement l'âme! CHADOQ t'appartiendra toujours, et à jamais! Ce fut un immense plaisir et un honneur de travailler avec toi, merci pour tout.

Tous ces projets n'auraient évidemment pas été possibles sans leurs capitaines, Antoine Browaeys et Thierry Lahaye.

Antoine, je t'ai rencontré la première fois en tant qu'élève au master LOM. J'ai été profondément impressionné par ton cours, ta pédagogie, ta façon de rendre accessibles des idées complexes grâce à des images simples, ainsi que par toute la passion qui s'en dégage. À la fin de l'année, malgré mon manque flagrant d'expérience dans le domaine, tu as décidé de me faire confiance en me permettant de rejoindre l'équipe de CHADOQ en tant que thésard. Et pour ça, je t'en serai éternellement reconnaissant. Durant ces quatre ans de thèse, j'ai apprécié tous les moments que nous avons passés

ensemble, que ce soit les réunions de travail, les repas au Magnan, les discussions en salle café, ou les trajets en bus/taxi pour aller et revenir des conférences. Tes compétences scientifiques sont extraordinaires, comme en témoigne la remise de la médaille d'argent du CNRS et ton entrée à l'Académie des sciences, auxquelles j'ai eu l'honneur d'assister durant ma thèse. En plus de tes qualités de physicien incroyable, ce qui m'a le plus marqué, c'est la relation privilégiée que tu entretiens avec chacun de tes thésards et postdocs. Malgré l'immense charge de travail que tu assumes chaque jour, tu te rends toujours disponible pour nous écouter, nous aider à régler un problème sur la manip, nous rappeler certaines bases de physique atomique que nous avons pu oublier, ou discuter des dernières idées les plus délirantes que nous venions juste d'avoir un vendredi soir au labo. Je pense vraiment que ce lien direct que tu offres avec tes équipes est en grande partie responsable de la force de ton groupe. Tu es une véritable source d'inspiration et, pour moi, tu représentes le physicien que j'aimerais devenir. Merci de m'avoir fait confiance, merci pour tous ces moments, merci pour tout!

Thierry, merci de m'avoir accueilli dans ce groupe. J'ai été (et suis toujours) impressionné par l'étendue de tes connaissances, le soin et l'exigence que tu apportes à chaque chose que tu fais, aussi minime soit-elle, et aussi pour ton inattendu talent à PAC-MAN. Malgré certains différents que nous avons pu avoir, tu as toujours su nous pousser à élever notre niveau d'exigence et à donner le meilleur de nous-mêmes. Tu m'as également appris à rédiger et restituer des travaux scientifiques, que ce soit des articles ou des présentations orales, et pour cela, j'aimerais te témoigner toute ma reconnaissance, merci.

J'aimerais ajouter un petit mot pour la future génération de CHADOQ et OMEDOQ : Lukas Klein, Romain Martin, Mu Qiao, Bastien Gély et Yuki Torii Chew. J'ai eu l'occasion de travailler avec certains d'entre vous et je peux affirmer que "l'esprit de CHADOQ" est en vous. En particulier, Bastien, surnommé le "tomographieur fou", ton intelligence n'a d'égal que ta bonne humeur. Chew, ton sens physique et ton intuition sont impressionnants, ainsi que ta capacité à récolter des "gossips" dans le groupe. Mu, tu fais preuve d'une force de travail et un talent qui force l'admiration, le tout avec un calme impérial. Et enfin, Romain, tu es un esprit brillant derrière un sourire ravageur. Je suis persuadé que le futur de la simulation quantique avec des atomes de Rydberg au sous-sol de l'institut est entre de très bonnes mains.

J'aimerais également remercier le reste du groupe optique quantique-atomes et leurs anciens membres : Florence Nogrette, Damien Bloch, Sara Pancaldi, Britton Hofer, Adrien Gavalda, Giulio Biagioni, Nathan Bonvalet, Guillaume Tremblier, Giovanni, Toni, Igor Ferrier-Barbut, Kai-Niklas Schymik, Giovanni Ferioli, Jamie Boyd, Sam Cohen, Florian Wallner et Antoine Glicenstein pour avoir partagé mon quotidien et pour tous les bons moments : les soirées pizzas/cinéma/quizz/coupe du monde/resto/barbecue, les courses (Eiken et Mud race), les joggings du vendredi midi, les parties de tennis, de foot ou de Mölkky, les escapades mémorables lors de conférences et le reste. Merci à cette grande équipe soudée, cette aventure n'aurait clairement pas été la même sans vous !

J'aimerais remercier toutes les équipes de théoriciens avec qui nous avons pu collaborer : Marcus Bintz, Vincent Liu, Johannes Hauschild, Shubhayu Chatterjee, Michael Schuler, Andreas Läuchli, Michael Zaletel, Norman Yao, Bingtian Ye, Maxwell Block, Fabio Mezzacapo, Tommaso Roscilde, Filippo Caleca, Francisco Machado, Sabrina Chern et Lucas Leclerc (le plus expérimentateur des théoriciens). Vous avez fait un travail formidable ; sans vous, nous n'aurions pas pu avoir la réussite que nous avons eue.

Enfin, j'aimerais exprimer ma gratitude envers toutes les personnes qui nous ont aidés, directement ou indirectement, dans notre projet. Je remercie l'ensemble du service administratif de l'institut et de l'EDOM (en particulier Nadia Chapiteau) pour avoir été si patient avec moi. Je remercie également le service de l'infrastructure de l'institut pour avoir fait en sorte que nous puissions travailler dans de bonnes conditions. En particulier, je voudrais remercier le directeur de laboratoire, Patrick Georges, qui s'est toujours rendu disponible pour nous aider. Je souhaite également remercier l'entreprise Pasqal, qui, dans des moments critiques, nous a souvent dépannés d'un laser ou d'un amplificateur laser.

Et pour finir, j'aimerais remercier mes amis et mes proches qui m'ont soutenu tout au long de cette aventure. En particulier, j'aimerais adresser un grand merci à mon frère Sylvain et à ma sœur Apolline pour votre soutien. Et enfin, mes derniers remerciements vont à mes parents, sans qui je ne serais jamais arrivé là où je suis. Des mots ne pourraient résumer toute la gratitude que j'ai pour vous et ce que vous avez fait pour moi, alors je vous dis tout simplement merci, merci pour tout!

Contents

Introduction

Contents

Over the last century, quantum mechanics has established itself as a powerful theory for describing nature. It provides an accurate framework for predicting the behavior of objects at a microscopic scale, such as atomic and subatomic particles, and has led to revolutionary technologies used in everyday life. Notable examples include the development of nanometer-scale transistors used in most electronic systems, solar panels, atomic clocks for global positioning system calibrations, and magnetic resonance imaging devices.

More recently, rapid technological progress has enabled physicists to isolate, control, and study individual quantum objects. Single charged particles can be trapped for days using electromagnetic traps [Dehmelt, 1990; Paul, 1990]; single photons can be stored in superconducting cavities for hundreds of milliseconds [Haroche, 2013; Yang *et al.*, 2016]; and individual neutral atoms can be cooled and trapped in optical tweezers for hours [Ashkin *et al.*, 1986; Phillips, 1998; Schymik *et al.*, 2021]. Manipulating these quantum particles has allowed physicists to precisely test and confirm the predictions of quantum theory including the rather counter intuitive concept of entanglement. Entanglement describes a particular state of a system where its sub-parts cannot be described separately, *i.e.*, the system cannot be factorized into states of its sub-systems. This was tested by a "violation of the Bell's inequality" [Bell, 1964] leading to the Nobel prize awarded to John F. Clauser, Anton Zeilinger and Alain Aspect [Aspect, Grangier, and Roger, 1982] in 2022.

Over the last 40 years, physicists reproduced the experiment in various forms: in particular, they showed that the conclusion remains valid for distances between the

particles separating satellites from the ground up to 1200 km [Yin *et al.*, 2017]. The development of the ability to control individual quantum particles combined with their "quantum" properties (quantum superposition of states or entanglement with other particles) offers new opportunities for various applications.

Quantum metrology. Quantum metrology relies on the use of quantum objects to measure physical parameters such as temperature or electric, magnetic and, in some cases, gravitational fields [Degen, Reinhard, and Cappellaro, 2017; Mehlstäubler, 2023]. They offer a higher sensitivity to external perturbations than classical sensors. As an example, Nitrogenvacancy (NV) centers allow scientists to perfom $\mathrm{pT}/\sqrt{\mathrm{Hz}}$ sensitive measurements [Balasubramanian *et al.*, 2008; Maze *et al.*, 2008] and are already used in various fields of physics for in-situ measurements [Lesik *et al.*, 2019; Barry *et al.*, 2020]. Quantum metrology also exploits entanglement as a resource offered by quantum mechanics allowing for a significant increase in sensitivity. For example, one of these strategies called squeezing, has evolved from proof-of-principle experiments to applications in several areas of research, such as gravitational wave detectors [Tse *et al.*, 2019], atom interferometers [Hosten *et al.*, 2016], and optical atomic clocks [Ludlow *et al.*, 2015; Pedrozo-Peñafiel *et al.*, 2020; Robinson *et al.*, 2022; Ye and Zoller, 2024].

Quantum cryptography. Quantum cryptography consists in harnessing quantum properties to encode, transfer, and decode information more securely than with classical means. Introduced in the early 1990s [Bennett and Wiesner, 1992; Bennett *et al.*, 1992], the idea is to combine the encoding of information on quantum objects with the ability to entangle them to make it physically impossible to hack. The most famous examples are quantum key distribution protocols allowing people to share a secret and detect if their communication is compromised by eavesdropping [Xu *et al.*, 2020]. Any attempt to intercept a message will immediately affect the properties of the key held by the secret holders.

Quantum simulation. Quantum simulation aims at studying many-body physics problems using a machine called *quantum simulator*.

Many-body physics problems are encountered almost everywhere in physics, such as in condensed matter, nuclear and high-energy physics. In condensed matter, for example, the objective is to understand how the interactions among the different

system constituents lead to macroscopic objects with distinct mechanical, optical, and electrical properties, and can give rise to emergent phenomena such as magnetism, superconductivity, and phase transitions. Since, the behaviour of all these interacting particles are described by the Schrödinger equation, one could in principle directly solve the equation and calculate *ab-initio* the macroscopic properties of the ensemble. However, the complexity increases exponentially with the number of particles due to the expansion of the Hilbert space. For the simplest spin-1/2 particles, theorists can only perform exact calculations for systems with up to approximately 50 particles, which is far from a macroscopic system. Therefore, to simulate these systems, making approximations is necessary. These approximations typically involve truncating the Hilbert space, *i.e.*, neglecting quantum effects such as particle entanglement, resulting in an effective classical model that is easier to solve [Reif, 2009]. For instance, the *mean field approximation* simplifies the many-body problem by approximating the effects of all other particles on any given particle with an average or mean field, reducing the many-body problem to an effective one-body problem that can be solved. However, when quantum effects play a dominant role, this strategy fails to model certain macroscopic behaviours. As an example one can cite high-temperature superconducting materials [Bardeen, Cooper, and Schrieffer, 1957; Keimer *et al.*, 2015], topological insulators governed by the quantum Hall effect [Klitzing, Dorda, and Pepper, 1980], or the existence of graphene theorized as impossible by the Mermin–Wagner theorem [Mermin and Wagner, 1966; Novoselov *et al.*, 2005]. They usually fall under the name of *strongly correlated systems.*

In 1980 and 1982, Yuri Manin and Richard Feynman suggested the idea of textitquantum simulators that would control a set of interacting quantum particles (refereed as *artificial quantum matter*), that reproduces the behavior of real world materials, *i.e.* the evolution of these artificial systems are governed by the same Schrödinger equation as for the natural ones. These quantum simulators would then provide the experimentalist direct access to measure the state of each particles, and thus would help to solve many-body physics problems of strongly correlated systems. Over the last few decades, multiple quantum simulation platforms based on different particle, ranging from neutral atoms and photons to ions and superconducting circuits, have emerged with the aim of performing quantum simulations in a regime where numerical calculations are impossible. Thanks to recent developments in the field [Georgescu, Ashhab, and Nori, 2014; Altman *et al.*, 2021], quantum simulations of up

to thousands of particles can now be performed.

The future stakes of quantum simulation are twofold. First, as mentioned, it will enable scientists to pursue the study of quantum many-body physics with systems too large to be classically simulated. Second, in collaboration with theorists, it will enable to benchmark new numerical techniques for larger system sizes.

Quantum computing. Quantum computing utilizes a quantum machine to solve complex problems more efficiently than classical computers. Quantum computers can be seen as the digital version of quantum simulators. While simulators only aim to solve classes of specific problems, quantum computers can be programmed to address a larger variety of problems, making them universal.

The idea is to carry the information via quantum-bits (qubits) encoded in the internal or external states of quantum particles, which allows using the properties of quantum mechanics as superposition or entanglement to speed up the calculation processes. One famous example that illustrates the power of quantum computers is the factorization of large integers into prime factors using the Shor algorithm [Shor, 1994]. In 2019, Google® claimed that their superconducting processor reached *quantum supremacy* [Arute *et al.*, 2019], meaning no classical computer can solve the same problem in any feasible amount of time [Preskill, 2012]. Although quantum supremacy is a controversial concept highly debated in the community [Herrmann *et al.*, 2023], this event reflects the potential that a quantum computer can represent over a classical one.

During my Ph.D., I worked on a quantum simulator based on individual neutral ^{87}Rb atoms trapped in an configurable array of optical tweezers and interacting via highly-excited states known as Rydberg states. In this manuscript, I describe our quantum simulator and report the experiments I conducted for almost 4 years. This introduction will first detail the main many-body physics problems we wish to study. Next, I will give a brief overview of the state-of-the-art of different platforms, and finally, I will focus on our specific quantum simulator.

1.1 Quantum simulation to study many-body physics problems

Condensed matter physicists seek to understand the macroscopic phenomena that can emerge from the microscopic properties of matter. At the microscopic level, there are usually two different classes of models used to describe the behavior of interacting particles.

Fermi/Bose-Hubbard model The first ones are the Fermi-Hubbard model that gives relatively simple descriptions of the electron's motion in a crystalline structure. More specifically, it provides an understanding of insulating, magnetic, charge density wave, and high-temperature superconducting effects in a solid material. This model considers an ensemble of spin-1/2 particles (representing the electrons) with spin degrees of freedom $\sigma = \{\downarrow, \uparrow\}$, localized at site i of a lattice (representing the nodes of a crystalline structure). We consider two processes: first, each particle can tunnel from site i to a neighbouring lattice site j with amplitude $-t$, and second, having two particles $|\uparrow\rangle$ and $|\downarrow\rangle$ on the same site costs an energy U. The Fermi-Hubbard Hamiltonian reads:

$$\mathcal{H} = -\hbar t \sum_{\langle i,j \rangle, \sigma} \left(f_{i,\sigma} f_{j,\sigma}^{\dagger} + f_{i,\sigma}^{\dagger} f_{j,\sigma} \right) + \hbar U \sum_{i} n_{i,\uparrow} n_{i,\downarrow}, \tag{1.1}$$

where $\langle i, j \rangle$ denotes the sum over neighbouring sites, $f_{i,\sigma}$ and $f_{i,\sigma}^{\dagger}$ being the fermionic annihilation and creation operators acting on site i, and $n_{i,\sigma} = f_{\sigma}^{\dagger} f_{\sigma}$ the corresponding number operator. Although this description seems very simple, solving this model is extremely hard. However, it turns out, that this model can already be implemented on quantum simulators using a fermionic quantum gas loaded into an optical lattice [Esslinger, 2010; Tarruell and Sanchez-Palencia, 2018]. It allows physicists to investigate the phase diagram of this model by experimentally varying its parameters U and t and observing how the behaviour of the particles is affected. In order to describe a wider variety of materials, all class of Hubbard models have been developed using different geometries, extending the range of the interactions beyond nearest neighbours, or describing the motion of other particles such as spinless bosons via the Bose Hubbard model (which is the bosonic version of the Hubbard model).

Spin models   The second class of many-body models are spin models. In contrast to Hubbard models, they describe spin-spin interactions for particles fixed in space. For electrons, this coupling comes from a combination of the Coulomb repulsion and the Pauli exclusion principle. Spin models are relevant to describe a wide variety of quantum magnetism phenomena ranging from the emergence of ferromagnetic/antiferromagnetic orders in material to the formation of more exotic magnetic phases, like spin liquids. For spin-1/2 particles, one common model used in the field reads:

$$\mathcal{H} = \hbar \sum_{\langle i,j \rangle} \left[J_\perp (\sigma_i^x \sigma_j^x + \sigma_i^y \sigma_j^y) + J_z \sigma_i^z \sigma_j^z \right], \tag{1.2}$$

with $\sigma^{x,y,z}$ being the usual Pauli matrices acting on the spins, and $\langle i,j \rangle$ denoting the sum runs over all neighbours sites. Depending on the ratio $J_z/J_\perp$ this Hamiltonian has different names and can lead to various collective phenomena:

- When $J_\perp = 0$, we obtain the Ising model [Ising, 1925]. The Ising model gives a powerful description of ferromagnetic/antiferromagnetic behaviours. For instance, if $J_z < 0$ in order to minimize the energy, the spins tend to point along the same direction (along ↑ or ↓), leading to a spontaneous magnetization of the material. On the contrary, if $J_z > 0$, the spins tend to point in opposite directions, leading to an antiferromagnetic order.

- When $J_z = 0$, we end up with the planar XY model. This model can produce non-trivial effects such as systems exhibiting ferromagnetic order in the (x, y) plane but antiferromagnetic order along the perpendicular direction z. Moreover when rewritten as $J_\perp (\sigma_i^x \sigma_j^x + \sigma_i^y \sigma_j^y) \propto J_\perp (\sigma_i^+ \sigma_j^- + \sigma_i^- \sigma_j^+)$ with $\sigma^\pm = (\sigma^x \pm i\sigma^y)/\sqrt{2}$ the creation and annihilation operators, the Hamiltonian can be reinterpreted as a spin transport model. An excitation (*e.g.* a spin ↑) can jump from one site i to another unoccupied site j (a spin ↓) with a amplitude $J_\perp$. Using this interpretation allows us to link spin models with Hubbard models. Under specific conditions, spin and Hubbard models describe the same physics; for example, the Bose-Hubbard model combined with infinite on-site interaction $t \ll U$ (also called the hard-core boson Hamiltonian) is strictly equivalent to the Heisenberg XXX model (see below).

- In the general case, when we just have J_z and $J_\perp \neq 0$ we end up with the anisotropic Heisenberg Hamiltonian (also known as the XXZ model). It is a

combination of the Ising model with the XY model. When $J_z = J_\perp$, we recover the fully isotropic Heisenberg Hamiltonian (XXX model).

Like the Hubbard models, these spin models have several variations. We can add linear terms $\delta \sum_i \sigma_i^{x,y,z}$ to simulate the addition of external magnetic fields (with strength δ), modify the geometry, or increase the spatial range of interactions beyond the nearest neighbour couplings. Changing these parameters can considerably affect the system properties and thus can extend the range of phenomena one can study.

Having introduced these two classes of Hamiltonians commonly used to study several many-body phenomena in the condensed-matter physics field, I now give a short overview of the various quantum simulator platforms available today.

1.2 Overview of the various platforms for quantum simulation

In order to build a quantum simulator, we have to satisfy three requirements:

- First, we must position individual particles in a controllable geometry so as to represent a spin or mimic a node in a crystal structure.

- Second, we must control the interaction between the particles and the external environment as well as between the particles themselves.

- Third, we must be able to initialize the system in specific states and measure each particle's state.

Various platforms fulfil these three requirements with different levels of control.

Ultracold atoms in optical lattices. These platforms rely on the ability to trap neutral atoms/molecules in a controlled spatial configuration. The most common trapping technique uses periodic trapping potentials generated from standing waves of off-resonant light, known as optical lattices [Bloch, 2005]. To load one particle in each lattice sites, the experimentalists start from a quantum degenerate gas and drive it through a phase transition into a Mott insulator [Greiner *et al.*, 2002]. The use of a *quantum gas microscope* [Bakr *et al.*, 2009] (*i.e.* the combination of lattices with high numerical aperture lenses or optical objectives) allows reaching single-site resolution

and extends the controllability of the system by offering the ability to address each site individually [Wang *et al.*, 2015].

Optical lattices with fermionic particles (such as ^{6}Li atoms) naturally implement the Fermi Hubbard models described in Eq. 1.1, where particles can hop from one lattice site to another. The parameters of the Hamiltonian can be varied: the geometry can be tuned by playing on the relative phase and amplitude of the optical lattice lasers. The ratio U/t can also be modified by varying the trap depth, thus resulting in tunable quantum simulators of hopping Hamiltonians [Esslinger, 2010]. Several groups have been able to measure characteristic phenomena of the Hubbards model, such as the observation of new topologic phases [Atala *et al.*, 2013], or the emergence of long-range antiferromagnetic orders [Tarruell and Sanchez-Palencia, 2018]. So far, all the platforms mentioned in this paragraph employ neutral atoms, but other particles as polar molecules can be used. More particularly, the natural dipole-dipole interaction occurring between polar molecules allows for the implementation of spin models [Zhou, Ortner, and Rabl, 2011; Yan *et al.*, 2013].

Trapped Ions. Trapped ion-based platforms rely on the trapping of individual ions via Penning or Paul traps [Brown and Gabrielse, 1986; Paul, 1990]. Spin models can be implemented by laser coupling the ion internal states with their collective vibrational modes [Cirac and Zoller, 1995]. High-fidelity operations can be performed involving tens of ions in a 1D chain [Monz *et al.*, 2011; Lanyon *et al.*, 2011] and in 2D crystals [Kiesenhofer *et al.*, 2023]. In addition, the laser coupling-based interactions allow implementing spin Hamiltonians with various interaction ranges. The strength of the interaction decreases as a power law $1/r^\alpha$ (r being the distance between two ions) with α ranging from $\alpha = 0$ (all-to-all couplings) to $\alpha = 3$ (dipolar-like interactions). This platform has probably the highest fidelity record for manipulating and reading atom states.

Superconducting circuits. In contrast to the two previous classes of quantum simulators, superconducting circuits do not rely on atoms or molecules but on *artificial atoms*. These artificial atoms exhibit discrete atom-like electronic structures resulting from the engineering of Josephson qubit circuits [Nakamura, Pashkin, and Tsai, 1999]. These circuits can then be coupled by exchanging microwave photons in cavities [Wallraff *et al.*, 2004], or by sharing mutual inductances [Chen *et al.*, 2014]. One of the main characteristic features of superconducting circuits is that the couplings do not rely

on the geometrical arrangement but on interconnected wiring. Therefore this simulator can be configured to implement a wide variety of spin Hamiltonians, including spin and Hubbard models [Salathé *et al.*, 2015; Barends *et al.*, 2015]. Moreover, these platforms exhibit high fidelity in single- and two-qubit operations [Krantz *et al.*, 2019; Kjaergaard *et al.*, 2020]. They can also be integrated into a compact on-chip design, making them very attractive for the future of quantum simulation and quantum computing [Devoret and Schoelkopf, 2013]. Multinational companies like Google® or IBM® are investigating in this technology. Most the superconducting circuits platforms used for quantum simulations work in digital mode, with the recent exceptions of [Rosenberg *et al.*, 2024; Andersen *et al.*, 2024].

Other platforms.   Other types of platforms are also promising candidates for quantum simulation. Among them, we can cite solid-state platforms, such as color centers (for example, NV centers in diamond), quantum dots or excitons-based platforms. We can also mention photons/atoms coupled to cavities-based platforms [Altman *et al.*, 2021].

Future improvements.   Independently of the technologies used, experimentalists aim at improving their platform in four different areas. First, they seek to increase the number of particles beyond the current limit of hundreds, which would enable the observation of new macroscopic phenomena. Second, they aim at enhancing the reliability of the various platforms by reducing experimental imperfections to faithfully perform quantum simulations (depending on the platform, improving the *reliability* can involve various technological improvements). Third, they seek to increase the cycling rate of the experiment. Due to the quantum nature of the system, experiments must be repeated multiple times to build statistics and reconstruct the wave function of the produced state, or at least gather partial information about it. Consequently, the frequency at which the machine operates determines the data accumulation rate. Last, the experimentalists aim at extending the range of applications for each platform by implementing new Hamiltonians.

After having described a variety of quantum simulators, I now focus on our Rydberg-based platform and present an overview of its evolution.

1.3 Evolution of Rydberg quantum simulators

In this section, I will briefly explain the main principles of these platforms. In Chapter 2, I will provide a detail description of the apparatus that I used during my Ph.D. thesis.

Rydberg atoms. The idea of Rydberg platforms started in the early 2000s with two proposals suggesting to use Rydberg atoms to build quantum gates [Jaksch *et al.*, 2000; Lukin *et al.*, 2001]. A Rydberg state is a high energy state whose principal quantum number can be increased to a large value $n \gtrsim 20$. Classically, a Rydberg atom is represented with one of its electrons orbiting far from the nucleus and the remaining core electrons. In this configuration, the atom behaves like an hydrogen atom exhibiting a large electric dipole. This large electric dipole allows two Rydberg atoms separated by a few micrometres to interact with dynamics timescales of a few microseconds shorter than the Rydberg lifetime of few hundreds microseconds. Thus, it ensures a long coherence time for the dynamics (see Table 1.1).

An important consequence of these interactions is known as the *Rydberg blockade.* It refers to the fact that two interacting atoms cannot simultaneously be excited to the Rydberg state due to the energy shift induced by the interaction (more details about the nature of this interaction will be given in Sec. 4.3.1). This Rydberg blockade generates entangled states between atoms and therefore has been proposed as a mean of creating quantum gates. In the early 2000s, this idea motivated numerous Rydberg gas experiments to try to show evidence of blockade in atomic gases. The first observations were obtained in 2004, opening the field of Rydberg-based quantum simulators/computers [Löw *et al.*, 2012]. However, in these gas experiments, the positions of the atoms were not controlled, leading only to poor control over Rydberg interactions that strongly depend on the distance between them.

One solution to this problem consists in using *optical tweezers* to individually trap each atom and thus pin their position at a target location.

Optical tweezer. In order to gain better control over the Rydberg interactions, atoms can be trapped using light either via optical lattices or optical tweezers. The experiment on which I worked during my Ph.D. uses arrays of optical tweezers to trap individual Rubidium atoms. A beam is tightly focused to a micrometer-sized spot,

Physical properties	n scaling	Order of magnitude
Binding energy E_n	n^{-2}	900 GHz
Energy energy $E_n - E_{n+1}$	n^{-3}	30 GHz
Orbital radius R	n^2	200 nm
Rydberg lifetime τ	n^3	200 μs
Polarisability α [Lai *et al.*, 2018]	n^7	200 MHz/(V/cm)^2
Ground-Rydberg dipole d_{gr}	$n^{-3/2}$	10^{-26} C.m
Rydberg-Rydberg dipole $d_{rr'}$	n^2	10^{-29} C.m
Van der Waals interaction strength C_6	n^{11}	20 GHz.$(\mu m)^6$
Resonant dipole interaction strength C_3	n^4	1 GHz.$(\mu m)^3$

Table 1.1.: Scaling law with n of a few properties of Rydberg states. The numerical values are calculated for one or two Rydberg atoms in the $n = 60$ state.

resulting in a potential where one neutral atom can be trapped via optical dipole light shifts (more details about this trapping mechanism are given in Sec. 2.1.2). This method developed by Philippe Grangier at Institut d'Optique (IOGS) [Schlosser *et al.*, 2001] enabled our team, jointly with the Mark Saffman's group, to observe Rydberg blockade between two atoms for the first time in 2009 [Gaëtan *et al.*, 2009; Urban *et al.*, 2009]. A few months later, both teams proved the generation of entangled states [Wilk *et al.*, 2010] and demonstrated the realization of the two-qubit C-NOT gate [Isenhower *et al.*, 2010], thus starting the race towards Rydberg/tweezer-based quantum simulators/computers.

Race towards quantum simulators/computers. Since the demonstration of the Rydberg blockade on individual atoms in 2009/2010, the Rydberg platforms have become promising for quantum simulation/computing and have undergone several improvements. These improvements are threefolds:

- First, the number of atoms used in controlled experiments has risen from a few to hundreds. Initially, the tweezer platforms suffered from stochastic loading. The tweezers were loaded with a single atom with a probability of 1/2, limiting the experiments to just a few atoms. In 2016, our group and the one of Mikhail Lukin developed a new technique to move a trapped atom from one tweezer to an other [Barredo *et al.*, 2016; Endres *et al.*, 2016]. It allows rearranging a random configuration of a half-loaded tweezers array into a deterministic one (more details in Sec. 2.1.2). This important breakthrough unlocked the number of atoms routinely used in experiments to hundreds. Currently, tweezer platforms
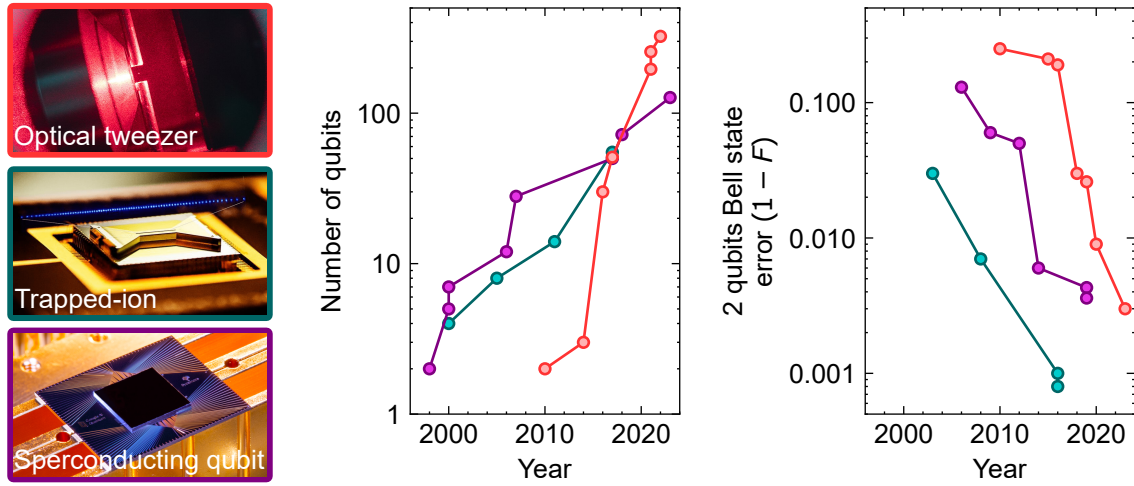
Figure 1.1: Evolution of tweezer, trapped-ion and superconducting qubit platforms over the last decades. Left panel: Illustrations (images taken from: the Van Swinderen Institute, the Duke University and [Arute *et al.*, 2019]). Center panel: Scalability (the references are: tweezer [Wilk *et al.*, 2010; Isenhower *et al.*, 2010; Barredo *et al.*, 2014, 2016; Labuhn *et al.*, 2016; Bernien *et al.*, 2017; Scholl *et al.*, 2021; Ebadi *et al.*, 2021; Schymik *et al.*, 2022], trapped-ion [Sackett *et al.*, 2000; Häffner *et al.*, 2005; Monz *et al.*, 2011; Zhang *et al.*, 2017], and superconducting circuit [Chuang, Gershenfeld, and Kubinec, 1998; Marx *et al.*, 2000; MIT, 2000; Sci, 2006; Nan, 2007; Will, 2017; Conover, 2018; Kim *et al.*, 2023]) Right panel: Fidelity (the references are: tweezers [Wilk *et al.*, 2010; Maller *et al.*, 2015; Jau *et al.*, 2016; Levine *et al.*, 2018, 2019; Madjarov *et al.*, 2020; Scholl *et al.*, 2023], trapped-ions [Leibfried *et al.*, 2003; Benhelm *et al.*, 2008; Ballance *et al.*, 2016; Gaebler *et al.*, 2016], and superconducting circuits [Steffen *et al.*, 2006; DiCarlo *et al.*, 2009; Chow *et al.*, 2012; Barends *et al.*, 2014, 2019; Arute *et al.*, 2019])

overscale the number of qubits used in other platforms, such as trapped ions or superconducting circuit platforms (see Fig. 1.1) [Endres *et al.*, 2016; Norcia *et al.*, 2024; Manetsch *et al.*, 2024; Pichard *et al.*, 2024].

- Second, the fidelity of quantum gates using atoms increased significantly over the last seven years. Initially, the Rydberg/tweezer platform fidelities have lagged behind their competitors such as trapped-ion and superconducting circuit platforms. Recent technical improvements such as reduced-noise lasers [de Léséleuc *et al.*, 2018] or optimized pulse sequences via optimal control [Koch *et al.*, 2022] led to rapid progress over the last decade. Two atoms quantum gate fidelities start to reach comparable efficiencies to the ones obtained with trapped ions and superconducting platforms (see Fig. 1.1). Currently, the main obstacles
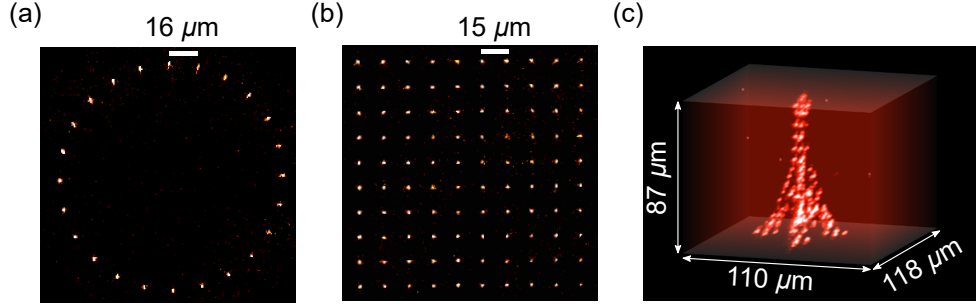
Figure 1.2: Arrays of individual atoms using different geometries. (a)/(b)/(c) Fluorescence image of individual Rubidium atoms (white dots) trapped in arrays of optical tweezers in 1D (with periodic boundary conditions), 2D and 3D. The 3D image has been take from [Barredo *et al.*, 2020].

are primarily technical limitations. With the development of new technologies, better efficiencies can be hoped for in the future [Scholl *et al.*, 2023].

- Third, over the last decade, Rydberg/tweezer-based quantum simulators have become a versatile platform allowing for the study of a wider range of Hamiltonians. Three main parameters can be chosen and varied. First, using a Spatial Light Modulator (SLM) we can achieve arbitrary geometry in 1, 2 and 3D [Barredo *et al.*, 2016, 2018, 2020] (see examples in Fig. 1.2). Second the addition of external fields using microwaves or light add linear terms to the Hamiltonian, thus modifying its properties. Third, the choice of the Rydberg states to encode the spin/qubit states corresponds to different interactions between the atoms. Using only one species, different Hamiltonian can be implemented. For example, for Rubidium, encoding the spin states between the ground state $|g\rangle = |\downarrow\rangle$ and a Rydberg state $|nS\rangle = |\uparrow\rangle$ leads to off resonant dipole-dipole interactions between the spins (also known as van der Waals interactions) that implement an effective Ising model. If we now choose to encode the spin states between two Rydberg states of opposite parity $|nS\rangle = |\uparrow\rangle$ and $|nP\rangle = |\downarrow\rangle$, the atoms are coupled via resonant dipole-dipole interactions that implement an effective dipolar XY model [Browaeys and Lahaye, 2020].

This thesis work. When I joined in the group in october 2020, most of the studies were focused on the 2D Ising model. During my four years as Ph.D. student, we extended our investigations to another spin Hamiltonian: the quantum XY model,

25

reading:

$$\mathcal{H}_{\mathrm{XY}} = \hbar \sum_{i,j} J_{i,j} \left(\sigma_i^x \sigma_j^x + \sigma_i^y \sigma_j^y \right). \tag{1.3}$$

The quantum XY spin model is particularly interesting for understanding various materials, ranging from magnetic insulators to high-temperature superconductors, and for studying emergent phenomena such as magnetism and spin transport properties [Browaeys and Lahaye, 2020]. In contrast with the Ising model, this XY model is in a sense more quantum since it does not exhibit classical ground states. Numerical simulations and experiments showed that this model captures many non-intuitive physical phenomena such as spin liquids, quantum criticality, continuous symmetry breaking, superconductivity, phase transitions, quantum entanglement, and topological order. Moreover, depending of the geometry and of the interaction range, this model exhibits various phase diagrams. Determining the boundaries of these phase diagrams and the nature of their corresponding quantum phase transitions is an active area of research.

Using the recent experimental developments, we performed experiments with up to hundreds of atoms, thus reaching a regime for which classical simulations are extremely difficult to perform in some cases. One of my main contributions to the lab was the development of single site manipulation of Rydberg atoms. It allowed us to prepare a wider range of many-body states exhibiting exotic behaviours.

Thesis outline. The first part of the manuscript (Part I) describes the technical improvements achieved during my Ph.D. Chapter 2 provides an overview of the working principle of the experiment. Chapter 3 details the development of the single site manipulation of Rydberg atoms using arrays of local addressing beams. Chapter 4 presents our preliminary results in addressing a current experimental limitation of the platform called static position disorder. In the second part of the manuscript (Part II), I present how we implement the dipolar XY model and study its ground states on various geometries. By combining our recent ability to address single Rydberg atoms with an adiabatic procedure, we first prepare the XY ground state on square arrays and probe its main characteristics (Chapter 5). Then we move to the study of the XY ground states on frustrated geometries which are expected to be exotic phases of matter such as spin liquids (Chapter 6). The third part (Part III) focuses on out-of-equilibrium physics also known as *quench experiments*. I show that the dipolar XY model can produce scalable spin squeezing (Chapter 7). Finally, I demonstrate that

using a method called quench spectroscopy, we can measure the dispersion relations of the XY model (Chapter 8).

Part I.

Upgrading the experimental apparatus

Chapter 2

Presentation of the experimental set-up

Contents

In this chapter, I give an overview of the experimental apparatus and present the different techniques used to control the atoms. The chapter is organized as follows:

- First, I explain how to trap individual atoms of ^{87}Rb in arrays of optical tweezers.

- Second, I describe the different ground state manipulations we perform on the atoms.

- Third, I present how to excite/deexcite the atoms in/from the Rydberg manifold and the various Rydberg state manipulations we use.

- Fourth, I end up by explaining how we control the magnetic/electric field environment seen by the atoms.

2.1 Individual ^{87}Rb atoms trapped in arrays of optical tweezers

2.1.1 Trapping and imaging a single atom

I begin by describing how starting from a solid piece of Rubidium, we trap one single atom in an optical tweezer.

Magneto-Optical Trap. The first step consists in cooling and trapping a cloud of atoms in a Magneto-Optical Trap (MOT) from which we load individual atoms in the optical tweezers. The experiment occurs in the apparatus depicted in Fig. 2.1. This device can be decomposed into the oven, the Zeeman slower, and the science chamber. We use ion pumps (pink colour) to place all parts under ultra-high vacuum and reach a pressure of a few $\sim 10^{-11}$ millibars, ensuring the isolation of the atoms from the outside environment. A few grams of a solid piece of Rubidium are placed in the oven and heated to $60\,^\circ\text{C}$. Rubidium evaporates, the vapour enters the Zeeman slower and exits into the science chamber with a typical speed of $\sim 10\,\text{m.s}^{-1}$. Using three pairs of counter-propagating beams (represented in red), we slow down the atoms in all directions [Metcalf and van der Straten, 1999]. The light at $780\,\text{nm}$, is composed of two frequencies: one slightly red-detuned from the cycling transition $(5S_{1/2}, F = 2) \leftrightarrow (5P_{3/2}, F = 3)$ ensuring the cooling and the other on resonance with the $(5S_{1/2}, F = 1) \leftrightarrow (5P_{3/2}, F = 2)$ transition repumping the atoms from $(5S_{1/2}, F = 1)$ to the cycling transition. In addition, a pair of coils inside the vacuum chamber in the anti-Helmholtz configuration generates a magnetic field gradient, thus trapping the atoms in an MOT (more details in Ref. [Beguin, 2013; de Léséleuc, 2021; Scholl, 2021]). This atomic cloud contains $\sim 10^7$ atoms at a temperature of $\sim 100\,\mu\text{K}$ and we will use it as a reservoir of atoms to fill the optical tweezers.

Trapping a single atom in an optical tweezer. We generate optical tweezers by focusing $820\,\text{nm}$ red detuned light (from the $(5S) \leftrightarrow (5P)$ transition) in the science
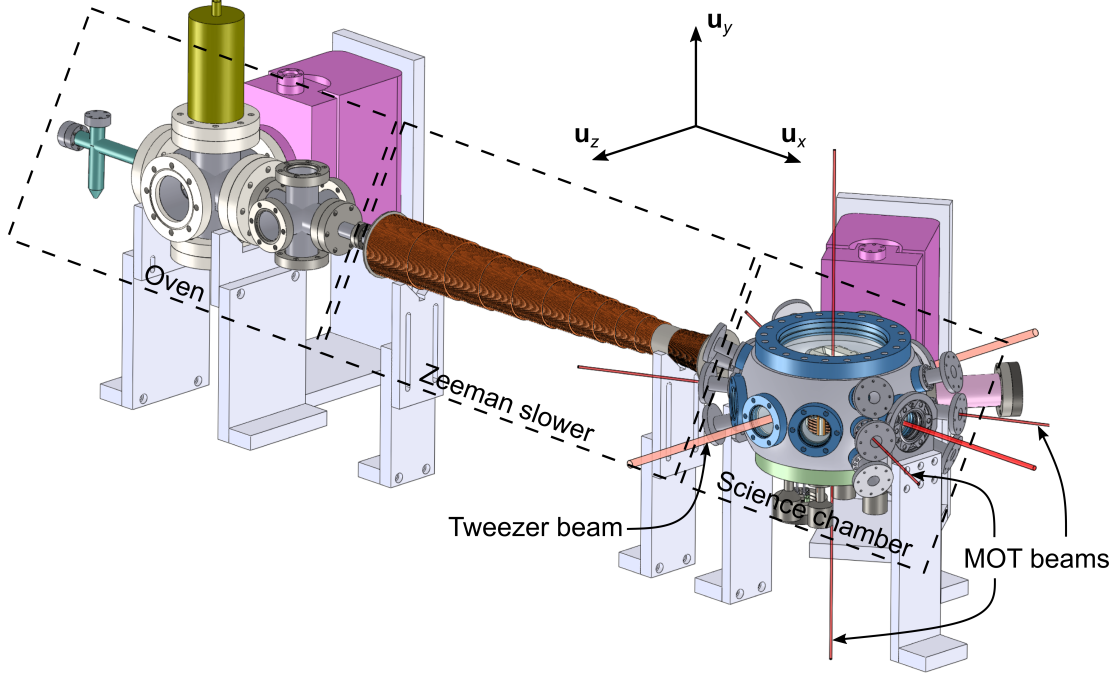
Figure 2.1: Experimental apparatus. It is composed of three parts: the oven, the Zeeman slower and the science chamber where we trap the atoms in a MOT before loading the optical tweezers.

chamber using a pair of aspherical lenses under vacuum with a numerical aperture of 0.5 and a focal length $f = 10\,\mathrm{mm}$ (see Fig. 2.3 and [Beguin, 2013]). The light spot is well described by a Gaussian profile of intensity:

$$I(r, z) = \frac{I_0}{1 + (z/z_\mathrm{R})^2} \exp\left(-\frac{2r^2}{w_0^2\left(1 + (z/z_\mathrm{R})^2\right)}\right), \qquad (2.1)$$

with a waist $w_0 = 1.1\,\mu\mathrm{m}$, and a Rayleigh range $z_\mathrm{R} = 4.6\,\mu\mathrm{m}$. Near the light spot, due to the induced dipolar force, an atom experiences a potential $U(r, z) = \hbar\Gamma_{5P}^2 I(r, z)/(8\Delta I_\mathrm{sat})$ with Γ_{5P} and I_sat the decay rate and saturation intensity of the $5P$ state, and $\Delta = \omega_\mathrm{tweezer} - \omega_{5S\leftrightarrow 5P}$ the tweezer light detuning[1]. The *trap depth* is the potential at the center of the tweezer $U_0 = U(x = 0, z = 0) \simeq h \times 20\,\mathrm{MHz} \simeq k_B \times 1\,\mathrm{mK}$ for a total power $P = \pi w_0^2 I_0/2 \approx 3\,\mathrm{mW}$. The sign of Δ being negative, this potential is attractive. However, since the dipole force is conservative, we must slow down the atom to trap it. The MOT beams achieve this step by applying a friction force on the atom while it is falling into the trap.

---

[1]For a rigorous calculation of the potential, one would need to sum up all the contributions of all the excited states as detailed in Ref. [Darquié, 2005].

We now answer the question: what if an atom enters a trap already filled with another one? Due to the tight focus of the tweezer light in combination with the MOT light, the two atoms undergo fast inelastic light-assisted collisions, which causes the ejection of both atoms from the trap [Schlosser *et al.*, 2001]. This *collisional blockade* mechanism prevents two atoms from being trapped in the optical tweezer simultaneously. Once the trap is empty, it can load another atom again. Consequently, the optical tweezer has only two states with 50% probability: either it contains zero or one atom.

Imaging the atoms.   Once trapped in the tweezers, the atoms scatter the MOT light in all directions. Using the aspherical lenses, we collect the 780 nm fluorescence light that we image on an EMCCD camera with an exposure time of 20 ms (see Fig. 2.3). Figure 2.2 shows the fluorescence signal averaged on 3×3 pixels centered around the trap (green square) as a function of time. The signal is a two-level function: a high/low signal corresponds to the presence/absence of an atom in the tweezer. Using an adjustable threshold function (red dashed line), we detect the presence/absence of the atom if the fluorescence signal is above/below this threshold. Figure 2.2 shows a typical histogram of fluorescence level distribution after thousands of images. The two level are well separated, leading to a detection error of less than 0.1%.

Lifetime of the atoms in the trap.   We need to ensure that the lifetime of the atoms in the tweezers is larger than the typical duration of an experiment of ~ 1 s. To measure this lifetime, we first load the atoms, image them (as in Fig. 2.2), wait, and image again to check if the atoms are still in their traps. We then compute the recapture probability by measuring how many atoms stay in their traps during this waiting time. By repeating the experiment for various waiting times, we estimate the lifetime of the atoms in the tweezers. As shown in Fig. 2.2 we measure a lifetime of 22 s which is long enough to perform experiments. We attribute this lifetime to elastic collisions with the background gas (at room temperature of 300 K), expelling the atoms from their trap. On another experimental apparatus, our team showed that this lifetime can be improved up more than 2 hours by lowering the background gas pressure using a cryogenic setup [Schymik, 2022].
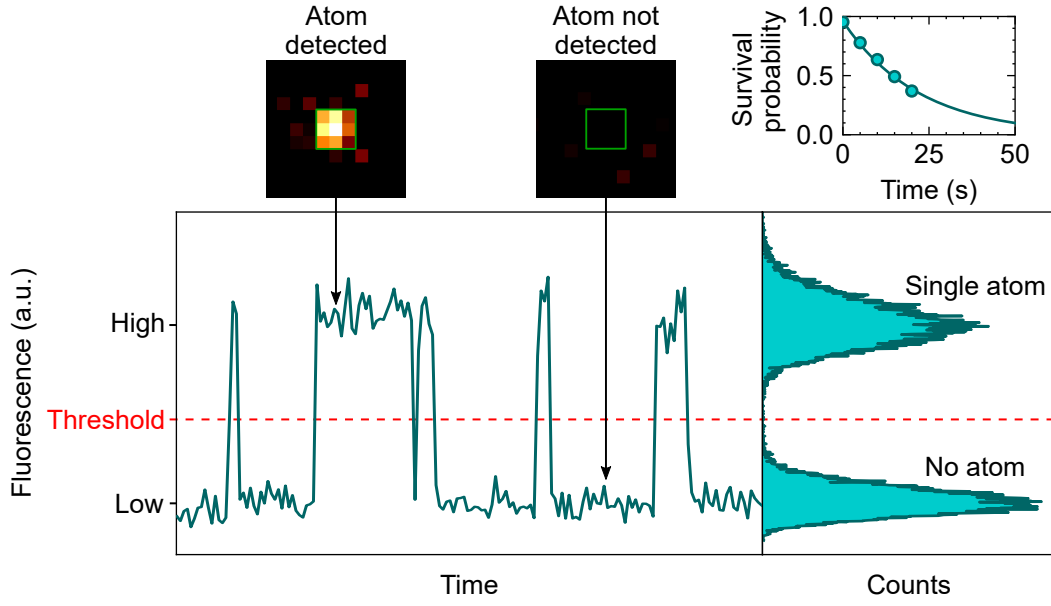
Figure 2.2: Fluorescence image. Upper left plot: Fluorescence images with/without an atom trapped in an optical tweezer. Bottom left panel: Averaged fluorescence signal in the green square as a function of time. Upper right plot: Survival probability as a function of the waiting time. The solid curves is a exponential function fit with a lifetime of 22 s. Bottom right panel: Histogram of the fluorescence signal after thousands of images.

2.1.2 Arrays of single atoms

I have presented how to trap and image a single atom. We must now trap single atoms in an array of optical tweezers to study many-body systems. The first challenge is to generate multiple optical tweezers, and the second is to fill all of them simultaneously.

Arrays of optical tweezers. Several methods exist to generate arrays of optical tweezers, such as the use of an array of microlenses [Schäffner *et al.*, 2020], Acousto Optic Deflectors (AODs), or holographic techniques. In 2014, our team demonstrated the generation of multiple tweezers using a Spatial Light Modulator (SLM). The idea is to send the tweezer light on a SLM imprinting a spatially-dependant arbitrary phase on the laser. Then, when focusing this laser in the chamber using the aspherical lens, it diffracts in several spots. Each of these spots is used as an optical tweezer. The 2D Fourier transform of the light pattern on the SLM gives the light pattern on the atomic plane. Since the SLM only controls the phase profile of the light and not its intensity profile, we use a Gerchberg-Saxton (GS) algorithm [Gerchberg and Saxton, 1972] to optimize the SLM phase pattern to generate the desired array of tweezers.
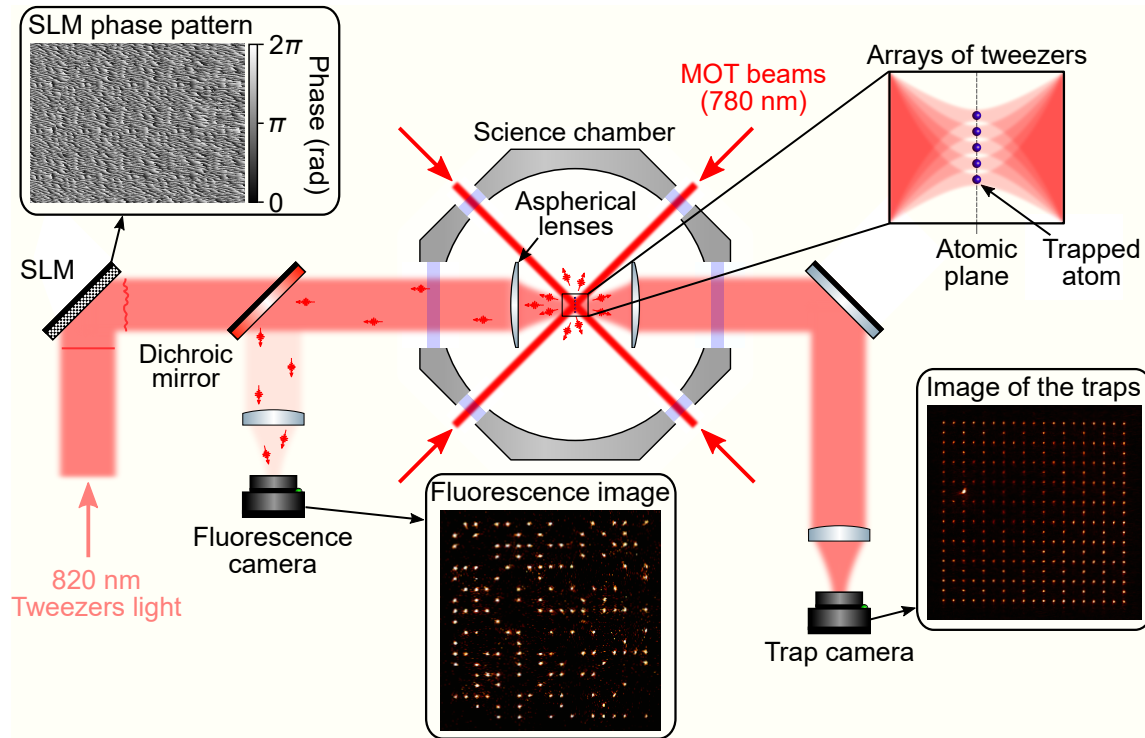
Figure 2.3: Sketch of the set-up to generate arrays of optical tweezers. The tweezers are generated using an SLM imprinting a phase pattern on the $820\,\text{nm}$ laser. A typical phase pattern is shown in the panel SLM phase pattern. The light is then focused in the science chamber diffracting in several optical tweezers. After the chamber, a camera images the traps (the most intense light spot corresponds to the 0th order diffraction peak of the SLM). An EMCCD camera also images the atomic plane and collect the fluorescence light emitted by the trapped atoms. A typical fluorescence image is shown.

This method offers the advantage of easily changing the tweezer array geometry by modifying the SLM phase pattern.

Figure 2.3 depicts the experimental setup. A control camera placed after the chamber images the atomic plane and shows the shape of the traps. The EMCCD camera also images the atomic plane and measures the fluorescence of the trapped atoms. A typical fluorescence image is shown in Fig. 2.3. Each bright dot corresponds to the presence of a single atom in a tweezer. As explained earlier, the collisional blockade mechanism randomly fills each trap with zero or one atom, resulting in a disordered distribution of atoms in space. As we wish to perform quantum simulations of ordered systems such as crystalline structures, this disorder is a problem.

From random to deterministic geometries.   To fill all the tweezers, several methods exist:

- The simplest approach consists of waiting until all the tweezers trap one atom simultaneously. This naive method only works for a small number of atoms. Each tweezer having a probability of $p_{\text{fill}} \approx 0.5$ to be filled, the time we need to wait to load N traps increase exponentially as p_{fill}^N.

- The second methods consists into increasing the loading probability p_{fill} by overcoming the collisional blockage mechanism. As an example, the use of grey molasses to drive light-assisted collisions in repulsive molecular states preventing the loss of both atoms when two of them enter the same trap already showed an improvement up to $p_{\text{fill}} \approx 0.9$ [Brown *et al.*, 2019]. Using this procedure, we can perform experiments with a larger number of atoms. However, this method still suffers from the same problem. If one wants to work with $N = 100$ atoms, in average, 10 atoms will be missing.

- Another idea consists in moving the atoms from one trap to another. Starting from a random configuration (as shown by the fluorescence image of Fig. 2.3), we rearrange the distribution of atoms across the array into a target configuration. The main disadvantage of this method is that at least twice as many traps are needed as the desired configuration since half of them are used as reservoir traps. However, despite this drawback, since the first proof of principle demonstrated by our team in 2016 [Barredo *et al.*, 2016], this method remains the most efficient for assembling the large arrays. I will now describe this method.

Assembling arrays of single atoms.   In order to move the atoms we use a *moving tweezer*. We independently generate this tweezer by sending 820 nm light through two crossed AODs. We then combine this light with the tweezer ones before entering the science chamber. The position and power of the moving tweezer are controlled by varying the radiofrequency (rf) signal sent to the AODs. To move one atom from one trap to an empty one, we follow the following procedure (see Fig. 2.4a). We first take the atom from the initial trap by overlapping the moving tweezer and ramping its power up to $\sim U_0$ in $\sim 400\,\mu\text{s}$. We then move the atom to the target location with a typical speed of $\sim 75\,\text{nm}/\mu\text{s}$. We release the atom by adiabatically switching off the moving tweezer power in $\sim 400\,\mu\text{s}$. When optimized, the transfer process is more than

99% efficient [Barredo *et al.*, 2016] and then can be repeated to move all the atoms to the desired trap position.

Figure 2.4b summarizes the experimental sequence to assemble arrays. We start by loading the atoms in the tweezers using the MOT in ~ 200 ms. We stop the loading by switching off the magnetic field gradient, thus dispersing the atomic cloud. After the loading, we apply the following sequence. First, we take a picture to identify which trap contains an atom. Second, we then calculate the different atom transfers required to end up in the target configuration [Schymik *et al.*, 2020] (in Fig. 2.4b we target a 10×10 square array). The list of moves is then sent to an Arduino Due$^{\circledR}$ converting the digital signals into analog ones. This step takes ~ 50 ms approximatively. Third, the Arduinos send the analog signals to rf-generators connected to the AODs piloting the moving tweezer and moving the atoms. This step takes ~ 100 ms for a target array of $N \sim 100$ atoms, and its time duration varies with N. Finally, we take a last image to check that the final configuration corresponds to the expected one. As shown in Fig. 2.4b, usually, for target arrays of hundreds of atoms, there is a chance to lose an atom due to background gas collision or loss during an atom transfer. To overcome these problems, we usually repeat this sequence twice before taking the final image (as illustrated in Fig. 2.4b). For target arrays of $N = 100$ atoms, at each repetition of the experiment, the probability of getting *defect-free arrays* (no atom missing in the traps where we want them and no extra atoms where we do not want them) is about 15% [Scholl, 2021].

I presented how to trap and image a single atom in an optical tweezer. I then described how we generate arrays of optical tweezers and how we assemble them to get target geometries. Starting from these arrays, we perform quantum simulation experiments. The following section will give an overview of the experimental sequence.

2.1.3 A typical experimental sequence

The experimental sequence is composed of four distinct steps:

- **Arrays of single atoms.** We first generate an array of single atoms as described in the previous section 2.1.2.

- **Ground state manipulations.** The second step consists of different ground
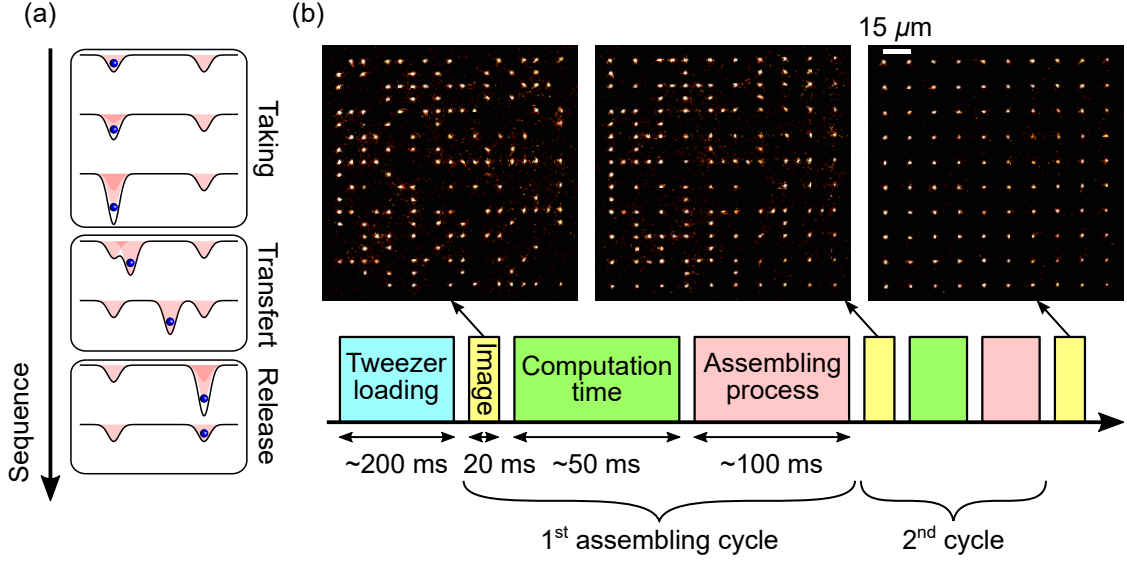
Figure 2.4: Assembling arrays of single atoms. (a) Different moving tweezer steps to move one atom from one trap to an other. (b) Experimental sequence to assemble a random configuration into the target one (here it is a square 10×10 array).

state manipulations to cool the atoms and prepare all of them in the same hyperfine ground state (see the following section 2.2).

- **Rydberg sequence.** The third consists in performing the many-body experiment (see Sec. 2.3). For example, for the simulation of the XY model, we isolate two specific states of the Rydberg manifold to encode the $|\uparrow\rangle$ and $|\downarrow\rangle$ states. We excite the atoms to these Rydberg states: either in $|\uparrow\rangle$, $|\downarrow\rangle$ or in a quantum superposition of both. Then, we let them interact under the dipole-dipole interaction, implementing the XY model. At the end of the dynamics, we transfer back the $|\uparrow\rangle$ atoms to the ground state. This Rydberg sequence takes about $10\,\mu$s.

- **Measurement.** After the Rydberg sequence, we take a fluorescence image. We only image the atoms in the ground state (meaning the atoms being in $|\uparrow\rangle$ at the end of the dynamics) while the others left in the Rydberg state are lost. Thus, we map the $|\uparrow\rangle/|\downarrow\rangle$ state to the presence/absence of the corresponding atom. We repeat the experiment to build statistics and assess the properties of the many-body state we generated.

Measuring the magnetizations.   From the series of snapshots, we compute several observables. The easiest one is the magnetization of each atom. For atom i, it reads: $\langle\sigma_i^z\rangle = 1/N_{\text{shot}} \sum_{l=1}^{N_{\text{shot}}} \sigma_i^z(l)$ with N_{shot} the number of taken snapshots and $\sigma_i^z(l) = 1$ ($\sigma_i^z(l) = -1$) if we detect the presence (absence) of the atom in snapshot l. Since the magnetization measurement follows a binomial law, we calculate its error bar (also called quantum projection noise): $u(\sigma_i^z) = \sqrt{(1 - \langle\sigma_i^z\rangle^2)}/\sqrt{N_{\text{shot}}}$. Assuming that we measure $\langle\sigma_i^z\rangle = 0$, taking 100 snapshots would give a precision of 0.1, 1000 shots give 0.03 and 10000 shots gives 0.01. The cycling rate of the experiment is between $f = 1$ and $2\,\text{Hz}$. Assuming we want to reach a precision of 0.03, and that we only keep 15% of the shots for which the initial array was perfectly assembled, then, we need to average the data over $1000\,\text{shots}/(15\,\%\times 1\,\text{Hz}) \approx 2\,\text{hours}$ for each point. The cycling rate and the probability to prepare defect-free arrays are the main limiting factors to the best precisions that we can achieve.

Measuring correlation functions.   Measuring the magnetization of each atom is insufficient to characterize many-body systems and in particular entanglement. Interesting properties are only revealed upon measuring correlations between the atoms. We can for example compute the two-body correlation function between atom i and j defined as $\langle\sigma_i^z\sigma_j^z\rangle = 1/N_{\text{shot}} \sum_{l=1}^{N_{\text{shot}}} \sigma_i^z(l)\sigma_j^z(l)$. As for the magnetization, $\sigma_i^z\sigma_j^z$ follows a binomial distribution from which we can calculate its error bar $u(\sigma_i^z\sigma_j^z) = \sqrt{(1 - \langle\sigma_i^z\sigma_j^z\rangle^2)}/\sqrt{N_{\text{shot}}}$. The main issue with this two-body correlation definition, is that $\langle\sigma_i^z\sigma_j^z\rangle$ only measures classical correlations. For two independent spins i and j exhibiting non zero magnetizations ($\langle\sigma_i^z\rangle \neq 0$ and $\langle\sigma_j^z\rangle \neq 0$), we measure a non-zero correlation $\langle\sigma_i^z\sigma_j^z\rangle = \langle\sigma_i^z\rangle\langle\sigma_j^z\rangle \neq 0$. Measuring non-zero correlations for independent spins is counter intuitive. For this reason, we prefer to use the *connected* correlations defined as $\langle\sigma_i^z\sigma_j^z\rangle_{\text{c}} = \langle(\sigma_i^z - \langle\sigma_i^z\rangle)(\sigma_j^z - \langle\sigma_j^z\rangle)\rangle = \langle\sigma_i^z\sigma_j^z\rangle - \langle\sigma_i^z\rangle\langle\sigma_j^z\rangle$. Spins always exhibit zero connected correlations when they are independent. Reciprocally, measuring a non-zero connected correlation necessarily implies that the two spins are in a statistical mixture of states, in a quantum superposition or are entangled.

2.2   Ground-state manipulations

After preparing an array of single atoms, we perform different ground state manipulations. The goals are twofold: first, we reduce the temperature of the atoms in their

trap, and second, using optical pumping, we prepare all of them in the same hyperfine ground state before starting the Rydberg excitation (see Sec. 2.3).

2.2.1 Cooling the atoms

Motivations. There are two reasons why we wish to cool the atoms. First, the tweezer lights apply a repulsive force on the atoms in a Rydberg state, expelling them from the traps. Consequently, to avoid losing the atoms during the Rydberg sequence, we switch off the trapping light and let them in free flight. During this time, if the atomic temperature is too high, the atoms will move so far away from the center of their trap that even if we deexcite them to the ground state and switch back on the tweezers we will not recapture them. An atom that should be recaptured and imaged will then be lost and counted as in $|\downarrow\rangle$ instead of $|\uparrow\rangle$.

Second, the atoms are not pinned to the center of their tweezer due to the atomic temperature. When the traps are turned off just before starting the Rydberg sequence, the atoms start with an initial position $\mathbf{r}_i^0$ (with respect to the center of their trap) and an initial velocity $\mathbf{v}_i$. Their motion can be modelled as $\mathbf{r}_i(t) = \mathbf{r}_i^0 + t\mathbf{v}_i$. Since the dipole-dipole interaction energy between two atoms i and j is highly sensitive to the distance $J_{ij} \propto 1/|\mathbf{r}_i - \mathbf{r}_j|^3$, its value varies during the Rydberg dynamics, fluctuates from one pair of atoms to another (supposed to be separated by the same distance) and differs from one repetition of the experiment to another (this latter effect is also called shot-to-shot positional disorder). All these detrimental effects contribute to a decrease in the fidelity of the experiment.

Motion of the atoms. The temperature of the atoms is about a few μK, much lower than the trap depth of U_0. Thus, the atoms explore a region close to the center of the trap. The trapping potential seen by the atoms can then be approximated by a harmonic potential with radial and longitudinal frequencies $\omega_\perp$ and $\omega_\parallel$ reading:

$$\omega_\perp = \sqrt{\frac{4U_0}{mw^2}} \ \text{ and } \ \omega_\parallel = \sqrt{\frac{2U_0}{mz_\mathrm{R}^2}}, \tag{2.2}$$

with m the mass of a ^{87}Rb atom, w the waist, z_R the Rayleigh range and U_0 the trap depth. If the energy of the atoms is higher than the zero point energy $\hbar\omega_{\perp,\parallel} \ll k_B T$, the statistical distributions of positions and velocities follow a Maxwell-Boltzmann
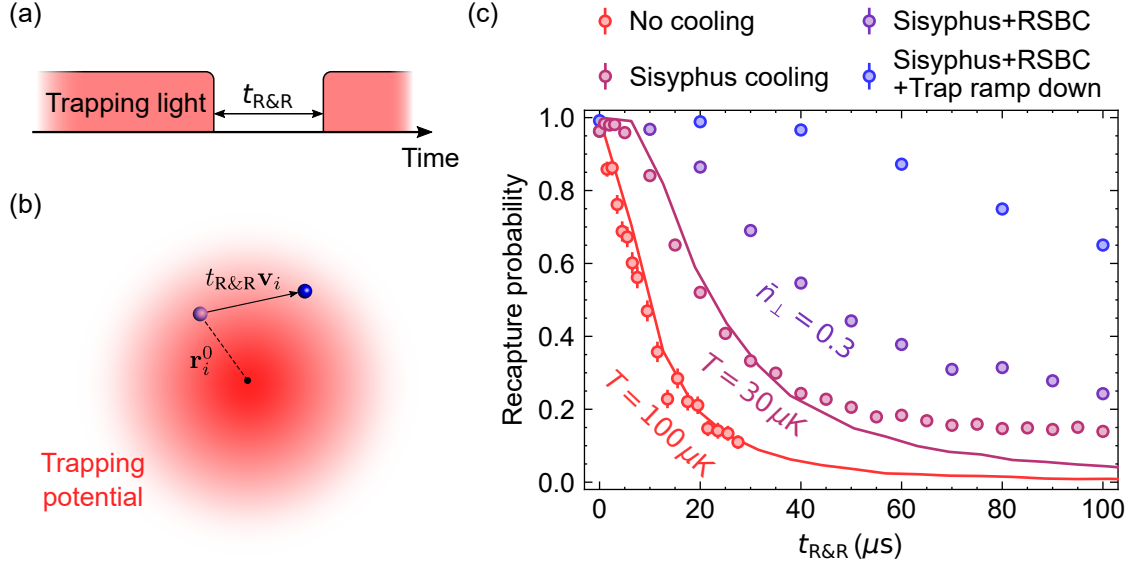
Figure 2.5: Release and recapture experiment. (a) Experimental sequence. (b) Sketch of the motion of one atom in its trap. (c) Results of the release and recapture experiments for different temperature obtained at different stages of the cooling procedure.

distribution with standard deviations of:

$$\sigma_{\perp,\parallel} = \sqrt{\frac{k_{\mathrm{B}}T}{m\omega_{\perp,\parallel}^2}} \quad \text{and} \quad \sigma_v = \sqrt{\frac{k_{\mathrm{B}}T}{m}} \tag{2.3}$$

These statistical distributions are used to calibrate the temperature of the atoms.

Release and recapture. The standard technique to measure the temperature of the atoms is to perform a *release and recapture* experiment [Tuchendler *et al.*, 2008]. After having loaded the atoms, we switch off the traps for a time duration $t_{\mathrm{R\&R}}$, turn back on the tweezer light and measure the probability of recapturing the atoms (see Fig. 2.5a). We repeat the experiment for various values of $t_{\mathrm{R\&R}}$. To extract the temperature, we compare the data to a classical Monte-Carlo simulation. After a time duration $t_{\mathrm{R\&R}}$ the position of an atom is $\mathbf{r}_i(t_{\mathrm{R\&R}}) = \mathbf{r}_i^0 + t_{\mathrm{R\&R}}\mathbf{v}_i$ with $\mathbf{r}_i^0$ and $\mathbf{v}_i$ following a Gaussian distribution of width $\sigma_{\perp,\parallel}$ and σ_v (see Eq. 2.3). We then compared the kinetic energy of the atom to the trapping potential at position $\mathbf{r}_i(t_{\mathrm{R\&R}})$. If $m\mathbf{v}_i^2/2 < U(\mathbf{r}_i(t_{\mathrm{R\&R}}))$ we consider that the atom is recaptured; otherwise we consider it is lost ((see Fig. 2.5b)). We repeat the simulation over 1000 times to compute the recapture probability. By adjusting the temperature in this model, we fit the experimental data with the simulation and thus infer the atomic temperature. We now move to the description of

the cooling procedure.

Cooling the atoms. We cool the atoms in three steps:

- First, we perform Sisyphus cooling (also called polarization gradient cooling) for $10\,\text{ms}$ [Wineland, Dalibard, and Cohen-Tannoudji, 1992]. To do so, we reduce the MOT light intensity and red-detune its frequency by $\approx 8\Gamma_{5P_{3/2}}$ from the $(5S_{1/2}, F = 2) \leftrightarrow (5P_{3/2}, F = 3)$ transition for $10\,\text{ms}$. The temperature decreases from $T = 100\,\mu\text{K}$ to $T = 30\,\mu\text{K}$. Figure 2.5c shows the results of the different release and recapture experiments performed before/after Sisyphus cooling. The solid curves are the simulations described in the previous paragraph. At $T = 30\,\mu\text{K}$, we observe for $t_{\text{R\&R}} > 40\,\mu\text{s}$ a discrepancy between the data and experiment that we have not investigated further. It could be due to the anisotropic temperature of the atoms ($T_\perp \neq T_\parallel$) or to the fact that at such low temperatures, classical simulations are no longer good approximations to describe the atomic motion.

- Second, we perform Raman Side Band Cooling (RSBC). When I started my Ph.D., we installed the RSBC setup to reach lower temperatures[2]. We measure the average radial vibrational number and find $\bar{n}_\perp = k_\text{B}T_\perp/(\hbar\omega_\perp) = 3$ before cooling and $\bar{n}_\perp = k_\text{B}T_\perp/(\hbar\omega_\perp) = 0.3$ after cooling (averaged over all the atoms of the array). In the release and recapture experiment, we also observe a significant improvement in the recapture probability (see Fig. 2.5c).

- Third, we adiabatically ramp down the tweezer light intensity. This adiabatic process (slower than $1/\omega_{\perp,\parallel}$) reduces the effective temperature, keeping the ratio $\omega_{\perp,\parallel}/T$ constant. Strictly speaking, this process does not cool the atoms since the average vibration mode occupation $\bar{n}_{\perp,\parallel}$ remains the same, and the process is reversible. However, it allows us to modify the ratio between $\sigma_{\perp,\parallel}$ and σ_v. If we adiabatically change the intensity by a factor α the new position and velocity distribution are given by $\sigma_{\perp,\parallel}/\alpha^{1/4}$ and $\sigma_v\alpha^{1/4}$. Figure. 2.5c shows the release and recapture results obtained after reducing the trapping light intensity by $\alpha \approx 1/100$.

---

[2]My co-worker Gabriel Emperauger dedicated a chapter in his thesis manuscript [Emperauger, 2025] to describe this experimental upgrade. Thus, I invite the reader to read his thesis for more information.
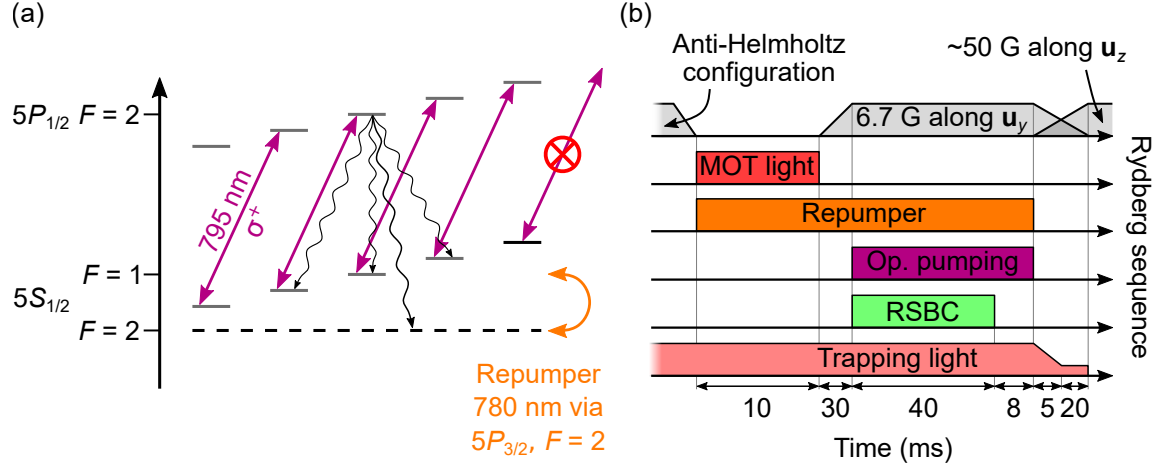
Figure 2.6: Optical pumping. (a) Principle of the optical pumping. (b) Summary of the ground state manipulation sequence (including cooling and optical pumping).

2.2.2 Optical pumping

Optical pumping. Before exciting all the atoms to the Rydberg state, we need to prepare them in the same hyperfine ground state. To achieve this, we use optical pumping. Figure 2.6a illustrates its principle. We first change the magnetic field configuration from anti-Helmholtz to Helmholtz configuration with a $6.7\,\mathrm{G}$ magnetic field along the $\mathbf{u}_y$ axis. Along this quantization axis, we send σ^+ polarized light resonant with the $(5S_{1/2}, F = 2) \leftrightarrow (5P_{1/2}, F = 2)$ transition. After a succession of excitations to $(5P_{1/2}, F = 2)$ and decays back to $(5P_{1/2}, F = 2)$, the atoms are optically pumped to the dark state $|g\rangle = \left|5S_{1/2}, F = 2, m_F = 2\right\rangle$. During this time, we also shine the repumper to ensure we repump in $(5S_{1/2}, F = 2)$ the atoms decaying to $(5S_{1/2}, F = 1)$. Using an independent experiment, we estimate an optical pumping inefficiency of $1 - \eta_{\mathrm{opt}} = 0.5\%$ [Scholl, 2021].

Ground-state manipulations sequence. Figure 2.6b summarizes all the ground state manipulations, including cooling and optical pumping. We first perform Sisyphus cooling for $10\,\mathrm{ms}$, then change the magnetic field configuration and apply the RSBC, optical pumping and repumper beams. After $40\,\mathrm{ms}$ of cooling, we turn off the RSBC and continue the optical pumping for $8\,\mathrm{ms}$ to ensure that all the atoms end up in $|g\rangle$. We then adiabatically ramp down the trapping light intensity while changing the magnetic field's orientation and strength. Finally, we switch off the traps and start the Rydberg sequence.

2.3 Rydberg state manipulations

I now present the different steps related to the atom manipulations involving Rydberg states. I first show how to excite/deexcite the atoms to/from the Rydberg states and then detail the different manipulations we perform in the Rydberg manifold.

2.3.1 Excitation and deexcitation

Rydberg excitation. We use a two-photon transition scheme to excite the atoms to the Rydberg state. A first laser at 420 nm drives the transition between the ground state $|g\rangle$ and the intermediate state $|i\rangle = \left|6P_{3/2}, F = 3, m_F = 3\right\rangle$ (see Fig. 2.7a). A second laser at 1013 nm drives the other transition between $|i\rangle$ and one of the Rydberg states $|r\rangle = \left|nS_{1/2}, m_J = 1/2\right\rangle$ (with n the principal quantum number of the target Rydberg state). The intermediate state has a short lifetime of $1/\Gamma_{|i\rangle} \approx 110$ ns. Therefore, we should avoid populating $|i\rangle$ to get the best Rydberg excitation efficiencies. Several methods exist, such as π-pulses or sweeps [Scholl, 2021]. We use a STImulated Raman Adiabatic Passage (STIRAP) technique [Vitanov *et al.*, 2017]. It offers the advantage of being resilient to experimental parameter fluctuations, such as intensity or frequency drifts. To perform STIRAP, the 420 and 1013 nm lasers are resonant with their respective transitions. We send two Gaussian pulses as depicted in the inset of Fig. 2.7c. I now give more details about each laser and describe the measurements we routinely perform to calibrate them.

420 nm laser. The 420 nm laser is produced via second harmonic generation of an amplified Toptica® diode laser at 840 nm. We send the 1 W output laser power through a double-path Acousto-Optic Modulator (AOM), an Electro-Optic Modulator (EOM), and a fiber. Finally, we collimate the light beam and send it to the atoms. At the position of the atomic plane, we measure a $1/e^2$ beam radius of $w_{420} = 250\,\mu$m. We also measure ~ 300 mW of laser power on the atoms corresponding to a Rabi frequency of $\Omega_{420}/(2\pi) \approx 80$ MHz for the $|g\rangle \leftrightarrow |i\rangle$ transition. The light is π polarized to $|g\rangle$ state to $|i\rangle$. To set the laser frequency on-resonance with $|g\rangle \leftrightarrow |i\rangle$ transition, we perform a *depump experiment*. We initialize all the atoms in $|g\rangle$ and then send a 420 nm pulse at low intensity. If the light is on-resonance with the $|i\rangle$ state, the
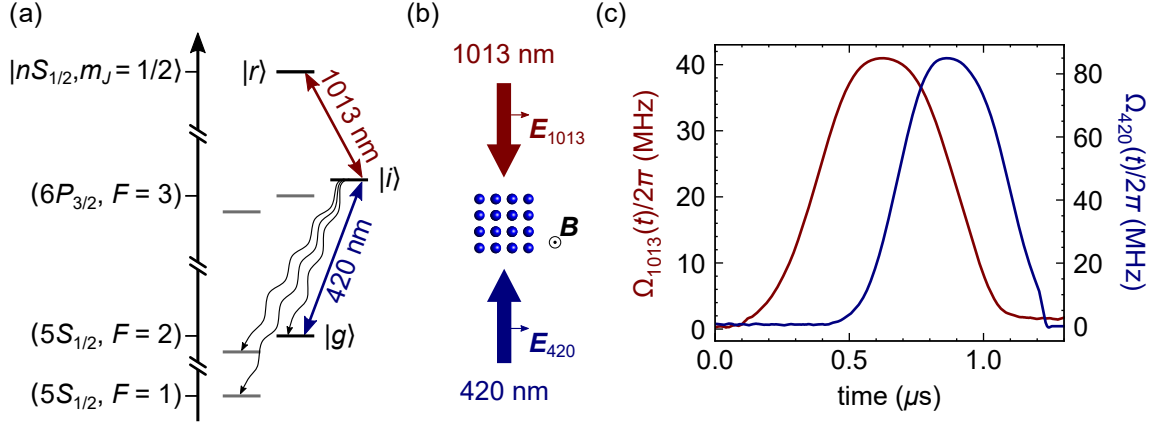
Figure 2.7: STIRAP. (a) Energy level diagram. (b) Orientations and polarizations of the Rydberg laser with respect of the atomic array and the quantization axis given by the magnetic field. (c) Rabi frequencies $\Omega_{420/1013}(t)$ during the STIRAP sequence.

atoms are excited and, shortly after, decay to $(5S_{1/2}, F = 1)$ or $(5S_{1/2}, F = 2)$[3]. If not, they will stay in $|g\rangle$. Therefore, we can then detect the resonances by measuring the population in $(5S_{1/2}, F = 1)$. To do so, we use a push-out light beam. The push-out light is $\sigma^{\pm}$ polarized at 780 nm resonant with the cycling transition $(5S_{1/2}, F = 2) \leftrightarrow (5P_{3/2}, F = 3)$. It allows us to heat the atoms in $(5S_{1/2}, F = 2)$ to expel them from their trap, whereas atoms in $(5S_{1/2}, F = 1)$ are not affected and thus remain in the tweezers. By sending the push out beam after the 420 nm one, we thus measure the population in $(5S_{1/2}, F = 1)$ (see blue data in Fig. 2.8a). By repeating this experiment for various laser detuning $\omega_{420} - \omega_{|g\rangle \leftrightarrow |i\rangle}$, we identify the transition frequency (using an Gaussian fit) and set the laser on resonance.

1013 nm. The 1013 nm laser is also produced by a Toptica® diode laser seeding an ALS® amplifier up to 8 W. The light is sent through an AOM and focused on the atoms using cylindrical lenses. It produces a elliptical light spot with a $1/e^2$ radius waist of $w_{1013} = 60 \, \mu$m along the perpendicular direction of the array and $250 \, \mu$m along the other allowing us to maximize the laser intensity on the atoms. The light is π polarized to couple the $|i\rangle$ state to $|r\rangle$.

To measure Ω_{1013}, we perform a depump experiment with the 1013 nm laser turned on at maximum power and set on resonance with the $|i\rangle \leftrightarrow |r\rangle$ transition. Due to the Autler–Townes effect, the state $|i\rangle$ is split into two states $(|i\rangle \pm |r\rangle)/\sqrt{2}$ shifted

---

[3]The selection rules forbid a direct decay from $|i\rangle$ to $(5S_{1/2}, F = 1)$. The atoms successively decay to others short-lived intermediate state $(4D)$ or $(6S)$, then in $(5P)$ and finally in $(5S)$ [Scholl, 2021].
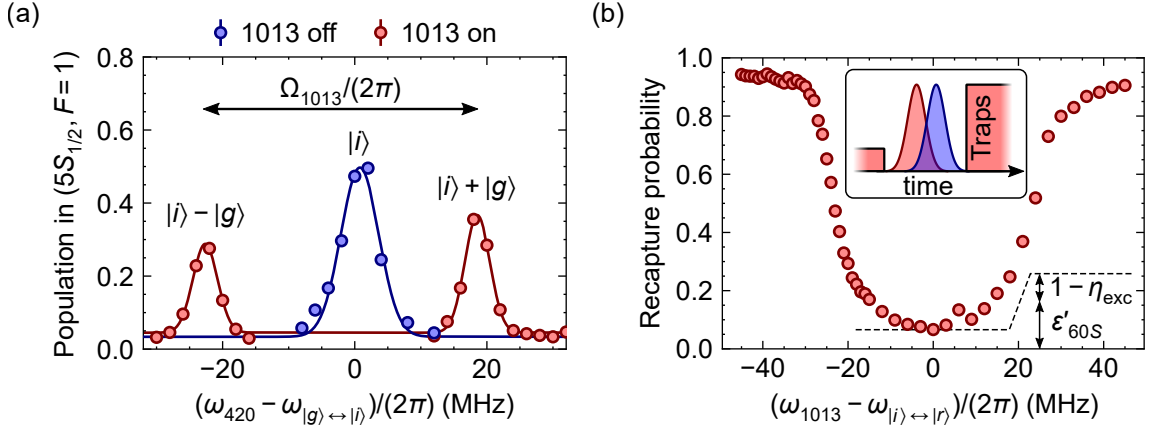
Figure 2.8: Calibration of the 1013 and 420 nm lasers. Here, $|r\rangle = \left|60S_{1/2}, m_J = 1/2\right\rangle$. (a) Depump experiment with/without the $1013\,\text{nm}$ laser (red/blue data). The solid curves are Gaussian fits. (b) Rydberg excitation using STIRAP. We plot the recapture probability as a function of ω_{1013}.

in frequency by $\pm\Omega_{1013}/2$. As shown in Fig. 2.8a, by measuring this splitting, we get $\Omega_{1013}/(2\pi) = 41\,\text{MHz}$ (here $|r\rangle = \left|60S_{1/2}, m_J = 1/2\right\rangle$). The Autler–Townes splitting is not perfectly symmetric around $|i\rangle$. Since the Rydberg laser is linearly polarized, they also couple to other intermediate states of the $6P_{3/2}$ manifold that results in light shifts breaking the symmetry of the Autler–Townes splitting. Thus, the Autler–Townes splitting that we measure may be slightly biased by this effect but still give a good estimate for Ω_{1013}.

To calibrate the laser frequency ω_{1013}, we perform Rydberg excitation using STIRAP. After switching off the traps, we send the two Gaussian pulses and switch back on the traps (see inset in Fig. 2.8b). Since the traps apply a repulsive ponderomotive force on the Rydberg atoms, we only recapture and image the non-excited atoms as shown in Fig. 2.8b. The spectrum exhibits a non-symmetric behaviour that we also attribute to the presence of other intermediate states.

Optimizing the Rydberg excitation.   Optimizing the Rydberg excitation efficiency is a crucial point for quantum simulation. If some atoms are not excited to the Rydberg state, they will not interact with their Rydberg atom neighbours. From the point of view of many-body physics, it is equivalent to having holes (meaning missing atoms) in the system. Holes affect many-body dynamics and thus can bias, reduce or even make impossible the observation of the signals we wish to measure. Moreover, since the non-excited atoms stay in the ground state during the Rydberg sequence, they
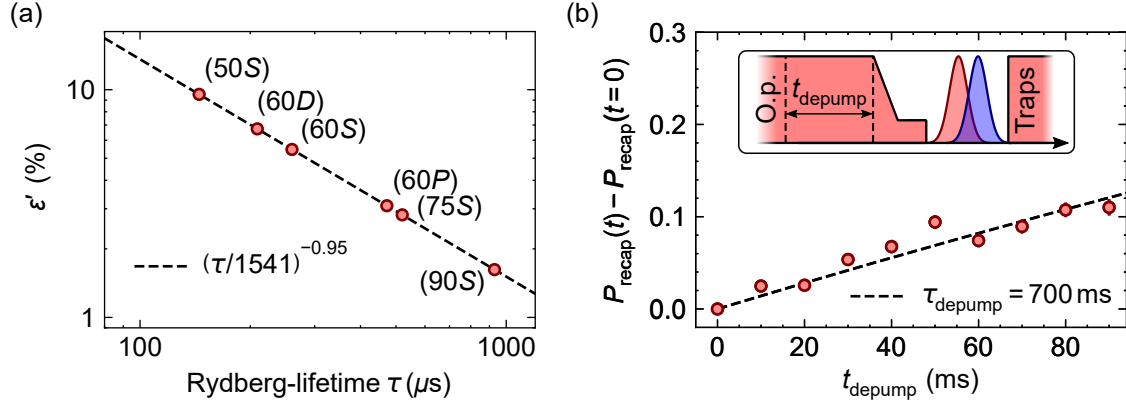
Figure 2.9: Optimizing STIRAP and minimzing ε'. (a) Simulation estimating ε' as a function of the spontaneous emission lifetime τ (lifetime at $T = 0\,\mathrm{K}$). (b) Recapture probability as a function of the depumping induced light scattering from the traps. The inset shows the experimental sequence.

will be recaptured and imaged at the end of the dynamics. As a result, we cannot distinguish them from the atoms that took part in the dynamics, ended up in $|\uparrow\rangle$, were transferred back to $(5S_{1/2})$ and imaged.

To measure the Rydberg excitation efficiency, we analyze the recapture probability of Fig. 2.8b. The lowest point reaches $7.5(2)\,\%$. This value is the sum of two contributions: detection errors $\varepsilon'_{(60S)}$ and Rydberg excitation inefficiency $1 - \eta_{\mathrm{exc}}$. A detection error occurs if one atom excited in the Rydberg state spontaneously decays to the ground state before being expelled by the trap ponderomotive force. The atom is then recaptured and imaged, whereas it was supposed to be lost. Using the simulation described in [de Léséleuc *et al.*, 2018], we calculate the detection error ε' as function of the Rydberg lifetime (see Fig. 2.9a). The Rydberg state $(60S)$ has a spontaneous emission lifetime of $260\,\mu\mathrm{s}$ (lifetime at $T = 0\,\mathrm{K}$) thus giving $\varepsilon'_{(60S)} = 5.5\,\%$. We then deduce (at first order) $1 - \eta_{\mathrm{exc}} = 7.5 - 5.5 = 2.0(2)\,\%$. Two effects lead to a reduction of the Rydberg excitation efficiency: an imperfect optical pumping and STIRAP.

When I started my Ph.D., $1 - \eta_{\mathrm{exc}}$ was around $\approx 5\,\%$. To decrease to $2.0\,\%$, we first manually optimized the STIRAP pulse shapes such as the amplitudes, widths and time delays. Second, we compressed the trap adiabatic ramp-down procedure from $15\,\mathrm{ms}$ to $5\,\mathrm{ms}$ to reduce the depumping induced by spontaneous Raman scattering from the traps [Miller, Cline, and Heinzen, 1993; Cline *et al.*, 1994]. After the optical pumping, due to eddy currents, we need to wait $25\,\mathrm{ms}$ to change the magnetic field configuration (see Sec. 2.4.1). During this waiting time t_{depump}, the atoms are slowly
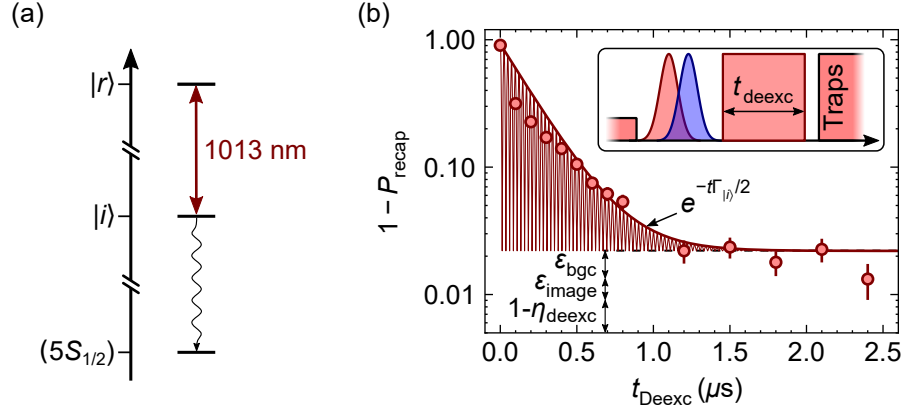
Figure 2.10: Deexcitation. (a) Energy level diagram. (b) Recapture probability as a function of the deexcitation time duration t_{deexc} for $|r\rangle = \left|60S_{1/2}, m_J = 1/2\right\rangle$. Thin solid curve: simulation. Thick solid curve: fit of the envelop with a decay rate of $\Gamma_{|i\rangle}/2$.

depumped from $|g\rangle$ to other hyperfine states in $(5S_{1/2})$ resulting in a decrease of the Rydberg excitation efficiency (meaning, an increase of recapture probability). As shown in Fig. 2.9b, to measure this depump rate, we measure the probability to recapture the atoms after the Rydberg excitation for different values of t_{depump}. We measure a lifetime of $700\,\mathrm{ms}$ consistent with the order of magnitude of $\sim 100/1000\,\mathrm{ms}$ given in [Cline *et al.*, 1994]. To reduce its effect, just after the end of the optical pumping stage, we first perform the adiabatic ramp down of the trapping light in $5\,\mathrm{ms}$, and then wait for the remaining $20\,\mathrm{ms}$. As the Raman scattering rate is proportional to the trap intensity, this configuration reduces the time the atoms spend with a high trap intensity, thus reducing the depumping.

We envisioned further optimizations to reduce $1 - \eta_{\mathrm{exc}}$. We plan to use optimal control [Ross, 2015] to optimize the STIRAP pulses. Another optical pumping beam propagating perpendicular to the array could also be added to optically pump the atom just before the Rydberg excitation.

Deexcitation. After the Rydberg sequence, we selectively deexcite the atoms from $|r\rangle$ to the ground state $(5S_{1/2})$, while leaving the others in the Rydberg manifold. To do so, we turn on the 1013 nm laser used to perform the STIRAP. The $|r\rangle$ atoms are then transferred to the intermediate state $|i\rangle$ from which they spontaneously decay back to the ground states $(5S_{1/2})$ (see Fig. 2.10a). To assess the speed at which this deexcitation occurs, we measure the recapture probability as a function of the deexcitation pulse duration t_{deexc}. Figure 2.10b shows the results. The atoms undergo

fast Rabi oscillation between the $|r\rangle$ and $|i\rangle$ states at frequency Ω_{1013} (thin solid curve). On average, half of the population is in $|i\rangle$, so the deexcitation rate can be approximated by an exponential decay with a rate of $\Gamma_{|i\rangle}/2$ (thick solid curve). For $|r\rangle = |60S_{1/2}, m_J = 1/2\rangle$ it gives a decay rate of $1/(\Gamma_{|i\rangle}/2) = 220\,\text{ns}$. Experimentally, we chose a duration $t_{\text{deexc}} = 2500\,\text{ns}$ thus ensuring that most the $|r\rangle$ atoms have time to decay back to the ground state. To estimate this process fidelity η_{deexc}, we analyze the recapture probability after $t_{\text{deexc}} = 2500\,\text{ns}$. It reached $1 - 0.023$. We measure that $\varepsilon = \varepsilon_{\text{image}} + \varepsilon_{\text{bgc}} = 1.3(2)\,\%$ comes from detection errors: $\varepsilon_{\text{image}} = 0.3(1)\,\%$ due to losses during the $20\,\text{ms}$ of imaging and $\varepsilon_{\text{bgc}} = 1.0(1)\,\%$ due to losses induced by background gas collisions with the atoms. We then deduce $1 - \eta_{\text{deexc}} = 1.0(2)\,\%$. During my Ph.D., we did not investigate the physical processes limiting the fidelity of this deexcitation. Therefore, there is still room for improvement on this front.

2.3.2 Microwave control of the Rydberg states

Motivations. Once the atoms are excited to the Rydberg manifold, we use a microwave field (MW) to transfer the atoms from one Rydberg state to another. We perform two types of microwave transfers (see Fig. 2.11a):

- **Spin states manipulation.** To implement the dipolar XY model, we encode our spin states between two Rydberg states of opposite parity [de Léséleuc *et al.*, 2017]. During my Ph.D., we mainly used $|\uparrow\rangle = |r\rangle = |nS_{1/2}, m_J = 1/2\rangle$ and $|\downarrow\rangle = |nP_{J'}, m_{J'}\rangle$. The spin states $|\uparrow\rangle$ and $|\downarrow\rangle$ are separated by $\omega_{|\uparrow\rangle\leftrightarrow|\downarrow\rangle}/(2\pi) \sim 1 - 20\,\text{GHz}$ and can be coupled using microwaves. It allows us to manipulate the spins for various applications, such as preparing them in a specific initial state ($|\uparrow\rangle$, $|\downarrow\rangle$ or in a superposition), modifying the XY Hamiltonian by adding single-particle terms as $\mathcal{H}_{\text{MW}} = \Omega_{\text{MW}} \sum_i \sigma_i^{x,y}$ or rotating the spins. These applications require good control over the amplitude, frequency and phase of the microwaves.

- **Freezing the XY dynamics.** Just before the deexcitation pulse, we introduce a microwave *freezing pulse* to transfer the $|\downarrow\rangle$ atoms to hydrogenic states. The goal is twofold. First, it allows us to stop the XY dynamics. Since we cannot switch off the dipole-dipole interactions between the atoms, to freeze the dynamics, we transfer in a few nanoseconds the $|\downarrow\rangle$ atom population to the hydrogenic manifold (h). Atoms in hydrogenic states are decoupled from those remaining in
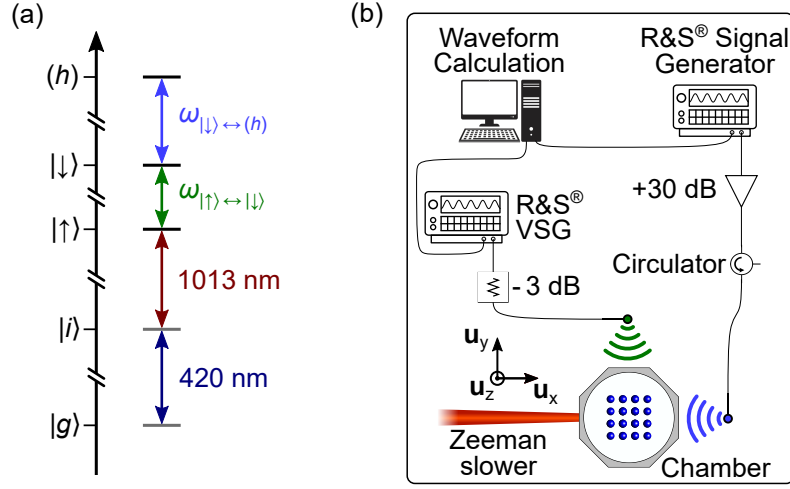
Figure 2.11: Microwave set-up. (a) Energy level diagram. (b) Sketch of the microwave set-up.

$|\uparrow\rangle$, avoiding detrimental effects of the interaction during the deexcitation pulse. Second, exciting the $|\downarrow\rangle$ atoms to (h) reduces the detection error ε': the atoms in these states cannot spontaneously decay directly to the ground state but must use various decay channels through the Rydberg manifolds. This process decreases the probability that a Rydberg atom decays in the ground state before being expelled by the traps, thus reducing ε'.

Microwave set-up. The microwave set-up is summarized in Fig. 2.11(b). From the computer, we generate the pulse waveform we wish to apply. For the $|\uparrow\rangle \leftrightarrow |\downarrow\rangle$ microwave transition, we use a Vectorial Signal Generator (VSG) from Rohde & Schwarz® (R&S®SMM100A). This device allows us to create arbitrary rf waveforms for frequencies up to $2\pi \times 20\,\text{GHz}$. We send this signal to an antenna on top of the science chamber (green signal). To generate the freezing pulse, we use a commercial signal generator from the same company (R&S®SMB100A) generating signals up to $2\pi \times 12.75\,\text{GHz}$. We then amplify the signal by $30 - 34\,\text{dB}$ and send it to the axial antenna (blue signal). Thanks to this configuration, we can independently control the two microwave signals.

Spin states manipulations. To test our ability to perform spin state manipulations with microwaves, we perform a single-atom Rabi oscillation between state $|\uparrow\rangle = |90S_{1/2}, m_J = 1/2\rangle$ and $|\downarrow\rangle = |90S_{3/2}, m_J = 1/2\rangle$ (see Fig. 2.12). Using STIRAP, we
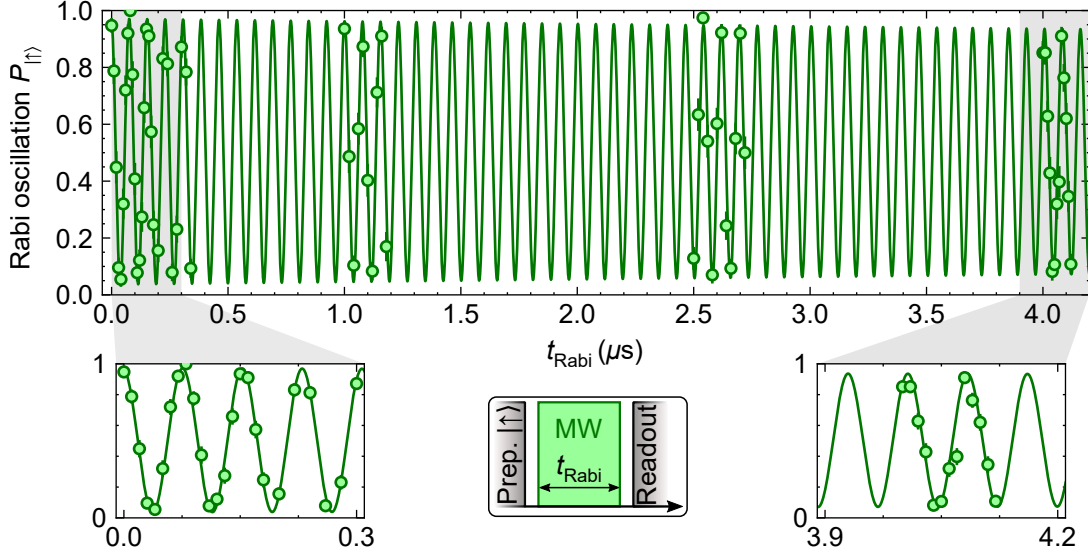
Figure 2.12: Rabi oscillation. Microwave Rabi oscillation between $|\uparrow\rangle = |90S_{1/2}, m_J = 1/2\rangle$ and $|\downarrow\rangle = |90S_{3/2}, m_J = 1/2\rangle$ at a frequency $\Omega_{\mathrm{MW}}/(2\pi) = 12.97\,\mathrm{MHz}$. The solid curve is a fit by a damped cosine function.

first excite the atoms to $|\uparrow\rangle$, send a microwave pulse tuned of the resonance $\omega_{|\uparrow\rangle\leftrightarrow|\downarrow\rangle}$, and apply the readout sequence (consisting of sending the deexcitation pulse, switching back on the tweezers and imaging). The intrinsic low noise of the VSG, combined with the extended lifetime of Rydberg states, allow for coherent of Rabi oscillations over several microseconds. We observe low damping of the oscillations after 50 cycles.

Freezing pulse. To calibrate the freezing pulse frequency, we perform two spectroscopy experiments. In the first one, we excite the atoms in $|\uparrow\rangle$, transfer them to $|\downarrow\rangle$ using a microwave π-pulse, send the freezing pulse (for 30 ns), and deexcite the remaining population in $|\downarrow\rangle$ via another π-pulse and the deexcitation pulse (blue curve in Fig. 2.13a). In the second one, we excite the atoms in $|\uparrow\rangle$, apply the freezing pulse (for 200 ns), and readout (black curve). By applying these sequences, we measure the transfer probability from $|\downarrow\rangle/|\uparrow\rangle$ to hydrogenic states (h) (for, $|\uparrow\rangle$ we use a longer freezing pulse duration to enhance the transfer rate). We repeat these experiments with various freezing pulse frequencies. Figure 2.13a shows the spectra using $|\uparrow\rangle = |60S_{1/2}, m_J = 1/2\rangle$ and $|\downarrow\rangle = |60P_{3/2}, m_J = -1/2\rangle$. Around $\sim 2\pi \times 7500\,\mathrm{MHz}$ we identify a broad three photon transition from $|\downarrow\rangle$ to probably $(h) = (58G)$. Characterizing all the peaks of this spectrum would be extremely difficult since any residual electric field in the vacuum chamber would result in mixing all the states of the
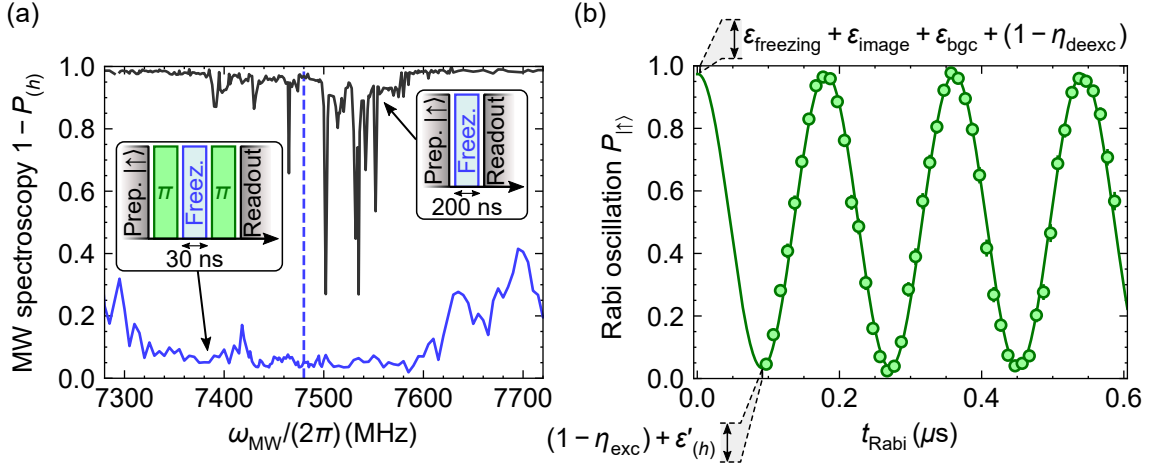
Figure 2.13: Freezing pulse. (a) Calibration of the freezing pulse microwave frequency. The black/blue data shows the transfer probability from the states $|\uparrow\rangle = \left|60S_{1/2}, m_J = 1/2\right\rangle$ and $|\downarrow\rangle = \left|60P_{3/2}, m_J = -1/2\right\rangle$ to the hydrogenic states (h). The insets show a sketch of the experimental sequences. (b) Single atom microwave Rabi oscillation on the $|\uparrow\rangle \leftrightarrow |\downarrow\rangle$ transition using the freezing pulse. The solid curve is a fit using a cosine function.

Rydberg manifold [Zimmerman *et al.*, 1979]. We choose a frequency, power and pulse duration to maximize the speed at which we transfer the $|\downarrow\rangle$ population to (h) while we minimize the effect on the $|\uparrow\rangle$ population. The best parameters correspond to a pulse duration of 30 ns and a frequency of $2\pi \times 7480$ MHz (vertical dashed blue line). With these parameters, we measure that a fraction $\varepsilon_{\text{freezing}} = 0.3(1)\,\%$ of the $|\uparrow\rangle$ population is transferred to (h), leading to an extra source of detection error. However, this new detection error is largely compensated by the reduction of ε' going from $\varepsilon'_{60P} = 2.6(2)\,\%$ to $\varepsilon'_{(h)} = 1.3(2)\,\%$.

We now add the freezing pulse to the readout sequence just before the deexcitation pulse and perform another single atom Rabi oscillation on the microwave $|\uparrow\rangle \leftrightarrow |\downarrow\rangle$ transition (see Fig. 2.13b). We measure that the recapture probability oscillates between $3.4(2)\,\%$ and $97.4(2)\,\%$. This contrast is consistent with the values of state preparation errors $(1 - \eta_{\text{exc}}) = 2.0(2)\,\%$ and detection errors $\varepsilon_\downarrow = \varepsilon'_{(h)} = 1.3(2)\,\%$ and $\varepsilon_\uparrow = \varepsilon_{\text{freezing}} + \varepsilon_{\text{image}} + \varepsilon_{\text{bgc}} + (1 - \eta_{\text{deexc}}) = 2.5(4)\,\%$ that we each measure independently.

Microwave limitations. Although microwaves provide an efficient tool to manipulate the atoms in the Rydberg manifold, they suffer from two main downsides. First, as the two antennas are placed outside the vacuum chamber, we cannot control the microwave polarisation due to the metallic parts surrounding the atoms. Therefore,

to isolate the $|\uparrow\rangle \leftrightarrow |\downarrow\rangle$ from irrelevant Zeeman sublevels, we need to apply a $50\,\mathrm{G}$ quantization magnetic field perpendicular to the array (see Sec. 2.4.1). Second, the microwave wavelength is $\sim 1\,\mathrm{cm}$ and significantly larger than the typical size of our arrays of optical tweezers of $\sim 100\,\mu\mathrm{m}$. It implies that the microwaves are global for all the atoms. To overcome this drawback, we combine the microwaves with local light shifts induced by addressing beams to perform local operations on the atoms.

2.3.3 Local addressing beams

Applying local light shifts.   To apply a local light shift on one atom, we pick up part of the $1013\,\mathrm{nm}$ light from the Rydberg excitation laser and we focus it on the atoms using the aspheric lenses creating a light spot on the atomic plane with a waist of a few micrometers (see Chapter 3 for more detail about the optical setup). To superimpose this addressing light spot with a target trap, we use this $1013\,\mathrm{nm}$ beam as an optical tweezer. We set its power such that the light spot creates a trapping potential with a trap depth sufficiently high to load single atoms (this power is not necessarily the one that we will use to apply local light shifts). Thus, the fluorescence light scattered by an atom trapped in this $1013\,\mathrm{nm}$ tweezer indicates us on the florescence camera, the position of the addressing light spot. We then move the addressing beam such that the position of the atoms trapped by this $1013\,\mathrm{nm}$ tweezer coincides with the one of the atoms trapped in the $820\,\mathrm{nm}$ target tweezer.

The $1013\,\mathrm{nm}$ addressing laser is detuned by Δ_{addr} from the $|i\rangle \leftrightarrow |\uparrow\rangle$ transition with a Rabi frequency Ω_{addr}. It induces a light-shift on the $|\uparrow\rangle$ state of $\delta_{\mathrm{addr}} = \Omega_{\mathrm{addr}}^2/(4\Delta_{\mathrm{addr}})$. The sign of δ_{addr} is set by the sign of Δ_{addr}, and the δ_{addr} amplitude can be dynamically varied during the Rydberg sequence by modulating the addressing laser intensity with an AOM and EOM. More details about the

Calibration of the addressing-induced light shifts.   To measure the light shift induced by the addressing beam, we perform microwave spectroscopy on the $|\uparrow\rangle \leftrightarrow |\downarrow\rangle$ transition. Using STIRAP and a microwave π-pulse, we first initialize all the atoms in $|\downarrow\rangle$, turn on the addressing light, send a microwave pulse at frequency ω_{MW} and read out the atom state. In Fig. 2.14b, we plot the recapture probability for the non-addressed atoms (grey data) and addressed atoms (red data). As expected, we find a resonance at $\omega_{|\uparrow\rangle\leftrightarrow|\downarrow\rangle}$ for the non-addressed atoms and measure a shift of

(a)

(b)
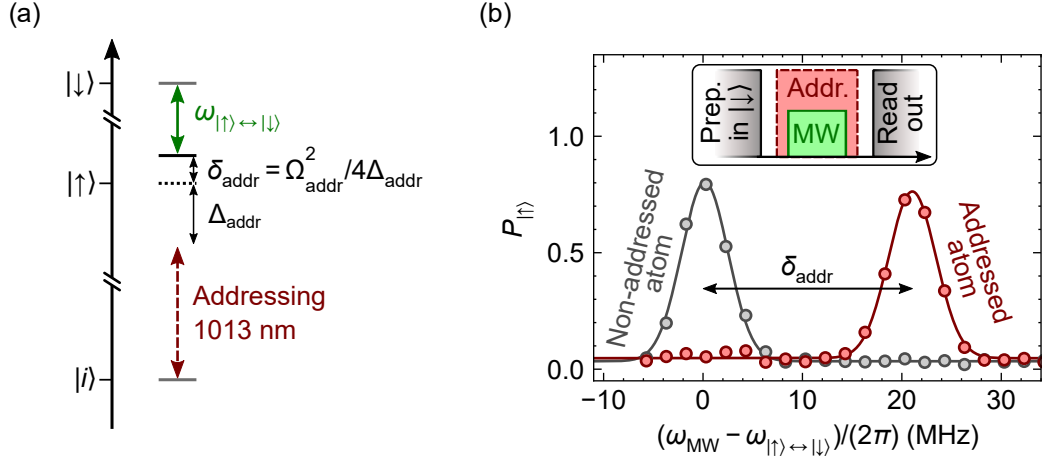
Figure 2.14: Light shift induced by the addressing beam. (a) Energy level diagram. The addressing is detuned by Δ_{addr} from the $|i\rangle \leftrightarrow |\uparrow\rangle$ transition to induced a light shift δ_{addr} on te addressed atoms. (b) Example of microwave spectroscopy to measure δ_{addr}. Here we use: $|\uparrow\rangle = \left|60S_{1/2}, m_J = 1/2\right\rangle$, $|\downarrow\rangle = \left|60P_{1/2}, m_J = -1/2\right\rangle$, $\Delta_{\mathrm{addr}}/(2\pi) \approx 400\,\mathrm{MHz}$ and $\approx 300\,\mathrm{mW}$ of light for the addressing beam. The solid curves are fits with Gaussian functions. The inset shows the experimental sequence.

$\delta_{\mathrm{addr}} = 2\pi \times 21\,\mathrm{MHz}$ for the addressed atom.

Spin exchange. Historically, the addressing technique was used in the group to prepare one atom in $|\downarrow\rangle$ while the others are in $|\uparrow\rangle$ [de Léséleuc *et al.*, 2017; Barredo *et al.*, 2020; Lienhard *et al.*, 2020]. This configuration is interesting for performing experiments called a *spin exchange*. The minimalistic spin exchange experiment uses two atoms; one initialized in $|\uparrow\rangle$ and the other in $|\downarrow\rangle$. To prepare $|\uparrow\downarrow\rangle$, we first start by initializing two atoms in $|\downarrow\rangle$ via STIRAP and a microwave π-pulse (the details of this experimental sequence will be discussed in detail in Sec. 3.2.1). We then turn the addressing light, inducing a light shift δ_{addr} on the addressed atoms. We re-apply a microwave π-pulse to bring down the non-addressed atom to $|\uparrow\rangle$. If the microwave Rabi frequency is lower than the addressing light shift $\Omega_{\mathrm{MW}} \ll \delta_{\mathrm{addr}}$, the microwaves then are off-resonant for the addressed atoms and thus let them in $|\downarrow\rangle$ (see Fig. 2.15a). Once we have prepared the initial state $|\uparrow\downarrow\rangle$, we let the two atoms interact freely for a time t_{XY} under the XY Hamiltonian and read out their states. The probability to measure $|\uparrow\downarrow\rangle$ oscillates with a frequency $2J$, with J being the XY interaction energy between the two atoms (see Chapter 5). This spin exchange is routinely used as a calibration experiment to measure J. An example of a spin exchange is shown in Fig. 2.15b.
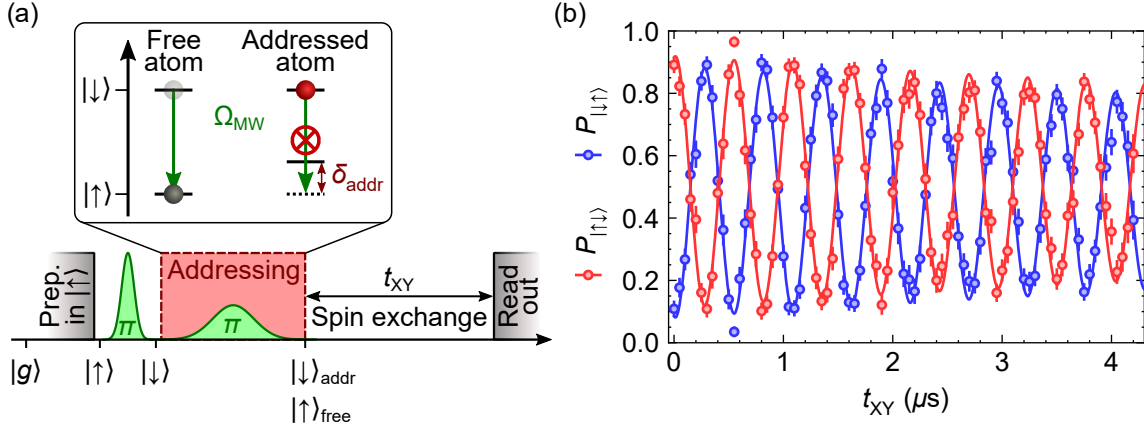
Figure 2.15: Two-atom spin exchange experiment. (a) Experimental sequence to prepare $|\uparrow\downarrow\rangle$. (b) Spin exchange experiment. The two atoms are separated by $30\,\mu m$ and we use $|\uparrow\rangle = |90S_{1/2}, m_J = 1/2\rangle$ and $|\downarrow\rangle = |90P_{3/2}, m_J = 3/2\rangle$. The probabilities $P_{|\uparrow\downarrow\rangle}$ and $P_{|\downarrow\uparrow\rangle}$ oscillate at a frequency $2J$ with $J/(2\pi) = 0.79\,\mathrm{MHz}$. The solid curves are a fit with a damped cosine function.

During my Ph.D. we extended the use of the addressing to two applications. First, we demonstrated a method to perform local rotations on Rydberg-encoded spins and measure multi-basis observables, meaning that we measure each spin along a different axis of the Bloch sphere. Second, we showed the ability to initialize arrays of up to $N = 100$ atoms in a Néel state along z, *i.e.* a staggered arrangement of spins $|\uparrow\rangle$ and $|\downarrow\rangle$. As we will see all along this manuscript, this initialization is particularly interesting since it allowed us to study the ground state and out-of-equilibrium physics of the dipolar model XY (see Chapter 5, 6 and 8). I give more details in Chapter 3, which is devoted to the description of these two experimental improvements.

2.4 Control of the magnetic and electric field environment

Rydberg atoms are sensitive to external magnetic and electric fields [Gallagher, 2006]. Therefore, measuring and controlling the magnetic and electric environment inside the science chamber is essential.

2.4.1 Magnetic field

Magnetic field configuration.   During the sequence, we use four different configurations of magnetic field:

- **Anti-Helmholtz configuration.** During the loading of the atoms from the MOT to the tweezers, we use a pair of coils inside the science chamber in the Anti-Helmholtz configuration to generate a magnetic gradient. Using three pairs of compensation coils placed outside the science chamber we adjust the position of zero magnetic field, to position the atomic cloud near the tweezers.

- **Zero magnetic field.** During the Sisyphus cooling stages, we switch off the magnetic field. We use the compensation coils to ensure the magnetic field is well-cancelled (see [Scholl, 2021]).

- **Helmholtz configuration along $\mathbf{u}_y$.** During the RSBC and optical pumping stages, we apply a $6.7\,\mathrm{G}$ magnetic field to define the quantization axis along $\mathbf{u}_y$. We use the pair of coils inside the science chamber to switch to Helmholtz configuration. We calibrated its value using a Raman sideband spectrum (see [Emperauger, 2025]).

- **Helmholtz configuration along $\mathbf{u}_z$.** Before starting the Rydberg sequence, we rotate the magnetic field along $\mathbf{u}_z$ using an extra pair of coils placed outside the vacuum chamber. As we will see in Sec. 5.1, the dipole-dipole interaction depends on the orientation of the quantization axis. We ensure isotropic XY interaction between the atoms by applying a magnetic field perpendicular to the array. As mentioned in Sec. 2.3.2, to isolate the $|\uparrow\rangle/|\downarrow\rangle$ Zeeman sublevels from the others, we apply a relatively strong magnetic field of $\sim 50\,\mathrm{G}$. This configuration is the one we use during the Rydberg sequence; therefore, its magnetic field must be carefully calibrated.

Calibration of the magnetic field.   We first measure the time we need to wait to rotate the magnetic field from $\mathbf{u}_y$ to $\mathbf{u}_z$. To do so, we measure the current in the $\mathbf{u}_z$ coils as a function of time for various values of magnetic fields (see Fig. 2.16a). At $t = 0$, the current is turned on and due to the large inductance of the coils, it follows an exponential rise up of $\sim 1/10\,\mathrm{ms}$. Then, we observe a transient with damped oscillations due to an overshoot of the voltage. According to these curves, for
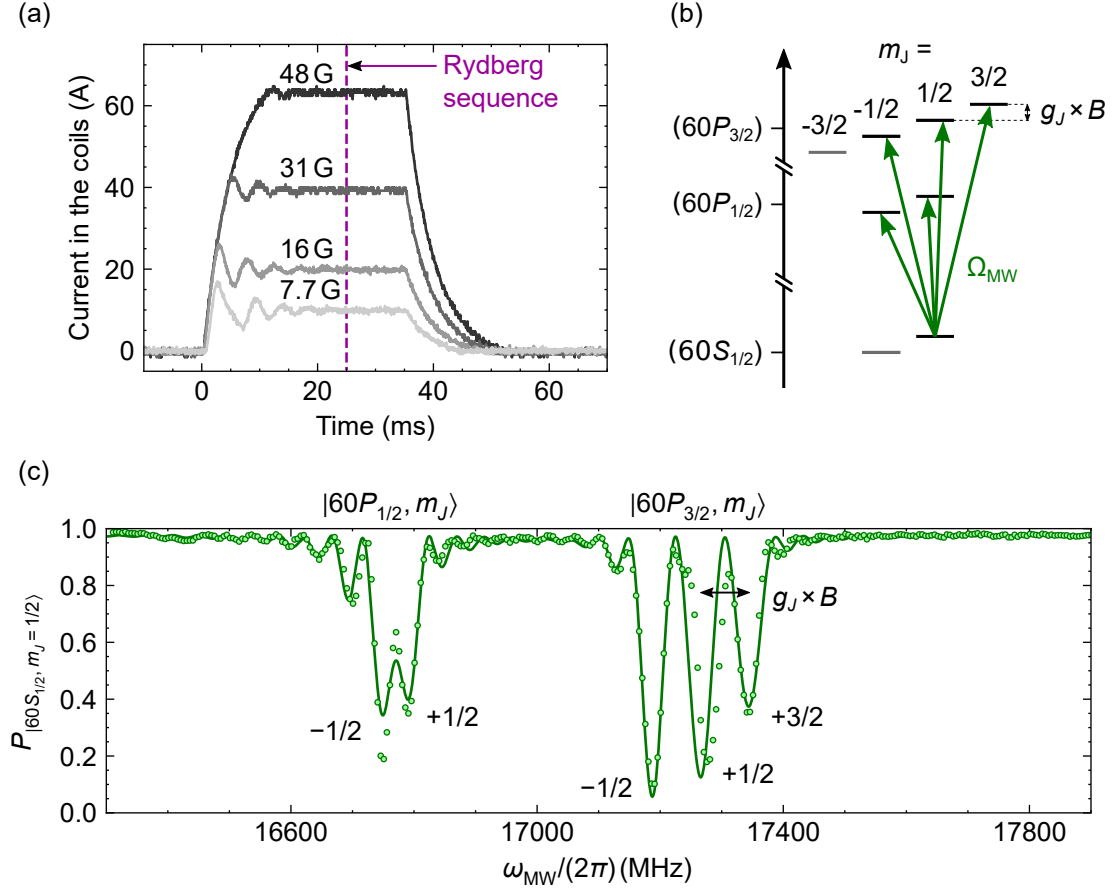
Figure 2.16: Calibration of the magnetic field. (a) Measurement of the current in the $\mathbf{u}_z$ coils as a function of time for various values of magnetic field. (b) Energy level diagram showing the different Zeeman sublevels of the $(60S)$ and $(60P)$ manifolds. (c) Microwave spectrum showing the different transitions between $\left|60S_{1/2}, m_J = 1/2\right\rangle$ and $(60P)$. The solid curve shows the simulation taking only the magnetic field intensity as a free parameters. Here $B = 43\,\text{G}$.

$B = 48\,\text{G}$, to ensure that the magnetic field has reached a steady value before starting the Rydberg sequence, we need to wait $20\,\text{ms}$. Independent experiments performed on Rydberg atoms (Ramsey experiments on the $\left|\uparrow\right\rangle \leftrightarrow \left|\downarrow\right\rangle$ transition) showed that the magnetic field still exhibits small oscillations after $20\,\text{ms}$ and only reaches a stable value after $25\,\text{ms}$ (see purple vertical dashed line).

To measure the magnetic field value, we perform a microwave spectrum. We first initialize all the atoms in $\left|60S_{1/2}, m_J = 1/2\right\rangle$, send a microwave pulse of frequency ω_{MW} and readout the state of the atoms. Figure 2.16c shows the recapture probability as a function ω_{MW}. We identify five main peaks corresponding to two transitions to the $(60P_{1/2})$ states and three to the $(60P_{3/2})$ (see Fig. 2.16b). To calibrate the

magnetic field, we perform a simulation (solid curve), taking the magnetic field strength as an adjustable parameter. By taking $B = 43\,\mathrm{G}$, we obtain a relatively good agreement with the experimental data[4]. The splitting between two Zeeman sublevels m_J and m'_J can be calculated using the Landé factor $g_J(\mathrm{MHz/G}) \simeq 1.4 \times (1 + (J(J+1) + S(S+1) - L(L+1))/(2J(J+1)))$ giving in frequency a splitting of $\Delta\omega/(2\pi) = g_J(m'_J - m_J)B$. As an example, if we consider the $(60P_{3/2})$ manifold and $B = 43\,\mathrm{G}$, we calculate a frequency splitting between successive Zeeman sublevels of $g_J \times B = 88\,\mathrm{MHz}$ consistent with the measurements. We typically use microwave Rabi frequencies of up to $\Omega_{\mathrm{MW}}/(2\pi) \sim 20\,\mathrm{MHz}$, so this splitting is large enough to isolate these Zeeman sublevels since $\Omega_{\mathrm{MW}}/(2\pi) \ll g_J \times B$.

2.4.2 Electric field

Electrodes. Due to the presence of charged particles in the science chamber, there is a residual electric field. This residual electric field mixes Rydberg states of different parity and thus prevents us from using a pure two-level system. To cancel this electric field, we use eight electrodes. They are placed inside the science chamber around the atoms, as shown in Fig. 2.17. We apply a potential $\pm V_x \pm V_y \pm V_z$ on each of them. This configuration is equivalent to having three pairs of electrodes along each direction with an applied voltage of $\pm V_{x,y,z}$. We tune the three voltages $V_{x,y,z}$ to cancel the electric field seen by the atoms.

The electric field produces a Stark shift on the $|\uparrow\rangle \leftrightarrow |\downarrow\rangle$ transition frequency which reads $\delta(E) = \delta_{|\downarrow\rangle}(E) - \delta_{|\uparrow\rangle}(E) = \frac{1}{2}(\alpha_{|\downarrow\rangle} - \alpha_{|\uparrow\rangle})E^2$ with $\alpha_{|\downarrow\rangle,|\uparrow\rangle}$ the electric polarizabilities of states $|\downarrow\rangle$ and $|\uparrow\rangle$. To measure this shift, we perform a Ramsey experiment on the $|\uparrow\rangle \leftrightarrow |\downarrow\rangle$ transition. After having initialized all the atoms in $|\uparrow\rangle$, we apply a first microwave $\pi/2$-pulse, wait $t_{\mathrm{Ramsey}} = 4\,\mu\mathrm{s}$, reapply a $\pi/2$-pulse and readout the state of the atoms. We repeat this measurement for various values of $V_{x,y,z}$. The microwave detuning evolves as $\delta_{\mathrm{MW}}(E) = \delta_{\mathrm{MW}}^0 + \delta(E)$ with δ_{MW}^0 the microwave detuning at $E = 0$. Thus, the recapture probability reads $P_{|\uparrow\rangle}(E) = A\cos(t_{\mathrm{Ramsey}}\delta_{\mathrm{MW}}(E)) + B = A\cos\!\big(t_{\mathrm{Ramsey}}(\delta_{\mathrm{MW}}^0 + \frac{1}{2}(\alpha_{|\downarrow\rangle} - \alpha_{|\uparrow\rangle})E^2)\big) + B$. As illustrated in Fig. 2.17, we measure the recapture probability as a function of V_y. We fit the data (solid curve) using the above formula, taking $E = V_y - V_y^0$. From this fit, we extract V_y^0, the potential for

---

[4]Since we do not control the power distribution in each polarization component (σ^-, π, σ^+) of the microwave field, it must be calibrated. We calibrated this distribution for $\omega_{\mathrm{MW}}/(2\pi) \sim 17300\,\mathrm{MHz}$ by measuring the Rabi frequencies between $\big|60S_{1/2}, m_J = 1/2\big\rangle$ and the $\big|60P_{3/2}, m_J\big\rangle$ states.
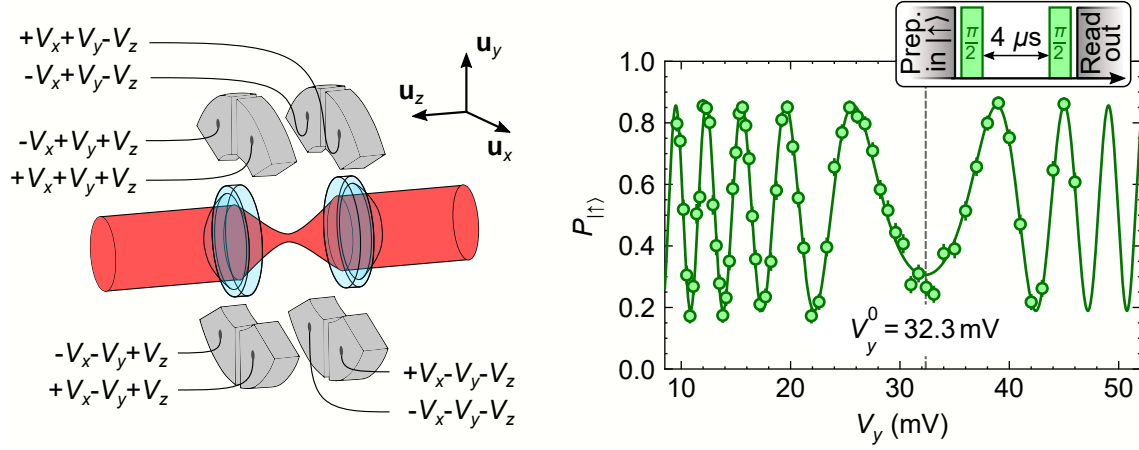
Figure 2.17: Calibration of the Electric field. (a) Sketch depicted the position of the eight electrodes (grey parts). (b) Ramsey experiment to find the zero point electric field along $\mathbf{u}_y$. We perform a Ramsey experiment with t_{Ramsey} and plot the recapture probability as a function of the applied voltage V_y. The solid curve is a fit using a cosine function $\cos\left(t_{\text{Ramsey}}\alpha(V_y - V_y^0)^2 + \phi\right)$ with ϕ, α and V_y^0 as free parameters. The zero electric field is reached for $V_y = V_y^0 = 32.3\,\text{mV}$. Here we use $|\uparrow\rangle = \left|75S_{1/2}, m_J = 1/2\right\rangle$ and $|\downarrow\rangle = \left|75P_{3/2}, m_J = -1/2\right\rangle$.

which the electric field along y is cancelled. We repeat this procedure for all directions and get $V_{x,y,z}^0$, the voltages to cancel the electric field.

2.5   Conclusion

In this chapter, I have presented an overview of the experimental apparatus. I described how, starting from a rubidium vapour, we generate assembled arrays of individual ^{87}Rb atoms trapped in optical tweezers. I described the different stages to cool the atoms and optically pump them to one specific ground state $|g\rangle$. I explained how to excite/deexcite the atoms to/from the Rydberg states. Then, I focused on the different Rydberg state manipulations we can perform using microwaves and addressing beams. Finally, I showed how we control the magnetic and electric environment seen by the atoms.

The following two Chapters will focus on two major improvements. Chapter 3 will describe in more detail the extension of the addressing technique to prepare classical Néel states and perform multi-basis observables. Chapter 4 will focus on the correction of the static positional disorder corresponding to the fact that the position of the

tweezers is only precise up to $100\,\mathrm{nm}$. This static positional disorder leads to spatial inhomogeneity of the interatomic interaction energy and can thus be detrimental to many body systems we wish to study.

Local control of Rydberg encoded spins

Contents

To build a fully programmable quantum simulator/computer, addressability is an important ingredient. First, it allows initializing the system in specific states required to observe exotic phenomena such as topological phases [Fukuhara *et al.*, 2013; Dumitrescu *et al.*, 2022]. Second, it allows applying local operations on the atoms. For example, in the context of quantum computation, these local operations are used for benchmarking qubit gates via quantum state tomography or randomized benchmarking [Knill *et al.*, 2008; Gambetta *et al.*, 2012; Gaebler *et al.*, 2012]. For quantum simulation, it is used to probe many-body quantum states by measuring multi-basis observables [Roushan *et al.*, 2017; Brydges *et al.*, 2019] or to certify the outcome of a simulation [Kokail *et al.*, 2019].

A multitude of platforms ranging from quantum gas microscopes [Impertro *et al.*, 2023] and trapped ions [Blatt and Roos, 2012; Monroe *et al.*, 2021] to polar molecules [Zhou, Ortner, and Rabl, 2011; Yan *et al.*, 2013; Ruttley *et al.*, 2024] and superconducting circuits [Houck, Türeci, and Koch, 2012; Kjaergaard *et al.*, 2020], already routinely use local rotations. For neutral atoms platforms, this also has already been demonstrated [Birkl and Fortágh, 2007; Isenhower *et al.*, 2010; Xia *et al.*, 2015] combining ground state manipulations [Yavuz *et al.*, 2006; Jones *et al.*, 2007] and addressing light. However, this procedure requires encoding the spin state in the hyperfine ground states of the alkali atoms. Therefore, it cannot be directly applied to our studies of the XY model, where the spin states are encoded in the Rydberg manifold.

During my Ph.D., we combined microwave manipulations of Rydberg states with the capability to induce local light shifts using addressing beams to perform local rotations. We used this ability to prepare the arrays in Néel states up to $N = 100$ atoms and to perform multi-basis measurements. The first part of this chapter will describe the technical improvements (see Sec. 3.1). The second will focus on preparing Néel states (see Sec. 3.2), and the third (see Sec. 3.3) will focus on our method to perform multi-basis measurements.

3.1 Scaling the addressing to many atoms

3.1.1 Arrays of local addressing beams

Using an SLM for the addressing. To apply local light shifts on several atoms, we send a 1013 nm laser light on a SLM that generates an addressing pattern on the atomic plane that we superimpose on the atoms (see Fig 3.1a). The 1013 nm light is produced by picking up part of the 1013 nm light from the Rydberg excitation laser and amplified up to 8 W using an ALS® amplifier. The choice of the SLM phase pattern determines which atom we address. As an example, an illustration of a 6×7 square array with half of the atoms addressed in a staggered configuration is shown in Fig. 3.1b. To create one addressing light spot at position x_i and y_i on the atomic plane, the SLM imprints the following phase:

$$\phi_j(x_s, y_s) = \frac{2\pi}{\lambda f}(x_s x_j + y_s y_j), \tag{3.1}$$
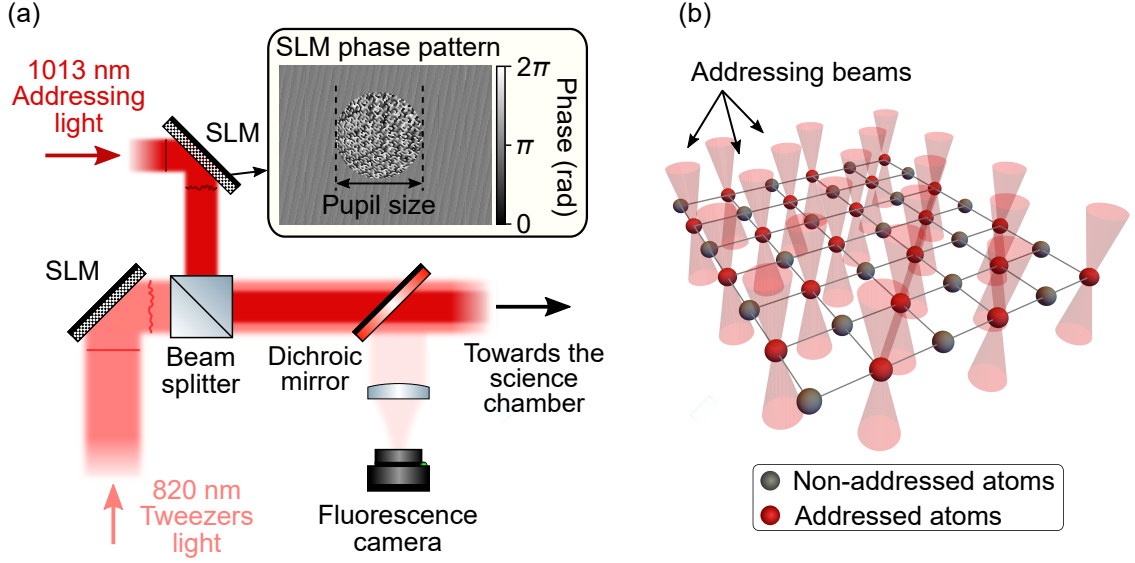
Figure 3.1: Addressability. (a) Sketch of the setup to generate the addressing beams. We use a second SLM to generate an addressing pattern that we superimpose on the atoms. (b) Schematic depicting an 6×7 square. Half of the atoms are addressed using addressing beams.

with x_s, y_s the spatial coordinates of the SLM, λ the addressing light wavelength, and f the focal length of the aspherical lenses. To create several addressing light spots, we sum all the addressing beam phases $\phi_j(x_s, y_s)$ resulting in the following phase:

$$\Phi(x_s, y_s) = \arg\left(\sum_{j=1}^{N_{\mathrm{addr}}} w_j e^{i\phi_j(x_s, y_s) + i\theta_j}\right). \tag{3.2}$$

with N_{addr} the number of atoms to address and θ_j and w_j being the relative phases and weights between the phase patterns of the individual addressing beam. These two last parameters are two degrees of freedom we can tune to vary the intensity in each spotlight.

Homogenizing the light-shifts. We wish to address all the addressed atoms with the same intensity to apply the same light shift. A dispersion of light shifts between different addressed atoms would be detrimental to the application of local operations since these atoms would undergo different rotations from each other. The aberrations induced by the optical path and interferences between each addressing beams naturally lead to inhomogeneities of the light spot intensities. To solve this problem, we use the Gerchberg-Saxton (GS) algorithm that optimizes the SLM phase pattern by playing
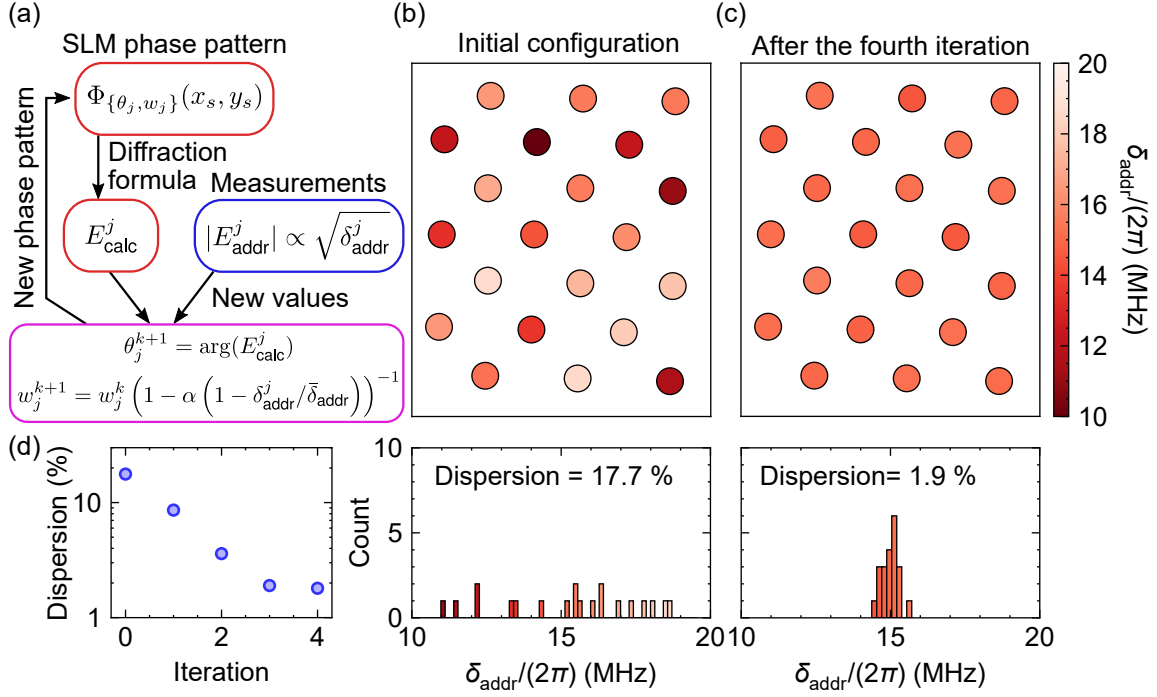
Figure 3.2: GS algorithm. (a) Sketch of the Gerchberg-Saxton optimization algorithm. The intensities $|E_{\text{meas}}^j|^2$ are given from the measured light shifts $|E_{\text{meas}}^j|^2 \propto \delta_{\text{addr}}^j$. (b)/(c) Light shift measurement before/after optimization. Top panel: Light shift measured by each atom. Bottom panel: histogram of the measured light shifts showing the dispersion (the size of the bar corresponds to the uncertainty on the light shift measurement). (d) Measured dispersion of the light shifts $\sigma(\delta_{\text{addr}})/\bar{\delta}_{\text{addr}}$ as a function of the number of iteration of the GS algorithm.

on the $\{\theta_j\}$ and $\{w_j\}$ values to correct the intensity inhomogeneity. Previous theses from the group already presented this algorithm in detail [Labuhn, 2016; de Léséleuc, 2021], which we use to homogenize the trap depth of each tweezer. Therefore, I will only give a brief description and show the equalization procedure on this 6×7 square array shown in Fig. 3.1b. The GS algorithm is iterative. If it is the first iteration, we randomly choose the θ_j values and take $w_j = 1$. Then, using the diffraction formula, we calculate the complex amplitude of light field $E_{\text{calc}}^j(x,y)$ at position (x_j, y_j) on the atomic plane:

$$E_{\text{calc}}^j = \iint e^{i\Phi(x_s, y_s) - i\phi_j(x_s, y_s)} dx_s dy_s \tag{3.3}$$

We then compare the calculated intensities $|E_{\text{calc}}^j|^2$ to the one experimentally measured $|E_{\text{meas}}^j|^2$. To get $|E_{\text{meas}}^j|^2$, we measure the light shifts induced on each addressed atom by performing microwave spectroscopy (see Sec. 2.3.3). As $\Omega_{\text{addr}}^2 \propto I_{\text{addr}}$,

the intensities $|E^j_{\mathrm{meas}}|^2$ are proportional to the light shifts. In Fig. 3.2b, we represent the light shifts measured on each addressed atoms using the initial SLM phase pattern. We compute a average value of $\bar{\delta}_{\mathrm{addr}}/(2\pi) = 15.0$ MHz with a relatively high dispersion of $\sigma(\delta_{\mathrm{addr}})/\bar{\delta}_{\mathrm{addr}} = 17.7\,\%$. Based on the comparisons between $|E^j_{\mathrm{calc}}|^2$ and $|E^j_{\mathrm{meas}}|^2$, the algorithm re-attributes new values to θ_j and w_j of the $k+1$-iteration trying to maximize the diffraction efficiency while equalizing the addressing light spot intensities:

$$\theta^{k+1}_j = \arg(E^j_{\mathrm{calc}})$$
$$w^{k+1}_j = w^k_j \left(1 - \alpha\left(1 - \delta^j_{\mathrm{addr}}/\bar{\delta}_{\mathrm{addr}}\right)\right)^{-1} \tag{3.4}$$

with α a gain factor $0 < \alpha \leqslant 1$. By performing a few iterations, we reduce the light shift dispersion. Figure 3.2d shows the measured dispersion as a function of the number of iterations. In four iterations, we reduce the dispersion down to $\sigma(\delta_{\mathrm{addr}})/\bar{\delta}_{\mathrm{addr}} \approx 1.9\,\%$ which is good enough to perform homogeneous rotations (see Fig. 3.2c). We observe that additional iterations do not improve the dispersion that plateaus around $\approx 2\,\%$. To go beyond this limit, one would need to fine-tune the optimization processes of the GS algorithm but as we will see in the next section, one main limiting factor are drifts misaligning the addressing pattern with the atoms.

3.1.2 Improving the addressing stability

Addressing and trap drift.   During my Ph.D., we noticed that the alignment between the addressing pattern and the traps slowly drifts with a typical time scale of a few hours. The first consequence is that the averaged light shift $\bar{\delta}_{\mathrm{addr}}$ (averaged on all the addressed atoms) decreases by almost $40\,\%$ in 14 hours. The second consequence is that the equalization of light shifts of $\approx 2\,\%$ reached with the GS algorithm degrades with time. After 14 hours, it increases to $16\,\%$. We did not manage to identify the sources of this drift but we suspect temperature fluctuations in the lab. To counter this drift, we increased the waist of the addressing light spot from 1.2 to $1.7\,\mu$m to make the alignment more resilient to drifts. We also developed an active feedback system to monitor and correct the addressing and trap positions. I will now describe these two improvements.

Size of the addressing light spot   To make the system more resilient to drifts, we increase the waist of the addressing light spot. To do so, we apply a circular phase
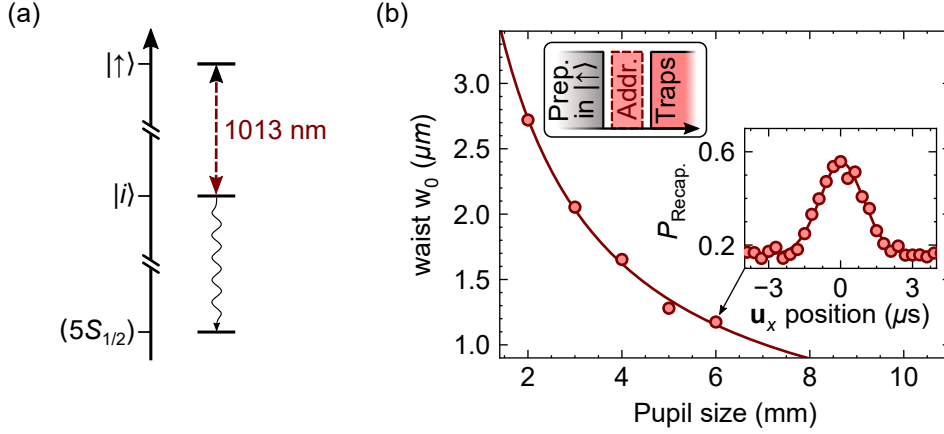
Figure 3.3: Size of the addressing light spots. (a) Energy level diagram. (b) Main panel: Measurement of the addressing light spot size as a function of the pupil size used on the addressing SLM phase pattern. The solid curve is a $\propto 1/(\text{pupil size})$ fit. Bottom right inset: Recapture probability as a function of the addressing displacement along $\mathbf{u}_x$ for a pupil size of 3 mm. The solid line is a Gaussian fit used to extract the waist w_0. Top left inset: experimental sequence.

mask on the addressing SLM phase pattern (see Fig. 3.1a). Inside this mask, the phase pattern is the same, and outside, we apply a grating pattern to send the light far away from the atoms. Thus, this phase mask is equivalent to an iris. By varying the size of this mask, we change the waist of the addressing light spots. To measure the waist, we proceed as follows. We first excite the atoms to $|\uparrow\rangle$ and then send an on-resonance addressing pulse ($\Delta_{\text{addr}} = 0$) of duration t_{addr}. Similarly to the deexcitation mechanism described in Sec. 2.3.1, the addressed atoms are transferred in $|i\rangle$ from which they spontaneously decay to the ground state (see Fig. 3.3a). By choosing $\Omega_{\text{addr}} \ll \Gamma_{|i\rangle}$, and $\Omega_{\text{addr}} t_{\text{addr}} \ll 2\pi$ the probability for an atom to be depumped is proportional to $\propto \Omega_{\text{addr}}^2/\Gamma_{|i\rangle} \propto I_{\text{addr}}$. To assess the addressing intensity profile, we measure this recapture probability P_{recap} and repeat this measurement for various positions of the addressing light spot. The bottom right inset in Fig. 3.3b shows the recapture probability as a function of the addressing position along $\mathbf{u}_x$, for a pupil size of 3 mm. Then, we fit P_{recap} by a Gaussian function from which we extract the waist. We measure different waists ranging from $1.0\,\mu\text{m}$ to $3.0\,\mu\text{m}$ for pupil size between 2 mm and 6 mm. The main drawback of increasing the waist is that it requires more power to reach the same peak intensity. Being limited in power, we choose an intermediate pupil size of 4 mm, increasing slightly the waist from 1.2 to $1.7\,\mu\text{m}$. Once this pupil size has been chosen, we also adapted the beam diameter of the laser to fit most of the
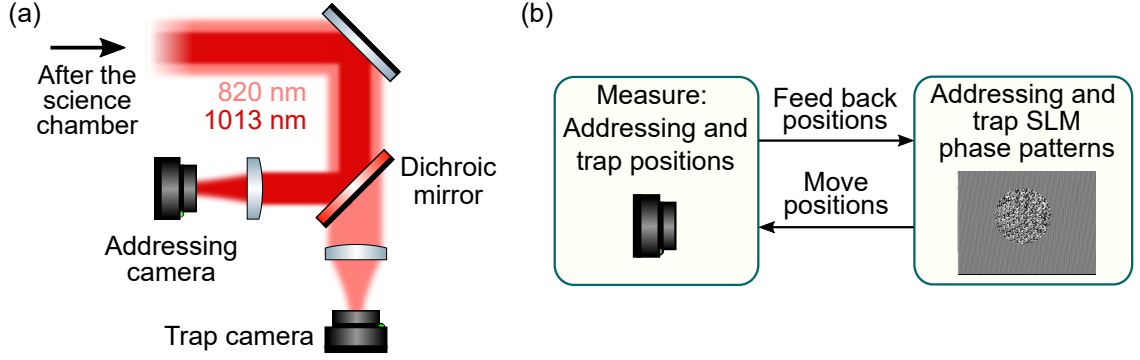
Figure 3.4: Position feedback of the addressing and trap beam positions. (a) Optical path showing of the addressing and trap beams after the science chamber. We use two cameras to monitor the positions. (b) Using the cameras, we record the positions of the traps and addressing light spots. We correct their positions by using the SLMs.

light power inside the iris.

Position feedback. To feed back the addressing and trap positions, we use two cameras after the science chamber imaging the atomic plane (see Fig. 3.4a). We take images, fit each light spot using 2D Gaussian fits, and extract the tweezer and addressing beam positions. The uncertainties of the fitted positions correspond to a displacement of 20 nm in the atomic plane. This uncertainty is low enough to capture position drifts of ~ 100 nm. If we measure a global displacement of the addressing or trap light spots compared to reference positions, we act on the SLM pattern to move them back to their reference positions (see Fig. 3.4b). In practice, if, on the camera, we measure a displacement Δx and Δy along the $\mathbf{u}_x$ and $\mathbf{u}_y$ direction, we apply a new phase pattern taking:

$$\phi_j(x_s, y_s) = \frac{2\pi}{\lambda f}(x_s(x_j - \Delta x) + y_s(y_j - \Delta y)). \tag{3.5}$$

The above correction does not degrade the intensity homogeneities of the addressing or trap pattern since we apply the same displacement on all the light spots. Using this position feedback, we measure that in 14 hours, the average light shift remains the same, and the dispersion only increases up to $\approx 5\,\%$, allowing to perform experiments over one day before having to realign and re-homogenize the addressing pattern. Further improvement could be envisioned to improve this feedback. For example, our protocol only uses one degree of freedom (per axis) to compensate for position drifts. One could add piezoelectric mirrors and additional cameras on the addressing and

69

trap optical paths to perform beam walk alignments.

3.2 Preparation of antiferromagnetic states along z

We now move to the preparation of classical antiferromagnetic state along z (also called Néel state), *i.e.*, a staggered arrangement of spins $|\uparrow\rangle$ and $|\downarrow\rangle$. As we will see all along this manuscript, this initialization is interesting as it is the starting point of many of our experiments to study the ground state [Sørensen *et al.*, 2010] and out-of-equilibrium physics of the dipolar model XY. In this section, I describe how to prepare these Néel states, discuss how to measure the fidelity and present a simple model to describe the errors.

3.2.1 Preparation

Néel state preparation sequence. To prepare a Néel state, we first excite all the atoms in $|\uparrow\rangle$ and then transfer them in $|\downarrow\rangle$ using a microwave π-pulse. We then turn on the addressing beams, applying a light shift δ_{addr} on the addressed atoms. We then transfer back the non-addressed atoms to $|\uparrow\rangle$ by applying a second microwave pulse on resonance. If the Rabi frequency of this second pulse is lower than the light shift $\Omega_{\mathrm{MW}} \ll \delta_{\mathrm{addr}}$, the microwaves are off-resonant for the addressed atoms and thus leave the addressed atoms in $|\downarrow\rangle$. As an illustration, Fig. 3.5a shows the preparation of a 6×7 square array in a Néel state preparation $|\uparrow\downarrow\uparrow\downarrow\cdots\rangle$. Half of the atoms are addressed in a staggered configuration (as depicted in Fig. 3.1b). The images show the array before/after preparation. As expected, we only see the non-addressed atoms recaptured and imaged during the read-out on the final image.

Before discussing the preparation fidelity, I first comment on the choice of this particular sequence. A naive approach to prepare Néel states would have been to first excite all the atoms to $|\uparrow\rangle$, turn on the addressing and then send the microwave pulse to prepare the addressed/non-addressed atoms in $|\uparrow\rangle/|\downarrow\rangle$. This sequence is simpler as we do not need to apply the microwave π-pulse but suffers from depumping induced by the addressing light. The addressing light couples the short-lived intermediate state $|i\rangle$ to $|\uparrow\rangle$. Due to state mixing, the lifetime of $|\uparrow\rangle$ is reduced to $\tau'_{|\uparrow\rangle} \simeq \tau_{|i\rangle} \left(\Delta_{\mathrm{addr}}/\Omega_{\mathrm{addr}}\right)^2 \simeq 1\,\mu\mathrm{s}$ with $\tau_{|i\rangle} = 110\,\mathrm{ns}$. This lifetime reduction thus leads to a fast depumping of the addressed from $|\uparrow\rangle$ to the ground states, thus limiting the Néel state preparation
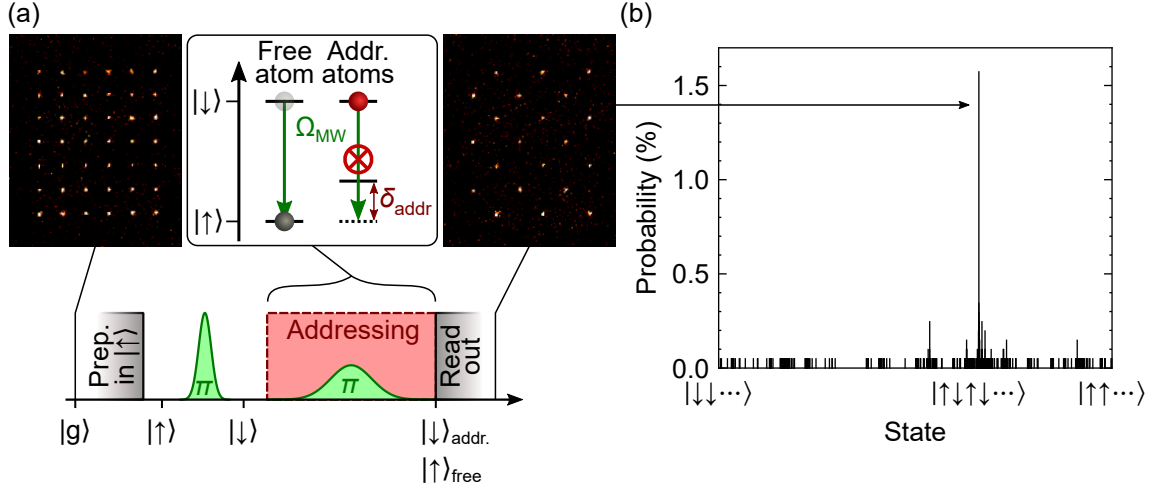
Figure 3.5: Classical Néel state preparation. (a) Experimental sequence to prepare a classical Néel. The images shows the results for a 6×7 square array. Here we use $|\uparrow\rangle = |60S_{1/2}, m_J = 1/2\rangle$ and $|\downarrow\rangle = |60P_{1/2}, m_J = -1/2\rangle$. The atoms are addressed in a staggered configuration as showed in Fig. 3.1b. (b) Corresponding state histogram measured after more than 2000 repetitions of the experiment. The desired Néel state (last image in (a)) $|\uparrow\downarrow\uparrow\downarrow \cdots\rangle$ is measured with a probability of $1.6(3)\,\%$.

fidelity. This is why, to avoid this effect, before the addressing pulse, we transfer all the atoms in the $|\downarrow\rangle$ state from which the addressed atoms cannot be depumped.

Measuring the preparation fidelity. The preparation fidelity is given by the probability to prepare the Néel state $|\uparrow\downarrow\uparrow\downarrow \cdots\rangle$. To estimate it, we apply the preparation protocol depicted in Fig. 3.5a and measure the state of the atoms. We then repeat this experiment and compute the probability $P_{|\uparrow\downarrow\uparrow\downarrow\cdots\rangle}$ to measure the target Néel state. For example, Fig. 3.5b shows the state histogram obtained after more than 2000 repetitions of the experiment for the 6×7 square array. The probability to measure the Néel state is $1.6(3)\,\%$. Due to various state preparation and detection errors, this probability is small. Therefore, measuring $P_{|\uparrow\downarrow\uparrow\downarrow\cdots\rangle}$ with good precision requires accumulating statistics on a lot of repetitions of the experiment and thus takes a long time, which makes it inconvenient to measure on a daily basis. Moreover, this probability decreases even more for larger arrays and becomes unpractical to measure.

To circumvent this issue, we use other observables to estimate the preparation fidelity. We measure the average probabilities $P_{|\downarrow\rangle}^{\mathrm{addr}}$ and $P_{|\uparrow\rangle}^{\mathrm{free}}$ to prepare the addressed and non-addressed atoms in $|\downarrow\rangle$ and $|\uparrow\rangle$. These probabilities can be interpreted as the probability per atom to be prepared in the correct state. Compared to $P_{|\uparrow\downarrow\uparrow\downarrow\cdots\rangle}$,
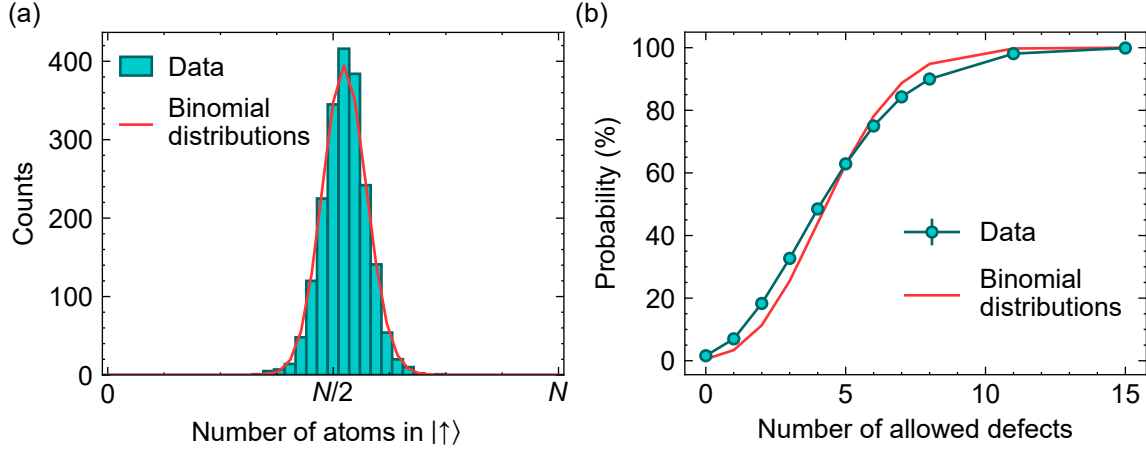
Figure 3.6: Analysis of the Néel state preparation. The data are the same as in Fig. 3.5b. (a) Histogram of the number of atoms measured in $|\uparrow\rangle$ for every repetition of the experiment. The red curve represent what would obtain if the addressed and non-addressed follow binomial distributions of probabilities $P_{|\downarrow\rangle}^{\text{addr}} = 85.7\,\%$ and $P_{|\uparrow\rangle}^{\text{free}} = 90.8\,\%$. (b) Green curve: Probability to measure non-perfect Néel state as a function of the number of allowed defects. Red curve: Expectation if the atoms follow the binomial distributions.

$P_{|\downarrow\rangle}^{\text{addr}}$ and $P_{|\uparrow\rangle}^{\text{free}}$ are easier to measure since they exhibit sizeable probabilities and do not require to average on many repetitions of the experiment since we already average on all the addressed and non-addressed atoms. Taking the same data as in Fig. 3.5b, we measure probabilities of $P_{|\downarrow\rangle}^{\text{addr}} = 85.7(2)\,\%$ and $P_{|\uparrow\rangle}^{\text{free}} = 90.8(2)\,\%$. From these probabilities, we estimate the probability of measuring the target Néel state:

$$P_{|\uparrow\downarrow\uparrow\downarrow\cdots\rangle} = \left(P_{|\downarrow\rangle}^{\text{addr}}\right)^{N/2} \times \left(P_{|\uparrow\rangle}^{\text{free}}\right)^{N/2} = 0.5\,\%, \tag{3.6}$$

and compare it to the one obtained by direct measurement $P_{|\uparrow\downarrow\uparrow\downarrow\cdots\rangle} = 1.6(3)\,\%$. We see a difference that we attribute to correlated errors between the atoms. When using Eq. 3.6, we assume that the state of all the atoms is independent from each other, but in reality, due to the XY interactions, the atoms interact during the preparation protocol leading to correlated errors. However, the two probabilities $P_{|\uparrow\downarrow\uparrow\downarrow\cdots\rangle}$ remain on the same order of magnitude $\sim 1\,\%$ indicating that using $P_{|\downarrow\rangle}^{\text{addr}}$ and $P_{|\uparrow\rangle}^{\text{free}}$ is a relatively good proxy to estimate the preparation fidelity.

We now have a practical mean to estimate the Néel state preparation fidelity. The fidelities we measure are small, indicating that the probability of preparing the Néel state is small. To assess which state we really prepare, we plot (taking the same data as in Fig. 3.5b) the histogram of the number of atoms measured in $|\uparrow\rangle$ for every

repetition of the experiment (see Fig. 3.6a). As expected, the histogram is centered around $N/2$ and due to preparation errors it exhibits a non-zero standard deviation of ≈ 2. This behaviour is very well reproduced by considering that the addressed and non-addressed atoms follow binomial distributions of probabilities $P_{|\downarrow\rangle}^{\text{addr}} = 85.7\,\%$ and $P_{|\uparrow\rangle}^{\text{free}} = 90.8\,\%$ (see red curve). It suggests that, in average, most of the atoms are prepared in the correct state and only a small fraction of them end up in the wrong state. To continue the analysis, we now plot the probability of measuring imperfect Néel states as a function of the number of defects, *i.e.*, the number of atoms detected in the wrong state (see Fig. 3.6b). The probability rapidly increases towards one as we allow defects. This rise up is well explained by considering binomial distributions taking as parameters the measured probabilities $P_{|\downarrow\rangle}^{\text{addr}} = 87.2\,\%$ and $P_{|\uparrow\rangle}^{\text{free}} = 90.6\,\%$ (red curve), resulting in a relatively good agreement with the data. Despite the low preparation fidelity, it suggests that most of the states we prepare are Néel states, including a few defects. Even if imperfect, we use this preparation protocol in experiments for probing many-body problems. To ensure that defects will not compromise the results of these experiments, we will need to benchmark them with a simulation, including the experimental imperfections. Therefore, we need to provide a model describing the preparation errors that can be included in a simulation.

3.2.2 Modelling the errors

Main sources of errors. To describe the preparation errors, we first identify the physical processes that limit the fidelity. We identify four main sources. I will describe then and briefly comment on the optimization that we performed to minimize their effects:

- **Rydberg excitation.** As described in Sec. 2.3.1, there is a non-zero probability $1 - \eta_{\text{exc}}$ to leave the atoms in the ground state during Rydberg excitation. To increase the Rydberg excitation fidelity, we optimized the STIRAP pulses (see Sec. 2.3.1).

- **XY interaction.** The main source of preparation imperfections is the dipolar XY interactions between the atoms. When all the atoms are in $|\uparrow\rangle$ or $|\downarrow\rangle$, the interactions do not affect their states since $|\uparrow\uparrow\cdots\rangle$ and $|\downarrow\downarrow\cdots\rangle$ are eigenstates of the XY Hamiltonian. However, when they are in a superposition of $|\uparrow\rangle$ and $|\downarrow\rangle$,

the interactions modify the state of the atoms. Thus, it decreases the fidelity to transfer the atoms between $|\uparrow\rangle$ and $|\downarrow\rangle$ using microwave pulses. To minimize this effect, we need these transfers to be as fast as possible, *i.e.*, we need to use the highest possible microwave Rabi frequency $J \ll \Omega_{\mathrm{MW}}$ (with J the XY interaction energy between two nearest neighbour atoms). Therefore, for the first microwave pulse (to transfer the atoms from $|\uparrow\rangle$ to $|\downarrow\rangle$), we apply a Gaussian π-pulse taking the largest Rabi frequency amplitude of $\Omega/(2\pi) = 20\,\mathrm{MHz}$ (limited by the Zeeman splitting induced by the magnetic field, see Sec. 2.4.1).

- **Crosstalk with the off-resonant microwaves.** We only apply a finite light on the addressed atoms. When transferring the non-addressed atoms from $|\downarrow\rangle$ to $|\uparrow\rangle$, a fraction of the addressed atoms are also transferred due to crosstalk with the off-resonant microwaves. To minimize this effect, we must choose the lowest microwave Rabi frequency $\Omega_{\mathrm{MW}} \ll \delta_{\mathrm{addr}}$. Therefore, minimizing both the impact of the interaction and of the crosstalk strongly constrains the choice of the Rabi frequency for this pulse $J \ll \Omega_{\mathrm{MW}} \ll \delta_{\mathrm{addr}}$. For typical values of $J/(2\pi) \approx 1\,\mathrm{MHz}$ and $\delta_{\mathrm{addr}}/(2\pi) \approx 10\,\mathrm{MHz}$, we experimentally found that the most efficient microwave pulse is a Gaussian pulse with a Rabi frequency amplitude of $\Omega_{\mathrm{MW}}/(2\pi) \approx 5\,\mathrm{MHz}$.

- **Detection errors.** Strictly speaking, detection errors do not decrease the preparation fidelity. However, they bias its measurement by introducing errors we cannot discriminate from preparation errors.

We have described all the physical processes limiting the preparation fidelity. We now move to the modelling of these errors.

Error tree. Taking all these errors into account in a simulation is intractable since it would require simulating the XY dynamics, including up to N atoms. To overcome this issue, we create a simple model to describe the errors that can be implemented in a simulation. To do so, we divide the sequence into multiple steps, each having a probability of success and fail (see the error tree in Fig. 3.7). During Rydberg excitation, $1 - \eta_{\mathrm{exc}}$ of the atoms remain in the ground state. Then, we apply the microwave pulses and the addressing. We denote η_{addr} and η_{free} the probability to prepare, from $|\uparrow\rangle$, the addressed and non-addressed atoms in $|\downarrow\rangle$ and $|\uparrow\rangle$. Then we readout the state with detection errors of $\varepsilon_{\uparrow}$ and $\varepsilon_{\downarrow}$ (see Sec. 2.3.2). From these
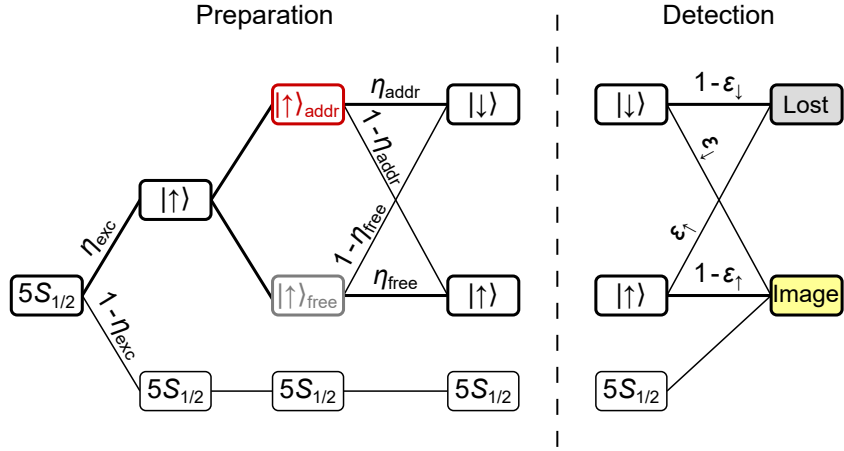
Figure 3.7: Néel state preparation: error tree. Left part: summarizes the different errors during the Néel state preparation. Right part: summarizes the different errors during the readout sequence.

Step	Symbol	Value	Main physical origin
Rydberg excitation	$1 - \eta_{\text{exc}}$	2%	Imperfect optical pumping, laser phase noise and spontaneous emission from $(6P_{3/2})$ [de Léséleuc *et al.*, 2018]
Microwave and addressing pulses	$1 - \eta_{\text{free}}$	7 %	Effect of the interactions during the pulses
	$1 - \eta_{\text{addr}}$	2 %	Effect of the interactions during the pulses and finite value of δ_{addr}
Read-out	$\varepsilon_{\downarrow}$	1.3 %	Hydrogenic state radiative lifetime $\varepsilon'_{(h)}$ see Sec. 2.3.2
	$\varepsilon_{\uparrow}$	2.5 %	$\varepsilon_{\text{freezing}} + \varepsilon_{\text{image}} + \varepsilon_{\text{bgc}} + (1 - \eta_{\text{deexc}})$ see Sec. 2.3.2

Table 3.1.: Summary of the experimental errors defined in Fig. 3.7. The values are given for the preparation of a Néel state of a 10×10 square array with $J/(2\pi) = 0.25\,\text{MHz}$, a mean light shift per addressed atoms of $\bar{\delta}_{\text{addr}}/(2\pi) = 11\,\text{MHz}$, and using $|\uparrow\rangle = |60S_{1/2}, m_J = 1/2\rangle$ and $|\downarrow\rangle = |60P_{3/2}, m_J = -1/2\rangle$.

probabilities, we compute the probability of measuring the addressed atoms in $|\downarrow\rangle$. At first order, it reads:

$$P_{|\downarrow\rangle}^{\mathrm{addr}} = 1 - (1 - \eta_{\mathrm{exc}}) - (1 - \eta_{\mathrm{addr}}) - \varepsilon_\downarrow. \tag{3.7}$$

Similarly, we compute the probability to measure the non-addressed atoms in $|\uparrow\rangle$:

$$P_{|\uparrow\rangle}^{\mathrm{free}} = 1 - (1 - \eta_{\mathrm{free}}) - \varepsilon_\uparrow. \tag{3.8}$$

Using a set of independent experiments, we calibrate η_{exc}, $\varepsilon_\uparrow$ and $\varepsilon_\downarrow$ (see Sec. 2.3). To measure η_{addr} and η_{free}, we experimentally measure $P_{|\downarrow\rangle}^{\mathrm{addr}}$ and $P_{|\uparrow\rangle}^{\mathrm{free}}$ and invert Eq. 3.7 and 3.8. As a reference, Table 3.1 shows the different errors that we measure for the preparation of a 10×10 square array Néel state using $J/(2\pi) = 0.25\,\mathrm{MHz}$ and $\bar{\delta}_{\mathrm{addr}}/(2\pi) = 11\,\mathrm{MHz}$. The preparation errors η_{addr} and η_{free} depend on the interaction energy J, on the geometry of the array and on the light shift $\bar{\delta}_{\mathrm{addr}}$ we apply. We must recalibrate these errors every time one of these parameters is changed. Once calibrated, the preparation errors can be easily included in a Montecarlo simulation. For each repetition of the simulation, the initial state of each atom is randomly chosen in $\{|\uparrow\rangle, |\downarrow\rangle, (5S_{1/2})\}$ following probabilities described by the error tree.

Further improvements. We have presented the protocol to prepare Néel states, explained how to estimate the fidelity, discussed the limitations and presented a simple error model that can be implemented in a Monte-Carlo simulation. I end up this section by giving a few ideas to improve the preparation fidelity. One could use optimal control to shape the microwave pulses to make the transfers of atoms between $|\uparrow\rangle$ and $|\downarrow\rangle$ more resilient to the XY interactions while minimizing the microwave crosstalk. Another idea would be to use the addressing light to selectively excite the addressed atom from the ground state to $|(n+1)S\rangle$ from which they barely interact with the non-addressed atom excited in $|nS\rangle = |\uparrow\rangle$. An additional microwave π-pulse would transfer the addressed atom to $|nP\rangle = |\downarrow\rangle$, thus preparing the Néel state. This sequence would require a second Rydberg excitation system for the $|(n+1)S\rangle$ state but would not suffer from the limitation in light shift and would reduce the effect of the XY interactions during the preparations.

3.3 Multi-basis measurements

We now move to the multi-basis measurements. Multi-basis measurements refer to the fact that each spin is measured in different bases. So far, Rydberg-encoded spins could only be measured all in the same basis: either along the z (natural basis of the read-out) or along x, y or any axis of the Bloch sphere by applying a microwave rotation just before the readout [Lienhard, 2019]. However, since the rotations are global, it was impossible to perform multi-basis measurements. Recently, many theory proposals highlighted the importance of crossed-basis observables to characterize exotic phases of matter [Perciavalle *et al.*, 2023; Versini *et al.*, 2023; Ruttley *et al.*, 2024] such as spin liquids [Yao *et al.*, 2018]. Motivated by the promise of expanding the range of many-body physics problems we can address, we developed an experimental method to perform arbitrary multi-basis measurements. This section is organized as follows: the first part is dedicated to the description of this protocol, the second part to the benchmarking on 3-atom entangled states and the last one to the tomography of these states. All the results presented in this section have been published [Bornet *et al.*, 2024].

3.3.1 Local rotations

Experimental sequence. The protocol relies on the combination of microwave pulses and addressing-induced light shifts to perform local rotations on the atoms before the readout. To perform these local rotations, we use the addressing beams to induce different light shifts on the atoms: either $0\delta_{\mathrm{addr}}$ (these atoms are not addressed), $1\delta_{\mathrm{addr}}$ or $2\delta_{\mathrm{addr}}$ (see Fig. 3.8). From now on, I will refer to the class of non-addressed atoms and the classes of atoms addressed with a light shift of $1\delta_{\mathrm{addr}}$ and $2\delta_{\mathrm{addr}}$ as the 0δ, 1δ and 2δ atoms. For simplicity, I will also denote δ the light shift. We use the following procedure to perform independent rotations on the three classes of atoms. First, we send a microwave pulse on resonance with the $|\uparrow\rangle \leftrightarrow |\downarrow\rangle$ transition (at frequency ω_0) to perform a global rotation on all the atoms. We then apply the addressing beams and send simultaneously a microwave field with two frequencies ω_0 and $\omega_0 + \delta$, resonant respectively with the 0δ and 1δ atoms (see Fig. 3.8). Each frequency component is independently controlled (relative phase and pulse duration), allowing for arbitrary qubit rotations on the 0δ and 1δ atoms while the 2δ atoms remain unaffected by this
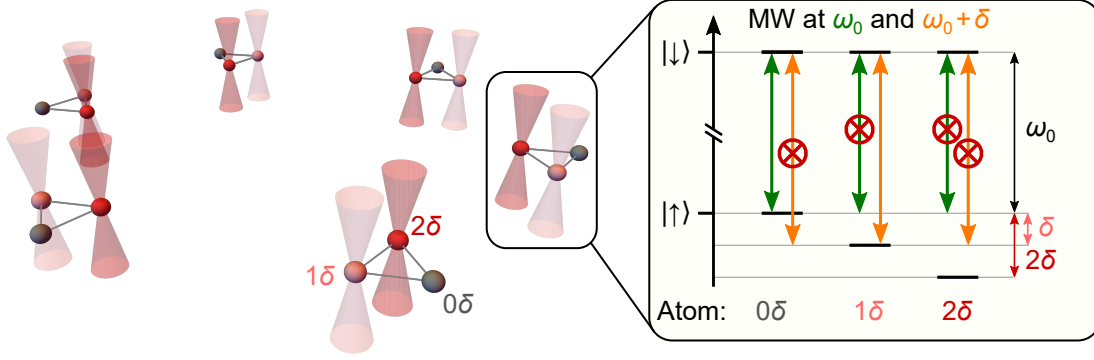
Figure 3.8: Multi-basis measurement protocol. The atoms are gather in groups of three in a equatorial configuration of length $12.3\,\mu$m. The triangles are separated by $60\,\mu$m.

second microwave pulse.

As an example, Fig. 3.9 shows the experimental sequence used to measure the state of the 0δ, 1δ and 2δ atoms along the y, z and x axes. With the first microwave pulse, we apply a $\pi/2$ global rotation around $-y$. We call $R^{-y}\left(\frac{\pi}{2}\right)$ the corresponding rotation operator. We then turn on the addressing and apply the local rotations. With the microwave frequency component at ω_0, we apply a local rotation $R^x_{0\delta}\left(\frac{\pi}{2}\right)$ on the 0δ atoms and with the one at $\omega_0 + \delta$ we apply $R^y_{1\delta}\left(\frac{\pi}{2}\right)$ on the 1δ atoms. The 2δ atoms remain unchanged by these pulses ($\mathbb{1}_{2\delta}$). During the addressing pulse, the light shifts also affect the states of the 1δ and 2δ atoms. They apply a rotation $R^z_{1\delta}(\phi)$ and $R^z_{2\delta}(2\phi)$ with $\phi = \delta t_{\text{addr}}$ being the phase accumulated during this addressing pulse of duration t_{addr}. This full sequence is thus equivalent to the following rotations:

$$
\begin{aligned}
&\left[R^x_{0\delta}\left(\tfrac{\pi}{2}\right) \otimes R^z_{1\delta}(\phi)\, R^y_{1\delta}\left(\tfrac{\pi}{2}\right) \otimes R^z_{2\delta}(2\phi)\, \mathbb{1}_{2\delta} \right] R^{-y}\left(\tfrac{\pi}{2}\right) \\
&= R^x_{0\delta}\left(\tfrac{\pi}{2}\right) R^{-y}_{0\delta}\left(\tfrac{\pi}{2}\right) \otimes R^z_{1\delta}(\phi)\, R^y_{1\delta}\left(\tfrac{\pi}{2}\right) R^{-y}_{1\delta}\left(\tfrac{\pi}{2}\right) \otimes R^z_{2\delta}(2\phi)\, R^{-y}_{2\delta}\left(\tfrac{\pi}{2}\right).
\end{aligned}
\tag{3.9}
$$

As $R^x_{0\delta}\left(\frac{\pi}{2}\right) R^{-y}_{0\delta}\left(\frac{\pi}{2}\right) = R^z_{0\delta}\left(\frac{\pi}{2}\right) R^x_{0\delta}\left(\frac{\pi}{2}\right)$ and as $R^y_{1\delta}\left(\frac{\pi}{2}\right) R^{-y}_{1\delta}\left(\frac{\pi}{2}\right) = \mathbb{1}_{1\delta}$ the sequence in in Eq. 3.9 thus amounts to the rotations:

$$
\begin{aligned}
&R^z_{0\delta}\left(\tfrac{\pi}{2}\right) R^x_{0\delta}\left(\tfrac{\pi}{2}\right) \otimes R^z_{1\delta}(\phi) \otimes R^z_{2\delta}(2\phi)\, R^{-y}_{2\delta}\left(\tfrac{\pi}{2}\right) \\
&= \left[R^z_{0\delta}\left(\tfrac{\pi}{2}\right) \otimes R^z_{1\delta}(\phi) \otimes R^z_{2\delta}(2\phi) \right] \left[R^x_{0\delta}\left(\tfrac{\pi}{2}\right) \otimes \mathbb{1}_{1\delta} \otimes R^{-y}_{2\delta}\left(\tfrac{\pi}{2}\right) \right].
\end{aligned}
\tag{3.10}
$$

In this equation, the first term $R^z_{0\delta}\left(\frac{\pi}{2}\right) \otimes R^z_{1\delta}(\phi) \otimes R^z_{2\delta}(2\phi)$ corresponds to z rotations. As when we apply the readout sequence, we project the states of the spins along the z-basis, these z-rotations have no effect on the measured probabilities and thus can
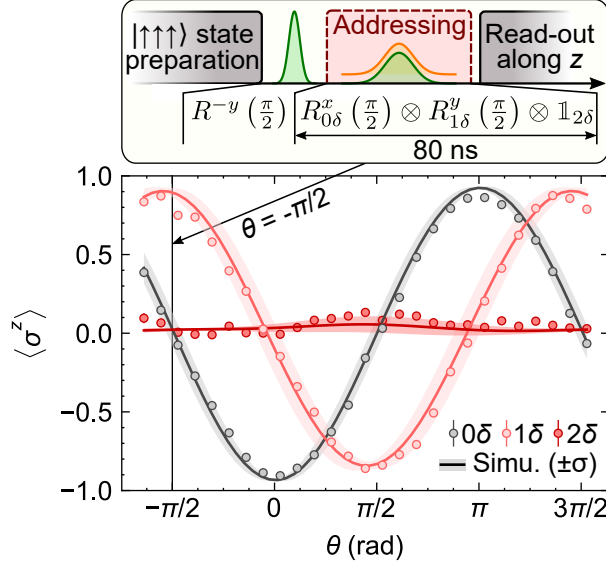
Figure 3.9: Ramsey experiment. Top panel: Experimental sequence to measure the 0δ, 1δ and 2δ atoms in the y, z and x basis. Bottom panel: Ramsey experiment to benchmark the multi-basis protocol. The first global microwave a global rotation $R^{x\cos(\theta)+y\sin(\theta)}\left(\frac{\pi}{2}\right)$. The addressing and microwave pulses at frequency ω_0 (green) and $\omega_0 + \delta$ (orange) perform the local rotations $R^x_{0\delta}\left(\frac{\pi}{2}\right) \otimes R^y_{1\delta}\left(\frac{\pi}{2}\right) \otimes \mathbb{1}_{2\delta}$. When $\theta = -\pi/2$ the sequence corresponds to the one shown in top panel. The solid curves are Monte-Carlo simulations with the shaded areas representing the standard deviation.

be ignored. It leaves us with the second term $R^x_{0\delta}\left(\frac{\pi}{2}\right) \otimes \mathbb{1}_{1\delta} \otimes R^{-y}_{2\delta}\left(\frac{\pi}{2}\right)$, which indeed corresponds to the rotations to be applied to measure the 0δ, 1δ and 2δ atoms in the y, z and x bases. We can generalize this example to show that by applying the right set of microwave rotations, we can measure the three classes of atoms in arbitrary bases.

Benchmarking. To illustrate and benchmark this protocol, we perform a Ramsey experiment. For this experiment, the atoms are arranged in groups of equilateral triangles, as shown in Fig. 3.8. Starting from all the atoms in $|\uparrow\rangle$, we apply a first global rotation $R^{x\cos(\theta)+y\sin(\theta)}\left(\frac{\pi}{2}\right)$, followed by the local rotations $R^x_{0\delta}\left(\frac{\pi}{2}\right) \otimes R^y_{1\delta}\left(\frac{\pi}{2}\right) \otimes \mathbb{1}_{2\delta}$ and finally read-out the states for various θ. When $\theta = -\pi/2$, this sequence of rotation is the same as the one described previously: we measure the 0δ, 1δ and 2δ atoms in the y, z and x bases. At this angle, we thus expect to measure a zero magnetization for the 0δ and 2δ atoms and a maximum magnetization for the 1δ ones. As we vary θ, we expect oscillations of the 0δ and 1δ-atom magnetizations dephased by $\pi/2$ while the 2δ one should remain constant at zero. Figure 3.9 shows the experimental results. They are in good agreement with the expectations. However, we observe finite contrast

of the oscillation magnetizations that we attribute to experimental imperfections. To confirm this, Lucas Leclerc (working at Pasqal®) performed Monte Carlo simulations including all the identified errors: state preparation errors (finite Rydberg excitation efficiency η_{exc}), detection errors ($\varepsilon_\downarrow$ and $\varepsilon_\uparrow$) and imperfections occurring during the local rotations sequence. We identify six physical processes limiting the rotation fidelities:

- **Crosstalk with the off-resonant microwaves.** We only apply a finite light shift of $1(2)\delta/(2\pi) = 23(46)\,\mathrm{MHz}$ on the addressed atoms. The light shifts are not much larger than the microwave Rabi frequency of $\Omega_{\mathrm{MW}}/(2\pi) = 5\,\mathrm{MHz}$. It means that the microwave frequency at $\omega_0/\omega_0 + \delta$ is not infinitely detuned from the $1\delta/0\delta$ and 2δ atom transition. These crosstalks with the off-resonant microwave affect the state of the atoms resulting in imperfect rotations of the atoms.

- **XY interactions during the rotations.** The rotation sequence takes $\sim 100\,\mathrm{ns}$, which is not very short compared to the typical XY time dynamics $2\pi/J \approx 1\,\mu\mathrm{s}$. These residual interactions affect the rotations and thus reduce the rotation fidelity.

- **Addressing-induced depumping.** Due to the spontaneous emission induced by off-resonant coupling to the short-lived intermediate state $|i\rangle$, the addressed atoms are slowly depumped to the ground state ($5S_{1/2}$). For $\Delta_{\mathrm{addr}}/(2\pi) = 400\,\mathrm{MHz}$ and $\delta/(2\pi) = 23\,\mathrm{MHz}$ we experimentally measure an effective lifetime of $\sim 2.3\,\mu\mathrm{s}$ and $\sim 1.1\,\mu\mathrm{s}$ for the 1δ and 2δ atoms in $|\uparrow\rangle$ consistent with the theoretical lifetimes $\tau'_{|\uparrow\rangle} \simeq \tau_{|i\rangle} \left(\Delta_{\mathrm{addr}}/\Omega_{\mathrm{addr}}\right)^2 \sim 1\,\mu\mathrm{s}$[1].

- **Addressing-induced atom losses.** The tightly focused addressing beams apply a ponderomotive force on the addressed atoms, pushing them away from their the center of their respective traps, thus preventing them from being recaptured. Experimentally, for $\delta/(2\pi) = 23\,\mathrm{MHz}$, we measure losses of $0.3(3)\,\%$ and $1.3(3)\,\%$ for the 1δ and 2δ atoms when sending a $80\,\mathrm{ns}$ addressing pulse.

- **Light-shifts inhomogeneities.** As explained in Sec. 3.1, the light shifts applied to the atoms are not perfectly homogeneous. We measured a dispersion on the

---

[1]For more precise calculations of $\tau'_{|\uparrow\rangle}$, we would need to take into account all the couplings to different Zeeman sublevels of the intermediate state ($6P_{3/2}$).

order of $1\,\%$ after calibration that can drift up to $3\,\%$ after one day without additional calibrations. When the addressing is on, the dispersion results in a variation of the phase accumulation of the 1δ atoms across the array. It leads to a spread of the atom rotation angle when sending the microwave pulses for local rotations.

- **Timing jitter.** We measure an electronic jitter of $\pm 2\,\mathrm{ns}$ between the addressing and the microwave pulses. Shot-to-shot, the jitter induces uncertainty of the phase accumulation of the 1δ atoms. It thus results of a shot-to-shot fluctuation of the atom rotation when applying the local rotation thus leading to imperfect microwave rotations.

Taking into account all these imperfections in the simulation yields a good agreement with the data.

Before moving to the next section, I first comment on the choice of this sequence. Another, more natural, experimental protocol to perform multi basis measurement would have been to apply three microwave frequencies tuned on the 0δ, 1δ and 2δ-atoms. However, residual spatial inhomogeneities on the 2δ light-shifts and time jitter degraded the rotation fidelities. However, we believe that with a better control of the light homogeneities, of the addressing/trap beams alignment and of the timings sequence, this sequence would be better than the one we use. We would not need the initial global microwave pulse, thus, the sequence would be shorter reducing the effect of the interaction during the rotation protocols.

3.3.2 Measurement of the chirality

Chiral states preparation. I now demonstrate how the local control enables the measurement and characterization of complex correlated states. In particular, we investigate the entangled states of three atoms placed in an equilateral triangle (as shown in Fig. 3.8) and interact via $\mathcal{H}_{\mathrm{XY}}$. In this configuration, the interactions lift the degeneracy between the states $|\uparrow\uparrow\downarrow\rangle$, $|\uparrow\downarrow\uparrow\rangle$ and $|\downarrow\uparrow\uparrow\rangle$. It leads to three new eigenstates $|W\rangle = (|\uparrow\uparrow\downarrow\rangle + |\uparrow\downarrow\uparrow\rangle + |\downarrow\uparrow\uparrow\rangle)/\sqrt{3}$ and the chiral states $|\chi^{\pm}\rangle = \left(|\uparrow\uparrow\downarrow\rangle + e^{\pm i2\pi/3}|\uparrow\downarrow\uparrow\rangle + e^{\pm i4\pi/3}|\downarrow\uparrow\uparrow\rangle\right)/\sqrt{3}$ separated in frequency by $3J$, as shown in Fig. 3.10a. Although all these states exhibit the same z magnetizations and two-body correlation functions, they can be distinguished through their chirality. The chirality χ
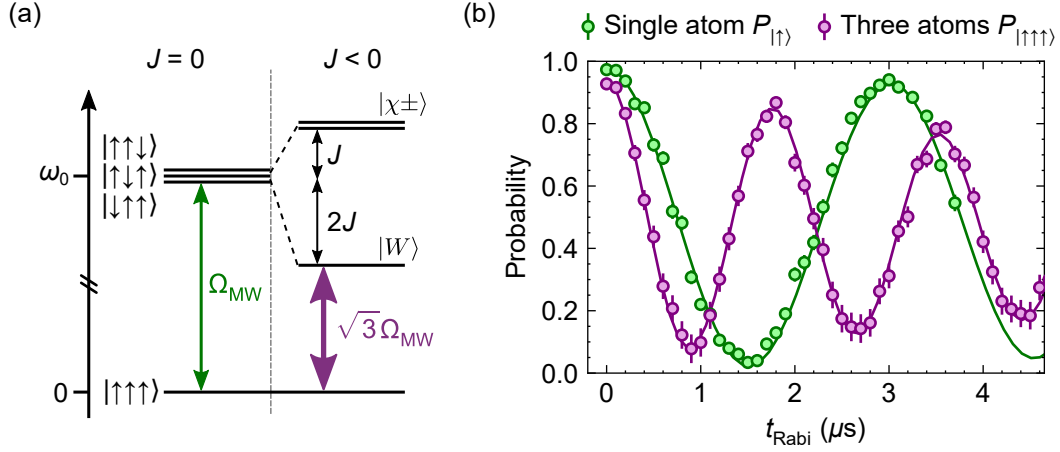
Figure 3.10: W state preparation. (a) Spectrum of 3 atoms in an equilateral triangle, interacting via the XY model. (b) Microwave Rabi oscillations. Green: single-atom Rabi oscillations. Purple: Microwave Rabi oscillation of three interacting atoms in an equatorial configuration with $P_{|\uparrow\uparrow\uparrow\rangle}$ the probability to measure the three atoms in $|\uparrow\rangle$. The solid curves are simulations including all identified experimental imperfections.

is a spin rotationally symmetric observable that breaks time-reversal symmetry and is defined for three spins i, j and k as $\langle\chi_{ijk}\rangle = \langle(\boldsymbol{\sigma}_i\times\boldsymbol{\sigma}_j)\cdot\boldsymbol{\sigma}_k\rangle$, with $\boldsymbol{\sigma}_i = \sigma_i^x\boldsymbol{x}+\sigma_i^y\boldsymbol{y}+\sigma_i^z\boldsymbol{z}$ [Tsomokos $et\ al.$, 2008]. For a product state, $\langle\chi_{ijk}\rangle$ is bounded by ± 1, as it corresponds to the volume spanned by the three spins $\langle\boldsymbol{\sigma}_{i,j,k}\rangle$. This limit can be overcome for entangled states, which can achieve a maximum value of $\pm 2\sqrt{3}$ for the chiral states $|\chi^{\pm}\rangle$.

To prepare these states, we first prepare the atoms in $|\uparrow\rangle$. We then apply a microwave pulse at frequency $\omega_0 + 2J$ to couple $|\uparrow\uparrow\uparrow\rangle$ to $|W\rangle$ (see Fig. 3.10b). The Rabi frequency is collectively enhanced by a factor $\sqrt{3}$, which we confirm by comparing the Rabi oscillations on the triangular configuration (purple) against a non-interacting case (green). These observed dynamics are well captured by numerical simulations made by Gabriel, including all experimentally characterized imperfections. Once the W-state is prepared, we turn on the addressing light for a time duration t_{φ} to imprint a phase 0φ, 1φ and 2φ on the 0δ, 1δ and 2δ atoms with $\varphi = \delta t_{\varphi}$. We thus prepare $|\varphi\rangle = (|\uparrow\uparrow\downarrow\rangle + e^{i\varphi}|\uparrow\downarrow\uparrow\rangle + e^{i2\varphi}|\downarrow\uparrow\uparrow\rangle)/\sqrt{3}$ (see Fig. 3.11a). By imposing $\varphi = 2\pi/3$, we prepare $|\varphi = 2\pi/3\rangle = |\chi^+\rangle$ and by imposing $\varphi = 4\pi/3$, we prepare $|\varphi = 4\pi/3\rangle = |\chi^-\rangle$.

Measurement of the chirality.   We now move to the measurement of the chirality. The chirality is the sum of six terms:

$$
\begin{aligned}
\langle \chi_{0\delta,1\delta,2\delta} \rangle = & \langle \sigma_{0\delta}^x \sigma_{1\delta}^y \sigma_{2\delta}^z \rangle + \langle \sigma_{0\delta}^y \sigma_{1\delta}^z \sigma_{2\delta}^x \rangle + \langle \sigma_{0\delta}^z \sigma_{1\delta}^x \sigma_{2\delta}^y \rangle \\
& - \langle \sigma_{0\delta}^y \sigma_{1\delta}^x \sigma_{2\delta}^z \rangle - \langle \sigma_{0\delta}^x \sigma_{1\delta}^z \sigma_{2\delta}^y \rangle - \langle \sigma_{0\delta}^z \sigma_{1\delta}^y \sigma_{2\delta}^x \rangle .
\end{aligned}
\tag{3.11}
$$

For each value of the imprinted phase φ, we measure the six different terms in Eq. 3.11 to compute the total chirality of the state $|\varphi\rangle$. This method is analogous to similar works using superconducting qubits [Roushan *et al.*, 2017]. Figure 3.11b shows the results (purple circles) as a function of φ and the theoretical expectations (black curve). Due to experimental imperfections, the amplitude is reduced, and the shape of the curve is slightly distorted. To understand these effects, Lucas performed a Monte-Carlo simulation including all the identified errors: preparation errors (finite η_{exc} + simulation of the $|\varphi\rangle$ preparation), local rotation imperfections (see previous section), detection errors ($\varepsilon_\downarrow$ and $\varepsilon_\uparrow$), and decoherence processes (Rydberg lifetimes and shot-to-shot positional disorder of the atoms). Including these errors leads to a good agreement between the simulation (purple curve) and the data. To assess which errors are dominant, we perform two other simulations. The first one assumes a perfect $|\varphi\rangle$ preparation and simulates the rest of the sequence (blue curve), and the second one simulates the $|\varphi\rangle$ preparation and assumes perfect multi-basis measurements (red curve). The first simulation fits the data better, indicating that the dominant errors come from the measurement errors. The imperfections in the spin rotations lead to measurements along bases slightly different from the target ones resulting in a distortion of the data curve as well as for the blue and purple simulation curves. Moreover, the reduction of contrast that we experimentally observe mainly comes from the measurement errors (imperfect rotations and detection errors), which decrease the chirality amplitude.

   In conclusion, we have shown that using these local rotations we can measure exotic observables such as the chirality. In Chapter 6 we will reuse this method to measure chiral-chiral correlations between two interacting triangles which represent our starting point for the investigation of exotic phases of matter such as chiral spin liquids.
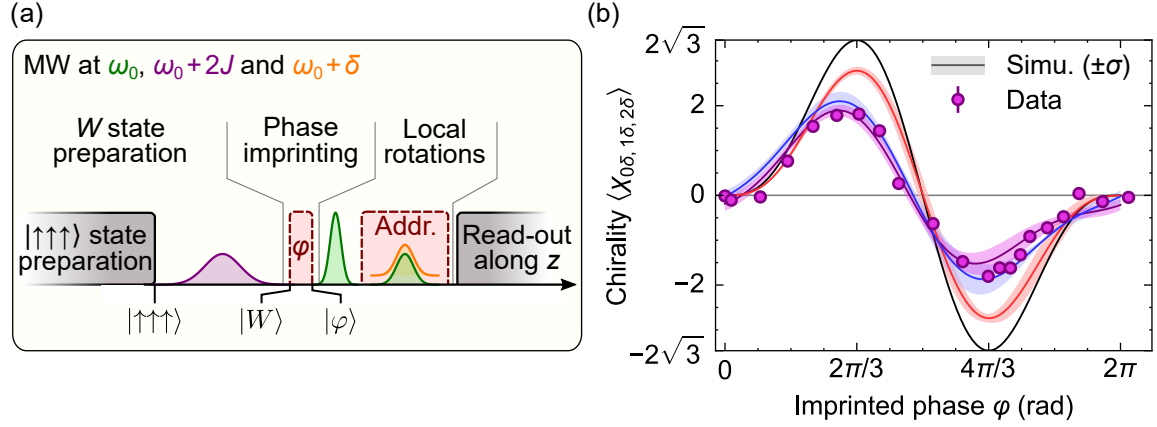
Figure 3.11: Measurement of the chirality. (a) Experimental sequence to prepare $|\varphi\rangle$ and measure its chirality. (b) Measurement of the $|\varphi\rangle$ chirality as a function of φ. The solid curves are the results of the Monte-Carlo simulations. Black: perfect simulation. Red: simulation of the $|\varphi\rangle$ preparation and perfect measurement. Blue: perfect $|\varphi\rangle$ preparation and simulation of the measurement sequence. Purple: simulation of all the steps. The shaded areas represent the simulations standard deviations.

3.3.3 Tomography

Density matrix reconstruction. We now use the ability to locally measure the atoms in different bases to perform full quantum state tomography of the $|W\rangle$ and $|\chi^{\pm}\rangle$ states and reconstruct their density matrix. Any density matrix of a 3-atom state can be decomposed in the following way:

$$\rho = \left(\frac{1}{2}\right)^3 \sum_{\{a,b,c\}\in\{I,x,y,z\}^3} \mathrm{tr}\left(\rho M^{a,b,c}\right) M^{a,b,c} \quad \text{with} \quad M^{a,b,c} = \sigma_1^a \otimes \sigma_2^b \otimes \sigma_3^c, \quad (3.12)$$

with $\sigma_i^I = \mathbb{1}_i$, and $\mathrm{tr}\left(\rho M^{a,b,c}\right) = \langle M^{a,b,c}\rangle$ being the expectation value when measuring the three spins in the a, b and c basis. To reconstruct the density matrix, the first naive approach is to measure all the expectation value $\mathrm{tr}\left(\rho M^{a,b,c}\right)$, *i.e.* we measure the state of each atom in the x, y and z basis corresponding to $3^3 = 27$ different measurements for a 3-atom state. Table 3.2 summarizes all the rotation local to performed to measure these 27 measurements. However, these expectation values cannot be experimentally measured with an infinite precision and may suffer from detection errors. Thus, applying blindly Eq. 3.12 after having measured all the $\langle M^{a,b,c}\rangle$ expectation values would lead to a non-physical density matrix that is, for example, not guaranteed to be non-negative definite. To overcome this issue, we use a maximum-likelihood

Basis $(0\delta,1\delta,2\delta)$	Rotations	$\phi_{\text{all}}(°)$	$\phi_{0\delta}(°)$	$\phi_{1\delta}(°)$
xxx	$\left[\mathbb{1}_{0\delta} \otimes \mathbb{1}_{1\delta} \otimes \mathbb{1}_{2\delta}\right] R^{-y}\left(\frac{\pi}{2}\right)$	-90	$\times$	$\times$
xxy	$\left[R_{0\delta}^{-y}\left(\frac{\pi}{2}\right) \otimes R_{1\delta}^{-y}\left(\frac{\pi}{2}\right) \otimes \mathbb{1}_{2\delta}\right] R^{x}\left(\frac{\pi}{2}\right)$	0	-90	-90
xxz	$\left[R_{0\delta}^{-y}\left(\frac{\pi}{2}\right) \otimes R_{1\delta}^{-y}\left(\frac{\pi}{2}\right) \otimes \mathbb{1}_{2\delta}\right] \mathbb{1}$	$\times$	-90	-90
xyx	$\left[\mathbb{1}_{0\delta} \otimes R_{1\delta}^{x}\left(\frac{\pi}{2}\right) \otimes \mathbb{1}_{2\delta}\right] R^{-y}\left(\frac{\pi}{2}\right)$	-90	$\times$	0
xyy	$\left[R_{0\delta}^{-y}\left(\frac{\pi}{2}\right) \otimes \mathbb{1}_{2\delta} \otimes \mathbb{1}_{2\delta}\right] R^{x}\left(\frac{\pi}{2}\right)$	0	-90	$\times$
xyz	$\left[R_{0\delta}^{-y}\left(\frac{\pi}{2}\right) \otimes R_{1\delta}^{x}\left(\frac{\pi}{2}\right) \otimes \mathbb{1}_{2\delta}\right] \mathbb{1}$	$\times$	-90	0
xzx	$\left[\mathbb{1}_{0\delta} \otimes R_{1\delta}^{y}\left(\frac{\pi}{2}\right) \otimes \mathbb{1}_{2\delta}\right] R^{-y}\left(\frac{\pi}{2}\right)$	-90	$\times$	90
xzy	$\left[R_{0\delta}^{-y}\left(\frac{\pi}{2}\right) \otimes R_{1\delta}^{-x}\left(\frac{\pi}{2}\right) \otimes \mathbb{1}_{2\delta}\right] R^{x}\left(\frac{\pi}{2}\right)$	0	-90	180
xzz	$\left[R_{0\delta}^{-y}\left(\frac{\pi}{2}\right) \otimes \mathbb{1}_{1\delta} \otimes \mathbb{1}_{2\delta}\right] \mathbb{1}$	$\times$	-90	$\times$
yxx	$\left[R_{0\delta}^{x}\left(\frac{\pi}{2}\right) \otimes \mathbb{1}_{1\delta} \otimes \mathbb{1}_{2\delta}\right] R^{-y}\left(\frac{\pi}{2}\right)$	-90	0	$\times$
yxy	$\left[\mathbb{1}_{0\delta} \otimes R_{1\delta}^{-y}\left(\frac{\pi}{2}\right) \otimes \mathbb{1}_{2\delta}\right] R^{x}\left(\frac{\pi}{2}\right)$	0	$\times$	-90
yxz	$\left[R_{0\delta}^{x}\left(\frac{\pi}{2}\right) \otimes R_{1\delta}^{-y}\left(\frac{\pi}{2}\right) \otimes \mathbb{1}_{2\delta}\right] \mathbb{1}$	$\times$	0	-90
yyx	$\left[R_{0\delta}^{x}\left(\frac{\pi}{2}\right) \otimes R_{1\delta}^{x}\left(\frac{\pi}{2}\right) \otimes \mathbb{1}_{2\delta}\right] R^{-y}\left(\frac{\pi}{2}\right)$	-90	0	0
yyy	$\left[\mathbb{1}_{0\delta} \otimes \mathbb{1}_{1\delta} \otimes \mathbb{1}_{2\delta}\right] R^{x}\left(\frac{\pi}{2}\right)$	0	$\times$	$\times$
yyz	$\left[R_{0\delta}^{x}\left(\frac{\pi}{2}\right) \otimes R_{1\delta}^{x}\left(\frac{\pi}{2}\right) \otimes \mathbb{1}_{2\delta}\right] \mathbb{1}$	$\times$	0	0
yzx	$\left[R_{0\delta}^{x}\left(\frac{\pi}{2}\right) \otimes R_{1\delta}^{y}\left(\frac{\pi}{2}\right) \otimes \mathbb{1}_{2\delta}\right] R^{-y}\left(\frac{\pi}{2}\right)$	-90	0	90
yzy	$\left[\mathbb{1}_{0\delta} \otimes R_{1\delta}^{-x}\left(\frac{\pi}{2}\right) \otimes \mathbb{1}_{2\delta}\right] R^{x}\left(\frac{\pi}{2}\right)$	0	$\times$	180
yzz	$\left[R_{0\delta}^{x}\left(\frac{\pi}{2}\right) \otimes \mathbb{1}_{1\delta} \otimes \mathbb{1}_{2\delta}\right] \mathbb{1}$	$\times$	0	$\times$
zxx	$\left[R_{0\delta}^{y}\left(\frac{\pi}{2}\right) \otimes \mathbb{1}_{1\delta} \otimes \mathbb{1}_{2\delta}\right] R^{-y}\left(\frac{\pi}{2}\right)$	-90	90	$\times$
zxy	$\left[R_{0\delta}^{-x}\left(\frac{\pi}{2}\right) \otimes R_{1\delta}^{-y}\left(\frac{\pi}{2}\right) \otimes \mathbb{1}_{2\delta}\right] R^{x}\left(\frac{\pi}{2}\right)$	0	180	-90
zxz	$\left[\mathbb{1}_{0\delta} \otimes R_{1\delta}^{-y}\left(\frac{\pi}{2}\right) \otimes \mathbb{1}_{2\delta}\right] \otimes \mathbb{1}$	$\times$	$\times$	-90
zyx	$\left[R_{0\delta}^{y}\left(\frac{\pi}{2}\right) \otimes R_{1\delta}^{x}\left(\frac{\pi}{2}\right) \otimes \mathbb{1}_{2\delta}\right] R^{-y}$	-90	90	0
zyy	$\left[R_{0\delta}^{-x}\left(\frac{\pi}{2}\right) \otimes \mathbb{1}_{1\delta} \otimes \mathbb{1}_{2\delta}\right] R^{x}\left(\frac{\pi}{2}\right)$	0	180	$\times$
zyz	$\left[\mathbb{1}_{0\delta} \otimes R_{1\delta}^{x}\left(\frac{\pi}{2}\right) \otimes \mathbb{1}_{2\delta}\right] \otimes \mathbb{1}$	$\times$	$\times$	0
zzx	$\left[R_{0\delta}^{y}\left(\frac{\pi}{2}\right) \otimes R_{1\delta}^{y}\left(\frac{\pi}{2}\right) \otimes \mathbb{1}_{2\delta}\right] R^{-y}\left(\frac{\pi}{2}\right)$	-90	90	90
zzy	$\left[R_{0\delta}^{-x}\left(\frac{\pi}{2}\right) \otimes R_{1\delta}^{-x}\left(\frac{\pi}{2}\right) \otimes \mathbb{1}_{2\delta}\right] R^{x}\left(\frac{\pi}{2}\right)$	0	180	180
zzz	$\left[\mathbb{1}_{0\delta} \otimes \mathbb{1}_{1\delta} \otimes \mathbb{1}_{2\delta}\right] \mathbb{1}$	$\times$	$\times$	$\times$

Table 3.2.: Microwave pulse sequence for the state tomography. First column: measurement basis for the 0δ, 1δ and 2δ atoms. Second column: applied rotations. Three last columns: relative phases of the microwave pulses used implement the corresponding rotations (ϕ_{all} refers to the global rotation and $\phi_{0,1\delta}$ to the local ones). The $\times$ symbol indicates that the corresponding pulse is off for this sequence.
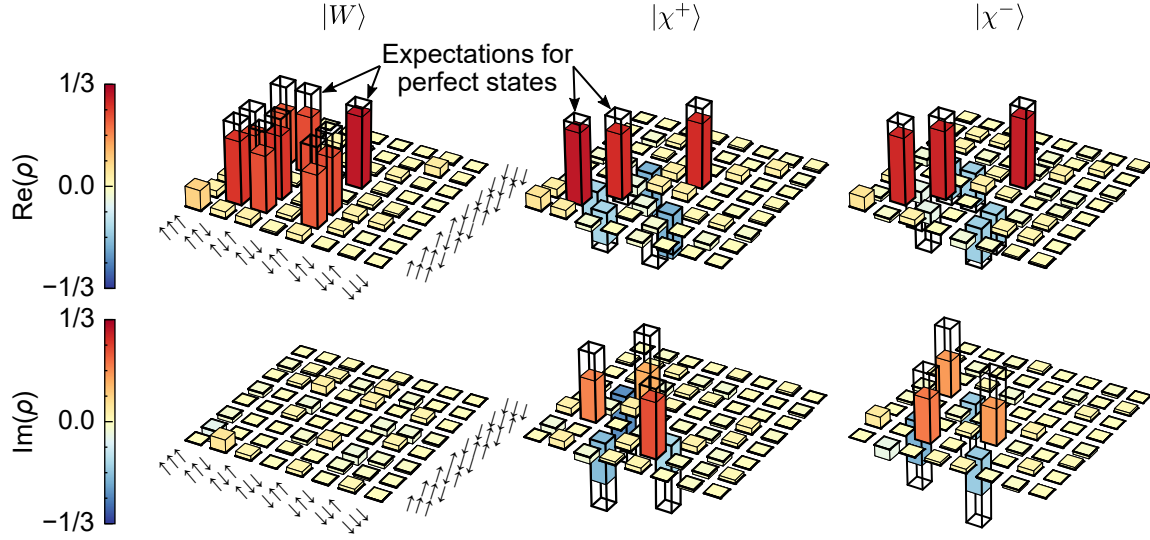
Figure 3.12: Quantum tomography. Real and imaginary part of the reconstructed density matrices for the $|W\rangle$, $|\chi^+\rangle$ and $|\chi^-\rangle$ states. The black bars represent the expectations for perfect states.

reconstruction algorithm to estimate the density matrix ρ, constraining it to be physical. We use the same method as the one presented in the Supplement Material of [Takeda *et al.*, 2021]. Any density matrix can be written as $\rho(T) = T^\dagger T / \operatorname{tr}(T^\dagger T)$ with T being a complex $2^3 \times 2^3 =$ lower triangular matrix with real diagonal elements. Thus T has 64 independent real parameters $(t_1, t_2, \cdots, t_{64})$ that minimize the following cost function:

$$C(T) = \sum_{\alpha \in \{x,y,z\}^3} \sum_{\beta \in \{\uparrow,\downarrow\}^3} \left(\langle \beta | R_\alpha^\dagger \rho(T) R_\alpha | \beta \rangle - P_\alpha^\beta \right)^2 .$$

Here, α is the basis in which we measure each atom, β is an experimental outcome, $|\beta\rangle$ its corresponding state, P_α^β the probability to measure β in the α basis and R_α the set of applied rotations to measure in α. For example, when measuring in the $\alpha = xyz$-basis, $R_{xyz} = \left[R_{0\delta}^{-y}\left(\frac{\pi}{2}\right) \otimes R_{1\delta}^x\left(\frac{\pi}{2}\right) \otimes \mathbb{1}_{2\delta} \right] \mathbb{1}$ (see Tab. 3.2). We perform the minimization using the L-BFGS-B algorithm provided by the SciPy Python package. Figure 3.12 shows, for one triangle, the real and imaginary parts of the density matrices ρ of the three states $|W\rangle$, $|\chi^+\rangle$ and $|\chi^-\rangle$. The black bars represent the expectations values for perfect states.

To test the reliability of this maximum-likelihood reconstruction algorithm and assess how different is the reconstructed density matrix from the experimental data, we plot in Fig. 3.13 the difference between the density matrix ρ given by the algorithm and the non-physical one ρ_{formula} obtained by calculation using Eq. 3.12 (data shown
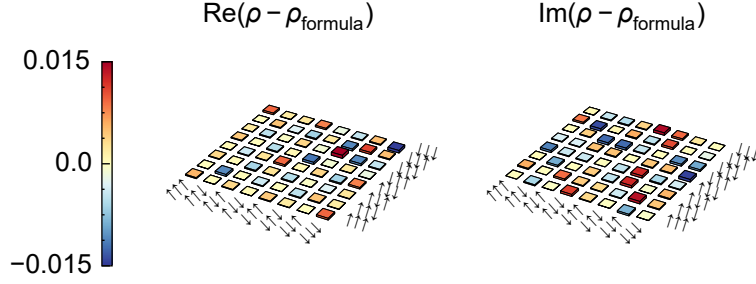
Figure 3.13: Reliability of the maximum-likelihood reconstruction algorithm. Real and imaginary part of the difference between the density matrix given by by the algorithm ρ and the non-physical one ρ_{formula} obtained by applying the formula in Eq. 3.12. The data are shown for the $|W\rangle$ state.

for the W-state). We observe small differences of the order of ≈ 0.01. Only small corrections are required to transform ρ_{formula} into a physical density matrix. These results first suggest that the experimental data already give a density matrix very close to be a physical and second, that the algorithm gives results very close to the data indicating of its reliability.

Entanglement criteria. From the reconstructed density matrices ρ, we compute the fidelity $F = \langle\psi|\rho|\psi\rangle$ of $0.74(1)$, $0.71(1)$ and $0.68(1)$. They are all above $2/3$, indicating of genuine three-partite entanglement [Acín *et al.*, 2001; Gühne *et al.*, 2003; Neeley *et al.*, 2010]. In addition, the produced W-state violates the Mermin-Bell inequality: $S = |\langle\sigma_{0\delta}^z\sigma_{1\delta}^z\sigma_{2\delta}^z\rangle - \langle\sigma_{0\delta}^x\sigma_{1\delta}^x\sigma_{2\delta}^z\rangle - \langle\sigma_{0\delta}^z\sigma_{1\delta}^x\sigma_{2\delta}^x\rangle - \langle\sigma_{0\delta}^z\sigma_{1\delta}^z\sigma_{2\delta}^x\rangle| \leqslant 2$ as we measure $S_{\text{exp}} = 2.083(26)$ [Mermin, 1990; Acín *et al.*, 2001; Eibl *et al.*, 2004]. Much like in the more conventional Bell-state case, this violation rules out a hidden-variable model for the measured correlations and provides another indicator of genuine three-qubit entanglement.

3.4 Conclusion

In this chapter, I have presented a new tool added to the experiment to address several atoms and perform local rotations. I have explained how to prepare the system in a Néel state and described our protocol to perform multi-basis measurements. Two main challenges remain to push the platform towards a fully programmable XY quantum simulator. First, the Néel state preparation and multi-basis measurement protocols that I have described suffer from a lot of imperfections. Increasing the

fidelity would allow us to probe more sensitive many-body phenomena, giving us more information about the system we wish to study. Second, the SLM phase pattern cannot be varied dynamically during the Rydberg sequence. We cannot use the same SLM pattern to prepare the system in a specific initial state (like a Néel state) and perform multi-basis measurements during the same sequence. One solution would be to use several SLMs with multiple addressing lasers. It would allow for preparing and measuring the system in arbitrary bases, thus broadening the range of many-body physics problems we can study.

Static positional disorder

Contents

One limitation of the platform is the positional disorder of the atoms. There are two types of positional disorder: *shot-to-shot* and *static positional disorder*. The shot-to-shot disorder refers to the fact that, due to the extension of the atom wave function in the traps and their residual atomic motion, the interatomic distances and, consequently, the interaction energies between pairs of atoms fluctuate from one repetition of the experiment to another. On the other hand, static positional disorder describes the fact that the center of each tweezer is not correctly positioned, resulting in a static disorder of interatomic distances and, thus, of the interaction energies. Some phases of matter we wish to prepare and study are sensitive to these disorders and may be impossible to obtain if these disorders exceed critical values [Thomson and Sachdev, 2017; Dey, 2020; Seifert *et al.*, 2023]. In Sec. 2.2.1, I have already the mentioned cooling procedures of the atoms that we apply before the Rydberg sequence to minimize the shot-to-shot positional disorder. Therefore, in this chapter, I will focus
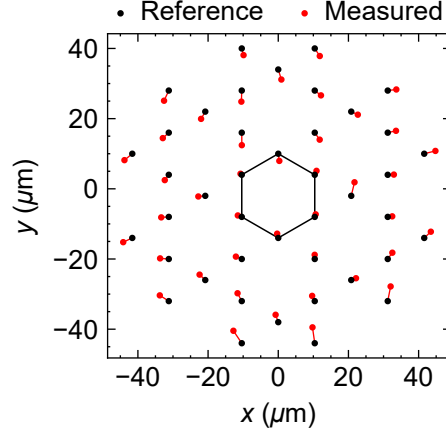
Figure 4.1: Position of the tweezers measured with the trap camera. Black markers: Show the reference position for a perfect Kagome configuration. Red markers: Measured positions with the trap camera. To highlight the differences between the measured and reference positions, we increase by a factor 10 the displacement of the measured position to their reference. Hexagon: Show six atoms in an hexagonal configuration.

on the static positional disorder. First, I will present how to measure it. Second, I will describe how to correct the positional disorder and show an example using a small system of six atoms. Finally, I will discuss promising routes to scale this correction method to larger system sizes.

4.1 Measurements of the atomic positions

4.1.1 Measurement using a camera

The first naive approach to measure the trap positions is to use the trap camera. We take an image of the atomic plane and fit each tweezer light spot using a 2D Gaussian fit to extract their positions. Figure 4.1 shows the measured position $\{\mathbf{r}_i\}$ of a Kagome array of tweezers (red markers) and compares them to reference positions $\{\mathbf{r}_i^{\mathrm{ref}}\}$ corresponding to a perfect geometry (black marker). It gives a static positional disorder of $250\,\mathrm{nm}$ (average distances from the references). The trap camera is placed after the science chamber and is optically conjugated with the atomic plane. Therefore, all the optical elements on the path can distort the light field and bias the results. To check whether the trap camera measurements are reliable, we compute the distances between the atoms and compare them with the distances measured from the interaction
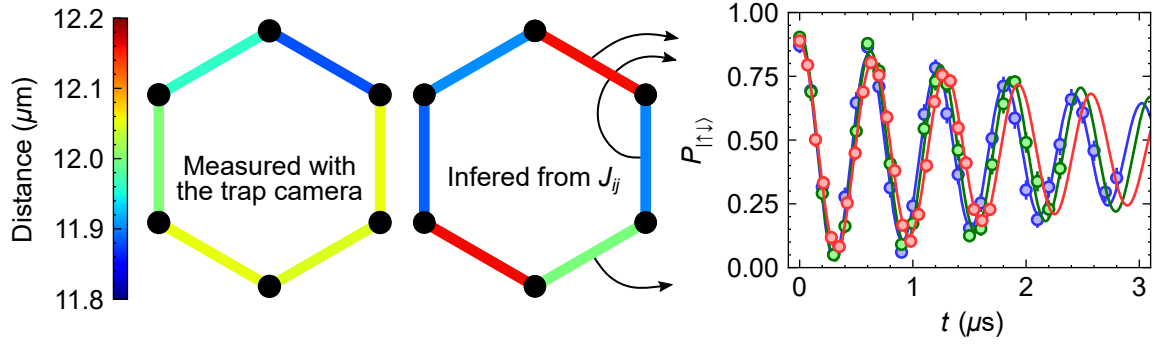
Figure 4.2: Measurement of the inter-atomic distances. Left: Measurement of the nearest neighbours distances on a six-atom hexagon (shown in fig. 4.1) using two different methods: the trap camera and spin exchange experiments. Right: Different spin exchange experiments corresponding to the three pairs with an arrow. The solid curves are fits using a damped cosine function from which we extract J_{ij}. Here we use $|\uparrow\rangle = \left|60S_{1/2}, m_J = 1/2\right\rangle$, $|\downarrow\rangle = \left|60P_{1/2}, m_J = -1/2\right\rangle$ for a mean interatomic distance of $12\,\mu$m.

energies between the atoms. The dipolar XY interaction energy J_{ij} between atom i and j decays as $J_{ij} \propto 1/|\mathbf{r}_i - \mathbf{r}_j|^3$. Measuring J_{ij} thus allows us to extract the distance between these atoms. To measure the interaction energy J_{ij} we perform a spin exchange experiment: we initialize the two atoms in $|\uparrow\downarrow\rangle$ (see Sec. 2.3.3 and Sec. 5.1.2) and let them interact freely for a time t under the dipolar XY model and readout. The probability to measure $|\uparrow\downarrow\rangle$ oscillates at a frequency $2J_{ij}/(2\pi)$. For each pair of atoms for which we wish to measure the inter-atomic distance, we repeat this spin exchange experiment (as an example, Fig. 4.2 shows the results of three spin exchange experiments realized on three pairs exhibiting different interaction energy). Each spin exchange experiment is realized with only the two atoms i and j to avoid the interactions with the other atoms to bias the J_{ij} measurement. Figure 4.2 shows a comparison of the measured distances on six pairs of atoms (shown by a hexagon symbol in Fig. 4.1) using the trap camera and the spin exchange experiments. The distances measured with the trap camera do not match the ones measured via the interaction energies. It indicates that the camera measurements are too biased and, therefore, cannot be used. The most probable hypothesis to explain this mismatch is optical aberrations on the optical path, which deform the trapping light in the camera plane compared with the trapping light in the atomic plane. This is a priori not a fundamental problem, and can hopefully be cured by using better optical system such as microscope objectives instead of aspheric lenses.
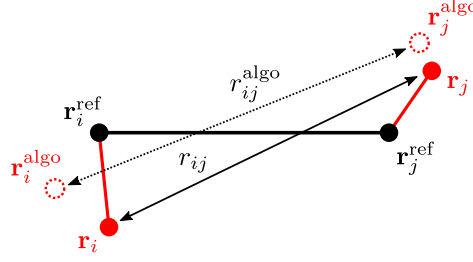
Figure 4.3: Sketch of atomic positions. The black disks show the reference positions $\mathbf{r}_i^{\mathrm{ref}}$ that correspond to the perfect geometry without positional disorder. The red disks show the position of the atoms $\mathbf{r}_i$ and the white disk represent the estimated positions $\mathbf{r}_i^{\mathrm{ref}}$ given by the algorithm.

4.1.2 Inferring the positions from nearest neighbours distances

Looking for a reliable way to directly measure the position of the atoms using a camera, we find that all these methods suffer from the same problem: the distortions induced by the optics bias the image and thus prevent reliable measurements of the atomic position. Therefore we looked at an indirect way to infer the position of the atoms.

The localization problem. To estimate the positions, we use the pair-wise distances between the atoms inferred from the interaction energy measurements $\{J_{ij}\}$. Estimating the absolute position of a set of objects knowing their relative distances from each other is a well-known problem called the *distance-based localization problem* [Mucherino *et al.*, 2012]. This problem is particularly interesting in the context of wireless sensor networks to develop indoor positioning systems where nodes need to determine their positions based on distance measurements to nearby nodes [Zekavat and Buehrer, 2019]. Inspired by these methods, we developed an optimization algorithm to estimate the position of the atoms based on the pair-wise distances. Our algorithm works as follows. We first assume that we experimentally measure distances $r_{ij} = |\mathbf{r}_i - \mathbf{r}_j|$ between pairs of atoms. The algorithm starts from the perfect geometry and virtually moves each atom to the position $\mathbf{r}_i^{\mathrm{algo}}$ and calculates the new virtual distances $r_{ij}^{\mathrm{algo}} = |\mathbf{r}_i^{\mathrm{algo}} - \mathbf{r}_j^{\mathrm{algo}}|$ (see Fig. 4.3). By varying the virtual position $\{\mathbf{r}_i^{\mathrm{algo}}\}$ of the atoms, the algorithm minimizes the following cost function:

$$C\left(\{\mathbf{r}_i^{\mathrm{algo}}\}\right) = \sum_{\{ij\}} \left(r_{ij} - r_{ij}^{\mathrm{algo}}\right)^2,\tag{4.1}$$

with $\{ij\}$ being all the pairs between atom i and j for which we experimentally measured the distance. We then end up with a virtual pattern that reproduces the experimental results and hopefully successfully guesses the position of the traps meaning that $\mathbf{r}_i^{\text{algo}} = \mathbf{r}_i$.

Benchmark of the algorithm.   To evaluate the performance of this algorithm at guessing the position of atoms based on their relative distance from each other, we apply the following procedure. We start from a perfect *virtual* pattern and randomly move the position of each trap by $\Delta \mathbf{r}_i$ to mimic a static positional disorder. We choose $\{\Delta \mathbf{r}_i\}$ to follow Gaussian distributions of width $100\,\text{nm}$ (typical value for the positional disorder). The *virtual* positions of the atoms thus read $\mathbf{r}_i = \mathbf{r}_i^{\text{ref}} + \Delta \mathbf{r}_i$. We then calculate the distances $r_{ij} = |\mathbf{r}_i - \mathbf{r}_j|$ between the atoms. These values mimic the experimental measurements. Experimentally we cannot measure all distances. For distances r_{ij} beyond nearest neighbour distances, measuring J_{ij} with a good precision is challenging as the period of a spin exchange oscillation $\pi/J_{ij} \propto /r_{ij}^3$ is very large compared to time scale of an experiment of typically a few microseconds. Therefore, for the sake of simplicity, we will thus only consider distances between nearest-neighbours atoms. After having computed these *virtual* distances, we give them to the algorithm, run it, and extract the estimated positions $\{\mathbf{r}_i^{\text{algo}}\}$. Thus, by comparing $\{\mathbf{r}_i\}$ and $\{\mathbf{r}_i^{\text{algo}}\}$ we can evaluate the precision of the algorithm. To do so, we compute $\varepsilon = \frac{1}{N} \sum_{i=1}^{N} |\mathbf{r}_i - \mathbf{r}_i^{\text{algo}}|$, being the average difference in position between the real positions and the one estimated by the algorithm. Figure 4.4 shows the histogram of ε obtained after 300 repetitions of this benchmark procedure and for three different geometries. For the square and Kagome geometries, ε has a mean value of $\bar{\varepsilon} \approx 23\,\text{mn}$ and reaches $\bar{\varepsilon} \approx 5\,\text{nm}$ for the triangular pattern. This difference arises from the fact that the triangular pattern is a *constrained geometry*. It means that measuring all distances between nearest neighbours automatically constrains all other distances, leading to a unique configuration of atomic positions. In contrast, the square and Kagome patterns are *non-constrained geometries*, so multiple configurations of positions can lead to the same measurement of the nearest neighbour distances. For example, as shown in Fig. 4.4a, four atoms in a square configuration exhibit the same nearest neighbour distances as for atoms in a rhombus configuration. This effect (also referred as the *universal rigidity problem* [Mucherino *et al.*, 2012]) leads to lower precision of the algorithm in the guess of the atomic positions when using non-constrained geometries. The algorithm precision will ultimately be a limitation for
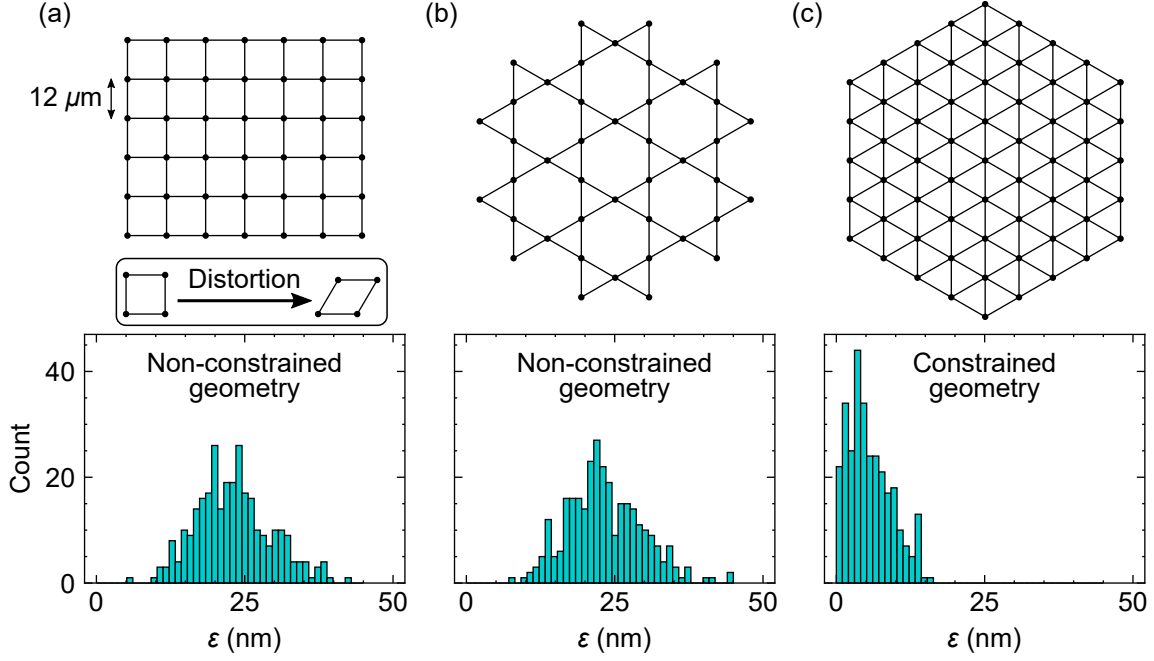
Figure 4.4: Benchmark of the algorithm: measurement of its precision. Histogram of ε obtained for 300 repetitions of the benchmark procedure using a (a) square, (b) Kagome and (c) triangular pattern. The nearest neighbours distances used in the algorithm are shown by black lines. (a) shows an example of distortion that can occur when using an non geometrical constrained geometry like a square array.

the correction of disorder in non-constrained geometries, but correcting the static positional disorder up to $\sim 20\,\mathrm{nm}$ would already be a large improvement.

Experimentally, when we measure the distance between two atoms, we measure it with a finite precision of $u(r_{ij})$. So far, in the benchmark, we assumed that we perfectly measure the distances with an infinite precision $u(r_{ij}) = 0$. We then need to check whether the algorithm is robust to measurement noises. To do so, we repeat the same benchmark procedure, adding a noise $u(r_{ij})$ to the r_{ij} values. We choose $\{u(r_{ij})\}$ to follow Gaussian distributions of width u. Fig. 4.5 shows, for the same three geometries, the averaged precision of the algorithm $\bar{\varepsilon}$ as a function of the amplitude of the noise u. The precision decreases with the noise. Experimentally, when we measure the distances via spin-exchange experiments, we estimate that the uncertainty is of $u(r_{ij}) \approx 10\,\mathrm{nm}$. According to Fig. 4.5, a noise of $u \approx 10\,\mathrm{nm}$ does not affect too much the precision of the algorithm for the square and Kagome pattern that remains around $\approx 25\,\mathrm{nm}$. For the triangular geometry, $\bar{\varepsilon}$ increases to $\approx 10\,\mathrm{nm}$, which is still good enough.
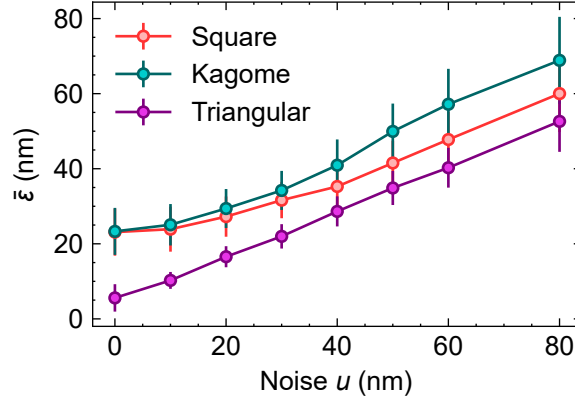
Figure 4.5: Benchmark of the algorithm: estimation of its robustness to noise.
Average precision of the algorithm $\bar{\varepsilon}$ as a function of the noise u introduced in the input data $r_{ij} + u(r_{ij})$. for three different geometries (see Fig.4.4). The benchmark procedure is repeated at least 100 times for each point. The standard deviations of ε are represented by the error bars.

We now have a way to estimate the positions of the atoms. We move to the position feedback to correct the static positional disorder.

4.2   Feedback on the positions

4.2.1   Feedback procedure

Feedback procedure.   The strategy to feedback the position of the atoms consists of three steps:

- **Measurement of the inter-atomic distances.** First as explained in the previous sections, we measure all the nearest-neighbours inter-atomic distances.

- **Estimation of the positional disorder.** Second, we run the algorithm to estimate the position of the atoms. It gives the correction to apply on the atomic positions to cancel the positional disorder.

- **Feedback.** Third, we modify the SLM phase pattern of the optical tweezers to correct the position of each tweezers.

We iteratively repeat this procedure until the corrections do not improve the measured

disorder. The two first steps of this procedure are detailed in the previous section. I will now explain the third step.

Feedback on the SLM phase pattern. Similarly to what we do for the addressing SLM (see Sec. 3.1.1), to generate an array of optical tweezers, we apply the following phase pattern of the trap SLM:

$$\Phi(x_s, y_s) = \arg\left(\sum_{j=1}^{N} w_j e^{i\phi_j(x_s,y_s)+i\theta_j}\right), \tag{4.2}$$

with x_s and y_s being the spatial coordinate of the SLM, θ_j and w_j being the relative phases and weights to apply to ensure homogeneous trap intensities, and $\phi_j(x_s, y_s)$ being the phase applied to create a trap at position x_j and y_j on the atomic plane:

$$\phi_j(x_s, y_s) = \frac{2\pi}{\lambda f}(x_s x_j + y_s y_j), \tag{4.3}$$

with λ the trapping light wavelength, and f the focal length of the aspherical lenses. To correct the position of atom j by a displacement $\Delta \mathbf{r}_j = (\Delta x_j, \Delta y_j)$ we apply a new phase pattern taking:

$$\phi_j(x_s, y_s) = \frac{2\pi}{\lambda f}(x_s (x_j - \Delta x_j) + y_s (y_j - \Delta y_j)). \tag{4.4}$$

During his master internship, Bastien Gély experimentally checked that applying small correction on the position of the order of $\sim 10\,\text{nm}$ does not degrade the intensity homogeneities of the traps [Bastien, 2023]. We now have all the tools to feed back the atomic positions and correct for the static positional disorder.

4.2.2 Results on a small system size

In this section, we correct the static position disorder on a small system size. We take the six atoms in the hexagonal configuration shown in Fig. 4.2 and apply the feedback procedure. To check if the procedure works, at each iteration, we compute the dispersion of measured nearest neighbour distances $\sigma(\{r_{ij}\})$ (see green curve in Fig. 4.6a). This dispersion starts at $\sigma(\{r_{ij}\}) \approx 117\,\text{nm}$ and decreases down to $24\,\text{nm}$, demonstrating that, as expected, the feedback procedure homogenizes the

nearest neighbour distances. We also plot as a function of the number of iterations the positional disorder $\frac{1}{N}\sum_{j=1}^{N}|\mathbf{r}_j^{\text{algo}} - \mathbf{r}_j^{\text{ref}}|$ estimated by the algorithm (see red curve in Fig. 4.6a). The estimated positional disorder starts at $\approx 70\,\text{nm}$ and reaches $\approx 14\,\text{nm}$, indicating that the feedback procedure works. As explained previously (Sec. 4.1.2), the algorithm does not perfectly predict the position of the atoms. As the hexagon is a non-constrained geometry, this precision is around $\bar{\varepsilon} \approx 23\,\text{nm}$. Due to this finite precision, we can reasonably think that the positional disorder of $14\,\text{nm}$ predicted by the algorithm is slightly biased and that the real positional disorder is in between zero and $\sqrt{(14\,\text{nm})^2 + (23\,\text{nm})^2} \approx 26\,\text{nm}$. Even if the real positional disorder reaches $\approx 26\,\text{nm}$ it still represents a significant improvement compared to the initial disorder of $\approx 70\,\text{nm}$ and demonstrate that this positional disorder correction protocol works.

We showed that we can reduce the positional disorder in this minimalistic six-atom system. We now wish to extend this method to larger system sizes. One of the main limitations of this feedback procedure is the time it takes to measure the distances using spin exchange experiments. Each requires approximatively 2 hours of data accumulation and must be done one pair after the other. If we use this feedback procedure on larger arrays of size N, the number of nearest neighbour distances to measure increases proportionally to N. Measuring all distances for a $N = 100$ atoms array would then require several days/weeks, which is unthinkable from an experimental point of view. Therefore, we need to find an alternative way to measure the distances that takes a reasonable amount of time and is scalable with the size of the array.

4.3   Scaling up to larger system sizes

Measuring all the nearest neighbour distances of a large array in a reasonable amount of time is a challenging problem to date. It remains an open problem for which the tweezer community is actively seeking a solution. In this section, I present some promising ideas we started exploring during my Ph.D. to address this problem.

4.3.1 Measuring van der Waals interactions

Another way to measure the distance between two atoms is to measure the van der Waal interaction energy between these atoms by performing a ground-Rydberg spectroscopy. The idea is to extend this method to measure all the different nearest
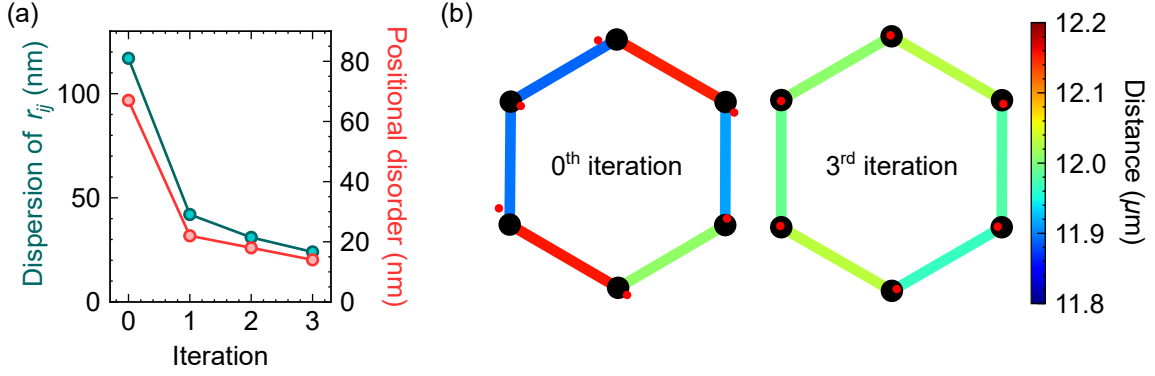
Figure 4.6: Feedback of the atomic positions on six atoms. (a) Green: Dispersion of the measured distances $\sigma(\{r_{ij}\})$ as a function of the number of feedback iterations. Red: Positional disorder $\frac{1}{N}\sum_{j=1}^{N}|\mathbf{r}_j^{\mathrm{algo}}-\mathbf{r}_j^{\mathrm{ref}}|$ estimated by the algorithm after each feedback iteration. (b) Measured distances before feedback (0th iteration) and after feedback (3rd iteration). The black circles show the reference positions $\mathbf{r}_j^{\mathrm{ref}}$ for the perfect hexagonal geometry and the red markers represent the positions $\mathbf{r}_j^{\mathrm{algo}}$ of the atoms estimated by the algorithm (we multiply each displacements by a factor 20 to highlight the positional disorder).

neighbour pairs of the system by performing only one spectroscopy experiment. First, I will briefly remind the reader of this method for two atoms (more details are given in former theses of the group [Scholl, 2021]) and then explain how we extended it to larger arrays.

Measuring the distance between two atoms via the van der Waals interaction.
Van der Waals interactions arise from off-resonant dipole-dipole interactions between nearby Rydberg atoms. If we consider two atoms i and j separated by a distance r_{ij}, the energy required to excite the two atoms in the Rydberg state is shifted by $V(r_{ij}) = C_6/r_{ij}^6$. Thus, measuring this energy shift allows us to infer r_{ij}. To measure V, we perform a ground-Rydberg spectroscopy using the 420 nm and 1013 Rydberg lasers. We set their frequencies with an intermediate detuning of Δ and a final detuning of δ as shown in Fig.4.7a. As we choose $\Delta/(2\pi) \sim 500\,\mathrm{MHz} \gg \Omega_{420}, \Omega_{1013}$, this configuration is equivalent to applying a single photon transition from $|g\rangle$ to $|r\rangle$ with an effective Rabi frequency of $\Omega_{\mathrm{eff}} = \Omega_{420}\Omega_{1013}/(2\Delta)$ and an effective detuning δ[1]. After having prepared the atoms in $|g\rangle$, we simultaneously apply a 420 and 1013 nm laser pulse, turn back on

---

[1] Here, I neglect the effects of the light shifts induced by the 420 nm and 1013 nm lasers that slightly modify the detuning of the effective single photon transition detuning. This detuning should be $\delta + \frac{\Omega_{420}^2 - \Omega_{1013}^2}{4\Delta}$.
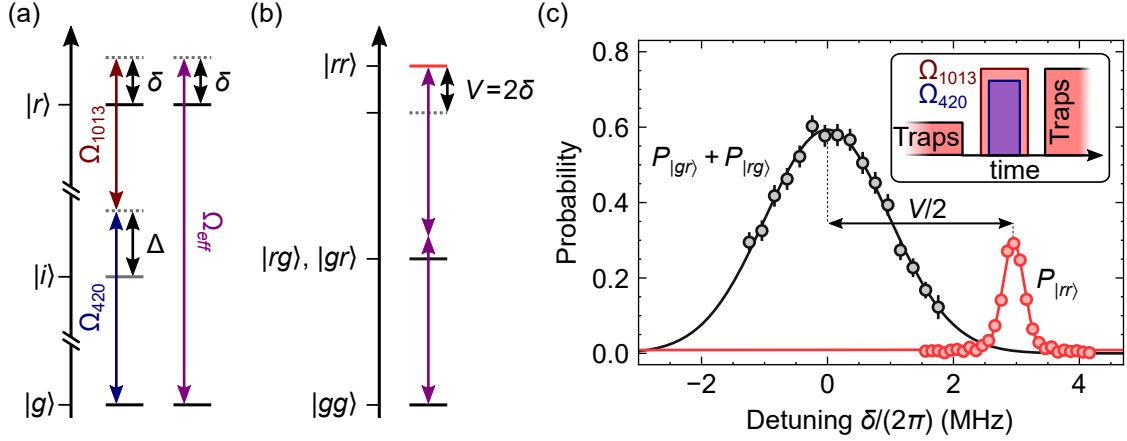
Figure 4.7: Measurement of the van der Waals shift. (a) Energy spectrum for a single atom. The two photon transition can be modelled by a one photon transition with an effective Rabi frequency Ω_{eff} and a detuning δ. (b) Energy spectrum for two interacting atoms with a van der Waals shift V. (c) Spectrum using the Rydberg lasers to measure the van der Waals shift V for two atoms separated by $12\,\mu\text{m}$ using $|r\rangle = |90S_{1/2}, m_J = 1/2\rangle$. We plot the probability to excite one (black) and two (red) atoms in $|r\rangle$ as a function of the detuning δ from the single atom transition frequency. The solid curves are Gaussian fits. The inset shows the experimental sequence.

the traps and image the atoms still in $|g\rangle$ (inset in Fig. 4.7c). We repeat the experiment for various values of the detuning δ. When setting the excitation lasers on resonance with the single atom transition ($\delta = 0$), the single excitation probability is maximum. When $\delta = V/2$, the laser couples $|gg\rangle$ to $|rr\rangle$ via an effective two-photon transition (as illustrated in Fig. 4.7b) and the probability to excite both atoms in $|r\rangle$ in thus maximum. As a example, Figure 4.7 shows experimental data obtained for two atoms separated by $\approx 12\,\mu\text{m}$ using as a Rydberg state $|r\rangle = |90S_{1/2}, m_J = 1/2\rangle$. We measure a shift of $V/2/(2\pi) = -2.95(2)\,\text{MHz}$. Using the Alkali.ne Rydberg Calculator (ARC) Python package, we compute a van der Waals coefficient of $C_6 = 16.83\,\text{GHz}.\mu\text{m}^6$ corresponding to distance between the atoms of $11.91(1)\,\mu\text{m}$ consistent with the expectation of $\approx 12\,\mu\text{m}$.

Van der Waals interactions on a small system size. We now extend this method to larger arrays. The idea is the following. We repeat the previously described experiment with all the atoms in the array. Then, for each nearest neighbour pair ij, we plot the probabilities to excite one and both atoms in $|r\rangle$ from which we compute a van der Waals shift V_{ij}. In contrast with the previous case, here, all the atoms participate to

the dynamics and thus may bias the shifts V_{ij} measured for each pair. In that case, $V_{ij} \neq C_6/r_{ij}^6$, so the van der Waals shift would no longer be a good observable for inferring the distances. To check that, we perform a simulation on a small system size. The simulation starts with a *virtual* array of six atoms in a perfect hexagonal configuration (same geometry as in previous sections). We randomly move each atom by displacements $\Delta \mathbf{r}_i$ to mimic a static positional disorder (with $\{\Delta \mathbf{r}_i\}$ following Gaussian distributions of width $100 \, \text{nm}$). Then, we simulate the ground-Rydberg spectroscopy experiment, and for each pair, extract the measured shift V_{ij} and compare it to its corresponding interatomic distance $r_{ij} = |\mathbf{r}_i - \mathbf{r}_j|$. Figure 4.8a shows V_{ij} (blue circles) for different pairs and different repetitions of the simulation as a function of the distances r_{ij}. We notice that the V_{ij} values are globally shifted by $\approx 40 \, \text{kHz}$ compared to the C_6/r_{ij}^6 curves. This $\approx 40 \, \text{kHz}$ shift is the result of a complex many-body effect. For each pair $\{ij\}$, the atoms i and j are surrounded by other atoms with which they interact, leading to a systematic shift of the V_{ij} energy. However, the different values of V_{ij} remain strongly correlated with r_{ij}. For a given value of V_{ij}, we can determine its corresponding distance within an uncertainty of $\pm 5 \, \text{nm}$ (represented by a black bar). Therefore, this simulation indicates that up to a rescaling factor used to eliminate the systematic bias, the V_{ij} values give access to r_{ij} with a relatively good precision. To eliminate the systematic bias, we will rescale each measured values of $\{V_{ij}\}$ by multiplying them by a factor α. This factor α is chosen such that the averaged value $\bar{V}$ of measured shifts $\{V_{ij}\}$ for all nearest neighbour pairs corresponds to a distance between the atoms of exactly $12 \, \mu\text{m}$, *i.e.* we have $\left(C_6/(\alpha \bar{V})\right)^{1/6} = 12 \, \mu\text{m}$.

We now experimentally try to measure these nearest neighbour distances. To compare these measurements to a reference, we start from the same six-atom hexagonal array already used in the previous section (we come back to the initial position configuration before the feedback described in Sec. 4.2.2). It will allow us to compare distances measured via the van der Waals interactions with the ones measured with spin exchange experiments. As shown in Fig. 4.8b, both methods give results in very good agreement, indicating that the van der Waals method is reliable to measure the nearest neighbour distances.

Before going to large system sizes, we try to correct the static positional disorder of this array using the van der Waals method. Similarly to the previous section, at each iteration, we compute the dispersion of nearest neighbour distances $\sigma(r_{ij})$ that we measure (green curve in Fig. 4.9a) and the positional disorder $\sum_{j=1}^{N} |\Delta \mathbf{r}_j^{\text{algo}}|/N$
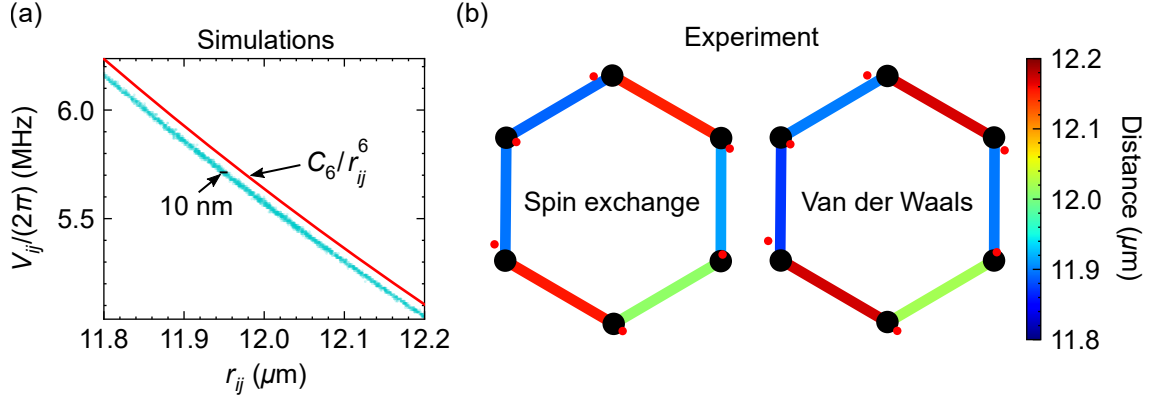
Figure 4.8: Van der Waals shift measurement for larger arrays. (a) Simulation of the different values of shift V_{ij} as a function of interatomic distance r_{ij} for different pairs and repetitions of the simulation. We used as parameters: $C_6/(2\pi) = 16.83\,\text{GHz}.\mu\text{m}^6$, an ground-Rydberg effective Rabi frequency of $\Omega_{\text{eff}}/(2\pi) = 0.45\,\text{MHz}$ and a Rydberg laser pulse duration of $4\,\mu\text{s}$. The red line shows the C_6/r_{ij}^6 function. (b) Experimental measurements of the nearest neighbours distances on a six-atom hexagon using the two methods. Left: spin exchange experiments. Right: we performed one ground-Rydberg spectroscopy experiment to measure all the van der Waals shifts (using $|r\rangle = \left|90S_{1/2}, m_J = 1/2\right\rangle$). The black circles show the reference positions $\mathbf{r}_j^{\text{ref}}$ for the perfect hexagonal geometry and the red markers represent the positions $\mathbf{r}_j^{\text{algo}}$ of the atoms estimated by the algorithm (we multiply each displacements by a factor 20 to highlight the positional disorder).

estimated by the algorithm (see red curve in Fig. 4.6a). Both decrease, reaching $\approx 10\,\text{nm}$ after four iterations, indicating that the feedback procedure works. The results are similar to those obtained using spin-exchange experiments described in the previous section (in Fig. 4.6). As a sanity check, we also measure the nearest neighbour distances using spin exchange experiments (green square marker) for the final pattern (4th iteration). The spin exchange and van der Waals data are in good agreement. It validates that the feedback procedure works just as well with the van der Waals method as with the spin exchange method. However, it took us only half a day to perform the feedback procedure using the van der Waals method, compared with three days to the spin-exchange one, demonstrating the benefit of this new method.

Van der Waals interactions for large system sizes. We showed on a small system size that inferring the distances via the measurements of van der Waals interactions works well. We now wish to generalize this method to any system size. Many questions need to be addressed to determine if this method is reliable for any system size and
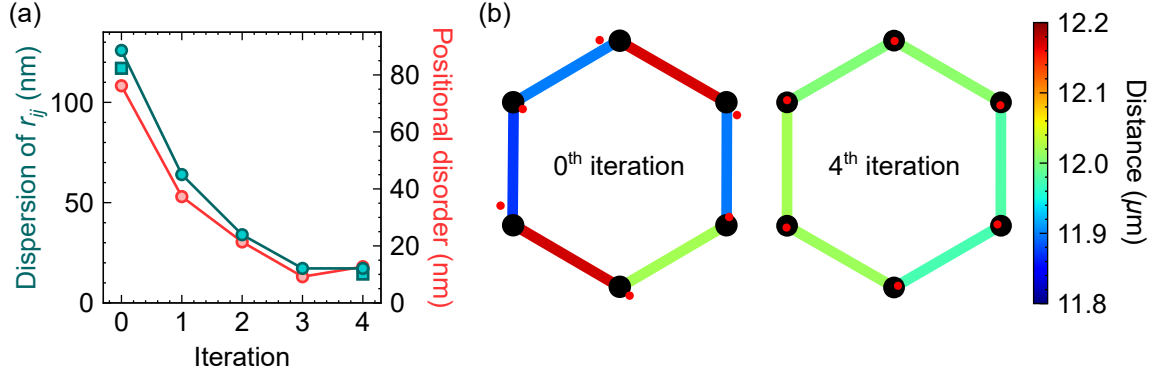
Figure 4.9: Feedback of the atomic positions on six atoms using the van der Waals shift measurement. (a) Green: Dispersion of the measured distances $\sigma(\{r_{ij}\})$ as a function of the number of feedback iterations. For the initial pattern (0th iteration) and (4th iteration) we also measure the distance using spin exchange experiment. These data are showed by square markers. Red: Positional disorder $\sum_{j=1}^{N} |\mathbf{r}_j^{\text{algo}} - \mathbf{r}_j^{\text{ref}}|$ estimated by the algorithm after each feedback iteration. (b) Measured distances before feedback (0th iteration) and after feedback (4th iteration). The black circles show the reference positions $\mathbf{r}_j^{\text{ref}}$ for the perfect hexagonal geometry and the red markers represent the positions $\mathbf{r}_j^{\text{algo}}$ of the atoms estimated by the algorithm (we multiply each displacements by a factor 20 to highlight the positional disorder).

geometry:

- **Effect of the interaction range.** The van der Waals interaction has a short-range interaction strength decaying as $1/r_{ij}^6$. Despite its short range, the interaction is not a nearest neighbour interaction. It thus may affect differently the V_{ij} values depending on the size of the system or the position of the $\{ij\}$ pair in the array.

- **Edge/Bulk effect.** As we increase the size of the system, not all atoms will have the same number of nearest neighbour atoms. On the edges, the atoms will have fewer nearest neighbour atoms and thus exhibit different dynamics while performing the ground-Rydberg spectroscopy. The V_{ij} values may be biased differently depending on the position of the pairs in the array.

- **Inhomogeneity effects.** The Rydberg lasers have a finite beam size, resulting in a gradient of light intensity in the array. Depending on the position of the atoms, the effective ground-Rydberg Rabi frequency Ω_{eff} seen by each atom is slightly different. Combined with many-body interactions, this gradient may result in space-dependant biases for V_{ij}.

Unfortunately, these questions are difficult to tackle numerically since they require to perform multiple simulations with large system sizes. In our group, we are currently addressing these questions experimentally by comparing, on large system sizes, the results obtained by spin exchange experiments and by the van der Waals method.

In conclusion, we have shown on a small system size of six atoms that measuring the van der Waals interactions allows us to infer the distances between nearest neighbours to correct the static positional disorder. Further studies are required to extend this method to larger system sizes.

4.3.2 Using many-body physics to measure the distances

As mentioned in the introduction of this chapter, some phases of matter we wish to prepare and study are extremely sensitive to static positional disorder. The idea is to use this sensitivity to static positional disorder to detect and measure the distances between the atoms. I will now present one example.

From two-body correlations to distance.   The ground state of the XY model for a Kagome geometry has been theoretically predicted to be a spin liquid [Bintz *et al.*, 2024]. During my Ph.D., we attempted to prepare this ground state and study its properties. Chapter 6 is dedicated to the preparation of spin-liquids and gives broader details about the experiments. Here, I will only show the results obtained after the preparation procedure and comment on how it could help us to measure the static positional disorder.

Figure 4.10a shows the nearest neighbour connected correlations along z ($\langle \sigma_i^z \sigma_j^z \rangle_{\rm c} = \langle \sigma_i^z \sigma_j^z \rangle - \langle \sigma_i^z \rangle \langle \sigma_j^z \rangle$) for a 114-atom Kagome array after the ground state preparation protocol. We measure negative correlations with a mean value of ≈ -0.135. Due to edge effects, the correlations are, on average, higher for pairs on the edges sharing fewer neighbouring atoms. If we ignore these pairs and only focus on pairs in the bulk, we still observe a relatively high dispersion of the correlation of 0.027. Here the data have been averaged over more than 14000 repetitions of the experiment, which is enough to reduce the error bar on the correlation down to $\leqslant 0.005$ and thus claim that the dispersion is due to a physical effect and is not due to a lack of statistics. Numerical simulations using the Density Matrix Renormalization Group (DMRG)
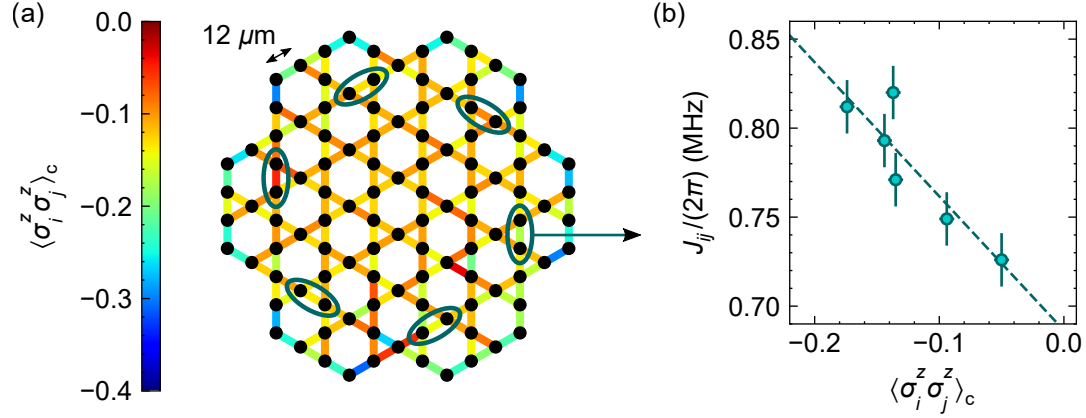
Figure 4.10: Correlations between correlations and interaction energy. (a) Nearest-neighbours correlations along z measured for a Kagome array of 114 atoms after the ground state preparation protocol (it corresponds to a time of $t = 2.5\,\mu$s in the experimental sequence described in Sec. 6.1.1 of Chapter 6). The data shown in this figure has been taken with assembled arrays containing at most three defects allowed. (b) For a few pairs (shown by green ellipses in (a)), we measure via spin exchange experiments the interaction energies J_{ij} and plot them as a function of the correlations measured along z. The dashed line is a linear fit.

algorithm performed by the group of Norman Yao in Harvard predicted that the XY ground state exhibits homogeneous nearest neighbour correlations. They also showed that when introducing static positional disorder with a typical value of $100\,$nm, the simulation predicts a dispersion in the correlations similar to the one we observe experimentally. To check whether the observed dispersion is due to static positional disorder, we perform spin-exchange experiments to measure the interaction energy J_{ij} of a few pairs (shown by green ellipses) in the bulk of the array. In Fig.4.10b, we plot J_{ij} as a function of the measured correlations. We observe a correlation between the z-correlations and the interaction energy, suggesting that the positional disorder indeed plays a role in the inhomogeneity of correlations. Considering that the z-correlations are proportional to J_{ij} (green dashed line with a slope of $0.75\,$MHz), we can estimate the dispersion of nearest neighbour distances. Excluding the edge pairs, we measure a dispersion on the correlation of 0.027 that gives a dispersion on the interaction energy of $\sigma(\{J_{ij}\}) = 0.027 \times 0.75\,\text{MHz} = 0.015\,\text{MHz}$ and thus a dispersion on the nearest neighbours distances of $\sigma(\{r_{ij}\}) = \sigma(J_{ij})\bar{d}^4/(3C_3) = 107\,\text{nm}$ (using $C_3 = 1340\,\text{MHz}.\mu\text{m}^3$ and $\bar{d} = 12\,\mu$m). This value is consistent with our previous measurement of $\sim 100\,$nm performed on small system sizes of six atoms (see Fig. 4.6a in a previous section). Therefore, it suggests that the static positional disorder plays a

dominant role in the inhomogeneity of the correlations.

Feedback procedure using many-body experiments. A new method relying on correcting the positional disorder based on the measurement of these nearest neighbours could then be developed. To do so, we must first understand a few problems:

- **Edge/bulk effects.** As explained, due to edge effects, the average correlations of the pairs depend on the number of nearest neighbour atoms they get and, thus, on their position. To convert the correlations into distances, we should assess how much these correlations are modified compared to bulk pairs.

- **Extra biases due to experimental imperfections.** Other experimental imperfections that are atom-dependent could lead to different biases on different pairs. For example, preparing these phases requires initialising the atoms in different Rydberg states. This preparation is not perfect (see Chapter 3), and the preparation fidelity may fluctuate from one atom to another. It could then introduce spatial biases on the correlation measurements when preparing the ground state.

Once again, these questions are complicated to address numerically since they require to simulate large system sizes.

In conclusion, we have shown that using a many-body experiment, we can measure correlations between the measured nearest neighbours correlations and their distances. Although further studies are needed, this result could be used to infer all nearest neighbour distances in a single experiment and thus speed up the static positional disorder feedback correction protocol. We could also consider different multi-body experiments that would be more sensitive to static positional disorder and easier to perform.

4.4   Conclusion

In this chapter, I have presented a method to estimate the positions of the atoms. This method relies on two steps. First, we use spin exchange experiments to infer the nearest neighbour distances between the atoms from measurements of the interaction energy. Second, we developed and benchmarked an algorithm to reconstruct the

positions of the atoms based on these nearest neighbour distance measurements. Then, we used this method to correct the positional disorder of a small system of six atoms in a hexagonal configuration, reducing the positional disorder from approximately $\approx 70\,\text{nm}$ to a few tens of nanometers. As this method is very time-consuming, requiring pair-by-pair spin-exchange experiments to measure the distances, we explored two other promising ways of evaluating all these distances in a single experiment. The first method involves performing ground-Rydberg spectroscopy to measure the van der Waals shifts between the atoms and thus infer the distances between them. The second method involves conducting a many-body experiment that is sensitive to the static positional disorder to measure it. Both methods require further studies to test their reliability on large system sizes. In conclusion, this work represents an intermediate step towards a scalable method for correcting static positional disorder.

Part II.

Ground state physics of the dipolar XY model

XY ground state on square arrays

Contents

In this chapter, I present our study of the ground state of the dipolar XY model for square geometries. The Hamiltonian reads:

$$\mathcal{H}_{\mathrm{XY}} = \frac{\hbar J}{2} \sum_{i<j} \frac{a^3}{r_{ij}^3} \left(\sigma_i^x \sigma_j^x + \sigma_i^y \sigma_j^y \right), \qquad (5.1)$$

where J is the nearest neighbour interaction energy strength, a the lattice spacing and r_{ij} the distance between spin i and j. For square arrays with nearest neighbour

interaction, the ground state has been predicted to be an AntiFerro-/Ferro-Magnetic (AFM/FM) state, depending on the sign of J. Moreover, since the Hamiltonian exhibits a continuous spin-rotational $U(1)$ symmetry ($\mathcal{H}_{XY}$ commutes with $\sum_i \sigma_i^z$), at finite temperature, the Mermin-Wagner theorem states that the system should not exhibit long-range order, *i.e.*, all the two body correlation functions reach zero when the distances between the spin go to infinity [Mermin and Wagner, 1966]. More recently, the case beyond nearest-neighbour interaction has been studied theoretically in the context of dipolar interactions, namely interaction energy decaying as $\propto 1/r_{ij}^3$ [Peter *et al.*, 2012]. It has been shown that long-range ordered FM phases are possible at finite temperatures. Furthermore, the long-distance tail of the dipolar interaction introduces frustration in the AFM phase, destabilizing the long-range order. When we started this project, none of these features had been observed experimentally.

In this chapter, I first introduce how we implement the dipolar XY model on our Rydberg system using resonant dipole-dipole interactions and show an example with two atoms. Second, I describe the ground state of four interacting atoms in a square configuration, and finally, I will discuss the preparation of the AFM/FM state for square arrays up to $N = 42$ atoms. Part of the results presented in this chapter have been subject to a publication [Chen *et al.*, 2023a] (more details can be found in the paper).

5.1 Implementation of the XY model

5.1.1 From resonant dipole-dipole interaction to the XY interaction

The dipole-dipole interaction between two Rydberg atoms i and j with electric dipole operators $\mathbf{d}_i$ and $\mathbf{d}_j$ reads:

$$V_{\mathrm{dd}} = \frac{\mathbf{d}_i \cdot \mathbf{d}_j - 3\left(\mathbf{d}_i \cdot \mathbf{n}_{ij}\right)\left(\mathbf{d}_j \cdot \mathbf{n}_{ij}\right)}{4\pi\varepsilon_0 r_{ij}^3}, \tag{5.2}$$

with $r_{ij} = |\mathbf{r}_i - \mathbf{r}_i|$ the interatomic distance and $\mathbf{n}_{ij} = (\mathbf{r}_i - \mathbf{r}_i)/r_{ij}$ a vector defining its direction. I will only consider transitions between states from the (nS) Rydberg manifold to the (nP) one. The selection rules state that the electric dipole operators can only couple a Rydberg state to another one with a difference of z-component of the total angular momentum of $|\Delta m_J| \leqslant 1$. We now call d_i^-, d_i^0 and d_i^+ the electric dipole

operators of atom i associated to transition with $\Delta m_J = -1$, 0 and $+1$. Taking as the quantization axis the direction of the magnetic field along $\mathbf{u}_z$ (see Sec. 2.4.1), we re-express the different component of the electric dipole operator $\mathbf{d}_i = d_i^x \mathbf{u}_x + d_i^y \mathbf{u}_y + d_i^z \mathbf{u}_z$ as $d_i^x = \left(d_i^- - d_i^+ \right)/\sqrt{2}$, $d_i^y = i\left(d_i^- + d_i^+ \right)/\sqrt{2}$ and $d_i^z = d_0^z$. Then, by expressing $\mathbf{n}_{ij}$ in spherical coordinates $\mathbf{n}_{ij} = \sin(\theta_{ij})\cos(\phi_{ij})\mathbf{u}_x + \sin(\theta_{ij})\sin(\phi_{ij})\mathbf{u}_y + \cos(\theta_{ij})\mathbf{u}_z$ with ϕ_{ij} and θ_{ij} the polar and azimuthal angles defining the $\mathbf{n}_{ij}$ direction, the interaction finally reads:

$$
\begin{aligned}
V_{\mathrm{dd}} = \frac{1}{4\pi\varepsilon_0 r_{ij}^3} &\left[\frac{1 - 3\cos^2(\theta_{ij})}{2} \left(2d_i^0 d_j^0 + d_i^+ d_j^- + d_i^- d_j^+ \right) \right. \\
&+ \frac{3}{\sqrt{2}}\sin(\theta_{ij})\cos(\theta_{ij}) \left(e^{-i\phi_{ij}} d_i^+ d_j^0 - e^{i\phi_{ij}} d_i^+ d_j^0 + e^{-i\phi_{ij}} d_i^0 d_j^+ - e^{i\phi_{ij}} d_i^0 d_j^- \right) \\
&\left. - \frac{3}{\sqrt{2}}\sin^2(\theta_{ij}) \left(e^{-2i\phi_{ij}} d_i^+ d_j^+ + e^{2i\phi_{ij}} d_i^- d_j^- \right) \right].
\end{aligned}
$$
(5.3)

Multiple terms appear and depend on the angle θ_{ij} between the quantization axis and the interatomic direction. To ensure isotropic interaction, we choose a quantization axis (set by the magnetic field) perpendicular to the array, *i.e.* $\theta_{ij} = 90°$ for all pairs $\{ij\}$. The magnetic field also allows us to isolate two Zeeman sublevels of the Rydberg manifold, thus restricting the transitions to only between these two states. In this chapter, we choose $|\uparrow\rangle = \left| 60S_{1/2}, m_J = 1/2 \right\rangle$ and $|\downarrow\rangle = \left| 60P_{1/2}, m_J = -1/2 \right\rangle$. The interaction energy is then just left with:

$$
V_{\mathrm{dd}} = \frac{1}{4\pi\varepsilon_0 r_{ij}^3}\frac{1}{2}\left(d_i^+ d_j^- + d_i^- d_j^+ \right)
$$
(5.4)

Then, taking $J_{ij} = \langle\downarrow|d^+|\uparrow\rangle \, \langle\uparrow|d^-|\downarrow\rangle / (4\pi\varepsilon_0 r_{ij}^3)$, we rewrite Eq. 5.4 in terms of spin operator:

$$
V_{\mathrm{dd}} = J_{ij}\left(\sigma_i^+ \sigma_j^- + \sigma_i^- \sigma_j^+ \right) = \frac{J_{ij}}{2}\left(\sigma_i^x \sigma_j^x + \sigma_i^y \sigma_j^y \right)
$$
(5.5)

thus leading to dipolar XY interaction with $J_{ij} \propto 1/r_{ij}^3$.
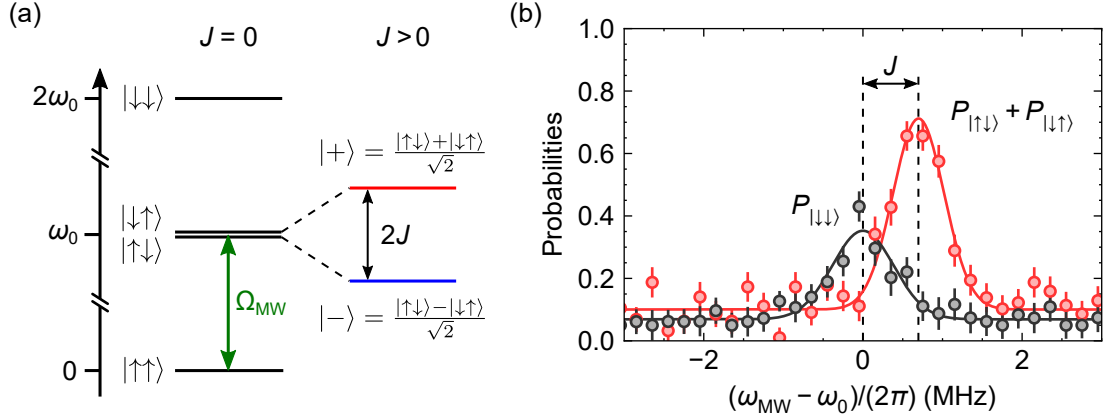
Figure 5.1: Two interacting atoms eigenstates. (a) Energy level diagram. (b) Microwave spectroscopy. We plot the probabilities to measure $|\downarrow\downarrow\rangle$ (black markers) and $|\uparrow\downarrow\rangle$ or $|\downarrow\uparrow\rangle$ (red markers). The solid curves are Gaussian fits.

5.1.2 Ground state of two interacting atoms

Valence bond. We now focus on the ground state of two atoms. Figure 5.1a shows the energy spectrum of two atoms with/without interaction. The interaction lifts the degeneracy between the $|\uparrow\downarrow\rangle$ and $|\downarrow\uparrow\rangle$ states leading to the two entangled eigenstates: the symmetric state $|+\rangle = (|\uparrow\downarrow\rangle + |\downarrow\uparrow\rangle)/\sqrt{2}$ and the antisymmetric state $|-\rangle = (|\uparrow\downarrow\rangle - |\downarrow\uparrow\rangle)/\sqrt{2}$ separated in frequency by $2J$. Although these two states exhibit the same magnetization and correlation function, we can distinguish them by measuring correlations in another basis. Table 5.1 summarizes all the connected correlations of the $|+\rangle$ and $|-\rangle$ states in the x, y and z bases. The $|-\rangle$ state (also called the *singlet state*) is rotationally invariant and always exhibits an antiferromagnetic correlation, *i.e.* it has a negative connected correlation whatever the basis of the measurement. In contrast, when measured along any direction of the equatorial Bloch sphere (along the x or y axis, for example), $|+\rangle$ exhibits a ferromagnetic correlation, *i.e.* it has a positive correlations.

These two states represent *valence bonds*: a particle or excitation represented here by the spin in $|\uparrow\rangle$ is shared between two sites represented here by the two atoms [Baskaran, 2009]. This interpretation led to the resonating valence bond theory used to describe electron pairing in high-temperature superconducting materials [Anderson, 1987; Baskaran, Zou, and Anderson, 1987]. As we will see later in this chapter and the following, we will use this interpretation to represent the ground state of the XY model and intuitively understand its main properties.

Basis	$|+\rangle$	$\langle\sigma_1^\alpha\sigma_2^\alpha\rangle - \langle\sigma_1^\alpha\rangle\langle\sigma_2^\alpha\rangle$	$|-\rangle$	$\langle\sigma_1^\alpha\sigma_2^\alpha\rangle - \langle\sigma_1^\alpha\rangle\langle\sigma_2^\alpha\rangle$
z	$\dfrac{|\uparrow\downarrow\rangle + |\downarrow\uparrow\rangle}{\sqrt{2}}$	-1	$\dfrac{|\uparrow\downarrow\rangle - |\downarrow\uparrow\rangle}{\sqrt{2}}$	-1
y	$\dfrac{|\uparrow\uparrow\rangle + |\downarrow\downarrow\rangle}{\sqrt{2}}$	$+1$	$\dfrac{|\uparrow\downarrow\rangle - |\downarrow\uparrow\rangle}{\sqrt{2}}$	-1
x	$\dfrac{|\uparrow\uparrow\rangle - |\downarrow\downarrow\rangle}{\sqrt{2}}$	$+1$	$\dfrac{|\uparrow\downarrow\rangle - |\downarrow\uparrow\rangle}{\sqrt{2}}$	-1

Table 5.1.: Connected correlations of the $|+\rangle$ and $|-\rangle$ states measured along different bases. First column: Measurement basis (for example measuring along x imply to apply a $\pi/2$ pulse around y to rotate the spins). Second and fourth columns: Expression of $|+\rangle$ and $|-\rangle$ in the corresponding basis. Third and fifth columns: Connected correlations of $|+\rangle$ and $|-\rangle$ in the corresponding basis.

Measurement of the interaction energy. The interaction energy J between the atoms can be measured in several ways. The first one is to perform microwave spectroscopy. Initially, we prepare both atoms in $|\uparrow\rangle$, send a microwave pulse and read out the state of the atoms. We repeat the experiment for various microwave frequencies (see Fig. 5.1b). When the microwave frequency is on-resonance with the single atom transition $\omega_{\mathrm{MW}} = \omega_0$, the probability to excite both atoms simultaneously in $|\downarrow\rangle$ is maximum (black data). When $\omega_{\mathrm{MW}} = \omega_0 + J$, the microwave couples $|\uparrow\uparrow\rangle$ to $|+\rangle$ and then, the probability to excite only one of the two atoms reaches its maximum (red data)[1]. Therefore, by identifying the shift between the two resonance frequencies to the $|\downarrow\downarrow\rangle$ and $|+\rangle$ states, we extract J. The main advantage of this experiment is that it also allows the measurement of the sign of J which is given by the sign of this shift.

Another way to measure the interaction energy between two atoms is to prepare the system in an out-of-equilibrium state, let it evolve under the XY model and read the state. With two atoms, two experiments are possible:

- **Spin exchange.** The first one is a spin exchange already discussed in Chapters 2 and 4. Using a combination of microwaves and addressing beams (see Chapter 3), we initialize the system in $|\uparrow\downarrow\rangle$. We can rewrite this initial state as $|\uparrow\downarrow\rangle = (|+\rangle + |-\rangle)/\sqrt{2}$. After interacting for a time t, the state reads $(e^{iJt}|+\rangle + e^{-iJt}|-\rangle)/\sqrt{2} = \cos(2Jt)|\uparrow\downarrow\rangle - i\sin(2Jt)|\downarrow\uparrow\rangle$. We thus expect the probabilities to measure $|\uparrow\downarrow\rangle$ and $|\downarrow\uparrow\rangle$ to oscillate with frequency $2J$. Figure 5.2a shows an example of a spin

---

[1]As the state $|-\rangle$ is not coupled to $|\uparrow\uparrow\rangle$ via microwaves, we do not observe any peak at a frequency $\omega_{\mathrm{MW}} = \omega_0 - J$.

exchange. As expected, we observe out-of-phase oscillations of the $P_{|\uparrow\downarrow\rangle}$ and $P_{|\downarrow\uparrow\rangle}$ probabilities (red and blue data). These oscillations exhibit damping that we attribute to shot-to-shot positional disorder. Including all the calibrated sources of imperfections in a Mont Carlo simulation (Rydberg lifetimes, preparation and detection errors and shot-to-shot positional disorder with $T = 4\,\mu\mathrm{K}$) led to a good agreement with the experimental data in terms of contrast, frequency and damping of the oscillations[2].

- **Two-atom Ramsey experiment.** The second one is a two-atom Ramsey experiment. After having initialized each atoms in $|\uparrow\rangle$, we apply a microwave $\pi/2$-pulse around y to prepare the system in $|\rightarrow_x\rightarrow_x\rangle = \left(\frac{|\uparrow\rangle+|\downarrow\rangle}{\sqrt{2}}\right)^{\otimes 2} \propto |\uparrow\uparrow\rangle + |\downarrow\downarrow\rangle + |\uparrow\downarrow\rangle + |\downarrow\uparrow\rangle$. After an interacting time t the $|+\rangle \propto |\uparrow\downarrow\rangle + |\downarrow\uparrow\rangle$ part of the wave function will accumulate a phase e^{-iJt} leading to the state $\propto |\uparrow\uparrow\rangle + |\downarrow\downarrow\rangle + e^{-iJt}(|\uparrow\downarrow\rangle + |\downarrow\uparrow\rangle)$. We then apply a second microwave $\pi/2$-pulse around y to read out the state in the x basis. We thus expect the probabilities to measure $|\uparrow\uparrow\rangle$ and $|\downarrow\downarrow\rangle$ to oscillate at a frequency J. Figure 5.2b shows an example of this Ramsey experiment using the same parameters as for the spin exchange one. The frequency is, as expected, reduced by a factor of two compared to the spin exchange one. The same Monte Carlo simulation is also in good agreement with the data.

In this section, I showed how we implement the dipolar XY models from resonant dipole interaction between Rydberg atoms. We then focused on two interacting atoms and described the properties of their eigenstates $|\pm\rangle$. Finally, I showed different ways to measure the interaction energy experimentally. I now move to the study of the ground states of the dipolar XY model for square geometries.

5.2 XY ground states of a four-atom square array

To forge an intuition about the ground state of the dipolar XY model for square arrays, we start by studying a minimalistic system of four atoms in a square configuration. I will first present helpful ansätze that give us intuitive pictures to describe

---

[2]See more details about the simulation and the modelling the experimental imperfections in the Gabriel Emperauger's thesis [Emperauger, 2025]
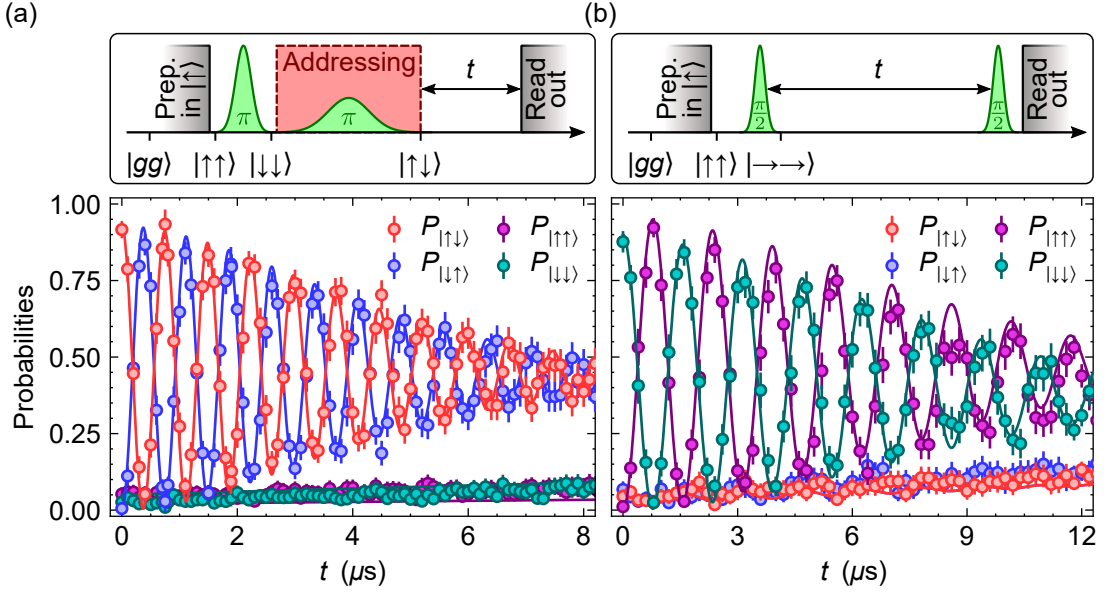
Figure 5.2: Spin exchange and two-atom Ramsey experiment. (a) Spin exchange and (b) two-atom Ramsey experiment. Top panel: experimental sequence. Bottom panel: Experimental results. Here we use $|\uparrow\rangle = |60S_{1/2}, m_J = 1/2\rangle$, $|\downarrow\rangle = |60P_{3/2}, m_J = 3/2\rangle$ with an interatomic distance of $15\,\mu$m. The solid curves are Monte Carlo simulations including Rydberg lifetimes, preparation and detection errors and shot-to-shot positional disorder.

the AFM/FM states. Then I will present our strategy to experimentally prepare the ground states. The parameters used until the end of this chapter are: a lattice spacing of $a = 12.5\,\mu$s, $J/(2\pi) = -0.77\,\text{MHz}$, $|\uparrow\rangle = |60S_{1/2}, m_J = 1/2\rangle$ and $|\downarrow\rangle = |60P_{1/2}, m_J = -1/2\rangle$.

5.2.1 Ansatz wave-functions for the AFM/FM states

Eigenstates. As illustrated in Fig. 5.3, we first calculate all the eigenstates of the four-atom square array and sort them by their total magnetization along z defined as $M^z = \sum_i \sigma_i^z/N$ with N the number of atoms. The lowest and highest energy state belongs to the $M^z = 0$ sector and respectively refers to the $|\text{AFM}\rangle_{\text{XY}}$ and $|\text{FM}\rangle_{\text{XY}}$ states when $J > 0$. When $J < 0$, the ground state is $|\text{FM}\rangle$. For the rest of the manuscript, we will refer to $|\text{AFM/FM}\rangle_{\text{XY}}$ as the AFM/FM ground states of the
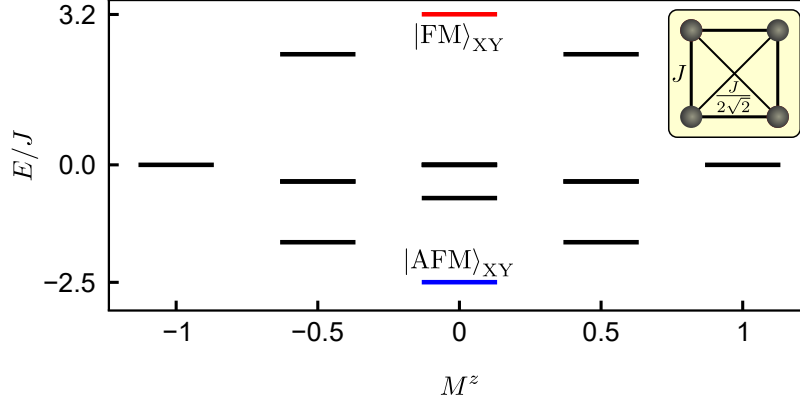
Figure 5.3: Eigenstates of the four atom square array. Eigenstates separated per magnetization sector. Here $J > 0$. The ground and highest energy state are the $|\text{FM}\rangle_{\text{XY}}$ and $|\text{AFM}\rangle_{\text{XY}}$ states. The inset shows the square configuration with the atom-atom interaction energy strength.

dipolar XY model for square geometries[3]. In both cases, the eigenstates have no simple analytical expression, but they are well represented by two Ansätze states that I will now describe.

Antiferro-/ferro-magnetic order along x and y. To intuitively understand this first ansatz, it is interesting to study the ground state of the Ising model for square arrays. The nearest neigbhour Ising model reads $\mathcal{H}_{\text{Ising}} = \hbar J \sum_{\langle i,j \rangle} \sigma_i^z \sigma_j^z$ with $\langle i,j \rangle$ summing over all the nearest neighbour pairs. To minimize the energy of the system, one would intuitively place all the spin along the $\pm z$ direction in a staggered configuration leading to a z antiferromagnetic order $|\uparrow\downarrow\uparrow\downarrow\cdots\rangle$. This state is called a Néel state. During the last five years, these Néel orders have been experimentally studied and observed on Rydberg platforms (including ours) [Labuhn *et al.*, 2016; Schauss, 2018; Scholl *et al.*, 2021; Ebadi *et al.*, 2021]. We now focus back on the XY model. It exhibits $\sigma_i^x \sigma_j^x$ and $\sigma_i^y \sigma_j^y$ interactions. As for the Ising model, one would create antiferromagnetic orders along x and y to minimize the energy of the system. This intuition leads us to the following ansatz:

$$|\text{AFM}\rangle_{\text{CSB}} = \int_0^{2\pi} |\rightarrow_\varphi \leftarrow_\varphi \rightarrow_\varphi \leftarrow_\varphi \cdots\rangle \, d\varphi/(2\pi), \tag{5.6}$$

---

[3]The lowest/highest energy spectrum for larger array is described by the *Anderson tower of states* [Wietek, Schuler, and Läuchli, 2017]. The spectrum is symmetric around $M^z = 0$ and the lowest/highest eigenstate energy of each M^z sector increases/decreases polynomially with their M^z value.

with $|\rightarrow_\varphi \leftarrow_\varphi \rightarrow_\varphi \leftarrow_\varphi \cdots\rangle = e^{-i\varphi \sum_i \sigma_i^z} |\rightarrow_x \leftarrow_x \rightarrow_x \leftarrow_x \cdots\rangle$ being a classical antiferromagnetic state along a direction of the equatorial plane of the Bloch sphere given by the angle φ (when $\varphi = 0$, this direction corresponds to x). This ansatz features the $U(1)$ symmetry of the XY Hamiltonian by being the superposition of all the antiferromagnetic states along all the directions of the equatorial plane. It means that the system should exhibit an antiferromagnetic order in any direction of the equatorial plane. Similarly, we define the ansatz of the ferromagnetic state[4] $|\text{FM}\rangle_{\text{CSB}}$ by replacing the antiferromagnetic state by $|\rightarrow_\varphi \rightarrow_\varphi \rightarrow_\varphi \rightarrow_\varphi \cdots\rangle$ in Eq. 5.6. For four atoms, we numerically calculate the overlap between these ansätze and the real ground states: $_{\text{XY}}\langle\text{AFM}|\text{AFM}\rangle_{\text{CSB}} \approx 97\%$ and $_{\text{XY}}\langle\text{FM}|\text{FM}\rangle_{\text{CSB}} \approx 99\%$. These high overlaps demonstrate that these ansätze faithfully represent the ground state.

Superposition of valence bond solids.   To minimize the energy, one would intuitively introduce anti-/ferro-magnetic bonds between the atoms. This intuition leads us to the second ansatz, introduced by Anderson in the context of spin liquids [Anderson, 1973, 1987] describing a quantum superposition of Valence Bond Solid (VBS). All atoms are paired in either $|\bullet\!\!-\!\!\bullet\rangle = |-\rangle$ for the antiferromagnetic state or in $|\bullet\!\!-\!\!\circ\rangle = |+\rangle$ for the ferromagnetic state. For four atoms, the ansätze thus read $|\text{AFM}\rangle_{\text{VBS}} = (|\overset{\bullet-\bullet}{\bullet-\bullet}\rangle + |\,\text{\small I I}\,\rangle)/\sqrt{3}$ and $|\text{FM}\rangle_{\text{VBS}} = (|\overset{\bullet-\bullet}{\bullet-\bullet}\rangle + |\,\text{\small I I}\,\rangle)/\sqrt{3}$. They exhibit a high overlap of $_{\text{XY}}\langle\text{AFM}|\text{AFM}\rangle_{\text{VBS}} \approx 99\%$ and $_{\text{XY}}\langle\text{FM}|\text{FM}\rangle_{\text{VBS}} \approx 97\%$ with the perfect ground states.

Using the different values of the correlation given in Tab. 5.1, we thus expect, for the $|\text{AFM}\rangle_{\text{VBS}}$ state, to measure negative nearest neighbours correlations in all bases. This property is consistent with the expectation of antiferromagnetic order along the (x,y) predicted by the previous ansatz $|\text{AFM}\rangle_{\text{CSB}}$. Similarly, for $|\text{FM}\rangle_{\text{VBS}}$, we expect to measure positive nearest neighbours correlations along the (x,y) plane consistent with the prediction of ferromagnetic order given by the $|\text{FM}\rangle_{\text{CSB}}$ ansatz state.

We now have two intuitive ansätze to describe the ground state of the dipolar XY model. We move to the study of the preparation of these ground states.

---

[4]The ansatz state for the ferromagnetic ground state is also known as the Dicke state $|\text{FM}\rangle_{\text{CSB}} = |\mathbf{J}^2 = (N/2)(N/2+1), J_z = 0\rangle$ [Dicke, 1954].
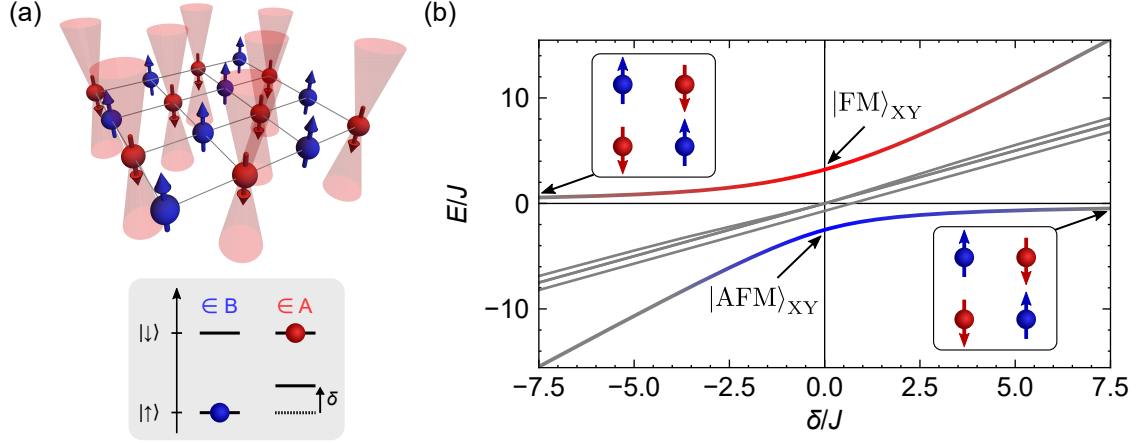
Figure 5.4: Preparation of the AFM and FM ground state. (a) Illustration showing the addressed atoms (sub-array A) prepared in $|\downarrow\rangle$ and the non-addressed atoms (sub-array B) prepared in $|\uparrow\rangle$. (b) Eigenenergies of the Hamiltonian in Eq. 5.7 as a function of δ for a four atom square array.

5.2.2 Adiabatic preparation of the ground state

The strategy to prepare the ground states $|\text{AFM/FM}\rangle_{\text{XY}}$ relies on an adiabatic procedure. As a reminder, an adiabatic process is a method used to prepare the ground state of a Hamiltonian $\mathcal{H}_0$ whose ground state cannot be easily prepared. In our case, $\mathcal{H}_0 = \mathcal{H}_{\text{XY}}$. To do so, we first implement the following Hamiltonian $\mathcal{H}_0 + \lambda \mathcal{H}_1$ where $\lambda \mathcal{H}_1$ is a driver Hamiltonian for which we know how to prepare the ground state, and $\lambda(t)$ a parameter whose we can arbitrarily and dynamically tune the value. Starting with $\lambda \gg 1$ we prepare the ground state of $\mathcal{H}_1$ which is approximately the ground state of $\mathcal{H} = \mathcal{H}_0 + \lambda \mathcal{H}_1$. Then, by adiabatically ramping down λ to zero, we connect the $\mathcal{H}_1$ ground state to the $\mathcal{H}_0$ ground state.

We choose the driven Hamiltonian to be a staggered effective-magnetic field along z that reads $\lambda \mathcal{H}_1 = \mathcal{H}_{\text{Z}} = \hbar\delta \sum_{i\in A}(1 + \sigma_i^z)/2$. This field only applies on the atoms in the sub-array A (defined in Fig. 5.4a) and does not apply on atoms belonging to the B sub-array. This field is achieved by using addressing beams focused on the A atoms applying a light shift δ as shown in Fig. 5.4a (more details about these addressing beams are given in Sec. 3.1). The total Hamiltonian thus reads:

$$\mathcal{H} = \mathcal{H}_{\text{XY}} + \mathcal{H}_{\text{Z}} = \frac{\hbar J}{2}\sum_{i<j}\frac{a^3}{r_{ij}^3}\left(\sigma_i^x\sigma_j^x + \sigma_i^y\sigma_j^y\right) + \hbar\delta\sum_{i\in A}(1 + \sigma_i^z)/2. \qquad (5.7)$$

By varying the intensity on these addressing beams, we modify the amplitude of the light-shifts δ, which allows us to dynamically vary the tunable parameter $\lambda = \delta/J$. Figure 5.4b shows the eigenenergies of the Hamiltonian $\mathcal{H}$ given in Eq. 5.7 for a 2×2 square array and $J > 0$. When $\delta/J \gg 1$, the ground state of $\mathcal{H} \approx \mathcal{H}_\mathrm{Z}$ is the Néel state $|\uparrow\downarrow\uparrow\downarrow \cdots\rangle$ where the atoms in A/B are in $|\downarrow\rangle/|\uparrow\rangle$.

To prepare the ground state of $\mathcal{H}_\mathrm{XY}$ we apply the following sequence. First, using the addressing beams we apply a large detuning $\delta/J \gg 1$ and perform a set of microwave pulses to prepare the system in the Néel state (see Sec. 3.2). Then, we adiabatically ramp down δ to connect the Néel state to the $|\mathrm{AFM}\rangle_\mathrm{XY}$ ground state as illustrated in Figure 5.4b. To prepare $|\mathrm{FM}\rangle_\mathrm{XY}$, we repeat exactly the same procedure, changing the sign of δ. Now when $-\delta/J \gg 1$, the Néel state is the highest energy state that we connect to $|\mathrm{FM}\rangle_\mathrm{XY}$ by adiabatically ramping down δ. Therefore, by applying exactly the same experimental sequence and simply choosing the sign of δ, we can either prepare the AFM state or the FM state. From an experimentalal point of view, this situation is very advantageous. Even if this procedure suffers from experimental imperfections, it will still allow us to perform comparative measurements between the $|\mathrm{AFM}\rangle_\mathrm{XY}$ and $|\mathrm{FM}\rangle_\mathrm{XY}$ states.

5.2.3 Experimental realization

The experimental sequence is summarized in Fig. 5.5a. After initializing the atoms in $|\uparrow\rangle$, we use microwave pulses and addressing beams to prepare the Néel state. We then adiabatically ramp down the light shift applied on the A atoms as $\delta(t) = \delta_0 e^{-t/\tau}$ with δ_0 the initial energy shift and τ a time constant setting the speed of the ramp. We numerically check that for an initial light shift of $\delta_0/(2\pi) = 15\,\mathrm{MHz}$ and an interaction energy of $J/(2\pi) = -0.77\,\mathrm{MHz}$, taking a ramping time of $\tau = 0.3\,\mu\mathrm{s}$ is adiabatic enough. After a time $t = 2\,\mu\mathrm{s}$ (end of the ramp when $\delta(t) \approx 0$), we measure the state of the system. To measure in the z-basis, we directly apply the readout sequence, and to measure along the x- or y-basis, we apply a global $\pi/2$-microwave pulse to rotate the system prior to the readout.

Figure 5.5 shows the magnetizations $\langle \sigma_i^{x,z} \rangle$ (coloured circles) and two body connected correlation $\langle \sigma_i^{x,z} \sigma_j^{x,z} \rangle_\mathrm{c} = \langle \sigma_i^{x,z} \sigma_j^{x,z} \rangle - \langle \sigma_i^{x,z} \rangle \langle \sigma_j^{x,z} \rangle$ (coloured bars) in the x- and z-basis for the preparation of $|\mathrm{AFM}\rangle_\mathrm{XY}$ and $|\mathrm{FM}\rangle_\mathrm{XY}$ state. The top line shows the expectations for perfect ground states; the second line shows the results of a

(a)

(b) $|\text{AFM}\rangle_{XY}$ measured in: $\quad |\text{FM}\rangle_{XY}$ measured in:
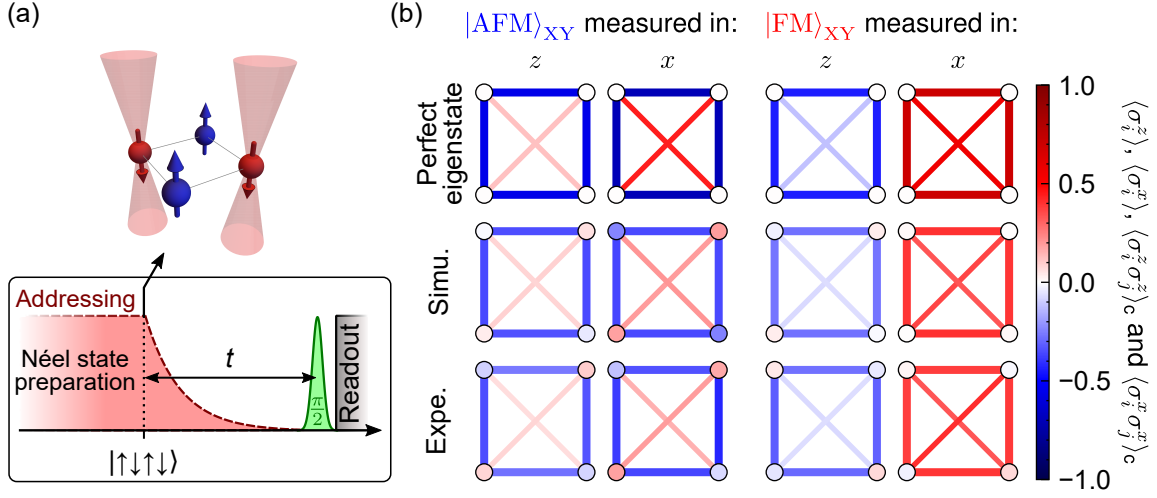
Figure 5.5: AFM and FM state for a four-atom square array: experimental results
(a) Sketch of the experimental sequence. At $t = 0$, we adiabatically decrease the addressing light intensity such that $\delta(t) = \delta_0 e^{-t/\tau}$ with $|\delta_0|/(2\pi) = 15$ MHz and $\tau = 0.3\,\mu$s. After $t = 2\,\mu$s, we measure the state of the system along z (without the $\pi/2$-microwave pulse) or x (with the $\pi/2$-microwave pulse). (b) Comparison between calculated perfect ground states (top line), simulations (middle line) and experimental results (bottom line). The colour of each circles and bars represents the values of the magnetizations of each atom and the connected correlation between each pair of atoms.

simulation performed by Lucas Leclerc, including experimental imperfections (shot-to-shot positional disorder, preparation and detection errors), and the bottom shows the experimental results. The experimental data are qualitatively in good agreement with the ground state calculations. The magnetization of each atom is close to zero for AFM and FM in all basis. The sign of the correlations are the same: along x, the FM state exhibits ferromagnetic order (positive nearest and next-neighbour correlations), and the AFM exhibits antiferromagnetic order (negative/positive nearest/next-nearest neighbour correlations), and along z, both AFM and FM states exhibit antiferromagnetic-like order (negative nearest neighbour correlations with weaker next-nearest neighbour correlations). The respective signs of the correlations can be understood from the ansätze states described previously. Quantitatively, the amplitudes of the measured correlations are lower and the AFM along x exhibits non-zero residual magnetization. As we observe the same effects on the benchmark simulations, we attribute these effects to experimental imperfections.

We have theoretically and experimentally studied the AFM and FM ground states on a small system size of four atoms. The main properties of these states (magnetizations and correlations) can be understood using the different ansätze states that I have described. Now that we have intuitive pictures to understand these ground states, I move to larger array sizes.

5.3 XY ground states of larger square arrays

As we increase the size of the array, two questions naturally arise. What will be the role of the long range tail of the dipolar interaction $J_{ij} \propto 1/r_{ij}^3$ and do long range effects emerge in these larger size systems. In a first section I will theoretically discuss these questions and in a second, I will present the experimental preparation of AFM and FM states with arrays of $N = 6 \times 7$ atoms. The third section is dedicated to the analysis and discussion of the different properties of the AFM/FM states, and finally, in a fourth section, we will explore their respective phase diagram.

5.3.1 Frustration and long-range order

In the previous section (see Sec. 5.2.1), I presented two intuitive ansätze to describe the ground state of the dipolar XY model. One property of the dipolar XY Hamiltonian that we did not include in these ansätze is the interaction range decaying as $1/r_{ij}^3$. These dipolar interaction will modify the properties of the ground states in two different ways that I describe now.

Long-range order. The XY model exhibits a continuous $U(1)$ symmetry. Theoretical works showed that the dipolar XY model features a Continuous Symmetry Breaking (CSB) [Deng, Porras, and Cirac, 2005; Peter *et al.*, 2012], that has for signature the emergence of a long-range order (*i.e.* $|\langle \sigma_i^x \sigma_j^x \rangle_{\mathrm{c}}|$ reaches a non zero value when r_{ij} goes to infinity). This property is well illustrated when considering an *all-to-all* coupling XY model $\mathcal{H}_{\mathrm{XY}}^{\text{all-to-all}} = \hbar J \sum_{i<j} \left(\sigma_i^x \sigma_j^x + \sigma_i^y \sigma_j^y \right)$. Then, the FM ground state is exactly given by $|\mathrm{FM}\rangle_{\mathrm{CSB}}$ being the superposition of all classical, symmetry-breaking product state $|\rightarrow_\varphi \rightarrow_\varphi \rightarrow_\varphi \rightarrow_\varphi \cdots\rangle$ each exhibiting a classical long-range order pointing at angle φ in the (x, y) plane. It turns out that the CSB property remains valid for shorter range interaction such as dipolar or nearest neighbour interaction [Kennedy, Lieb, and

Shastry, 2004].

The dipolar interactions are commonly considered as short-range interactions in 2D, namely interaction $J(\mathbf{r})$ for which $\int J(\mathbf{r})\, d^d\mathbf{r}$ does not diverge, with d being the dimensionality of the system. For power law interaction $J(\mathbf{r}) \propto |\mathbf{r}|^{-\alpha}$, this condition is achieved if $\alpha > d$. In our case, this condition is achieved with $\alpha = 3$ and $d = 2$. For finite temperature state $T > 0$ (*i.e.* state for which the energy is slightly higher than the ground state), the Mermin-Wagner theorem states that, for short-range interaction, the continuous symmetries cannot be spontaneously broken and thus do not give rise to long range orders [Mermin and Wagner, 1966]. However, in the context of the Mermin-Wagner theorem, short-range interactions are defined as interactions for which $\int |\mathbf{r}|^2 J(\mathbf{r})\, d^d\mathbf{r}$ does not diverge. For power-law interactions, it implies that $\alpha > d + 2$, a condition which is not satisfied for our system. Thus, although the dipolar interactions are generally considered as short-range, they are sufficiently long-range enough to be excluded by the Mermin-Wagner theorem. In summary, for $T \geqslant 0$, we expect the FM ground state to exhibit long-range order.

Frustration. The long-distance tail of the dipolar interaction introduces frustration in the $|\text{AFM}\rangle_{\text{XY}}$ case. It is impossible to create antiferromagnetic bonds for all the pairs of atoms. This effect is present for small and large system sizes, an example of frustration with four spins is illustrated in Fig. 5.6: a classical anti-ferromagnet along x exhibits frustration along its diagonals, increasing its energy by $2 \times J/(2\sqrt{2})$. However, frustration mainly alters the properties of the antiferromagnetic states at long distances. The ground state is still expected to exhibit long-range order; however, for $T > 0$, the frustration reduces the stability of the AFM phase and is expected to prevent the formation of a long-range order [Bruno, 2001; Defenu *et al.*, 2023]. As we need a relatively large system size to observe this effect, we did not discuss it when we presented the results for four atoms in Sec. 5.2.

To summarize, the dipolar XY Hamiltonian exhibits $1/r_{ij}^3$ interaction range which cannot be approximated neither as an *all-to-all* nor as a *nearest neighbour* interaction range. It modifies the properties of the ground states: for the FM, it contributes to the emergence of a long-range order, while for the AFM state, frustration destabilizes this order at $T > 0$. More elaborated ansätze could be considered to include these effects in their description of the ground states. As an example, for four atoms, $|\text{AFM}\rangle_{\text{VBS}} \propto |\!\begin{smallmatrix}\bullet\!-\!\bullet\\\bullet\!-\!\bullet\end{smallmatrix}\rangle + |\begin{smallmatrix}\bullet\\\bullet\end{smallmatrix}\ \begin{smallmatrix}\bullet\\\bullet\end{smallmatrix}\rangle + \varepsilon |\!\times\!\rangle$ and $|\text{FM}\rangle_{\text{VBS}} \propto |\!\begin{smallmatrix}\bullet\!-\!\bullet\\\bullet\!-\!\bullet\end{smallmatrix}\rangle + |\begin{smallmatrix}\bullet\\\bullet\end{smallmatrix}\ \begin{smallmatrix}\bullet\\\bullet\end{smallmatrix}\rangle + \varepsilon |\!\times\!\rangle$ with $|\varepsilon| \ll 1$
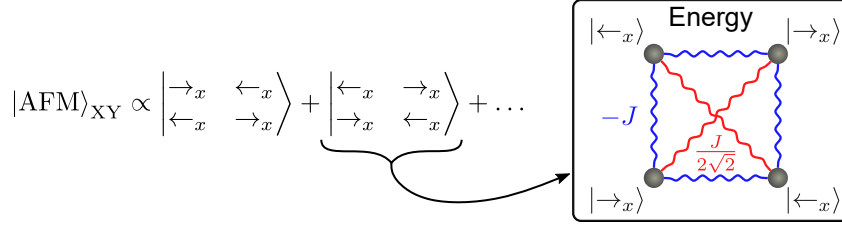
Figure 5.6: Illustration of frustration induced by the long range tail of the dipolar interactions. The dipolar interactions introduces frustration in square anti-ferromagnet along x. It requires an extra energy $2 \times J/(2\sqrt{2})$.

could be used to account for dipolar interaction. However, searching for appropriate ansätze is hard, and we did not investigate this question further. We now move to the experimental preparation and study of the AFM and FM states with larger arrays.

5.3.2 Preparation of the AFM/FM ground states on larger arrays

We start with a square array of 6×7 atoms and follow the same procedure described in Sec. 5.2.2. We experimentally and numerically (simulations performed by the team of Norman Yao in Harvard) checked that for $\delta_0/(2\pi) = 15\,\mathrm{MHz}$ and $J/(2\pi) = 0.77\,\mathrm{MHz}$, a ramp time of $\tau = 0.3\,\mu\mathrm{s}$ is adiabatic enough. After the end of the ramp, at $t = 2\,\mu\mathrm{s}$ when $\delta \approx 0$, we measure the state of the system. Figure 5.7a shows the magnetization, nearest neighbour and next-nearest neighbours connected correlations measured along the x axis (see Fig. 5.5b). Similarly to the four-atom array, the AFM state reveals an antiferromagnetic order with negative/positive nearest/next-nearest neighbour correlations, and the FM state exhibits ferromagnetic order with positive correlations.

To better characterize these phases and check if they exhibit long-range order, we plot the map of the correlation function $C_{\mathbf{r}}^x$ defined as

$$C_{\mathbf{r}}^x = \frac{1}{N_{\mathbf{r}}} \sum_{\{i,j|\mathbf{r}_{ij}=\mathbf{r}\}} \langle \sigma_i^x \sigma_j^x \rangle_{\mathrm{c}}, \tag{5.8}$$

with $\{i,j|\mathbf{r}_{ij} = \mathbf{r}\}$ summing on all the $\{i,j\}$ pairs separated by $\mathbf{r}$ and $N_{\mathbf{r}}$ the corresponding number of such pairs. Figure 5.7b shows the average correlation $C_{\mathbf{r}=(r_x,r_y)}^x$ as function of a displacement r_x along $\mathbf{u}_x$ and r_y along $\mathbf{u}_y$ on the array. We observe the characteristic staggered correlations for the AFM, while the correlations are always positive for the FM. From these correlation maps, we now calculate the
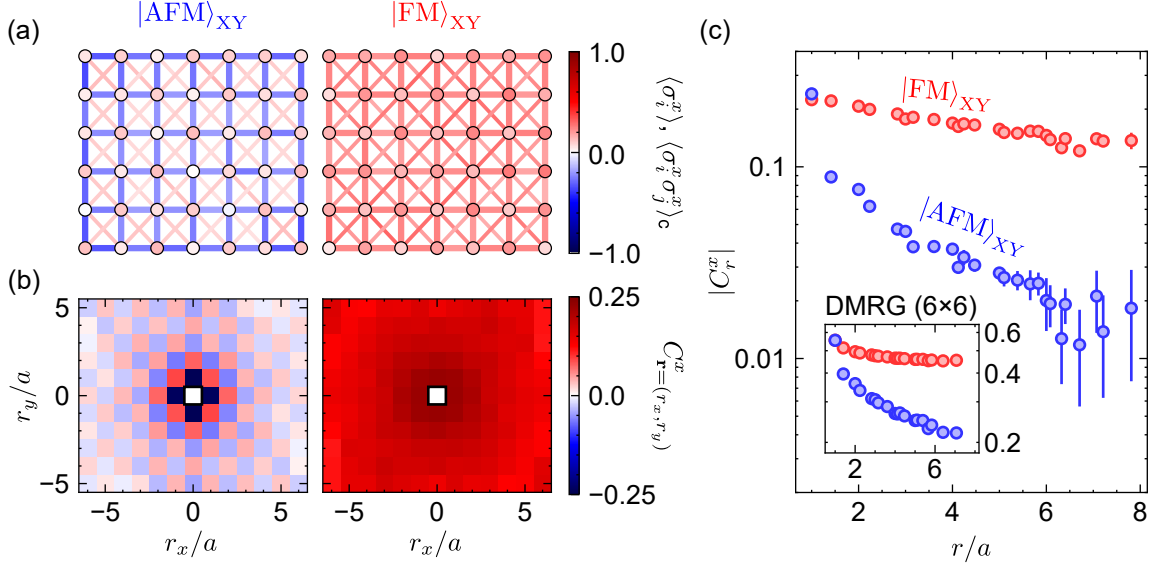
Figure 5.7: Antiferro-/ferro-magnets with a 6×7 **square array.** The data are measure at $t = 2\,\mu$s. (a) Magnetization $\langle \sigma_i^x \rangle$, and nearest neighbour/next-nearest neighbours connected correlations $\langle \sigma_i^x \sigma_j^x \rangle_c$ along x for the FM and AFM state. (b) Maps of correlation function $C_{\mathbf{r}=(r_x,r_y)}^x$ for AFM and FM states. (c) Average correlation $|C_r^x|$ as a function of the distance r. The inset show the results on a DMRG simulation for a 6×6 square array.

mean correlation C_r^x averaged over all pairs $\{i,j\}$ whose atoms are separated by a distance $|\mathbf{r}_{ij}| = |\mathbf{r}| = r$:

$$C_r^x = \frac{1}{N_r} \sum_{\{i,j|r=|\mathbf{r}_{ij}|\}} \langle \sigma_i^x \sigma_j^x \rangle_c, \tag{5.9}$$

Figure 5.7c shows $|C_r^x|$ as a function of r. For the AFM and FM states, the correlations decrease as r increases with a faster decay for the AFM, which we attribute to the frustration that hinders the formation of long-range correlations. However, for both phases, we still measure non-zero correlations for the largest distances of the system $r/a \approx 7$. This observation is consistent with our expectation of a long-range order for the AFM and FM ground state.

To assess the role played by the experimental imperfections, which are mostly common for both the AFM and FM cases due to the same experimental procedure being used, we also plot the results of the Density Matrix Renormalization Group (DMRG) simulation (performed by the Harvard team) for a similar system size of $N = 6 \times 6$ atoms without including any errors (see inset). Qualitatively, the results align well with the experimental data: the AFM correlation decays faster than the FM correlation but still shows non-zero correlation at long distances. Quantitatively, the correlation

amplitudes are weaker. For the FM state, there is approximately a factor 3 of difference between the amplitude of the measured correlations and the simulated ones. For the AFM state, at short distances, we also observe a factor 3 of difference between the experimental and simulated correlations, but at long distances, this factor increases up to 10. We attribute these differences to several sources of imperfections: preparation errors (finite fidelity of the initial Néel state preparation), detection errors ($\varepsilon_\uparrow$ and $\varepsilon_\downarrow$, see Sec. 2.3), and decoherence effects (Rydberg lifetimes and positional disorder). The detection errors contribute to a decrease in the amplitude of the measured correlations; in a first approximation, they lead to an overall reduction of the C_r^x correlations by a factor $1 - 2(\varepsilon_\uparrow + \varepsilon_\downarrow)$ (see more details in Appendix A). Assessing the effects of preparation errors and different decoherence mechanisms is more complex as they affect the system dynamics, requiring simulations that include these imperfections, which are challenging to perform for such system sizes. However, we can qualitatively understand their effects as follows: these imperfections prevent us from preparing the perfect AFM/FM ground states. Instead, we prepare finite-temperature states with $T \approx 0$. Theoretically, in the thermodynamic limit, at non-zero temperature $T > 0$, frustration is expected to destabilize the AFM phase and prevent the formation of long-range order, while for the FM phase, long-range order is still preserved. Therefore, we intuitively expect the preparation errors and decoherence effects to be particularly detrimental to the formation of AFM long-distance correlations. This prediction aligns with the observations: measured and simulated FM correlations are similar up to a factor of 3, while for the AFM correlations, this gap increases at long distances. However, we believe that these imperfections remain sufficiently weak such that we still observe non-zero AFM correlations at long distances.

5.3.3 Is the $U(1)$ continuous symmetry broken ?

As mentioned earlier, the ansätze $|\text{AFM/FM}\rangle_{\text{CSB}}$ enforces the $U(1)$ symmetry by being the superposition of all the classical AFM/FM states along all the direction of the equatorial plane (see Eq. 5.6). A natural question then arises: do we produce a quantum superposition of these classical states or, at each repetition of the experiment, does the system randomly pick a direction φ on the xy plane and produce the corresponding classical state, thus breaking the $U(1)$ symmetry. In the second case, we have a statistical mixture of all classical states. To answer this question, we
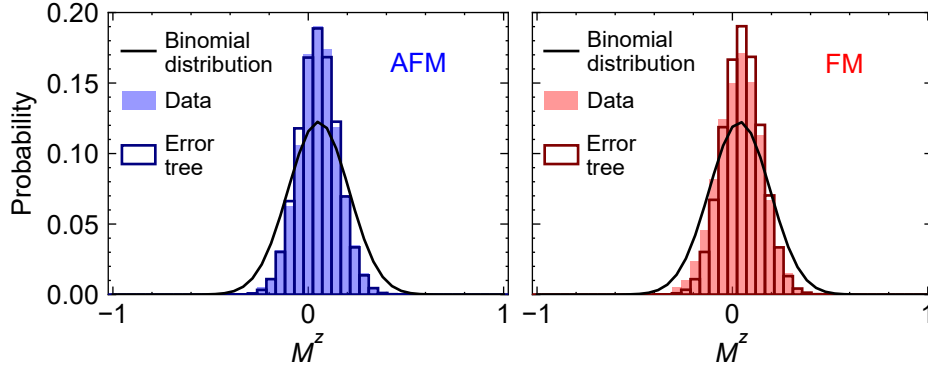
Figure 5.8: Histogram of the averaged z magnetization for the AFM and FM states. Histogram of M^z. The shaded area represent the data, the coloured rectangles represent what we would expect if we consider the preparation and detection errors given by the error tree in Fig. 3.7. The black curve shows the expectation values for a binomial distribution.

analyze the statistical distribution of the average magnetization along z denoted $M^z = \sum_i \sigma_i^z / N$. On can show that for the two ansätze $|\text{AFM}\rangle_{\text{CSB}}$ and $|\text{FM}\rangle_{\text{CSB}}$, the variance $\text{Var}(M^z) = \langle (M^z)^2 \rangle - \langle M^z \rangle^2$ is zero. However, for a statistical mixture of AFM/FM classical states, the variance would reach $N\text{Var}(M^z) = 1$.

Figure 5.8 shows, with coloured shaded areas, the histogram of M^z for both the AFM and FM states. From these histograms, we compute for the AFM: $N\text{Var}(M^z) = 0.46$ and for the FM state: $N\text{Var}(M^z) = 0.56$. Both variances are below one, indicating that we do not prepare classical magnets. These non-zero values can be understood by taking into account the state preparation and detection errors described by the error tree presented in Fig. 3.7. Applying these errors to the ideal distribution leads to the histograms represented by coloured rectangles which reproduce well the experimental data.

The concept of symmetry breaking describes how some systems spontaneously break their symmetry by choosing a preferential direction or orientation. This statement is valid at the thermodynamic limit (*i.e.*, for macroscopic system sizes) where any defect in the system or external residual electric/magnetic field can favour one of these configurations. In this case, the system collapses to the corresponding symmetry-broken classical state. However, in our experiment, the system has a relatively small size and is placed in a very well-controlled environment, allowing us to preserve the $U(1)$ symmetry.
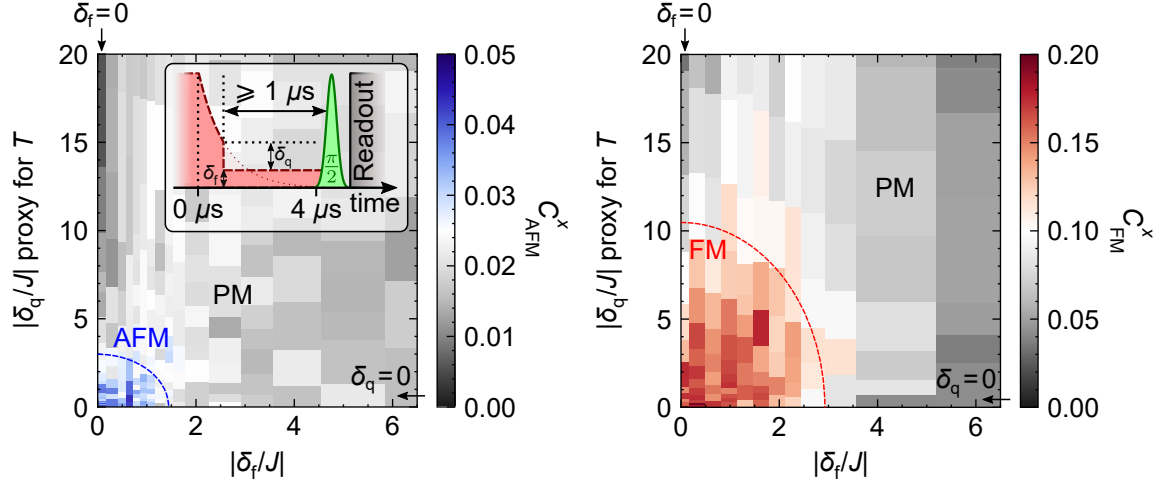
Figure 5.9: Phase diagram of the AFM and FM states. Phase diagram of the AFM (left) and FM (right) state. We measure $C^x_{\mathrm{AFM/FM}}$ defined in Eq.5.10 as a function of δ_{q} and δ_{f}. The dashed lines are a guide to te eyes to shown the boundaries between the PM and AFM/FM phase. The inset in left panel shows the experimental sequence. We always measure the state of the atoms after $4\,\mu$s thus letting an equilibrium time after the quench of $\geqslant 1\,\mu$s.

5.4 Exploration of the AFM/FM phase diagram

In the previous sections, we studied the AFM and FM ground state. In this section, we now probe their respective phase diagram as a function of their temperature and the applied light shift δ. In the first part, I focus on the exploration of these phase diagrams, and then in a second and third part, I investigate the quantum phase transition occurring at $T = 0$ and the thermal one at $\delta = 0$.

5.4.1 Probing the AFM/FM phase diagram via quench experiments

We showed on a 6×7 square array that we measured long-distance correlations consistent with the prediction of long-range order at $T = 0$ for the AFM and FM ground state. As mentioned previously, this behaviour should persist at a finite temperature $T > 0$ for the FM state, while the long-range correlations should vanish as the AFM long-range order is forbidden.

To change the "effective temperature" of the state, we introduce a partial quench of amplitude δ_{q} into the ramp, reaching a final light shift of δ_{f}. The quench δ_{q} introduces

an excess energy in the system and thus can be seen as a proxy for the temperature. After the quench, we then maintain the light shift at δ_f until we reach $4\,\mu$s of experiment time as shown in the inset of Fig. 5.9. For the set of values $\{\delta_q, \delta_f\}$ we wish to explore, this experimental sequence allows us to get an equilibrium time of at least $1\,\mu$s between the quench and the readout. We experimentally checked that this time is sufficient for the quenched state to thermalize, *i.e,* to reach steady values for the magnetizations and correlation functions. After each ramp set by the $\{\delta_q, \delta_f\}$ parameters, we measure along x the average two body connected correlation $C^x_{\mathrm{AFM/FM}}$ defined as:

$$C^x_{\mathrm{AFM/FM}} = \frac{1}{N(N-1)} \sum_{i \neq j} (\pm 1)^{(\mathbf{u}_x \cdot \mathbf{r}_{ij} + \mathbf{u}_y \cdot \mathbf{r}_{ij})/a} \langle \sigma^x_i \sigma^x_j \rangle_c, \qquad (5.10)$$

with $\mathbf{r}_{ij}$ separating atom i and j, and the sign is -1 for the AFM state, and $+1$ for the FM state. This observable is a good order parameter to characterize long-range correlation: the longer-range and stronger the correlation are, the higher is $C^x_{\mathrm{AFM/FM}}$. Fig. 5.9 shows the AFM and FM phase diagrams. For small values of δ_f and δ_q (corresponding to low-temperature states), the AFM phase exhibits AFM order with an average connected correlation of $C^x_{\mathrm{AFM}} \approx 0.04$. As we increase either δ_f or δ_q, C^x_{AFM} decreases towards zero indicating melting into a disordered phase named the Para-Magnetic (PM) phase. We now perform the same analysis for the FM phase. Compared to the AFM case, the region where the system exhibits FM order is significantly larger. This observation is consistent with the fact that the long-range interactions induce frustration destabilizing the AFM phase while it helps to maintain the FM order in the FM phase.

We now focus and study the thermal phase transition ($\delta_f = 0$) and the quantum one ($\delta_q = 0$).

5.4.2 Thermal phase transition

The thermal phase transition happens at $\delta_f = 0$ (vertical cuts in Fig. 5.10). The physics is described by a Berezinskii–Kosterlitz–Thouless (BKT) transition [Berezinsky, 1971; Kosterlitz and Thouless, 1973; Kosterlitz, 1974; Ryzhov *et al.*, 2017]. Below a critical temperature $T < T^{\mathrm{FM}}_c$, the FM state exhibits long-range order, characterized by an algebraic decay of the correlation at short distances that stabilizes and reaches
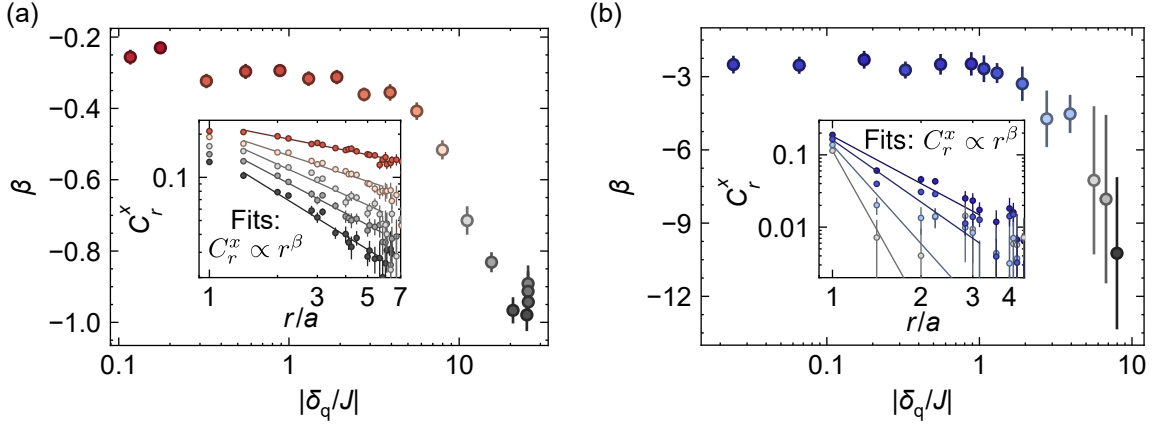
Figure 5.10: Thermal phase transition of the FM/AFM state. (a)/(b) FM/AFM state. Insets: Power-law fit of the average correlations $|C_r^x|$ as a function of r for various value of $|\delta_{\mathrm{q}}/J|$ ($|\delta_{\mathrm{q}}/J| = [1.9, 8.0, 11.1, 15.5, 25.0]$ for the FM state and $|\delta_{\mathrm{q}}/J| = [5.9, 4.2, 1.6, 0.02]$ for the AFM state). The solid curves represent the fits. Main plots: Exponent β extracted from the power-law fits. The error bars represent the uncertainty of the fit estimating β.

a finite value at long distances. In the AFM case, at finite temperature lower than its critical temperature $0 < T < T_{\mathrm{c}}^{\mathrm{AFM}}$, the state exhibits quasi-long range with correlations decaying to zero as a power-law. Above $T_{\mathrm{c}}^{\mathrm{AFM/FM}}$, thermal fluctuations dominate and lead to the disordered phase (PM phase). The BKT theory then predicts an exponential decay of the correlations [Kunz and Pfister, 1976].

To estimate $T_{\mathrm{c}}^{\mathrm{FM}}$, we use all the data performed at $\delta_{\mathrm{f}} = 0$ and fit for short distances r the averaged correlations C_r^x by a power-law function $C_r^x \propto r^{\beta(T)}$. Inset of Fig. 5.10a show different fit of C_r^x at various values of δ_{q} for the FM phase. In Fig. 5.10a, we plot the fitted power-law exponent β as a function of δ_{q}. We observe that for low values of δ_{q}, β reaches a plateau around $\beta \approx -0.3$. As we continue to increase $\delta_{\mathrm{q}}/J > 3$, β decreases, indicating that the FM order begins to disappear. The Minimally Entangled Typical Thermal States (METTS) algorithm run by the Harvard team, allows us to give a calibration of δ_{q} as a function of an effective temperature. The results are shown in [Chen *et al.*, 2023a] and gives for $\delta_{\mathrm{q}}/J \sim 3$ an effective temperate of $T/J \sim 1.7$. At the same time, simulations of the FM phase diagram predict a phase transition at $T_{\mathrm{c}}^{\mathrm{FM}}/J = 1.5$, which is consistent with our data.

We now focus on the AFM phase for which the perform the same procedure analysis (see Fig. 5.10b). As for the FM state, power law exponent β exhibits a plateau for $\delta_{\mathrm{q}}/J \lesssim 1$ and decreases for higher values. For $\delta_{\mathrm{q}}/J \sim 1$, METTS simulations give
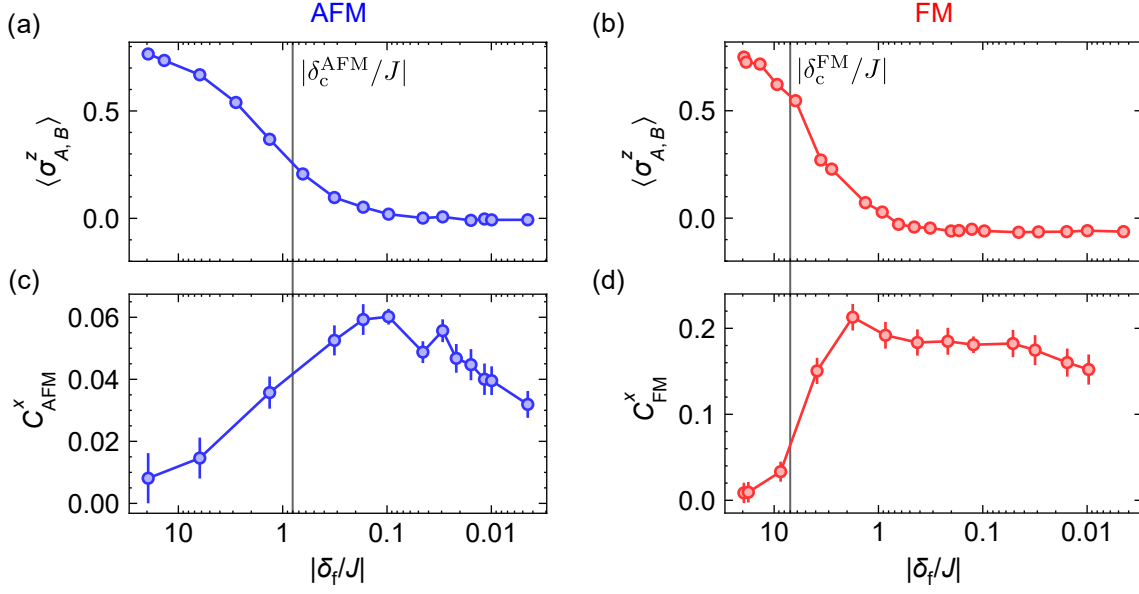
Figure 5.11: Quantum phase transition of the AFM/FM state. (a) and (b): Staggered magnetization $\langle \sigma^z_{A,B} \rangle$ as a function of δ_f. (c) and (d): Order parameter $C^x_\text{AFM/FM}$ as a function of δ_f. The vertical grey line highlights the critical light shift $\delta^\text{AFM/FM}_\text{c}$.

us an effective temperature of $T/J \sim 0.7$ consistent with the simulation of the AFM phase diagram predicting $T^\text{AFM}_\text{c}/J \sim 0.5$ [Chen *et al.*, 2023a]

We have qualitative agreements between the estimated critical temperature and the ones predicted by simulations. As expected, the FM phase has a higher T_c than the AFM one since the dipolar interactions tend to stabilize the FM order against thermal fluctuations. I now move to the quantum phase transition.

5.4.3 Quantum phase transition

The quantum phase transition happens at $\delta_\text{q} = 0$ (horizontal cuts in Fig. 5.9). At any value of $\delta_\text{f} = 0$, the prepared state correspond to ground state of $\mathcal{H}_\text{XY} + \mathcal{H}_\text{Z}(\delta_\text{f})$ (see Eq. 5.7). As $\mathcal{H}_\text{Z}(\delta_\text{f})$ preserves the $U(1)$ symmetry, we then expect the AFM/FM phase to exhibit AFM/FM order for sufficiently small δ_f light shift. Between the AFM/FM phase and the AM phase, we expect a continuous Quantum Phase Transition (QPT) at some critical values, $\delta^\text{AFM/FM}_\text{c}$ of the applied light shift δ_f [Defenu *et al.*, 2023].

To probe these QPTs, we plot as a function of δ_f, the average z staggered magnetization $\langle \sigma^z_{A,B} \rangle$ defined as $\langle \sigma^z_{A,B} \rangle = \sum_{i \in B} \langle \sigma^z_i \rangle / N - \sum_{i \in A} \langle \sigma^z_i \rangle / N$ (see Fig. 5.11a and b) and the order parameters $C^x_\text{AFM/FM}$ (see Fig. 5.11c and d). For this experiment,

as we do not quench the system and only study ground state physics, we remove the equilibrium time of $\geqslant 1\,\mu s$ introduced previously (see the experimental sequence shown in the inset of Fig. 5.9) and come back to the initial adiabatic ramp profile $\delta_{\mathrm{f}}(t) = \delta_0 e^{-t/\tau}$. The staggered magnetization starts close to one (due to preparation and detection errors, this value is slightly lower than one) and decreases towards zero as we decrease δ_{f}. At the same time, correlations in xy plane build up and are characterized by an increase of $C^x_{\mathrm{AFM/FM}}$ to a non-zero value. As we continue to lower δ_{f}, $C^x_{\mathrm{AFM/FM}}$ reaches a maximum value and slowly decay. Since the lowest values of δ_{f} correspond to the longest durations of the experiment, we conjecture that this decay at long times arises from decoherence effects such as shot-to-shot positional disorder or Rydberg state lifetimes. We also observe that the speed at which $\langle \sigma^z_{A,B} \rangle$ decreases and $C^x_{\mathrm{AFM/FM}}$ reaches its maximum is faster for the FM state. Theoretically, these speeds are given by the critical light shift $\delta^{\mathrm{AFM/FM}}_{\mathrm{c}}$. Since the long-range tail of the dipolar interaction reinforces the FM order while frustration destabilizes the AFM phase, we expect the QPT to occur at a larger value of δ_{f} for the FM compared to the AFM case. DMRG simulations ran by the Harvard team predict that for a 6×7 square array, $\delta^{\mathrm{AFM}}_{\mathrm{c}}/J = 0.8$ and $\delta^{\mathrm{FM}}_{\mathrm{c}}/J = 7.1$ [Chen *et al.*, 2023a] represented by vertical lines in Fig. 5.9. This analysis is consistent with our experimental observations.

5.5 Conclusion

In this chapter, I have presented how we implement the dipolar XY model from resonant dipole interactions between Rydberg atoms. Then, I have focused on the AFM/FM ground state of the dipolar XY Hamiltonian for 2D square geometries. We have first studied the case of a small four-atom square array, which allows us to forge intuition about the main properties of the AFM/FM states. We then moved to larger square arrays of 6×7 atoms and measured long-range correlations consistent with the prediction of long-range order in the AFM and FM ground state. Finally, by introducing partial quench in the adiabatic preparation, we explore the $\{T, \delta\}$ phase diagram of the AFM/FM phases. We studied the thermal and quantum phase transitions and showed that due to the frustration induced by the long-range tail of the dipolar interaction, the AFM phase exhibits lower critical temperature and critical δ value. These results demonstrate that the platform can implement and study the XY model and verify theoretical predictions.

An interesting question to ask is what would happen if we repeated the above experiment while scaling up the number of atoms to a mesoscopic or macroscopic size. Will we still measure the same properties? For example, we showed that our relatively small system of $N = 6 \times 7$ atoms preserves the $U(1)$ symmetry. However, due to continuous symmetry breaking, the AFM/FM ground states are expected, in the thermodynamic limit, to break this $U(1)$ symmetry and collapse into a classical state, thus behaving like real-world materials. This raises the question of how much we need to grow the system size to reach this quantum/classical frontier. If there is a limit, what imposes this limit? Answering these questions will require several developments and technological advancements in the near future to scale up the number of atoms and minimize experimental imperfections.

Exploring exotic phases of matter: Spin liquids

Contents

In the previous chapter, we have shown that frustration arises due to the long tail of the dipolar interaction. The choice of the geometry can also produce frustration. The most common example is a system of three spins in an equilateral triangle configuration with the Ising model $\mathcal{H}_{\mathrm{Ising}} = \hbar J \sum_{\langle i<j \rangle} \sigma_i^x \sigma_j^x$ (see Fig. 6.1), where all spins cannot simultaneously anti-align along the x axis. This frustration even occurs with nearest-neighbour interactions and thus consequently significantly modifies the AFM state properties. We usually describe these ground states by a superposition of states in which all spins tend to align along different directions to minimize the energy. In the case of strongly frustrated systems, this superposition can result in a new exotic phase of matter matter called spin liquid [Lee, 2008; Balents, 2010; Savary and Balents, 2016; Broholm *et al.*, 2020]. The literature of spin liquid is vast and not easy to follow: as far as we know, there is no clear definition of spin liquid states and no rigorous description about the features they should exhibit. Generally speaking, spin liquid states are characterized by their apparent disorder, with no obvious magnetic order or

Energy
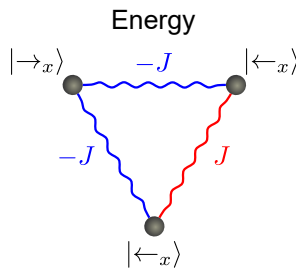
Figure 6.1: Example of frustration induced by the geometry. The triangle geometry introduces frustration in a anti-ferromagnet along x.

spin structure. They do not break rotational or translation symmetries; they look like liquid-like states. Their quantum nature is revealed by measuring their long-range entanglement and various exotic properties, ranging from emergent artificial gauge fields [Lee, Nagaosa, and Wen, 2006], factionalized excitations [Kalmeyer and Laughlin, 1987], and connexions with superconductivity [Anderson, 1987].

Many experiments performed on real-world materials, such as organic compounds, have already been performed at low temperatures via neutron scattering or nuclear magnetic resonance methods. These systems exhibit a lack of order, and their low-energy excitation spectrums are compatible with the theoretical predictions [Han *et al.*, 2012; Fu *et al.*, 2015]. However, only global observables such as spin susceptibility, heat, and thermal conductivity can be measured, limiting the variety of diagnostics that experimentalists can perform on these systems. More recently, several groups using quantum simulators started to investigate these field. Using superconducting qubits, measurement of long-range entanglement have been demonstrated on topological state [Satzinger *et al.*, 2021], representing a significant step toward the realization and measurement of spin liquids using such platforms. Evidence of spin liquid have also been observed using arrays of Rydberg atoms [Semeghini *et al.*, 2021]. In contrast with real-world material experiments, quantum simulators provide single site resolution which allows the experimentalist to measure non-local observables, thus giving a more direct access to the study of spin liquids.

In parallel to these efforts, many theory works showed that spin Hamiltonian on frustrated arrays could lead to their AFM ground state being a spin liquid. For example, many works predicted that the nearest neighbour isotropic Heisenberg Hamiltonian AFM ground state on Kagome lattices should be a Dirac Spin Liquid (DSL) [Hastings, 2000; Ran *et al.*, 2007; Yan, Huse, and White, 2011; He *et al.*, 2017; Zhu *et al.*, 2018]. Recent studies conducted by Norman Yao's team at Harvard showed

that the dipolar XY model could lead to a DSL and Chiral Spin Liquid (CSL) [Yao *et al.*, 2018; Bintz *et al.*, 2024]. Motivated by these results, the Harvard team contacted us to experimentally investigate the DSL and CSL state using our Rydberg platform. These works are still in progress, and in this chapter, I will present the preliminary results we obtained. The first section will focus on the investigation of the DSL, and the second one on the CSL.

6.1 Probing a Dirac spin liquid

In this section, we attempt to prepare and observe the DSL. DSLs are characterized by their gapless excitations whose elementary excitations called *spinons* behave like Dirac fermions, similar to those in graphene. DSL states feature a linear energy-momentum relationship, resulting in Dirac cones in their dispersion relations. I first describe the experimental preparation and the different phase transitions we cross to prepare the DSL. Then, I analyze the main properties of the state we prepare. Finally, to better characterize it, we study its excitations, trying to observe Friedel oscillations, which could be a signature of the Dirac cones in the system. In this section, all the experiment were performed using the same parameters as for the previous chapter: $a = 12.5\,\mu\text{s}$, $J/(2\pi) = -0.77\,\text{MHz}$, $\left|\uparrow\right\rangle = \left|60S_{1/2}, m_J = 1/2\right\rangle$ and $\left|\downarrow\right\rangle = \left|60P_{1/2}, m_J = -1/2\right\rangle$.

6.1.1 Experimental preparation

We start with a Kagome array of $N = 114$ atoms as shown in Fig. 6.2. The procedure to prepare the AFM ground state is the same as the one described in the previous chapter (see Sec. 5.2.2). We rely on a adiabatic procedure using the following Hamiltonian:

$$\mathcal{H} = \mathcal{H}_{\text{XY}} + \mathcal{H}_{\text{Z}} = \frac{\hbar J}{2} \sum_{i<j} \frac{a^3}{r_{ij}^3} \left(\sigma_i^x \sigma_j^x + \sigma_i^y \sigma_j^y\right) + \hbar\delta \sum_{i \in A} (1 + \sigma_i^z)/2, \qquad (6.1)$$

where $\mathcal{H}_{\text{Z}}$ is effective-magnetic field along z of strength δ applied on half of the atom in the sub-array denoted A defined in Fig. 6.2b (the other atoms are in the sub-array B). This field is achieved using addressing beams focusing on the atoms
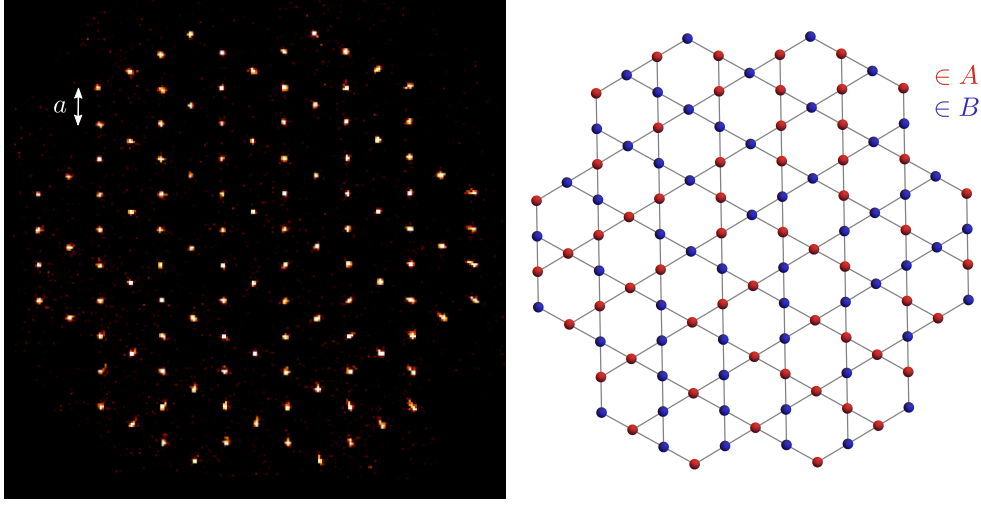
Figure 6.2: Kagome geometries and glider state. Left: Fluorescence image of the $N = 114$ atoms Kagome geometry. Right: Glider state. The atoms in A are addressed and initialized in $|\downarrow\rangle$ and the ones in B are initialized in $|\uparrow\rangle$. Here the lattice spacing is $a = 12.5\,\mu$m.

in A. For $|\delta/J| \gg 1$, the ground state of $\mathcal{H} \approx \mathcal{H}_{\mathrm{Z}}$ is similar to the Néel state for square geometries where the atoms in A/B are in $|\downarrow\rangle/|\uparrow\rangle$. We call this state the *glider state*. To apply the ground state we follow the following adiabatic procedure. After having initialized all the atoms in $|\downarrow\rangle$, we apply a large light shift $|\delta/J| \gg 1$ and using microwave pulses apply local rotations (see Sec. 3.1)) to prepare the ground state: the glider state. We then adiabatically ramp down the applied light shift $\delta(t) = \delta_0 e^{-t/\tau}$ to zero to reach the AFM ground state. The positions of the A/B atoms have been chosen to optimize the coupling between the glider and the ground state during the adiabatic preparation. For example, having at least one atom from A and from B on every elementary triangle of the Kagome array allows for a better distribution of the z magnetization over the array. The exact position of every $|\uparrow\rangle/|\downarrow\rangle$ spins results from an optimization using DMRG simulations performed by the Harvard team.

Adiabaticity criteria.　We must evaluate the time constant τ for which the ramp $\delta(t)$ is adiabatic. Numerical simulations of the dynamics are intractable for our system size, making it difficult to predict the energy gaps and the appropriate ramp speed. We thus need to determine the adiabaticity criteria experimentally. To do so, we first choose $\tau = 0.3\,\mu$s. In Fig. 6.3a, we plot the average z staggered magnetization $\langle \sigma_{A,B}^z \rangle = \sum_{i \in B} \langle \sigma_i^z \rangle / N - \sum_{i \in A} \langle \sigma_i^z \rangle / N$ and the average nearest neighbour connected
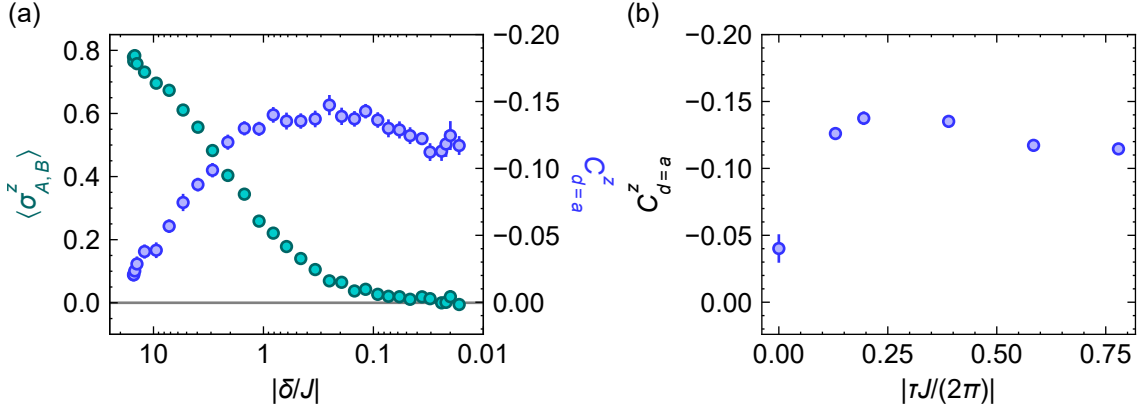
Figure 6.3: Checking the adiabaticity of the ramp. (a) Average staggered magnetization $\langle \sigma_{A,B}^z \rangle$ and average nearest neighbour connected correlations $C_{d=a}^z$ measured along z as a function of δ for a ramp time constant of $\tau = 0.3\,\mu\text{s}$. (b) Correlation $C_{d=a}^z$ as a function of τ measured at the end of the ramp when $|\delta/J| \approx 0.04$. The point at $|\tau J/(2\pi)| = 0$ corresponds to a quench from δ_0 to zero, the data point corresponds to a measurement performed after an equilibrium time of $0.5\,\mu\text{s}$.

correlation $C_{d=a}^z$ measured along z as a function of δ. As we decrease δ, the glider state melts into the AFM state, manifested by the collapse of the staggered magnetization $\langle \sigma_{A,B}^z \rangle$ while negative nearest neighbour correlations build up. At small δ, we observe a small decay of the correlations. Since small values of δ correspond to the longest t, we attribute this decay to decoherence effects (Rydberg lifetimes and shot-to-shot positional disorder).

To check if this ramp time is adiabatic, we vary the ramp time constant τ and measure the $C_{d=a}^z$ correlations at the end of the ramp when $|\delta/J| \approx 0.04$ (see Fig. 6.3b). As we increase $|\tau J/(2\pi)|$, the correlations increase until $|\tau J/(2\pi)| \approx 0.2$, reaching a saturation value around $C_{d=a}^z \approx -0.13$. It suggests that for $|\tau J/(2\pi)| < 0.2$ the ramp is slow enough to perform an adiabatic preparation of the AFM ground states. As $\tau = 0.3\,\mu\text{s}$ satisfies this condition, we will keep this ramp time constant.

Phase transition from VBSs to a DSL. As already introduced in the previous chapter (see Sec. 5.2.1), one common ansatz to describe spin liquids relies on the *Valence Bond Solids* (VBSs) description. As a reminder, a VBS describes a state where all spins are maximally entangled to nearest neighbour forming a product state of singlet states $|\!\multimap\!\rangle = |-\rangle = (|\uparrow\downarrow\rangle - |\downarrow\uparrow\rangle)/(2\pi)$. For six atoms in a hexagonal configuration, an example of VSB reads $|\,\text{⬡}\,\rangle$. Although VBSs have no magnetic order (*i.e.* no magnetization), they break the rotational and translation symmetries and thus

137
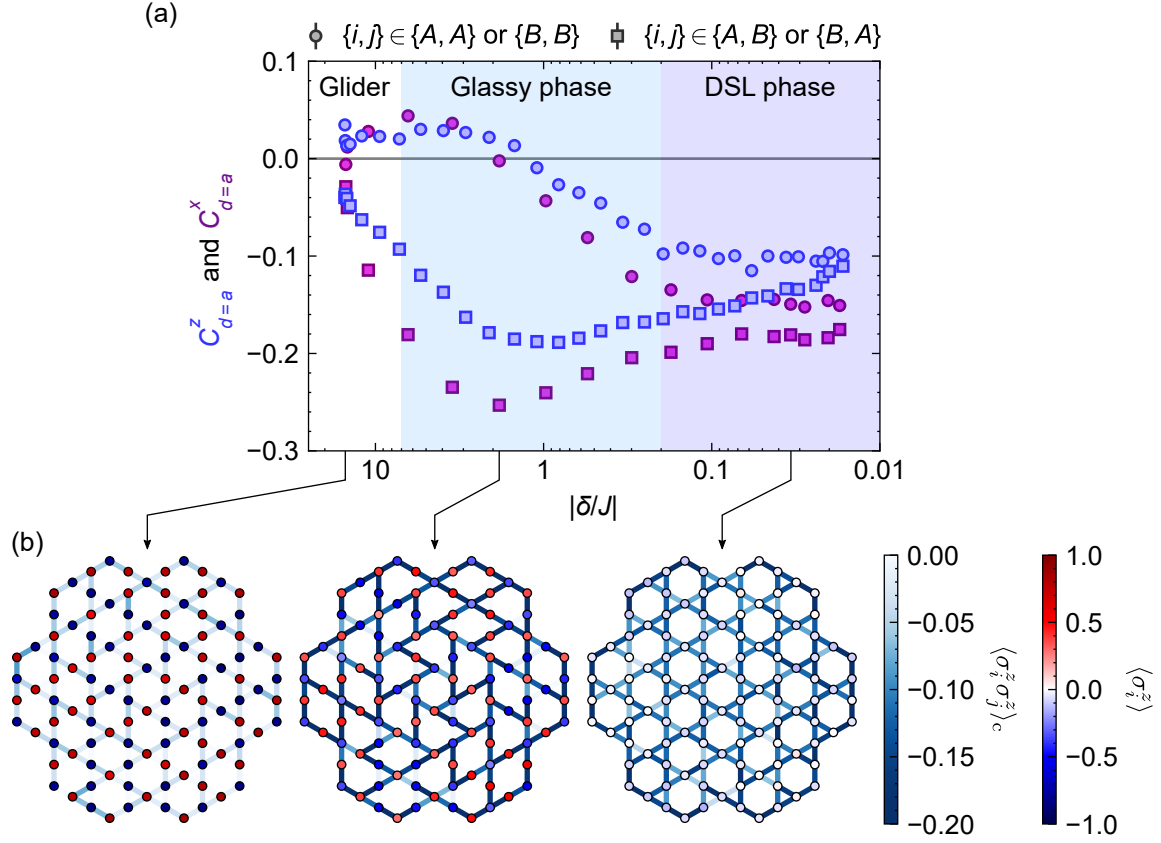
Figure 6.4: Phase transitions from the Glider state to the DLS state. (a) Average nearest neighbour correlations measured along z (blue curves) and x (purple curve) as a function of δ. The circle/square marker data shows the average performed on the nearest neighbour pairs whose atoms of the pairs belong to the same sub-array: either both in A or B (circle markers) or to different sub-array (square markers). We identify three phases: the glider state, the glassy phase and the DSL phase. The background colours are a guide to the eye to represent these different phases. (b) For each phase, we represent the z magnetization $\langle \sigma_i^z \rangle$ of each atom (coloured circles) and the connected nearest neighbours correlation $\langle \sigma_i^z \sigma_j^z \rangle_c$ of each pair (coloured bonds). The data shown in this figure has been taken with assembled arrays containing at most three defects allowed.

are not spin liquids. However, building a quantum superposition of a broad distribution of different VBSs erases these symmetries and can lead to long-range entanglement, producing a spin liquid [Balents, 2010; Zhou, Kanoda, and Ng, 2017]. These states are refereed as Resonating Valence Bond (RVB) in the literature [Anderson, 1973]. This RVB state would correspond to $\propto |\text{⦾}\rangle + |\text{⦾}\rangle$ for the hexagon configuration.

During the ramp down of δ, DMRG simulations performed by the Harvard team on smaller system sizes, predict that the systems should cross two phase transitions.

The first occurs at relatively high values of $|\delta/J|$ and connects the glider state to the glassy phase. As we start to decrease $|\delta/J|$, the addressed atoms in $|\downarrow\rangle$ start to couple to the non-addressed one in $|\uparrow\rangle$ leading to antiferromagnetic bonds. In the meantime, the atoms from the same sub-array (either A or B) remain uncorrelated. We can intuitively represent this state as a superposition of specific VSBs only coupling the atoms from A to the one in B via nearest neighbour $|\!\circ\!\!-\!\!\circ\rangle$ bonds. Although the state already exhibits a high degree of entanglement, it is not yet a spin liquid since it breaks the rotational and translation symmetry. We call this phase the *glassy phase*. As we continue to decrease δ, the second transition occurs; the glassy phase melts into the DSL with uniform correlations between all the nearest neighbour pairs, thus recovering the rotational and translation symmetries.

To experimentally identify these different phases, we plot in Fig. 6.4a the correlations averaged over all nearest neighbour pairs whose atoms belong to the same sub-array (circle markers) or different sub-array (square markers). We measure the correlations along x (purple data) and along z (blue data). To better highlight these phase transitions, we also plot in Fig. 6.4b the magnetization $\langle \sigma_i^z \rangle$ of each atom (coloured circles) and the nearest neighbour correlation $\langle \sigma_i^z \sigma_j^z \rangle_{\mathrm{c}}$ measured along z (coloured bonds) at different stages of the ramp: glider, glassy and DSL phase. In both basis, the data exhibit similar behaviour. At high $|\delta/J|$ values, we measure almost no correlations which is expected for the glider being a product state. We attribute the residual non-zero correlation to the effect of the XY interactions during the glider state preparation (see Sec. 3.2 in Chapter 3 for more details). As we ramp down the addressing field intensity, negative correlations between atoms from different sub-arrays build up while atoms from the same sub-arrays remain uncorrelated. As expected, as we continue to decrease δ, we enter the DSL phase, and these correlations homogenize, reaching a steady value of ≈ -0.11 along z and ≈ -0.16 along x. We notice that the correlations are still not perfectly uniform between each pair. We attribute part of this imperfection to edge effects (the correlations on the edges are slightly higher) and to static positional disorder (that we discussed in Sec. 4.3.2 of Chapter 4) that may favour the formation of some specific VSBs.
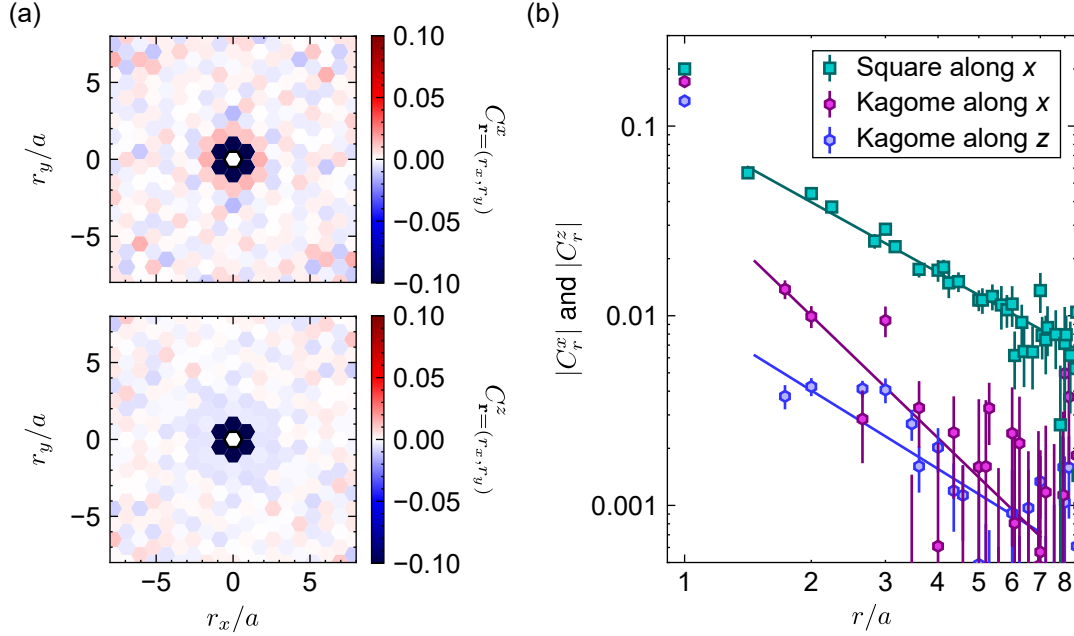
Figure 6.5: Correlation as a function of the distance. (a) Maps of correlation function $C^x_{\mathbf{r}=(r_x,r_y)}$ and $C^z_{\mathbf{r}=(r_x,r_y)}$ at the end of the ramp. (b) Absolute values of the average correlations $|C^x_r|$ and $|C^z_r|$ measured along x and z as a function of the distance r between two atoms. The data shown by hexagon markers show the data for the Kagome $N = 114$ atoms array. The square markers represents the data measured along x for an AFM state using a $N = 10 \times 10$ atoms square array. The data shown is this figure has been taken with assembled arrays containing at most three defects.

6.1.2 Properties of the ground state

We now focus on the main properties of the state we prepare at the end of the ramp ($|\delta/J| \approx 0.03$) in the DSL phase.

A disordered phase. We first analyze the magnetization. As shown in Fig. 6.4b, the z magnetization of each atom in the DSL phase is at zero. The state does not exhibit classical magnetic order, which is consistent with the RVB spin liquid ansatz. However, this lack of magnetization is not enough to distinguish this state from another non-liquid state; for example, the AFM/FM ground states on square geometries share this same property and are not spin liquids.

We now look at the two body correlation functions. Figure 6.5a shows the map of correlation $C^{x,z}_{\mathbf{r}=(r_x,r_y)}$ (already defined in Eq. 5.8) measured along x and z. In both basis, the state exhibits relatively strong nearest neighbour correlations. Going to the

next-nearest neighbour, we distinguish positive/negative correlations along x/z. As we increase further the distance $\mathbf{r} = r_x\mathbf{u}_x + r_y\mathbf{u}_y$, the amplitude of the correlations quickly decay towards zero. This behaviour is different from what we expect for the AFM ground state of square arrays which exhibits (at $T = 0$) a AFM long-range order along x. To better analyze this difference, we plot in Figure 6.5b the average of the correlations $|C_r^{x,z}|$ as a function of the distance $|\mathbf{r}| = r$ (already defined in Eq. 5.9). The $|C_r^{x,z}|$ correlations (purple and blue curves) quickly decrease and after a few lattice sites reaching the noise floor after $r/a \sim 4$,. As a guide to the eye, the solid curves show power-law fits $|C_r^{x,z}| \propto r^\beta$ with exponent parameters of $\beta \approx -1.4$ along z and $\beta \approx -2.1$ along x (we believe these fits are too hazardous to conclude anything for them).

For comparison, using the same experimental parameters, we now prepare the AFM ground state of a square array with a similar size of $N = 10 \times 10$ atoms and plot the correlation $|C_r^x|$ as a function of r (green curve). At a distance of $r/a = 1$, the square array exhibit a correlation value similar to the one measured with the Kagome array. For higher distances, the correlations decrease, but in contrast with the kagome array this decay is very slow. For long distances $r/a > 4$, we still measure non zero correlation. This comparative measurement between the Kagome and square configuration illustrates that for similar system size, the choice of the geometry can significantly alter the properties of the XY ground state. The square geometry is insufficiently frustrated, allowing the emergence of long-distance AFM correlations. In contrast, the highly frustrated Kagome geometry prevents both spin-ordering and long-range correlations.

In summary, the phase that we prepare does not exhibit any magnetization. Moreover, the frustration induced by the geometry leads to a fast decay of the correlations with the distance, suggesting that this state does not possess any apparent magnetic order. A lack of order is a good indication of a spin liquid but is not a sufficient condition to prove it [Savary and Balents, 2016]. Spin liquids are also characterized by a high level of entanglement.

Entanglement.   We now try to detect entanglement in the system (the analysis I will now describe has been inspired by the spin squeezing project presented in Chapter 7). To do so, we compute the variance $\mathrm{Var}(M^{x,y,z})$ of every average magnetization $M^{x,y,z} = \sum_i \sigma_i^{x,y,z}/N$ measured along the x, y and z axis. It has been shown in [Tóth
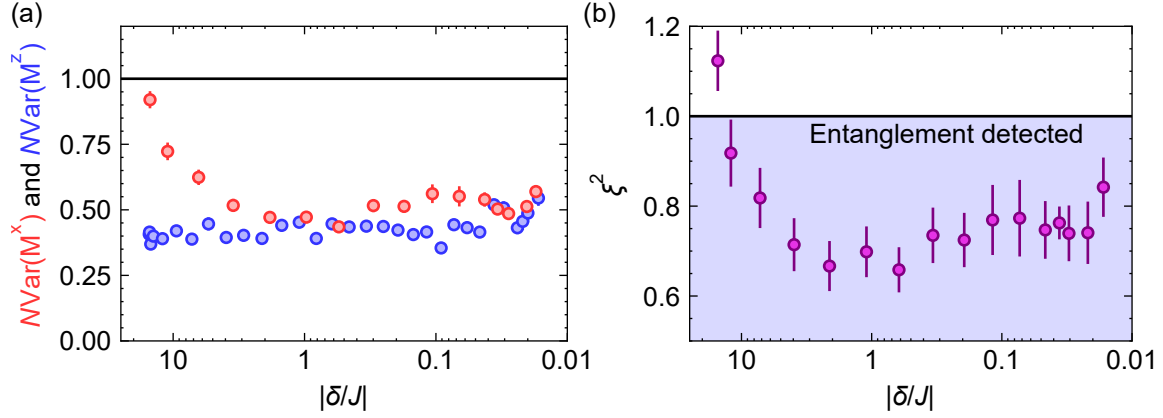
Figure 6.6: Detection of entanglement. (a) Evolution of $N\text{Var}(M^x)$ and $N\text{Var}(M^z)$ as a function of δ during the ramp down. (b) Evolution of ξ^2 (see Eq. 6.2) as a function of δ. We did not measure the full curve of $N\text{Var}(M^y)$ as a function δ. Since $\mathcal{H}_{\text{XY}} + \mathcal{H}_{\text{Z}}$ exhibits a $U(1)$ symmetry, we assume that $N\text{Var}(M^x) = N\text{Var}(M^y)$ to compute ξ^2. The data shown is this figure has been taken with assembled arrays with at most three defects allowed.

et al., 2009] that entanglement is detected if the following inequality is satisfied:

$$\xi^2 = \frac{N\text{Var}(M^x) + N\text{Var}(M^y) + N\text{Var}(M^z)}{2} < 1 \,, \tag{6.2}$$

with ξ^2 the entanglement witness. This entanglement witness is particularly well appropriate for detecting entanglement in a state formed of VBSs. For the RVB state or just for a single VBS state, we expect $N\text{Var}(M^{x,y,z}) = 0$ and thus $\xi^2 = 0$ [Tóth and Mitchell, 2010]. In comparison, for the glider state, we have $N\text{Var}(M^z) = 0$, and $N\text{Var}(M^x) = N\text{Var}(M^y) = 1$ and recover $\xi^2 = 1$. Figure 6.6a shows the evolution of $N\text{Var}(M^x)$ and $N\text{Var}(M^z)$ as a function of the δ during the adiabatic preparation. As expected $N\text{Var}(M^x)$ starts around ≈ 1, and as we reduce $|\delta/J|$, $N\text{Var}(M^x)$ decreases down to ≈ 0.5 while $N\text{Var}(M^z)$ remain constant around ≈ 0.45. Due to experimental imperfections $N\text{Var}(M^x)$ and $N\text{Var}(M^z)$ reach non-zero values at the end of the ramp. From these curves, we now compute ξ^2 (we did not take the measurement along y, so to compute ξ^2, we use the fact that since $\mathcal{H}_{\text{XY}} + \mathcal{H}_{\text{Z}}$ exhibits a $U(1)$ symmetry, we assume that $N\text{Var}(M^x) = N\text{Var}(M^y)$). Figure 6.6b shows ξ^2 as a function of δ. Similarly to $N\text{Var}(M^x)$, ξ^2 starts around one and decreases below one as we ramp down δ indicating that entanglement is detected. Once again, due to experimental imperfections, ξ^2 does not reach a zero value and saturates at $\xi^2 \approx 0.75$. This analysis shows that the state we prepare is entangled. However, this criteria does not provide

more information about the structure of entanglement, and it does not allow us to discriminate between a spin liquid state and another state that is not one. For example, running the same analysis on the AFM ground state data of square arrays we presented in the previous chapter (analysis not shown here) also leads to the detection of entanglement whereas this state is not a spin liquid.

This study of the entanglement is only a first step toward a more in-depth investigation of this entanglement. The Harvard team is currently studying observables based on many-body correlation functions to better characterize the phase we prepare.

6.1.3 Friedel oscillations

Friedel oscillations. The spin liquids are also characterized by their exotic excitation spectrum. Using the *parton theory* approach [Savary and Balents, 2016], one can re-express the dipolar XY Hamiltonian in terms of fermionic operators $\sigma_i^+ = f_{i,\uparrow}^\dagger f_{i,\downarrow}$ and $\sigma_i^- = f_{i,\downarrow}^\dagger f_{i,\uparrow}$ with $f_{i,\{\uparrow,\downarrow\}}$ and $f_{i,\{\uparrow,\downarrow\}}^\dagger$ being the annihilation and creation operator acting on fermionic excitations named *spinons* and $n_{i,\{\uparrow,\downarrow\}} = f_{i,\{\uparrow,\downarrow\}}^\dagger f_{i,\{\uparrow,\downarrow\}}$ the number operator [Auerbach, 1994]. We can then insert this representation into the spin Hamiltonian, apply the single occupancy constraint $n_{i,\uparrow} + n_{i,\downarrow} = 1$ and treat the result within the mean field approximation theory. This theoretical framework is very effective for studying and characterizing various spin liquids [Savary and Balents, 2016]. DSLs states are characterized by Dirac spinon excitations whose band structures exhibit two Dirac cones located at $\mathbf{k} = \pm(\pi/(2\sqrt{3}), \pi/2)$ in the Brillouin zone [Hermele *et al.*, 2008; Meng *et al.*, 2010; He *et al.*, 2017; Zhu *et al.*, 2018]. Being able to probe this excitation spectrum would be a positive signature of a DSL. One way to do it, is to insert a local impurity in the system. This impurity would scatter the spinons between the two Dirac points and thus potentially induce a Friedel oscillation response that we can measure. More theoretical details are given in [Bintz *et al.*, 2024].

Experimental realization. To produce Friedel oscillations, we apply the following procedure. From the Glider state, we ramp down δ to prepare the DSL but now apply an additional local light-shift δ_{loc} on one of the atoms of the array (shown with a black cross in Fig. 6.7a). The light-shift on this perturbed atom reads $\delta(t) = \delta_0 e^{-t/\tau} + \delta_{\mathrm{loc}}$ while the light-shift on the other addressed atoms remain $\delta(t) = \delta_0 e^{-t/\tau}$. We produce this extra light shift by focusing an independent addressing beam on the atom to
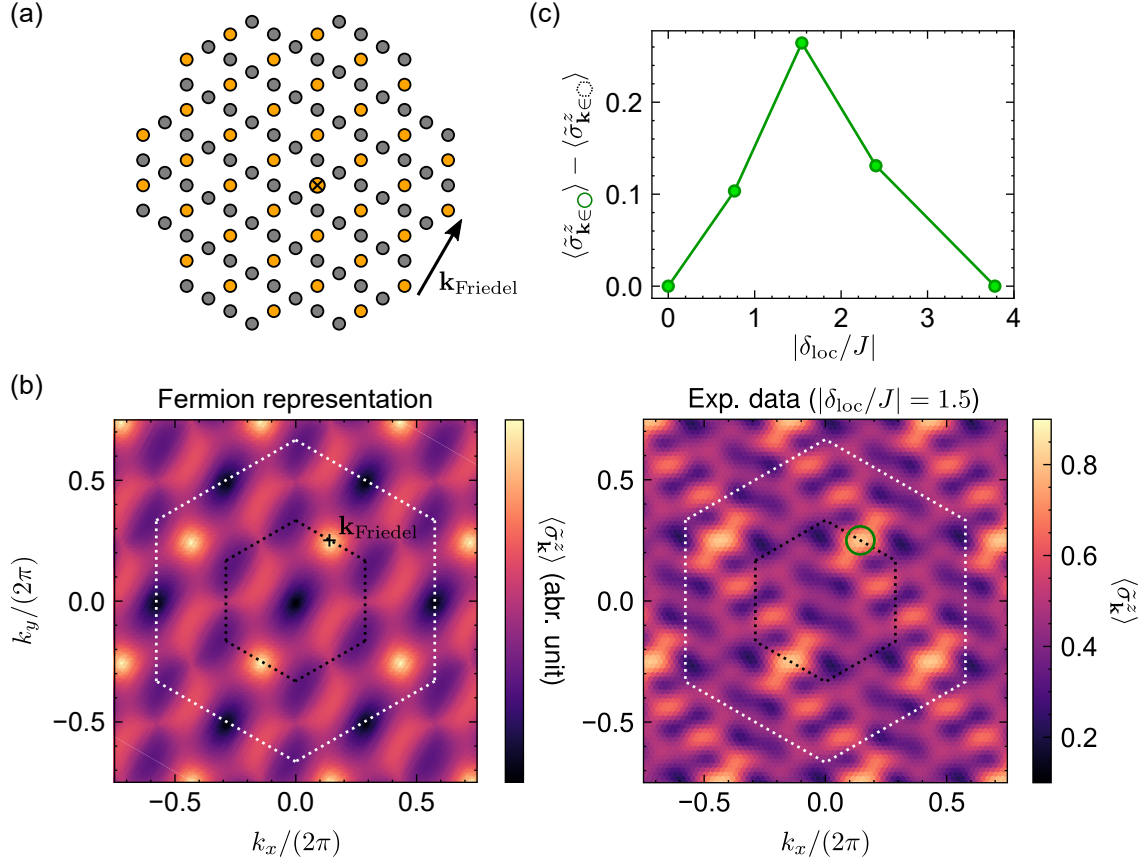
Figure 6.7: Friedel oscillations. (a) To observe Friedel oscillations, we plot $\langle \tilde{\sigma}^z_{\mathbf{k}} \rangle$ restricting ourselves to the sub-array showed by yellow circles. The circle with a black cross shows the position of the local perturbation and $\mathbf{k}_{\mathrm{Friedel}}$ represents the propagation of the Friedel oscillations. (b) Results obtained using the free fermionic representation, $\langle \tilde{\sigma}^z_{\mathbf{k}} \rangle$ exhibits a peaks at $\mathbf{k} = \pm(\pi/(2\sqrt{3}), \pi/2)$ corresponding to Friedel oscillations. The black dashed line hexagon shows the Brillouin zone and the white shows an extended Brillouin zone. (c) Bottom: Experimental results measured for $|\delta_{\mathrm{loc}}/J| = 1.5$. Top: Averaged value of $\langle \tilde{\sigma}^z_{\mathbf{k}} \rangle$ in the green circle minus the averaged value in the black hexagon as a function of $|\delta_{\mathrm{loc}}/J|$.

which we wish to apply the local perturbation. At the end of the ramp ($|\delta/J| \approx 0.04$), we measure the state of the system along z. We repeat the experiment for various values of the perturbation strength δ_{loc} and then compute the averaged 2D Fourier transform of the magnetization defined as:

$$\langle \tilde{\sigma}^z_{\mathbf{k}} \rangle (\delta_{\mathrm{loc}}) = \sum_j e^{i \mathbf{r}_j \cdot \mathbf{k}/a} \left[\langle \sigma^z_j \rangle (\delta_{\mathrm{loc}}) - \langle \sigma^z_j \rangle (\delta_{\mathrm{loc}} = 0) \right] \tag{6.3}$$

with $\mathbf{r}_j$ the position of atom j and $\langle \sigma^z_j \rangle (\delta_{\mathrm{loc}}) - \langle \sigma^z_j \rangle (\delta_{\mathrm{loc}} = 0)$ the extra z-magnetization measured on atom j at the end of the ramp induced by the local perturbation of

strength δ_{loc}. We expect to observe the Friedel oscillations at locations $\pm(\pi/(2\sqrt{3}), \pi/2)$ in the Brillouin zone. In real-space, it corresponds to an oscillation period of $2\sqrt{3}a$ along the direction $\mathbf{k}_{\mathrm{Friedel}}$ shown in Fig. 6.7a. It turns out that the Harvard team showed that one way to isolate the Friedel signal and thus to maximize our chance to observe it, is to consider the sub-array shown by the yellow circles in Fig. 6.7 where all these atoms are all separated along $\mathbf{k}_{\mathrm{Friedel}}$ by a multiple of half the Friedel oscillation period. We now restrict the sum in Eq. 6.3 to the atoms belonging to this sub-array. Following this analysis method, the Harvard team calculated the Friedel response expected at $|\delta_{\mathrm{loc}}/J| \sim 0.3$ using a free fermion model on a large Kagome cluster of more than $N = 2000$ sites [Bintz *et al.*, 2024]. The results are shown in Fig. 6.7b. We observe that $\langle \tilde{\sigma}_{\mathbf{k}}^z \rangle$ reaches a peak located at $\mathbf{k} = \pm(\pi/(2\sqrt{3}), \pi/2)$ signature of Friedel oscillations.

We now turn to the experimental data. The bottom panel in Fig. 6.7c shows $\langle \tilde{\sigma}_{\mathbf{k}}^z \rangle$ measured for a local perturbation of $|\delta_{\mathrm{loc}}/J| = 1.5$. As for the fermionic representation, the system exhibits a signal at $\mathbf{k} = \pm(\pi/(2\sqrt{3}), \pi/2)$, which is consistent with the existence of Friedel oscillations. However, this signal strongly depends on the amplitude of the perturbation. The top panel of Fig. 6.7c shows the average Friedel signal denoted $\langle \tilde{\sigma}_{\mathbf{k} \in \bigcirc}^z \rangle$ (average of $\langle \tilde{\sigma}_{\mathbf{k}}^z \rangle$ inside the green circle) to which we subtract the background signal denoted $\langle \tilde{\sigma}_{\mathbf{k} \in \bigcirc}^z \rangle$ (average of $\langle \tilde{\sigma}_{\mathbf{k}}^z \rangle$ inside the black dashed line hexagon) as a function of $|\delta_{\mathrm{loc}}/J|$. As we increase the perturbation strength, $\langle \tilde{\sigma}_{\mathbf{k} \in \bigcirc}^z \rangle - \langle \tilde{\sigma}_{\mathbf{k} \in \bigcirc}^z \rangle$ increases, reaches a maximum around $|\delta_{\mathrm{loc}}/J| \approx 1.5$ and decreases back for larger values. The signal seems to appear only for a specific range of $|\delta_{\mathrm{loc}}/J|$ values. Theoretical and experimental investigations are still in progress to understand this behaviour.

Conclusion about the DSL. In conclusion, I now answer the question: is the state that we prepare a spin liquid? The honest answer is that we do not know. We showed that the phase we prepared looks disordered with no apparent magnetic order but exhibits entanglement. We also showed that by introducing a perturbation in a system, we observe a response consistent with Friedel oscillations predicted by the spinon picture. Although all these observed features are compatible with the behaviour of a DSL state, further investigations are required to characterize this phase. On the theoretical side, additional studies are conducted to understand the DSL phase better and find relatively simple observables (simple in the sense that we can measure them experimentally) that provide a positive signature of the DSL. On the experimental front, further analyses are required to assess the effects of the

experimental imperfections on the state we prepare. In particular, considerable efforts are being made to reduce both shot-to-shot and static positional disorder (using cooling procedures as explained in Sec. 2.2.1, and correcting the position of the atoms as detailed in Chapter 4), which we believe are particularly detrimental to the formation of DSLs.

6.2 Probing chiral spin liquids

In this section, we turn to a second type of spin liquids called Chiral Spin Liquid (CSL) states [Kalmeyer and Laughlin, 1987; Baskaran, 1989; Wen, Wilczek, and Zee, 1989]. In contrast to DSL states, CSLs are gapped phase that spontaneously break the *time reversal symmetry* and exhibit topological order characterized by chiral edge states [Wen, 1991]. Theoretical works already predicted that frustrated geometry could lead to a CLS. For example, the ground state of the Heisenberg model on Kagome geometries is a good candidate [Messio, Bernu, and Lhuillier, 2012; He, Sheng, and Chen, 2014]. Recently, the Harvard team pointed out that using the dipolar XY model with a modified Kagome geometry called *breathing Kagome*, the AFM ground state is also predicted to be a CSL. Figure 6.8 shows different breathing Kagome configurations whose nature of the ground state depends on the breathing parameter β defined in the figure. For $\beta \approx 1.5$ the state is predicted to be a CSL. Inspired by these results, the Harvard contacted us to experimentally explore how to experimentally prepare and characterize a CSL. This project is still ongoing, and I will summarize our preliminary results in this section. Part of these results have been published in [Bornet *et al.*, 2024]. In this section all the experiment were performed using the following parameters: $a = 12.3\,\mu s$, $J/(2\pi) = -0.82(1)\,\mathrm{MHz}$, $|\uparrow\rangle = \left|60S_{1/2}, m_J = 1/2\right\rangle$ and $|\downarrow\rangle = \left|60P_{1/2}, m_J = -1/2\right\rangle$.

6.2.1 Minimalistic system of six atoms

Signature of a CSL state.   One way to identify a CSL is to show that the state spontaneously breaks the time-reversal symmetry [Wen, 1991]. This can be achieved by measuring non-zero chiralities of each elementary triangle of the array. For three spin i, j and k, the chirality is defined as $\chi_{ijk} = (\boldsymbol{\sigma}_i \times \boldsymbol{\sigma}_j) \cdot \boldsymbol{\sigma}_k$, with $\boldsymbol{\sigma}_i = \sigma_i^x \boldsymbol{x} + \sigma_i^y \boldsymbol{y} + \sigma_i^z \boldsymbol{z}$ [Tsomokos *et al.*, 2008]. The chirality operator can be expressed as the sum of six
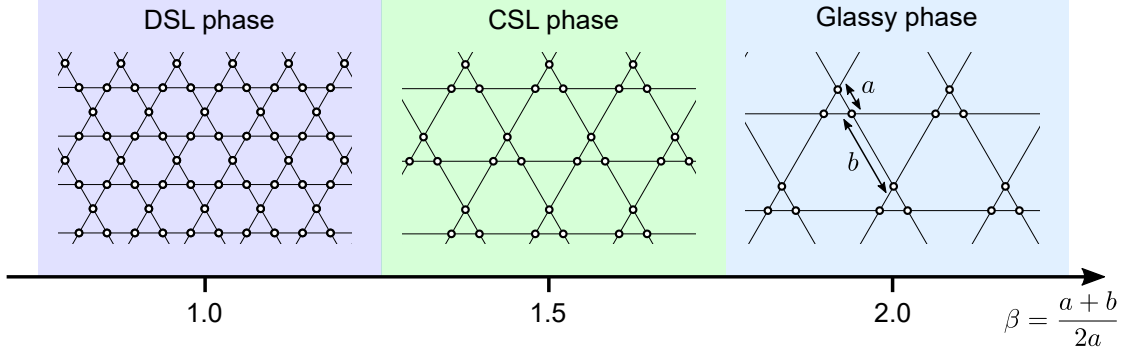
Figure 6.8: Sketch of the breathing Kagome phase diagram. Different breathing Kagome geometries and there respective AFM ground state as a function of the breathing parameter β.

observables $\chi_{ijk} = \sigma_i^x \sigma_j^y \sigma_k^z - \sigma_i^x \sigma_j^z \sigma_k^y + \sigma_i^y \sigma_j^z \sigma_k^x - \sigma_i^y \sigma_j^x \sigma_k^z + \sigma_i^z \sigma_j^x \sigma_k^y - \sigma_i^z \sigma_j^y \sigma_k^x$ that each can be measured independently. However, measuring these terms is not straightforward since it requires performing local rotations before the readout. In Sec. 3.3.1 of Chapter 3, I show how we perform arbitrary local rotations by applying different light-shift intensities on different atoms combined with global microwave pulses. In particular, we showed that measuring the chirality of three interacting atoms in a triangle is possible. Therefore, we decided, as a first study, to apply this method to a minimalistic system of two facing triangles as illustrated in Fig. 6.9a and try to measure the relevant observables needed to identify a CSL states. I will first theoretically study its ground state and explain how we experimentally prepare and characterize it.

Effective spin model. To understand the ground state of a system composed of two interacting triangles, we can decompose the dipolar XY Hamiltonian in two terms. The first one describes the interactions within each triangle, and the second describes the interactions between two triangles. Let us focus on the first part. For three interacting spins i, j and k in an equatorial triangle configuration, the XY Hamiltonian reads:

$$\mathcal{H}_{\mathrm{XY}}^{\triangle} = \frac{\hbar J}{2} \left(\sigma_i^x \sigma_j^x + \sigma_j^x \sigma_k^x + \sigma_i^x \sigma_k^x + \sigma_i^y \sigma_j^y + \sigma_j^y \sigma_k^y + \sigma_i^y \sigma_k^y \right). \tag{6.4}$$

We now use the chirality identity $\chi_{ijk}^2 = 15 - (\boldsymbol{\sigma}_i + \boldsymbol{\sigma}_j + \boldsymbol{\sigma}_k)^2$ to rewrite the Hamiltonian as follow:

$$\mathcal{H}_{\mathrm{XY}}^{\triangle} = \frac{\hbar J}{4} \left(9 - \left(\sigma_i^z + \sigma_j^z + \sigma_k^z \right)^2 - \chi_{ijk}^2 \right). \tag{6.5}$$
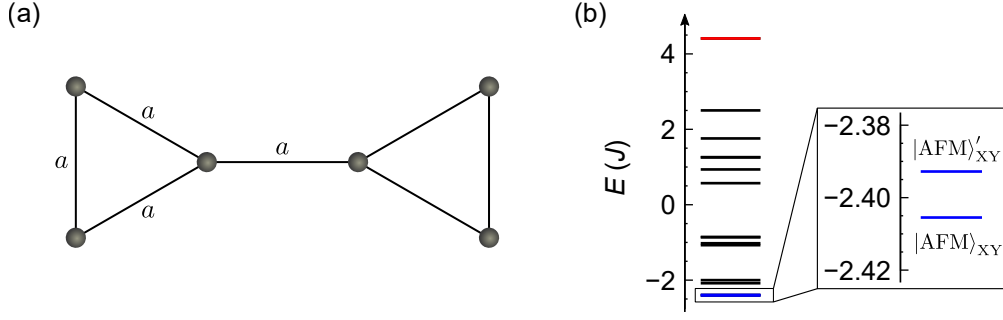
147

Figure 6.9: Energy diagram of a minimalistic system of six spins. (a) Minimalistic system of two triangles facing each other. (b) Energy diagram in the $NM^z = -2$ sector.

The first term of this equation is just an offset energy and thus can be ignored. The second term $\left(\sigma_i^z + \sigma_j^z + \sigma_k^z\right)^2$ corresponds to the z-magnetization sector and the third one χ_{ijk}^2 correspond to the chirality operator squared. As these two terms commute $\left(\left[\left(\sigma_i^z + \sigma_j^z + \sigma_k^z\right)^2, \chi_{ijk}^2\right] = 0\right)$, any eigenstates of $\mathcal{H}_{\text{XY}}^\triangle$ are defined by the eigenvalues of these two operator. We now restrict ourselves to states with a total z magnetization of $\sigma_i^z + \sigma_j^z + \sigma_k^z = -1$. The chirality operator χ_{ijk} has three eigenvalues 0 and $\pm 2\sqrt{3}$. They correspond to the following eigenstates $|W\rangle = (|\uparrow\downarrow\downarrow\rangle + |\downarrow\uparrow\downarrow\rangle + |\downarrow\downarrow\uparrow\rangle)/\sqrt{3}$ and the two chiral states $|\chi^\pm\rangle = \left(|\uparrow\downarrow\downarrow\rangle + e^{\pm i2\pi/3}|\downarrow\uparrow\downarrow\rangle + e^{\pm i4\pi/3}|\downarrow\downarrow\uparrow\rangle\right)/\sqrt{3}$. When $J > 0$, in order to minimize the energy, one would intuitively maximize χ_{ijk}^2 by placing the system in $|\chi^\pm\rangle$ or in a superposition of both. We now add the interaction $H_{\text{XY}}^{\triangle\triangle'} = \frac{\hbar J}{2} \sum_{i\in\triangle} \sum_{j\in\triangle'} \frac{a^3}{r_{ij}^3} \left(\sigma_i^x \sigma_j^x + \sigma_i^y \sigma_j^y\right)$ between two different triangles $\triangle$ and $\triangle'$. The total Hamiltonian thus reads $\mathcal{H}_{\text{XY}} = H_{\text{XY}}^\triangle + H_{\text{XY}}^{\triangle'} + H_{\text{XY}}^{\triangle\triangle'}$. As the triangles are more separated than the lattice spacing a, the interaction strength of $H_{\text{XY}}^{\triangle\triangle'}$ is, on average, lower than the ones within a triangle and, therefore, can be treated using the perturbation theory. Thus, it leads to terms coupling the different chiralities of each triangle (I will not detail these calculations that are rather complicated and can be found in [Norman Yao's team in Harvard]). Good ansätze for the AFM ground state of two weakly interacting triangles are Bell-like states of chiralities defined as $\left|\Phi_\theta^+\right\rangle = \left(\left|\chi_\triangle^+ \chi_{\triangle'}^+\right\rangle + e^{i\theta}\left|\chi_\triangle^- \chi_{\triangle'}^-\right\rangle\right)/(3\sqrt{2})$ or $\left|\Phi_\theta^-\right\rangle = \left(\left|\chi_\triangle^+ \chi_{\triangle'}^-\right\rangle + e^{i\theta}\left|\chi_\triangle^- \chi_{\triangle'}^+\right\rangle\right)/(3\sqrt{2})$. We now compare these ansätze to the ground state. As illustrated in Fig. 6.9b, calculations show that the system has two ground states quasi-degenerated that we will call $|\text{AFM}\rangle_{\text{XY}}$ and $|\text{AFM}\rangle'_{\text{XY}}$. From these calculations, we compute overlaps of $\left\langle \Phi_{\pi/3}^+ \middle| \text{AFM}\right\rangle_{\text{XY}} \approx 86\,\%$ and $\langle\Phi_\pi^-|\text{AFM}\rangle'_{\text{XY}} \approx 86\,\%$ which indicates that the ansätze describe well the ground states.

For both ansätze, the mean chirality of each triangle $\langle\chi_{ijk}\rangle$ is zero. The spontaneous

breaking of the time-reversal symmetry is thus only revealed by measuring the connected chiral-chiral correlation[1] between the two triangles defined as

$$\langle \chi_{ijk} \chi_{i'j'k'} \rangle_{\text{c}} = \langle \chi_{ijk} \chi_{i'j'k'} \rangle - \langle \chi_{ijk} \rangle \langle \chi_{i'j'k'} \rangle, \tag{6.6}$$

with χ_{ijk} the chirality of the first triangle and $\chi_{i'j'k'}$ the chirality of the second. For the Ansätze states this value reaches $\langle \chi_{ijk} \chi_{i'j'k'} \rangle_{\text{c}} = \pm(2\sqrt{3})^2 = \pm 12$ and for the two ground states, it reaches $\langle \chi_{ijk} \chi_{i'j'k'} \rangle_{\text{c}} \approx \pm 9$. This minimalistic array of six atoms illustrates the underlying key mechanisms leading to a CSL with a larger system size: the chirality of each triangle couples to each other, leading to a chiral long-range order, *i.e.* $\langle \chi_{ijk} \chi_{i'j'k'} \rangle_{\text{c}}$ reaches a non-zero value when the distance between the triangle goes to infinity [Norman Yao's team in Harvard].

6.2.2 Measurement of chiral-chiral correlations

We now try to experimentally prepare the ground state of this six-atom system and measure chiral-chiral correlations. To prepare the ground state, we intend to repeat the procedure used for the DSL state (see Sec. 6.1.1): we prepare a Glider state using the addressing beams and adiabatically lower the applied light shifts to connect to the ground state. The issue is that we also wish to use these addressing beams to perform local rotations at the end of the sequence to measure the atoms in different basis. Since we have only one addressing set-up (one addressing laser and one addressing SLM), and since the addressing pattern cannot be changed dynamically during the Rydberg sequence, we must perform the state preparation and measurement with the same addressing pattern. This constraint led us to realize the following experimental sequence.

Ground state preparation. As depicted in Fig. 6.10a, in each triangle, we address one atom with an initial light shift 2δ, one with light shift δ, and one is not addressed (I will now refer to these atoms as the 2δ, 1δ and 0δ atom for the first triangle and as

---

[1] Usually, connected correlations refer to correlations defined via the Ursell functions described in [Kubo, 1962]. For a six-body connected correlation, this definition would require subtracting all the lower-order connected correlations that contribute to the non-connected six-body correlation. When computing the connected chiral-chiral correlation, we only subtract $\langle \chi_{ijk} \rangle \langle \chi_{i'j'k'} \rangle$ from the non-connected 6-body correlation function $\langle \chi_{ijk} \chi_{i'j'k'} \rangle$. The connected chiral-chiral correlation, as it is defined, is thus only "partially" connected according to the Ursell definitions.

the $2\delta'$, $1\delta'$ and $0\delta'$ atom for the second). This configuration allows us to prepare a glider state with the addressed/non-addressed atoms prepared in $|\downarrow\rangle/|\uparrow\rangle$. We then adiabatically decrease the light shift as $\delta(t) = \delta_0 e^{-t/\tau}$ with $\delta_0/(2\pi) = 23\,\mathrm{MHz}$ and $\tau = 0.55\,\mu\mathrm{s}$ (we numerically checked that this ramp speed is adiabatic enough).

The choice of the atoms we address determines the ground state we prepare. Fig. 6.10a and b show two configurations we call a and b. Using symmetry arguments, we can show that configuration a will lead to the preparation of $|\mathrm{AFM}\rangle_{\mathrm{XY}}$ and the b one will lead to $|\mathrm{AFM}\rangle'_{\mathrm{XY}}$. We define $\mathcal{M}$ the mirror symmetry operator along the $\mathbf{u}_y$-axis and $\mathcal{I}$ the inversion symmetry operator around the center point of the array (see Fig. 6.10a and b). Calculations demonstrate that $|\mathrm{AFM}\rangle_{\mathrm{XY}}$ respects the $\mathcal{M}$-symmetry ($\mathcal{M}|\mathrm{AFM}\rangle_{\mathrm{XY}} = +|\mathrm{AFM}\rangle_{\mathrm{XY}}$) and is antisymmetric with $\mathcal{I}$ ($\mathcal{I}|\mathrm{AFM}\rangle_{\mathrm{XY}} = -|\mathrm{AFM}\rangle_{\mathrm{XY}}$) while $|\mathrm{AFM}\rangle'_{\mathrm{XY}}$ is antisymmetric with $\mathcal{M}$ ($\mathcal{M}|\mathrm{AFM}\rangle'_{\mathrm{XY}} = -|\mathrm{AFM}\rangle'_{\mathrm{XY}}$) and respects $\mathcal{I}$ ($\mathcal{I}|\mathrm{AFM}\rangle'_{\mathrm{XY}} = +|\mathrm{AFM}\rangle'_{\mathrm{XY}}$). The glider state of configuration a is symmetric with $\mathcal{M}$. As its corresponding Hamiltonian $\mathcal{H}_{\mathrm{XY}} + \mathcal{H}_{\mathrm{Z}}$ commutes with $\mathcal{M}$ ($[\mathcal{H}_{\mathrm{XY}} + \mathcal{H}_{\mathrm{Z}}, \mathcal{M}] = 0$), the $\mathcal{M}$-symmetry is preserved during the ramp down and thus connects the glider state to $|\mathrm{AFM}\rangle_{\mathrm{XY}}$. Similarly, the glider state of configuration b respects the $\mathcal{I}$ symmetry. As its corresponding Hamiltonian $\mathcal{H}_{\mathrm{XY}} + \mathcal{H}_{\mathrm{Z}}$ commutes with $\mathcal{I}$ ($[\mathcal{H}_{\mathrm{XY}} + \mathcal{H}_{\mathrm{Z}}, \mathcal{I}] = 0$), the adiabatic procedure prepares $|\mathrm{AFM}\rangle'_{\mathrm{XY}}$.

Measurements. As then end of the ramp down, we wish to measure the connected chiral-chiral correlations that can be expressed as the sum of 36 terms:

$$
\begin{aligned}
\langle \chi_{0\delta,1\delta,2\delta}\chi_{0\delta',1\delta',k\delta'}\rangle_{\mathrm{c}} =& \langle\sigma^x_{0\delta}\sigma^y_{1\delta}\sigma^z_{2\delta}\sigma^x_{0\delta'}\sigma^y_{1\delta'}\sigma^z_{k\delta'}\rangle - \langle\sigma^x_{0\delta}\sigma^y_{1\delta}\sigma^z_{2\delta}\rangle\langle\sigma^x_{0\delta'}\sigma^y_{1\delta'}\sigma^z_{k\delta'}\rangle \\
&+ \langle\sigma^y_{0\delta}\sigma^z_{1\delta}\sigma^x_{2\delta}\sigma^y_{0\delta'}\sigma^z_{1\delta'}\sigma^x_{k\delta'}\rangle - \langle\sigma^y_{0\delta}\sigma^z_{1\delta}\sigma^x_{2\delta}\rangle\langle\sigma^y_{0\delta'}\sigma^z_{1\delta'}\sigma^x_{k\delta'}\rangle \\
&+ \langle\sigma^z_{0\delta}\sigma^x_{1\delta}\sigma^y_{2\delta}\sigma^z_{0\delta'}\sigma^x_{1\delta'}\sigma^y_{k\delta'}\rangle - \langle\sigma^z_{0\delta}\sigma^x_{1\delta}\sigma^y_{2\delta}\rangle\langle\sigma^z_{0\delta'}\sigma^x_{1\delta'}\sigma^y_{k\delta'}\rangle \\
&+ \langle\sigma^y_{0\delta}\sigma^x_{1\delta}\sigma^x_{2\delta}\sigma^y_{0\delta'}\sigma^x_{1\delta'}\sigma^z_{k\delta'}\rangle - \langle\sigma^y_{0\delta}\sigma^x_{1\delta}\sigma^z_{2\delta}\rangle\langle\sigma^y_{0\delta'}\sigma^x_{1\delta'}\sigma^z_{k\delta'}\rangle \\
&+ \langle\sigma^x_{0\delta}\sigma^z_{1\delta}\sigma^y_{2\delta}\sigma^x_{0\delta'}\sigma^z_{1\delta'}\sigma^y_{k\delta'}\rangle - \langle\sigma^x_{0\delta}\sigma^z_{1\delta}\sigma^y_{2\delta}\rangle\langle\sigma^x_{0\delta'}\sigma^z_{1\delta'}\sigma^y_{k\delta'}\rangle \\
&+ \langle\sigma^z_{0\delta}\sigma^y_{1\delta}\sigma^x_{2\delta}\sigma^z_{0\delta'}\sigma^y_{1\delta'}\sigma^x_{k\delta'}\rangle - \langle\sigma^z_{0\delta}\sigma^y_{1\delta}\sigma^x_{2\delta}\rangle\langle\sigma^z_{0\delta'}\sigma^y_{1\delta'}\sigma^x_{k\delta'}\rangle \\
&+ \cdots,
\end{aligned}
\tag{6.7}
$$

each having to be independently measured to reconstruct $\langle \chi_{0\delta,1\delta,2\delta}\chi_{0\delta',1\delta',k\delta'}\rangle_{\mathrm{c}}$. As explained in Sec. 3.3.1 of Chapter 3, we can apply arbitrary local rotations on the atoms from the same class, *i.e.* addressed with the same light-shift intensity either 2δ, 1δ or 0δ (non-addressed atoms) which constrains our measurement basis. Two atoms addressed
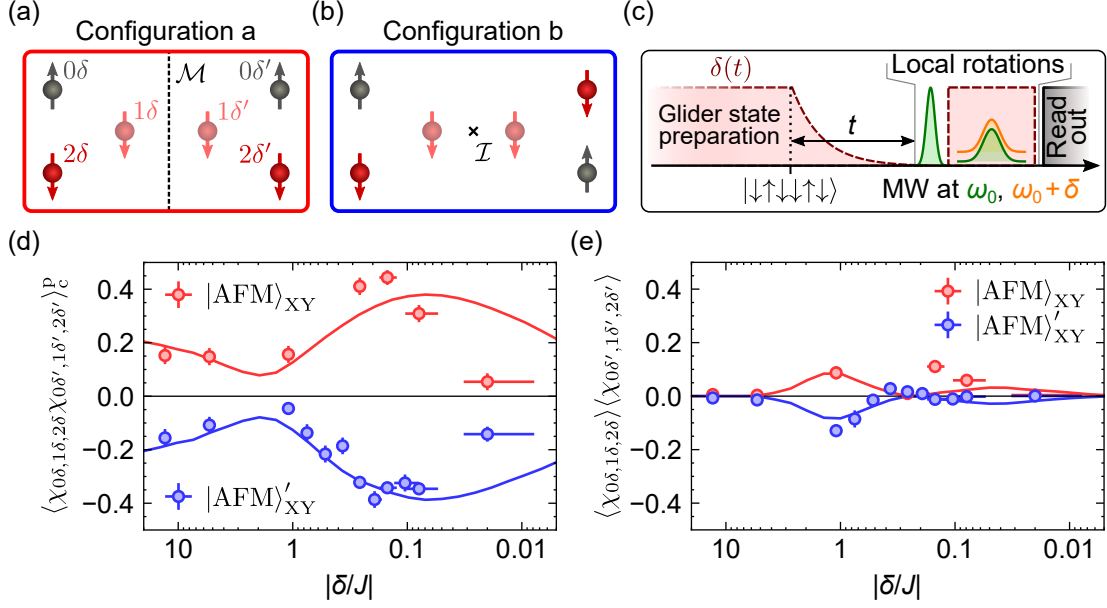
Figure 6.10: Preparation and characterization a six-atom minimalistic system ground state. (a)/(b) Glider state corresponding to configuration a/b. (c) Experimental sequence. (d) Measurement of partial connected chiral-chiral correlations $\langle \chi_{0\delta,1\delta,2\delta} \chi_{0\delta',1\delta',2\delta'} \rangle^{\mathrm{p}}_{\mathrm{c}}$ as a function of δ for the first ground state $|\mathrm{AFM}\rangle_{\mathrm{XY}}$ (red data) and the second one $|\mathrm{AFM}\rangle'_{\mathrm{XY}}$ (blue data). (e) Plot showing the product of the chirality of each triangle $\langle \chi_{0\delta,1\delta,2\delta} \rangle \langle \chi_{0\delta',1\delta',2\delta'} \rangle$. The solid curves represent the simulations performed by the Harvard team.

with the same light shift cannot be measured in different basis. The consequence is that experimentally we can only measure the first six terms of $\langle \chi_{0\delta,1\delta,2\delta} \chi_{0\delta',1\delta',2\delta'} \rangle_{\mathrm{c}}$ shown in Eq. 6.7. It turns out that simulation performed by the Harvard group shows that only this subset of measurements is sufficient to be representative of $\langle \chi_{0\delta,1\delta,2\delta} \chi_{0\delta',1\delta',k\delta'} \rangle_{\mathrm{c}}$. We now call the $\langle \chi_{0\delta,1\delta,2\delta} \chi_{0\delta',1\delta',k\delta'} \rangle^{\mathrm{p}}_{\mathrm{c}}$ the partial connected chiral-chiral correlations corresponding to the sum of the six first terms in in Eq. 6.7. In good approximation we have $\langle \chi_{0\delta,1\delta,2\delta} \chi_{0\delta',1\delta',k\delta'} \rangle^{\mathrm{p}}_{\mathrm{c}} \approx \langle \chi_{0\delta,1\delta,2\delta} \chi_{0\delta',1\delta',k\delta'} \rangle_{\mathrm{c}}/6$. Before presenting the experimental results, I mention the fact that the addressing pattern cannot be dynamically modified during the Rydberg sequence is currently a limitation of the platform. In the future generation of the experiment, multiple addressing lasers and SLMs are envisioned to circumvent this limitation. The ground state preparation and measurement could then be performed with independent addressing patterns, thus unlocking access to all terms of the chiral-chiral correlation.

Figure 6.10c summarizes the experimental sequence. After having prepared the glider state, we adiabatically ramp down δ to reach the ground states, apply the

local rotation sequence (more details are given in Sec. 3.3.1) and finally read out the state of the atoms. Fig.6.10d shows the partial connected chiral-chiral correlations measured during the adiabatic ramp down for the preparation of $|\text{AFM}\rangle_{\text{XY}}$ (red data) and $|\text{AFM}\rangle'_{\text{XY}}$ (blue data). At the beginning of the ramp $|\delta/J| \sim 10$, we observe unexpected non-zero correlations that we attribute to the experimental limitations that I now explain. To perform the local rotation, we need the addressing light shifts to be set at their maximum value. As an AOM controls the light intensity, we thus need to change its rf power from its current value for a given $\delta(t)$ to its maximum value. This change takes $\approx 100\,\text{ns}$. During this transient time, to avoid the addressing light changing the state of the atoms in an uncontrolled way, we switch off the light using an EOM. The system is thus quenched from $\delta(t)$ to $\delta = 0$ and undergoes undesirable dynamics during the transient time before starting the local rotation sequence. During these dynamics, the system starts to build up chiral-chiral correlations that we measure experimentally. This effect is well captured by numerical simulations (solid curves) performed by the Harvard team, which include experimental imperfections (positional disorder, preparation and measurement errors). As we lower $|\delta/J|$, the effect of the undesirable dynamics decreases since the state becomes closer to the XY ground states, which results in a decrease in the chiral-chiral correlations. As we continue to decrease $|\delta/J|$ the system starts to develop correlations. At $|\delta/J| \approx 0.1$, as expected, we measure positive correlations for $|\text{AFM}\rangle_{\text{XY}}$ and negative correlation for $|\text{AFM}\rangle'_{\text{XY}}$ which are consistent with the $\left|\Phi_\theta^\pm\right\rangle$ ansätze described earlier (see Sec. 6.2.1) and in good agreement with the simulations. At low values of light shifts $|\delta/J| < 0.1$, the duration of the ramp is relatively long, and the system starts to suffer from decoherence effects that lead to a reduction of the correlations (mostly induced by shot-to-shot positional disorder). We now focus on the individual chiralities of each triangle. Fig. 6.10e shows with the same ordinate scale the product of the chiralities of each triangle $\langle \chi_{0\delta,1\delta,2\delta} \rangle \langle \chi_{0\delta',1\delta',k\delta'} \rangle$. For both ground states, this observable exhibits small oscillations with relatively low amplitude compared to the chiral-chiral correlations. These measurements demonstrate our ability to measure chiral-chiral correlation and illustrate the pairing mechanism of chiralities between two coupled triangles.

This work constitutes a preliminary study towards the experimental realization and characterization of CSL states. Many efforts and progress remain to be made. First, as mentioned earlier, adding another addressing setup would allow us to measure the full connected chiral-chiral correlation. Second, we need to increase

the system size up to a few $N \sim 100$ atoms to prepare a CSL and be able to measure the chiral-chiral correlation between triangles separated by a long distance. Third, we need to improve the fidelity of the state preparation and multi-basis measurement protocol to perform more precise measurements of the chiral-chiral correlations. For example, in Fig. 6.10d we measure a maximum amplitude of the partial chiral-chiral correlation of $\langle \chi_{0\delta,1\delta,2\delta} \chi_{0\delta',1\delta',k\delta'} \rangle_c^p \approx 0.4$ while ground state calculations predict an amplitude of $\langle \chi_{0\delta,1\delta,2\delta} \chi_{0\delta',1\delta',k\delta'} \rangle_c^p \approx \langle \chi_{0\delta,1\delta,2\delta} \chi_{0\delta',1\delta',k\delta'} \rangle_c / 6 \approx 9/6 = 1.5$. The experimental imperfections reduce the signal strength by a factor $1.5/0.4 \approx 4$, suggesting room for fidelity improvement (see more details in Sec. 3.3.1).

6.3 Conclusion

In this chapter, I have shown our preliminary results towards the experimental study of spin liquids using frustrated geometries. In the first part, I have presented the results of the ground state preparation of a $N = 114$ atoms array which has been predicted to be a DSL. We showed that, as expected, the state does not possess any magnetic order. Using an entanglement witness, we then showed that despite its apparent disorder, the phase we prepare is entangled. Next, we introduced a perturbation in the system and tried to probe its response. We measured spatial oscillations of the magnetization, which are consistent with Friedel oscillations expected for a DSL. We then turn our attention to the chiral spin liquid (CSL) and focused on a simple case of two interacting triangles. We showed our ability to measure (partial) chiral-chiral correlations that are key observables to characterize the CSL state, revealing the spontaneous breaking of the time-reversal symmetry.

Part III.

Non-equilibrium dynamics of the dipolar XY model

Chapter 7

Spin squeezing

Contents

In the previous two chapters, we studied the ground state of the dipolar XY model for various geometries. We now turn to out-of-equilibrium dynamics. Out-of-equilibrium systems can lead to a rich collection of intriguing phenomena, such as exotic spin diffusion behaviours, dynamic phase transitions, unusual thermalization processes and the formation of highly entangled states. This entanglement can be used as a resource for various applications such as quantum cryptography, quantum computing, or quantum metrology. Quantum metrology relies on the use of these entangled states to improve the precision of measurements beyond the standard quantum limit [Giovannetti, Lloyd, and Maccone, 2011]. Over the past decade, the use of squeezed states of light or spin ensembles has evolved from proof-of-principle experiments to applications in several areas of research ranging from gravitational wave detectors [Tse *et al.*, 2019], atom interferometers [Hosten *et al.*, 2016] to optical atomic clocks

[Pedrozo-Peñafiel *et al.*, 2020; Robinson *et al.*, 2022]. For atomic systems, the generation of *scalable* squeezing (*i.e.*, squeezing that improves with the system size) has been demonstrated using a variety of platforms, including trapped ions, atomic ensembles coupled to light, and ultracold gases [Pezzè *et al.*, 2018]. In these platforms, the interactions involved to generate spin-squeezed states exhibit all-to-all couplings. The most commonly used Hamiltonian is the One Axis Twisting model (OAT) defined as $\mathcal{H}_{\mathrm{OAT}} = \hbar J \sum_{i<j} \sigma_i^z \sigma_j^z$ [Kitagawa and Ueda, 1993; Ma *et al.*, 2011]. Before starting this project, no spin system using short-range interactions (namely interactions decaying as $J_{ij} \propto 1/r_{ij}^\alpha$ with $\alpha \geq d$, with d the dimensionality of the system) producing squeezing had been experimentally demonstrated.

However, as pointed out in recent theoretical proposals [Perlin, Qu, and Rey, 2020; Comparin *et al.*, 2022; Comparin, Mezzacapo, and Roscilde, 2022a; Young *et al.*, 2023], ensembles of dipolar XY-interacting spins should also generate scalable spin-squeezing. These proposals are all the more relevant since the dipolar XY model can be naturally implemented in various platforms using ultracold molecules [Yan *et al.*, 2013; Bao *et al.*, 2023; Holland, Lu, and Cheuk, 2023], trapped ions [Monroe *et al.*, 2021], defects in solids [Cai *et al.*, 2013], superconducting qubits [Dalmonte *et al.*, 2015] and Rydberg atoms, thus enlarging the class of systems amenable to squeezing. Furthermore, tweezer-based platforms are particularly interesting for building more accurate clocks, as they allow for the minimization of interaction-induced clock shifts [Madjarov *et al.*, 2019; Young *et al.*, 2020]. Therefore, motivated by the promise to improve this new generation of atomic clocks, we experimentally tried to show that scalable squeezing can be generated using dipolar XY Rydberg interactions. This work has been realized in collaboration with Norman Yao's team at Harvard and Tommaso Roscilde's team in Lyon.

This chapter is organized as follows. In the first section, I will present how to generate and measure spin squeezing using a square array of up to $N = 100$ Rydberg atoms interacting under the dipolar XY model (see Fig. 7.1a). In the second section, I run several analyses to better characterize the squeezed states we produce. Finally, in the third section, I present our preliminary work to go beyond proof-of-principle and develop methods to use these squeezed states for metrological applications. Most of the results presented in this chapter have been published in [Bornet *et al.*, 2023]. For all the results in this chapter, we use the following parameters: $a = 15\,\mu\mathrm{m}$, $J/(2\pi) = -0.25\,\mathrm{MHz}$, $|\!\uparrow\rangle = \left|60S_{1/2}, m_J = 1/2\right\rangle$ and $|\!\downarrow\rangle = \left|60P_{3/2}, m_J = -1/2\right\rangle$.
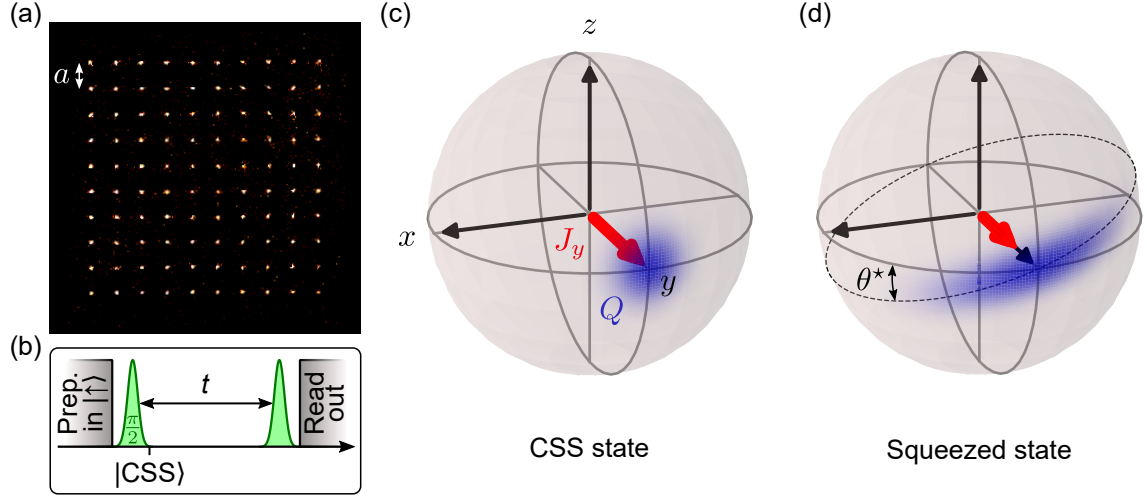
Figure 7.1: Generation of spin squeezing. (a) Fluorescence image of a $N = 10 \times 10$ square array. (b) Sketch of the experimental sequence. (c) representation of the coherent spin state in the generalized Bloch sphere. The red arrow represent the spin length J_y and the blue Q area represents the Husimi Q-distribution. (b) Simulation of a 6×6 square array after an interacting time of $t = 0.250\,\mu$s. The state exhibits squeezing.

7.1 Generation of scalable spin squeezing

In this section, I will first describe our experimental procedure for preparing and characterising spin-squeezed states for a $N = 6 \times 6$ square array. Then, I will present how the amount of squeezing, defined as the Ramsey squeezing parameter, varies with the number of particles, confirming that the dipolar XY model can generate scalable spin squeezing.

7.1.1 A quench experiment to generate squeezing

Experimental sequence. The experimental procedure we follow to produce squeezing is depicted in Fig. 7.1b. We first initialized all the atoms in $|\uparrow\rangle$ and quench the system by applying a microwave $\pi/2$-pulse around x thus preparing a *Coherent Spin State* (CSS) along y denoted $|\rightarrow_y \rightarrow_y \rightarrow_y \rightarrow_y \cdots\rangle = |\text{CSS}_y\rangle$. Figure 7.1c represents this CSS state in the generalized Bloch sphere. We let the system evolve under the XY Hamiltonian for a time t_{XY}. Due to the interactions, the initially isotropic spin

Figure 7.2: Elliptical distribution of the spin fluctuations. Measurement of $\mathrm{Var}\left(J_\theta\right)$ as a function of θ for a 6×6 square array after an interaction time of $t = 0.25\,\mu\mathrm{s}$. Each black/grey circle represents a value of the variance $4\math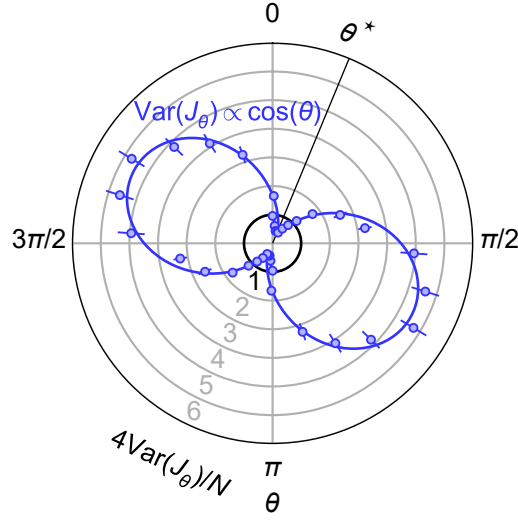rm{Var}\left(J_\theta\right)/N$. For example, the small black circle $4\mathrm{Var}\left(J_\theta\right)/N = 1$ show the Standard Quantum Limit (SQL). The blue curve represents a fit using a cosine function and the black line represents the axis of minimum variance measured at the angle $\theta^\star$.

distribution in the (x, z) plane (shown by the Husimi-Q distribution[1] represented in blue) acquires an elliptical shape, rotated around y by an angle $\theta^\star$ as shown in Fig. 7.1d. Then, we rotate the spins by applying a second microwave pulse and readout the state. The phase and duration of this second pulse can be tuned in order to measure the state along all the different axes of the Bloch sphere. From the measurements, we compute the average and variance of the collective spin operators defined as $J_{x,y,z} = \frac{N}{2}M^{x,y,z} = \frac{1}{2}\sum_i \sigma_i^{x,y,z}$. We define J_θ the collective spin vector in the (x, z) plane perpendicular to the y axis:

$$J_\theta = \cos(\theta)J_z + \sin(\theta)J_x. \tag{7.1}$$

In order to quantify the amount of squeezing we produce, we need to compute

---

[1]The Husimi-Q distribution of a state $|\psi\rangle$ is defined as follow. For a point on the generalized Bloch sphere with spherical coordinate (θ, φ), the Husimi-Q distribution takes as value the overlap $|\langle\psi|\mathrm{CSS}_{(\theta,\varphi)}\rangle|^2$ between the state $|\psi\rangle$ and $\left|\mathrm{CSS}_{(\theta,\varphi)}\right\rangle = \left|\rightarrow_{(\theta,\varphi)}\rightarrow_{(\theta,\varphi)} \cdots \rightarrow_{(\theta,\varphi)}\right\rangle$ being a CSS state pointing along the (θ, φ) direction [Husimi, 1940].

the Ramsey squeezing parameter [Wineland *et al.*, 1992, 1994] defined as:

$$\xi_{\mathrm{R}}^2 = \frac{N \min_\theta \left(\mathrm{Var} \left(J_\theta \right) \right)}{\langle J_y \rangle^2}, \tag{7.2}$$

with $\mathrm{Var} \left(J_\theta \right) = \langle J_\theta{}^2 \rangle - \langle J_\theta \rangle^2$. To do so, for a given interaction time t, we repeat the experiments for various rotation angles θ and identify the one that minimizes the variance. Figure 7.2 shows the evolution of $\mathrm{Var} \left(J_\theta \right)$ as function of θ for a 6×6 square array after an interaction time of $t = 0.25\,\mu\mathrm{s}$. The observed shape of $\mathrm{Var} \left(J_\theta \right)$ is characteristic of an elliptical distribution of the spin fluctuations and allows us to determine $\theta^\star$.

Squeezing in a 6×6 array.   We now study the dynamical evolution of the variance and spin length for a $N = 6 \times 6$ square array. The spin length, given by the measurement of $\langle J_y \rangle$ (red circles on Fig. 7.3a), decays towards zero with increasing interaction time due to the beating of a large number of eigenfrequencies of XY Hamiltonian. During this time, the minimum variance of $J_{\theta^\star}$ (blue circles) initially decreases below the Standard Quantum Limit (SQL), reaches a minimum, and then increases, exceeding the SQL at large times. The solid lines show the numerical simulations (including preparation and detection errors and positional disorder) performed by the Harvard team that are in good agreement with the experimental data. Using the measurements of $\langle J_y \rangle$ and $\mathrm{Var} \left(J_{\theta^\star} \right)$, we can now compute the squeezing parameter ξ_{R}^2 (or $10 \log_{10} \left(\xi_{\mathrm{R}}^2 \right)$ when expressed in dB).

We show in Fig. 7.3b the squeezing parameter as a function of the interaction time. The data indicate that ξ_{R}^2 decreases, reaches a minimum $\xi_{\mathrm{R}}^2{}^\star$ at a time $t^\star$ and increases again. The system remains in a squeezed state (*i.e.* $\xi_{\mathrm{R}}^2 < 1$) only for about $0.5\,\mu\mathrm{s}$ corresponding to $|tJ/(2\pi)| = 0.125$. We measure a minimum squeezing parameter of -2.7 dB. The theory predicts a squeezing of ≈ -6 dB. Part of this discrepancy arises from preparation and detection errors, which modify the values of $\langle J_y \rangle$ and $\mathrm{Var} \left(J_{\theta^\star} \right)$. Including these imperfections in a simulation (purple shadow area) leads to a reasonable agreement with the experimental data. As we squeezing is particularly sensitive to detection errors, we plot the different simulations taking as detection errors $\varepsilon_\uparrow = 1.0 \pm 1.0\,\%$ and $\varepsilon_\uparrow = 2.5 \pm 1.0\,\%$ with a range of $\pm 1\,\%$. This $\pm 1\,\%$ range represents our confidence interval for the estimation of these detection errors.
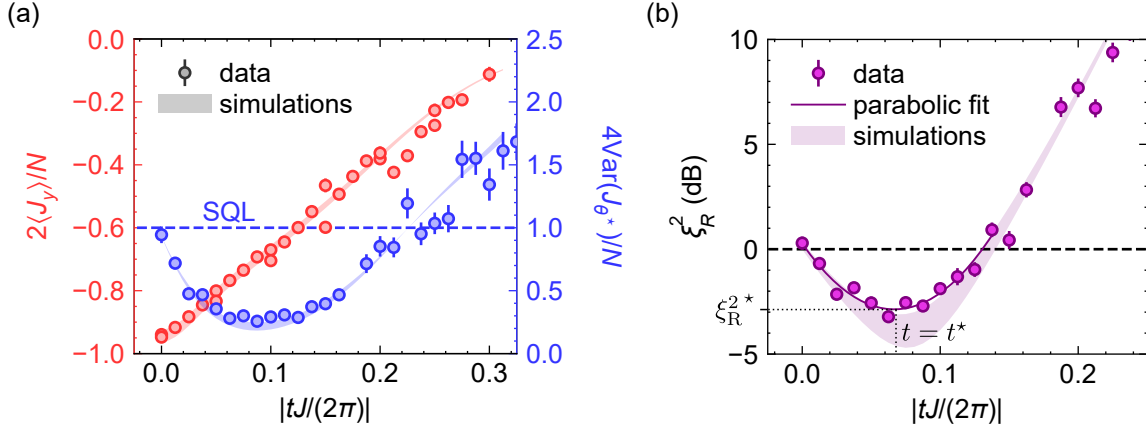
Figure 7.3: Dynamical evolution of the spin length and variance for a $N = 6 \times 6$ square array. (a) Evolution of $\langle J_y \rangle$ and $\mathrm{Var}\,(J_{\theta^\star})$ as a function of t. The shadow areas represent the numerical simulation including positional disorder, preparation errors and detection errors of $\varepsilon_\uparrow = 1.0 \pm 1.0\,\%$ and $\varepsilon_\uparrow = 2.5 \pm 1.0\,\%$. (b) From $\langle J_y \rangle$ and $\mathrm{Var}\,(J_{\theta^\star})$ we compute ξ_{R}^2. The solid curve represents a parabolic fit ξ_{R}^2 at early times from which we extract the optimal squeezing parameter $\xi_{\mathrm{R}}^{2\,\star}$ and its corresponding optimal squeezing time $t^\star$.

Why does the dipolar XY model generate scalable squeezing? To intuitively understand how the dipolar XY model generates squeezing, we can compare this model to an all-to-all coupling XY model. The latter can be expressed as the contribution of two terms:

$$\mathcal{H}_{\mathrm{XY}}^{\text{all-to-all}} = \hbar J \sum_{i<j} \left(\sigma_i^x \sigma_j^x + \sigma_i^y \sigma_j^y + \sigma_i^z \sigma_j^z \right) - \hbar J \sum_{i<j} \sigma_i^z \sigma_j^z = \mathcal{H}_{\mathrm{XXX}}^{\text{all-to-all}} - \mathcal{H}_{\mathrm{OAT}}, \quad (7.3)$$

with the first term $\mathcal{H}_{\mathrm{XXX}}^{\text{all-to-all}}$ being the Heisenberg Hamiltonian and $\mathcal{H}_{\mathrm{OAT}}$ the OAT model [Kitagawa and Ueda, 1993]. As $\mathcal{H}_{\mathrm{XXX}}^{\text{all-to-all}}$ and $\mathcal{H}_{\mathrm{OAT}}$ commute ($\left[\mathcal{H}_{\mathrm{XXX}}^{\text{all-to-all}}, \mathcal{H}_{\mathrm{OAT}} \right] = 0$), and since the initial state $|\mathrm{CSS}_y\rangle$ is an eigenstate of $\mathcal{H}_{\mathrm{XXX}}^{\text{all-to-all}}$, the dynamics are then governed by $\mathcal{H}_{\mathrm{OAT}}$. Thus $\mathcal{H}_{\mathrm{XY}}^{\text{all-to-all}}$ leads to spin squeezing. even though the dipolar XY Hamiltonian is a relatively short-range interaction model, this property remains valid [Perlin, Qu, and Rey, 2020; Comparin *et al.*, 2022; Comparin, Mezzacapo, and Roscilde, 2022a; Block *et al.*, 2023].

7.1.2 Is the squeezing generated by the dipolar XY model scalable?

Spin length and variance. Hamiltonians demonstrating scalable spin squeezing, namely those whose squeezing parameter scales as N^ν (with $\nu > 0$), are highly
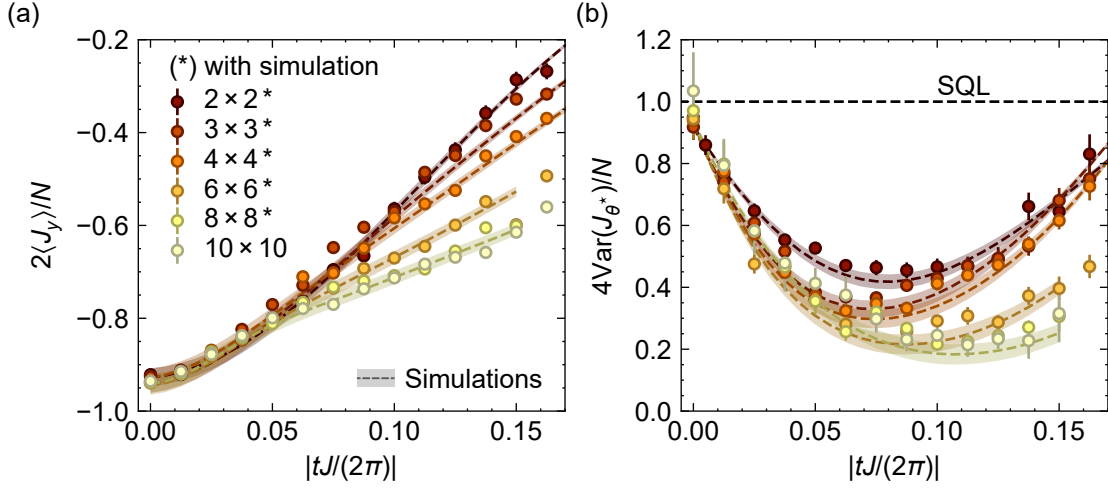
Figure 7.4: Dynamical evolution of the spin length and variance for different system sizes. (a)/(b) Evolution of $\langle J_y \rangle / \mathrm{Var}\,(J_{\theta^\star})$ as a function of t and N. The dashed lines represents the numerical simulation and the shadow areas represent the same simulations taking the detection errors within a range of $\varepsilon_\uparrow = 1.0 \pm 1.0\,\%$ and $\varepsilon_\uparrow = 2.5 \pm 1.0\,\%$.

attractive for metrological applications. To assess the scalability of spin squeezing in the dipolar XY model, we repeat the above experiments for various system sizes.

Figure 7.4a shows the evolution of spin length as a function time for various system sizes N. We observe the same qualitative behaviour for all sizes: the averaged y magnetization decays towards zero. However, the speed of this depolarization depends on the system size: we observe a slower decay as we increase the system size. This effect may seem counter-intuitive. We might think that the larger the system size, the more eigenenergies and eigenfrequencies are involved in the dynamics, which should lead to a faster evolution. To intuitively understand this phenomenon, we compare the FM ground state of the dipolar XY model $|\mathrm{FM}\rangle_{\mathrm{XY}}$ with the CSS state. Due to the continuous symmetry breaking, as we increase N, the energy difference between $|\mathrm{FM}\rangle_{\mathrm{XY}}$ and $|\mathrm{CSS}_y\rangle$ decreases as we increase N (and reaches ≈ 0 at the thermodynamic limit). It implies that for larger N, the eigenfrequencies involved in the dynamics are smaller, thus leading to slower magnetization decay. Quantitatively, this decay rate can be estimated using the *rotor/spin-Wave* theory [Roscilde, Comparin, and Mezzacapo, 2023b]. The Lyon's team showed that in first approximations, the dipolar XY model is equivalent to an OAT model that reads:

$$\mathcal{H}_{\mathrm{rotor}} = J_z^{\,2}/(2I_N) \text{ with } 1/(2I_N) \sim \hbar J/(N^2) \sum_{i \neq j} a^3/r_{ij}^3 \propto 1/N \qquad (7.4)$$
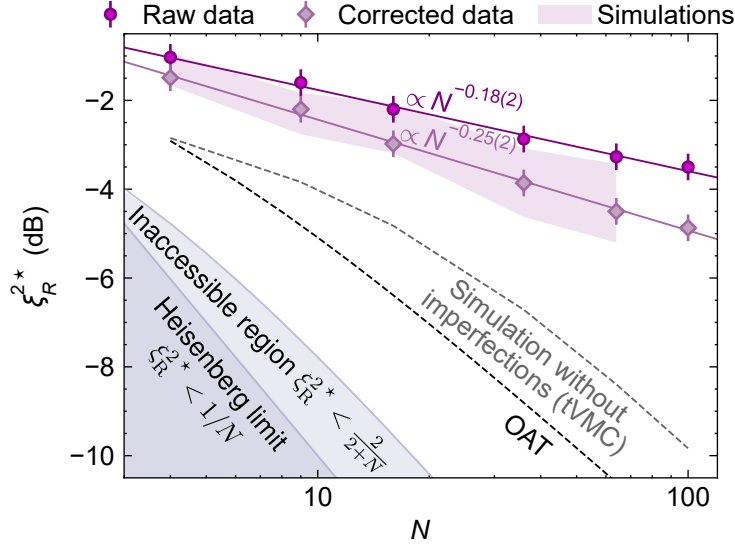
Figure 7.5: Scalability of the squeezing. Best squeezing parameter $\xi_R^{2\,\star}$ as a function of the system size N. The purple curve shows the raw data, the pink curve show the data corrected for the detection errors (see Appendix A). The solid curves are power law fit of the data. The shadow area represent the simulation taking the detection errors within a range of $\varepsilon_\uparrow = 1.0 \pm 1.0\,\%$ and $\varepsilon_\uparrow = 2.5 \pm 1.0\,\%$. The other dashed curves represents tVMC simulations without any imperfection and the prediction for a perfect OAT model. As a reference, the grey areas show the inaccessible region corresponding to $\xi_R^{2\,\star} < 2/(2 + N)$ [Pezzè *et al.*, 2018] and the Heisenberg limit $\xi_R^{2\,\star} < 1/N$.

where $1/(2I_N)$ is called the *the moment of inertia*. For the one axis twisting model $\mathcal{H}_{\mathrm{OAT}} = \hbar\chi J_z^2$ the time scale required to depolarize the state grows as $t \propto 1/(\chi\sqrt{N})$ [Kitagawa and Ueda, 1993]. Thus, the depolarization time in our system scales as $t \propto I_N/\sqrt{N} \propto \sqrt{N}$. The $\mathcal{H}_{\mathrm{rotor}}$ model is only an approximation and, for example, does not explain the fact that for early times $tJ/(2\pi) < 0.05$, the decay of the magnetization is independent of the system sizes. This effect only arises when considering linear spin-wave correction in the theory, which we will discuss in the next chapter.

Figure 7.4b shows the evolution of the minimum variance as a function time for various system sizes N. As for the spin length, all evolution exhibits the same behaviour as for the $N = 6 \times 6$ system: decreasing, reaching a minimum and increasing back up to the SQL. We observe that as we increase N, the minimum value of $\mathrm{Var}\left(J_{\theta\star}\right)$ decreases, and the time required to reach this minimum increases. These features are well explained by considering that the dynamics are driven by the effective OAT model $\mathcal{H}_{\mathrm{rotor}}$.

Scalability of the squeezing. As for the $N = 6 \times 6$, we now compute the squeezing parameter as a function of t for each system size. From each of these curves, we extract the best squeezing parameter $\xi_{\mathrm{R}}^{2\,\star}$ and its corresponding optimal squeezing time $t^\star$. Figure 7.5 shows the evolution of $\xi_{\mathrm{R}}^{2\,\star}$ as a function of N. The squeezing increases with the system size (purple curve) reaching $-3.5\,\mathrm{dB}$ for a $N = 10 \times 10$ array. We fit these data by power-law functions and extract an exponent of $\nu = 0.18(1)$. Recent theoretical studies [Comparin, Mezzacapo, and Roscilde, 2022a; Block *et al.*, 2023] have found a scaling exponent close to the value $\nu = 2/3$ predicted for the OAT model. We attribute this difference to the experimental imperfections. Taking into account these imperfections in the simulations (purple shadow area) leads to a reasonable agreement with the data. As explained in Appendix A, an analytical procedure allows us to correct the squeezing parameter for the detection errors $\varepsilon_\uparrow$ and $\varepsilon_\uparrow$. When this correction (pink curves) is applied, the new power law exponent reads $\nu = 0.26(1)$. The remaining difference mainly comes from errors in the initial state preparation of $|\mathrm{CSS}_y\rangle$ and the residual dynamical evolutions due to the XY interactions during the microwave pulse rotations.

In conclusion, this work shows that up to $N = 100$ spins, the dipolar XY model can experimentally generate scalable squeezing as expected by the theory.

7.2 Characterisation of the squeezed states

I will now show several analyses and investigations we performed to better characterize the squeezing we produced in the previous section.

7.2.1 Entanglement depth

A squeezing parameter $\xi_{\mathrm{R}}^2 < 1$ implies the presence of entanglement in the system. To characterize this entanglement, we quantify the entanglement depth, namely the size of the smallest non-separable sub-system of spins [Estève *et al.*, 2008]. We plot the variance as a function of the y magnetization for a few system sizes as shown in Fig. 7.6. For states below the black solid curve (corresponding to $\xi_{\mathrm{R}}^2 = 1$, squeezing is detected. The grey dashed lines represent lower bounds on the entanglement depth k obtained by calculating the minimum attainable variances as a function of the spin length for a system of k spins (see [Sørensen and Mølmer, 2001; Gross, 2012]). If a data
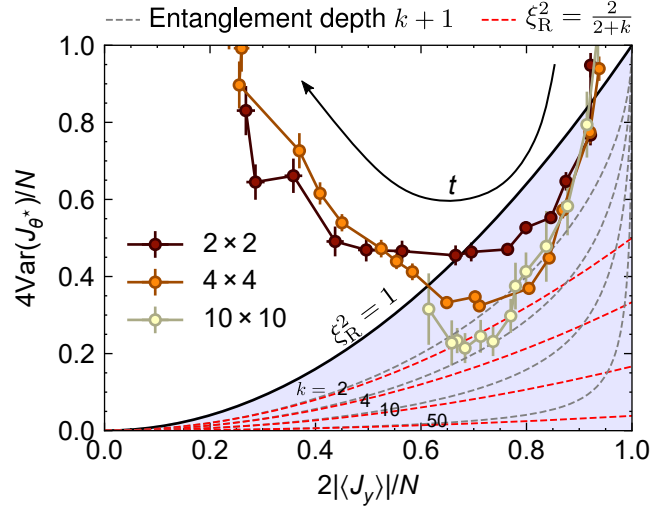
Figure 7.6: Entanglement depth as a function of the system sizes. Parametric plot showing the minimum variance $\mathrm{Var}\,(J_{\theta^\star})$ as a function of the spin length $\langle J_y \rangle$. The black arrow shows the direction of increasing interaction time. The black line and blue area shows the region $\xi_R^2 < 1$ where entanglement is detected. The grey dashed curves represent the $k+1$ entanglement depth limit and the red dashed curves show the limits $\xi_R^2 = 2/(2+k)$ for a some values of k.

point falls below the line labelled by k, the entanglement depth is at least $k+1$. For the smallest system size $N = 2 \times 2$, we measure an entanglement depth of $k = 1 + 1$, and for the largest one, it approximately reaches $k = 4 + 1$.

There is no direct relation between the squeezing parameter ξ_R^2 and the entanglement depth. However, the squeezing parameter sets a lower bound on the entanglement depth. More precisely, if $\xi_R^2 \leq 2/(2 + k)$, the entanglement depth is at least higher or equal to $k+1$. Figure 7.6 illustrates this relation. The red dashed curves show constant values of the squeezing parameter at $2/(2 + k)$. All the red curves are below their corresponding entanglement depth curve, thus showing a minimum entanglement depth of at least $k+1$. However, only knowing the entanglement depth of the system does not give any information about the value of the squeezing parameter. When the system saturates the entanglement depth, $k = N$, the maximum squeezing parameter attainable is $\xi_R^2 \leq 2/(2 + N)$. In the figure above, this configuration corresponds to the region where $2|\langle J_y \rangle|/N \to 0$. In this situation, for large N, we recover a Heisenberg-like scaling with ξ_R^2 proportional to $1/N$.
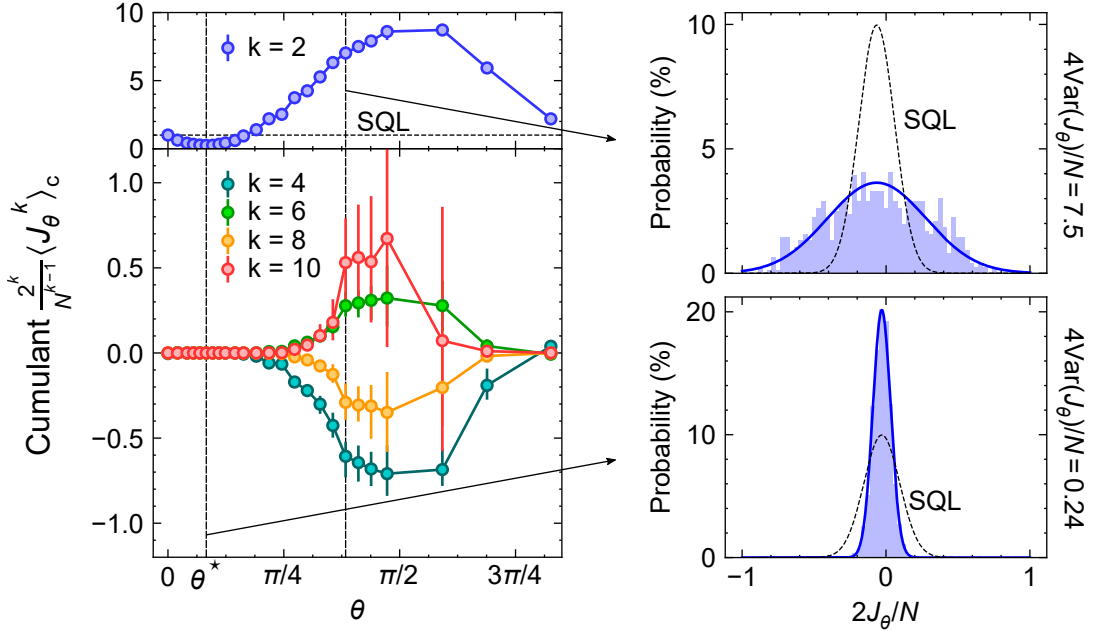
Figure 7.7: Non Gaussian squeezing. Left panel: Cumulant function $\langle J_\theta^k \rangle_c$ as a function of θ for a $N = 8 \times 8$ array measured after an interaction time $t = 0.40\,\mu$s. The error bars has been calculated using Bootstrapping methods. Bottom panels: Two histograms of J_θ corresponding to an angle of $\theta = \theta^\star = 0.32\pi/4$ (minimum variance) and $\theta = 1.6\pi/4$. The blue curves show Gaussian distribution with the same variance as their respective experimental data set. The black dashed curves show the SQL limit (variance of $4\mathrm{Var}(J_\theta)/N = 1$).

7.2.2 Non-gaussian spin squeezing

In the context of squeezing in general, squeezed states are usually described using Gaussian statistics in a sense that for all angle θ, J_θ follows a Gaussian distribution. In this section, we assess whether Gaussian statistics describe our squeezed states. To do so, we define for an observable $\mathcal{O}$, the kth-order cumulant functions $\langle \mathcal{O}^k \rangle_c$ described by the the Ursell functions [Kubo, 1962]:

$$
\begin{aligned}
\langle \mathcal{O} \rangle_c &= \langle \mathcal{O} \rangle \\
\langle \mathcal{O}^2 \rangle_c &= \langle \mathcal{O}^2 \rangle - \langle \mathcal{O} \rangle^2 = \mathrm{Var}(\mathcal{O}) \\
\langle \mathcal{O}^3 \rangle_c &= \langle \mathcal{O}^3 \rangle - 3\langle \mathcal{O} \rangle\langle \mathcal{O}^2 \rangle + 2\langle \mathcal{O} \rangle^3 \\
\langle \mathcal{O}^4 \rangle_c &= \langle \mathcal{O}^4 \rangle - 4\langle \mathcal{O}^3 \rangle\langle \mathcal{O} \rangle - 3\langle \mathcal{O}^2 \rangle^2 + 12\langle \mathcal{O}^2 \rangle\langle \mathcal{O} \rangle^2 - 6\langle \mathcal{O} \rangle^4 \\
\langle \mathcal{O}^k \rangle_c &= \langle \mathcal{O}^k \rangle - \sum_{i=1}^{k-1} \binom{k-1}{i} \langle \mathcal{O}^i \rangle \langle \mathcal{O}^{k-i} \rangle_c.
\end{aligned}
\tag{7.5}
$$

A squeezed state follows a Gaussian statistics if for all angle θ we have J_θ we have $\langle J_\theta{}^{k\geqslant 3}\rangle_c = 0$. For a $N = 8 \times 8$ array, we measure J_θ after an interaction time of $t = 0.40\,\mu$s for various angle θ and compute the different cumulant functions $\langle J_\theta^k\rangle_c$ (see Fig. 7.7). For $k = 2$, the cumulant function corresponds to the variance (blue curves), and as expected, we recover a cosine function signature of an elliptical distribution of the uncertainty. We now look at higher-order cumulants. Since the J_θ histograms are symmetric and centred around zero, then for odd k-order, we get $\langle J_\theta^{k=2n+1}\rangle_c = 0$. Therefore, we only focus on even k-order. We observe that close to the angle $\theta^\star$ of minimum variance, all cumulant orders are at zero, suggesting that the statistics are Gaussian. We observe that along the anti-squeezing direction (angle of maximum variance), the cumulants exhibit a non-zero value, thus showing that the statistics are no longer Gaussian. We attribute this effect to the finite length of the collective spin $-N/2 \leqslant J_\theta \leqslant N/2$: the ellipse of uncertainty cannot infinitely expand and thus get distorted, resulting in non-Gaussian statistics. Qualitatively, the sign of each cumulant orders can be intuitively understood by comparing this state to the state of maximum variance, *i.e.* the Greenberger-Horne-Zeilinger (GHZ) state [Greenberger, Horne, and Zeilinger, 1989] defined as $|\text{GHZ}_\theta\rangle \propto |\rightarrow_\theta\rightarrow_\theta \cdots\rangle + |\leftarrow_\theta\leftarrow_\theta \cdots\rangle$ with $|\rightarrow_\theta\rightarrow_\theta \cdots\rangle$ being a classical ferromagnetic state along the θ direction. The Lyon's team showed that for interaction time longer than the typical squeezing time ($t \sim \pi I_N/(2\pi)$), the quench dynamics lead to the generation of GHZ states [Comparin, Mezzacapo, and Roscilde, 2022b]. For the $|\text{GHZ}_\theta\rangle$ state, it can be shown that $\langle J_\theta^{k=4n+2}\rangle_c > 0$ and $\langle J_\theta^{k=4n}\rangle_c < 0$. Experimentally, we observe a similar behaviour, which indicates that the system started to evolve towards GHZ states.

7.2.3 Improving the squeezing using the single-site resolution

An important aspect of the spin squeezing is that it only uses global observables: spin length $\langle J_y\rangle$ and variance $\text{Var}\,(J_{\theta^\star})$. As our platform allows us to measure the state of every atom individually, one could ask if there is a way to use this single-site resolution to improve the squeezing. To answer this question, let us consider the following example. We consider two independent systems A and B: A is a squeezed state of N spins with a squeezing parameter of $\xi_R^2 \leqslant 1$, and B is a coherent spin state $|\text{CSS}_y\rangle$ also composed of N spins. The phase sensitivity of a Ramsey interferometer is

given by $\sigma = \sqrt{\mathrm{Var}\,(J_{\theta^\star})}/|\langle J_y \rangle|$ [Pezzè *et al.*, 2018]. For the two systems, it thus reads:

$$\sigma_A = \frac{\xi_{\mathrm{R}}}{\sqrt{N}} \text{ and } \sigma_B = \frac{1}{\sqrt{N}} \tag{7.6}$$

We now focus on the phase sensitivity σ_{AB} given by two systems combined. As they are independent, we can write:

$$\sigma_{AB} = \frac{\sqrt{\sigma_A^2 + \sigma_B^2}}{2} = \sigma_A \sqrt{\frac{1}{4}\left(1 + \frac{1}{\xi_{\mathrm{R}}^2}\right)}. \tag{7.7}$$

If $\xi_{\mathrm{R}}^2 = 1$, we recover the expected $\sigma_{AB} = 1/\sqrt{2N}$ sensitivity. The situation becomes interesting when $\xi_{\mathrm{R}}^2 < 1/3$. In this case, we have $\sigma_A < \sigma_{AB}$, meaning that the phase sensitivity is better if we only use the subsystem A rather than both of them. This example shows that by having access to the single-site resolution, we can selectively choose the subsystem that minimizes the phase sensitivity.

Based on this example, we developed a method to optimize the phase sensitivity using the single site resolution information provided by the platform. To do so, we re-define the collective spin operator as:

$$\widetilde{J}_{x,y,z} = \frac{1}{2}\sum_{i=1}^{N} \alpha_i \sigma_i^{x,y,z}, \tag{7.8}$$

with $\{\alpha_i\}$ a set of real number coefficients that we use as free parameters for optimization. We also re-define the collective spin operator in the (x, z) plane $\widetilde{J}_\theta = \cos(\theta)\widetilde{J}_z + \sin(\theta)\widetilde{J}_x$. The new squeezing parameter[2] $\widetilde{\xi}_{\mathrm{R}}^2$ is now defined as:

$$\widetilde{\xi}_{\mathrm{R}}^2 = \frac{\left(\sum_i \alpha_i\right)\min_\theta\left(\mathrm{Var}\left(\widetilde{J}_\theta\right)\right)}{\langle \widetilde{J}_y \rangle^2}. \tag{7.9}$$

The phase sensitivity now reads:

$$\sigma = \sqrt{\mathrm{Var}\left(\widetilde{J}_{\theta^\star}\right)}/|\langle \widetilde{J}_y \rangle| = \frac{\widetilde{\xi}_{\mathrm{R}}}{\sqrt{\sum_i \alpha_i}}. \tag{7.10}$$

If we take all the coefficients equal to $\alpha_i = 1$, we would thus recover the former

---

[2]Note that this new definition of the squeezing parameter is no longer a good witness for the detection of entanglement.
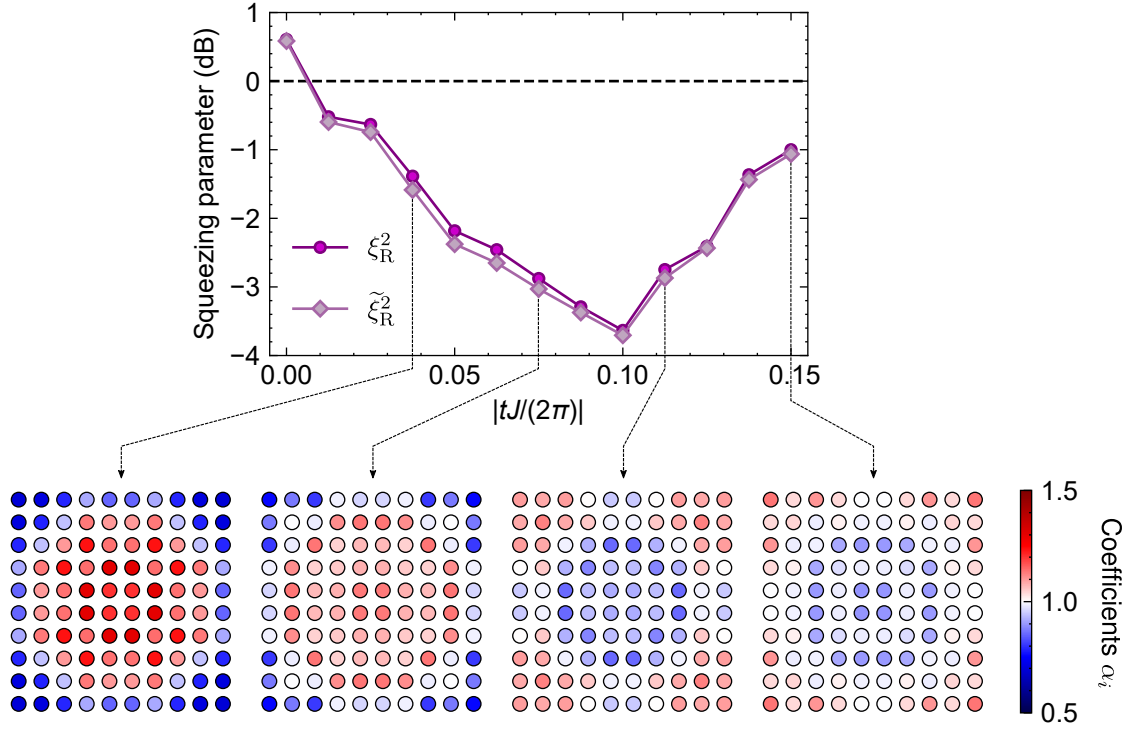
Figure 7.8: Comparison between $\xi_{\mathbf{R}}^2$ and $\widetilde{\xi}_{\mathbf{R}}^2$ The purple curve shows the squeezing parameter $\xi_{\mathbf{R}}^2$ as a function of t for the $N = 10 \times 10$ array. The pink curve shows $\widetilde{\xi}_{\mathbf{R}}^2$ after optimization of the gains $\{\alpha_i\}$. At different time, we represent with coloured circles the coefficients α_i attributed for each atoms. The data shown in this figure has been taken with assembled arrays containing at most three defects.

definitions of the collective spin vectors and squeezing parameters. Setting some coefficients at $\alpha_i = 0$ and keeping the others at $\alpha_i = 1$ corresponds to the situation described in the above example, where we only select a subpart of the full system. In the general case, we do not necessarily need to restrict ourselves to take binary values 0 or 1 for the $\{\alpha_i\}$ coefficients. Choosing non-binary values allows us to finely optimize the squeezing parameters by enhancing the contributions of spins that strongly participate to the squeezing (for these atoms, we take $\alpha_i > 1$) while reducing the impact of atoms weakly correlated with the rest of the systems (for these atoms, we choose $\alpha_i < 1$).

Using a minimizer algorithm, we now optimize the $\{\alpha_i\}$ coefficient to minimize $\widetilde{\xi}_{\mathbf{R}}^2$. In order to compare $\widetilde{\xi}_{\mathbf{R}}^2$ and $\xi_{\mathbf{R}}^2$ we constraint the algorithm to satisfy $\sum_i \alpha_i = N$. We also use the geometrical symmetries of the square array to reduce the number of free parameters to optimize. Figure 7.8 shows the squeezing parameter $\xi_{\mathbf{R}}^2$ (purple curve) as a function of time for the $N = 10 \times 10$ array. For each time, we run the minimizer

program and determine the set of optimized coefficients leading to $\widetilde{\xi}_{\mathrm{R}}^2$ (pink curves). We observe a modest improvement in the squeezing of up to $0.2\,\mathrm{dB}$. Figure 7.8 also show the coefficients attributed to each atom at different interaction times. We observe that the coefficient values vary depending on whether the atoms are on the edges or in the bulk of the array. We attribute this effect to the finite size of the array combined with the relatively short-range nature of the dipolar XY interaction. Interestingly, this spatial distribution of the coefficient values evolves with the interaction time, suggesting it is closely related to the quench dynamics. We did not investigate this effect further.

In conclusion, having access to the single-site resolution can help to improve the squeezing. We showed on our data on a $N = 10 \times 10$ square array that an optimization of the squeezing leads to an improvement up to $0.2\,\mathrm{dB}$ of the phase sensitivity. We can generalize this method to all squeezing systems for which we have the single-site resolution.

7.3 Towards metrological applications

As explained in the previous sections, scalable spin squeezing can be achieved with the dipolar XY model. The problem is that the system only remains squeezed for a short time, which limits its applicability to metrology. This problem arises because the XY interactions cannot be easily switched off. Motivated by metrological applications, we then address this problem using microwave manipulations of the spins. In the first approach, we apply microwave rotations, such that the squeezing both improves and lasts longer (a strategy known as *adiabatic/multistep* squeezing). The second method is based on the coherent transfer of the $\lvert\uparrow\rangle$ population to another Rydberg state from which they stop interaction with the population in $\lvert\downarrow\rangle$.

7.3.1 Adiabatic/Multistep squeezing

Adiabatic/multistep squeezing relies on the use of microwave coupling $\Omega(t)\sum_i \sigma_i^y$ between the spin states to influence the squeezing dynamics. This type of approach, known as the *twist and turn*, has already been demonstrated for the OAT model and was used to enhance the squeezing parameter [Muessel *et al.*, 2015; Sorelli *et al.*, 2019]. The main idea is the following. The squeezing dynamics can be intuitively understood
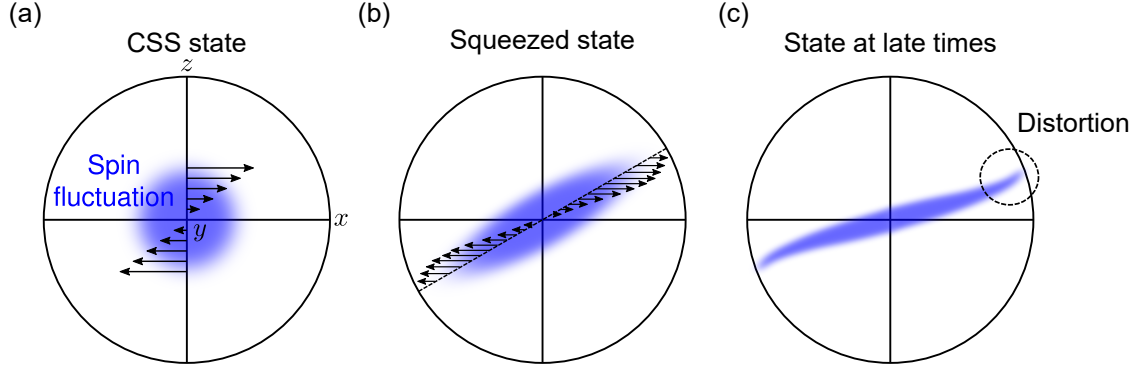
Figure 7.9: Sketch the spin uncertainty shape during the squeezing dynamics. Sketch representing the distribution of spin fluctuation (Husimi Q function) on the generalized Bloch sphere. The steering force projected along x induced by the OAT model is represented by the black arrows. (a) CSS state (b) Squeezed state (c) State at late times, we observe deviation from a perfect elliptical distribution.

using a semi-classical approach. We first consider an OAT model $H_{\mathrm{OAT}} = \hbar\chi J_z^2$ (which we know is a good approximation to describe the squeezing dynamics of the dipolar XY model). The corresponding time evolution operator reads $U = e^{-i\chi t J_z^2} = e^{i\phi J_z/\hbar}$ which corresponds to a global rotations around z of the spins with an angle $\phi = -\hbar\chi t J_z$. As illustrated in Fig. 7.9a, for the initial CSS state, this rotation operator corresponds to a steering force along x applied on the spin uncertainty (Husimi Q function) that is proportional to J_z. This steering force deforms the spin uncertainty distribution that expends along x into an elliptical shape, resulting in spin-squeezing (see Fig. 7.9b). Because the spin uncertainty "evolves on a sphere", for points at the extremity of the ellipse, the steering force no longer points along x (but along $-y$), and thus, the ellipse stops expending along x, resulting in a distortion of its shape (as shown in Fig. 7.9c). The distortion causes the squeezing to stop growing, ultimately leading to its decrease for longer interaction times. These distortions can be minimized by rotating the ellipse during the dynamics, ensuring that its major axis remains aligned along x. It thus preserves the squeezing for a longer time and also (as a positive side effect) allows us to reach better squeezing parameters. Two different strategies are possible to rotate the ellipse.

Multistep squeezing. At carefully chosen times during the dynamics, we rotate the elliptical distribution of the spin fluctuations around the y axis to align its major axis along the equator. The experimental sequence optimized for $N = 6 \times 6$ and comprising
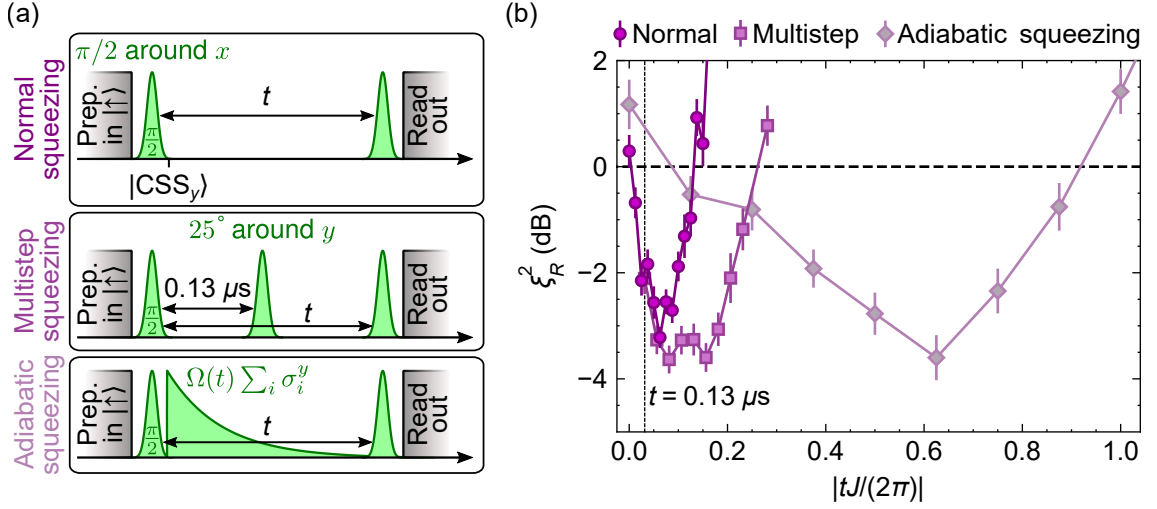
Figure 7.10: Multistep and adiabatic squeezing on an $N = 6 \times 6$ **array.** (a) Sequences for normal, multistep and adiabatic squeezing. For the adiabatic squeezing, the microwave ramp reads $\Omega = \Omega_0 e^{-t/\tau}$ with $\Omega_0/(2\pi) = 4\,\text{MHz}$ and $\tau = 0.5\,\mu\text{s}$. (b) Squeezing parameter measured as a function of time for each of the three sequences.

one intermediate rotation is depicted in Fig. 7.10a. We initialize the system in $|\text{CSS}_y\rangle$ and let the atoms interact for $t = 0.13\,\mu\text{s}$. Then, we rotate the ellipse by $\theta^\star = 25°$ around the y axis. After a total interaction time of t, we measure the spin length and the minimum variance to compute the squeezing parameter. Fig. 7.10b compares, for the same total interaction time, the original sequence described earlier in Sec. 7.1 and this multistep sequence. The effects of the latter are twofold. First, the system remains squezed for twice as long. Second, the minimum squeezing parameter is lower by approximately 1 dB, reaching a value of $-3.6\,\text{dB}$.

Adiabatic squeezing. The adiabatic squeezing can be seen as the continuous version of the multistep squeezing. Instead of applying discrete rotations via microwave pulses at specific times, here we continuously drive a microwave field $H_Y = \Omega(t) \sum_i \sigma_i^y$ to keep the major axis of the ellipse oriented along x (see Fig. 7.10a). In contrast with the normal and multistep squeezing protocol, this experiment is not a quench experiment but an adiabatic process. At $t = 0$ and for $|\Omega(t = 0)/J| \gg 1$, the initial state $|\text{CSS}_y\rangle$ is the ground state of the Hamiltonian $\mathcal{H} = \mathcal{H}_{\text{XY}} + \mathcal{H}_{\text{Y}}$. Adiabatically ramping down
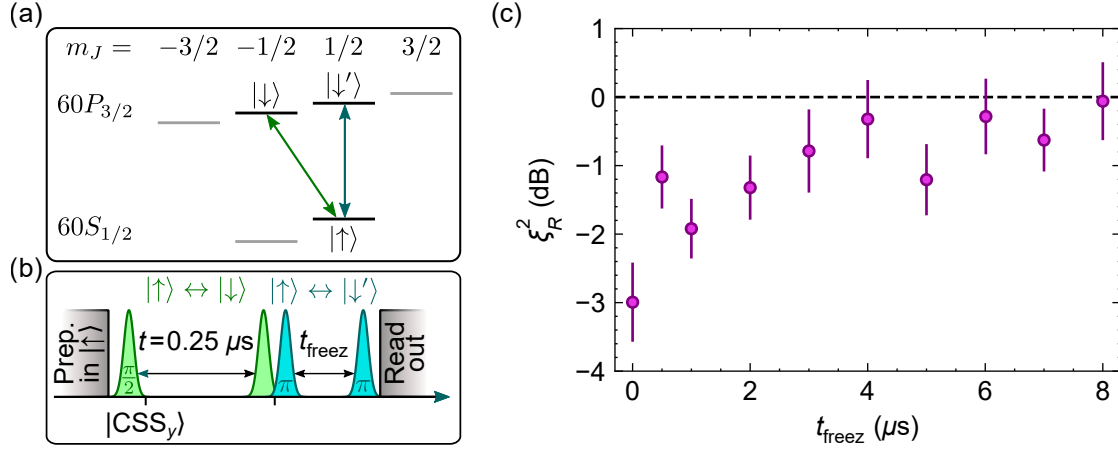
Figure 7.11: Coherent freezing of the spin squeezing. (a) Sketch of the Rydberg manifolds. Using microwave pulses, we coherently drive the $|\uparrow\rangle \leftrightarrow |\downarrow\rangle$ and $|\uparrow\rangle \leftrightarrow |\downarrow'\rangle$ transitions. (b) Experimental sequence to generate and freeze squeezed state for a $N = 6 \times 6$ array. (c) Squeezing parameter measured as a function of the freezing time t_{freez}.

$\Omega(t)$ to zero thus connect $|\mathrm{CSS}_y\rangle$ to the ferromagnetic ground state $|\mathrm{FM}\rangle_{\mathrm{XY}}$[3] studied in Chapter 5. During this adiabatic process, the system exhibits squeezing [Comparin et al., 2022]. Experimentally we set a ramp of $\Omega(t) = \Omega_0 e^{-t/\tau}$ with $\Omega_0/(2\pi) = 4\,\mathrm{MHz}$ and $\tau = 0.5\,\mu$s and measure the squeezing as a function of time (see Fig. 7.10b). We observe that the state remains squeezed for an interaction time six/three times longer than with the original/multistep squeezing sequence. Moreover, as for the multistep step squeezing, the system reaches better squeezing parameters of $\xi_{\mathrm{R}}^{2\,\star} \approx -3.5\,\mathrm{dB}$. In principle, one could adiabatically decrease Ω until we reach the best squeezing parameter $\xi_{\mathrm{R}}^{2\,\star}$ and then maintain Ω at a constant value to preserve this squeezed state as long as needed.

7.3.2 Manipulation of the spin states

Coherent freezing of the dynamics.   In the previous section, we showed that using multistep/adiabatic squeezing protocols, we can extend the time windows for which the system exhibits squeezing. However, it requires an active microwave drive and thus may be inconvenient for practical metrological applications. A method we explore to

---

[3]We also experimentally investigated the adiabatic preparation of the ferromagnetic XY ground state using this adiabatic squeezing protocol. These studies are out of the scope of my thesis, but a detailed presentation of these results can be found in the Gabriel Emperauger's thesis [Emperauger, 2025]

circumvent this issue is to coherently transfer the atoms from $|\uparrow\rangle = \left|60S_{1/2}, m_J = 1/2\right\rangle$ to another Rydberg state $|\downarrow'\rangle = \left|60P_{3/2}, m_J = 1/2\right\rangle$ from which they do not interact with the remaining population in $|\downarrow\rangle$ (see Fig. 7.11a). The experimental sequence is illustrated in Fig. 7.11b. On a $N = 6 \times 6$ array, we initialize the system in $|\mathrm{CSS}_y\rangle$ and let it interact freely for $t = 0.25\,\mu\mathrm{s}$ to produce a squeezed state and then apply the measurement pulse to rotate the system (either along y to measure the spin length y or either along the (x, z) plane to measure the variance along θ). Then, we freeze the system by applying a microwave π-pulse between the state $|\uparrow\rangle$ and $|\downarrow'\rangle$ and wait a time t_{freez}. To unfreeze the dynamics or readout the state, we re-apply a microwave π-pulse to transfer back the atoms from $|\downarrow'\rangle$ to $|\uparrow\rangle$. Figure 7.11 shows the squeezing parameter ξ_{R}^2 as a function of of the freezing time t_{freez}. We observe that the state remains squeezed for a few microseconds, representing a significant improvement compared to the squeezing time scale of a few hundred nanoseconds. We also measured that the squeezing slowly decreases with time. We attribute these effects to two experimental imperfections. First, due to the relatively strong interaction strength $J' = -4J$ between $|\uparrow\rangle$ and $|\downarrow'\rangle$, the microwave transfers between these states are not perfectly efficient and thus reduce the squeezing. Second, the experiment lasts a few microseconds, which starts to be relatively long compared to the Rydberg lifetimes of $\sim 200\,\mu\mathrm{s}$. We thus believe that finite Rydberg lifetimes slowly reduce the squeezing as t_{freez} increases. We did not investigate the reasons for this decay further but just wanted to show that this coherent manipulation of the spin states is a promising route to freeze the squeezing dynamics.

Time reversal of the dynamics. Before concluding this chapter, I would like to mention a project we started using the microwave manipulation of the spin states to enhance metrological measurement. As described above the interaction energy $J' = -4J$ between $|\uparrow\rangle$ and $|\downarrow'\rangle$ has the opposite sign of J. It means that being able to coherently transfer the $|\uparrow\rangle / |\downarrow\rangle$ to $|\uparrow\rangle/|\downarrow'\rangle$ would thus allow us to change the sign of the XY Hamiltonian $\mathcal{H}_{\mathrm{XY}} \to -4\mathcal{H}_{\mathrm{XY}}$ and thus to perform *time-reversal* of the dynamics. This time-reversal ability is particularly interesting to realize *spin scrambling* protocols that enhance the precision of a measurement [Davis, Bentsen, and Schleier-Smith, 2016; Swingle *et al.*, 2016; Colombo *et al.*, 2022; Li *et al.*, 2023]. The idea is the following: we first quench the system and wait for it to build entanglement. We then apply the perturbation signal we wish to measure and perform time reversal to return to an effective interaction time of $t = 0$. If there is no perturbation, we recover the initial
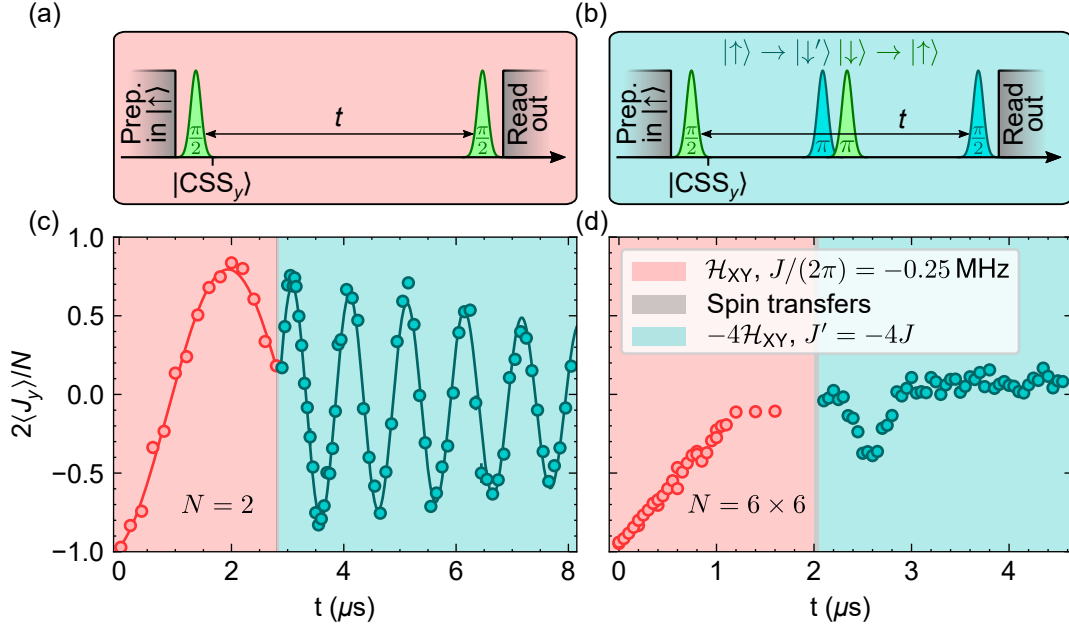
Figure 7.12: Time reversal. (a) Sequence to measure the spin length $\langle J_y \rangle$ as a function of time. (b) Same sequence with the time reversal. In the middle of the dynamics we transfer the $|\uparrow\rangle/|\downarrow\rangle$ to $|\downarrow'\rangle/|\uparrow\rangle$. These transfers take $t \approx 50$ ns. (c)/(d) Spin length $\langle J_y \rangle$ as a function of time for a $N = 2/N = 6 \times 6$ atoms system. We apply the time reversal sequence after a interaction time of $t = 2.8/t = 2.0\,\mu$s. The solid curves in (c) show fits using cosine functions.

state. However, if we now apply a small perturbation, it will slightly modify the state. In analogy to the butterfly effect in chaos theory and similarly to error propagation in quantum circuits, applying the time reversal procedure causes this perturbation to propagate through the system, resulting in a final state significantly different from the initial one. Detecting this difference thus indicates that a signal has been detected.

The key ingredient of this protocol is the time reversal of the dynamics. To test our ability to perform it, we implement the following sequence. We first quench the system by preparing $|\text{CSS}_y\rangle$ and let it evolve under $\mathcal{H}_{\text{XY}}$. To perform the time-reversal we apply a first microwave π-pulse between $|\uparrow\rangle$ and $|\downarrow\rangle$ closely followed by an other π-pulse between $|\uparrow\rangle$ and $|\downarrow\rangle$. This protocol sequentially transfers the $|\uparrow\rangle$ spin population to $|\downarrow'\rangle$ and then transfer $|\downarrow\rangle$ to $|\uparrow\rangle$. The system now freely evolves under $-4\mathcal{H}_{\text{XY}}$. Finally, after a total interaction time t, we rotate the state using a $|\uparrow\rangle \leftrightarrow |\downarrow'\rangle$ microwave pulse and readout the state. Figure. 7.12a and b summarize the sequence to measure the spin length $\langle J_y \rangle$ with and without the time reversal protocol. As a benchmark, we start by measuring the evolution of the y magnetization for a $N = 2$ atoms system (see

Fig. [7.12]c). We first let the system evolve under $\mathcal{H}_{\mathrm{XY}}$ for $t = 2.8\,\mu\mathrm{s}$ and measure that, as expected, the magnetization oscillates with a frequency $J/(2\pi)$ (red data)[4]. After applying the time reversal sequence (green data), we observe that the magnetization oscillates backwards with a frequency $-4J/(2\pi)$, indicating that we succeeded in inverting the dynamics time flow. We repeat the same experiment on a larger array $N = 6 \times 6$ (see Fig. [7.12]d). We first let the system evolve under $\mathcal{H}_{\mathrm{XY}}$ for $t = 2.0\,\mu\mathrm{s}$ and observe the decay of the spin length towards zero (we have already presented these data in Sec. [7.1.1]). We then apply the time reversal and observe that the system re-polarizes after $t = 2.0/4 = 0.5\,\mu\mathrm{s}$ under $-4\mathcal{H}_{\mathrm{XY}}$ and re-depolarizes for longer times. Even if the amplitude of the $\langle J_y \rangle$ revival is not as high as the initial magnetization at $t = 0.0$, the system partially recovered its initial state. We did not investigate further this experiment. We conjecture that this reduction of magnetization amplitude arises from a combination of experimental imperfections (effects of XY interactions during the microwave pulses) and different residual Van der Walls interaction energies between states $|\downarrow\rangle$ and $|\downarrow'\rangle$ that affect differently the dynamics before/after the time reversal.

This work only represents the first step towards spin scrambling experiments using the dipolar XY model. A collaboration with Norman Yao's Harvard team is ongoing to continue this work. I also would like to mention that the similar work led by Matthias Weidemüller's team in Heidelberg have recently been published [Geier *et al.*, 2024].

7.4 Conclusion

In this chapter, I have shown that we experimentally produce squeezed states using the dipolar XY model. I showed that the squeezing parameter grows as we increase the system size, thus confirming theoretical works that predict scalable spin squeezing. I then investigated the nature of this squeezing: I characterized its entanglement depth, showed that it cannot be described by Gaussian statistics and demonstrated that by using the single-site resolution provided by the platform, we improve the squeezing. Motivated by metrological applications, I have presented different protocols to extend the duration of the squeezing dynamics. The multistep/adiabatic squeezing methods

---

[4]This experiment is similar to the two-atom Ramsey experiment already presented in Fig. [5.2] of Sec. [5.1.2])

rely on microwave rotations to influence the squeezing dynamics making it last longer with better squeezing parameters. The second method consists in freezing the squeezing dynamics by coherently transferring the spin population to Rydberg states that do not interact. It allows us to preserve the squeezing for a few microseconds, much longer than the typical squeezing dynamics. Finally, I showed the first proof of the principle of time-reversal of the dynamics using this spin manipulation. It opens the door to new methods for quantum metrology, such as spin scrambling.

Dispersion relation

Contents

In Chapter 5 I discussed how the long range tail of the dipolar XY interaction $J \propto 1/r_{ij}^3$ modifies the properties of its AFM/FM ground state. More generally, one could ask how the dipolar tail alters the properties of the low energy spectrum and of their elementary excitations/quasiparticles. In the context of spin Hamiltonian these elementary excitations/quasiparticles are usually spin waves characterized by a dispersion relation giving their energy $\omega_{\mathbf{k}}$ as a function of their wavevector $\mathbf{k}$. Having access to this dispersion relation is particularly interesting since it allows us to predict the behavior of the system at low energies. Being able to measure a dispersion relation of a system is therefore a major challenge.

To measure the dispersion relation of real world materials, condensed matter physicist usually probe the linear response of systems using a variety of different methods ranging from pump-probe spectroscopy, angle-resolved photoemission spectroscopy to inelastic neutron scattering [Forster, 2019; Lovesey, 1980, 1986; Sobota, He, and Shen, 2021]. For artificial quantum systems, the usual approach to probe the dispersion relation is the following. First we prepare the ground state of the system, second, we introduce a specific excitation in the system and third, we measure its response from which we extract the dispersion relation. However, applying this three-steps sequence

is usually challenging. It requires preparing the ground state of the system which is not necessarily easy, and it can only be done on quantum simulator platforms which provides a coherence time long enough to perform all these steps.

To circumvent these issues, an other method to measure the dispersion relation called *quench spectroscopy experiment* was proposed in 2018 [Mitra, 2018]. The idea is the following. We first quench the system by preparing it in an out-of-equilibrium state, thus injecting a finite density of excitations into the system. Then, we measure its dynamical evolution. During the dynamics, the system starts to produce spin-spin correlations whose spatial organisation is dictated by the propagation of the excitations governed by the dispersion relation [Cevolani *et al.*, 2018; Despres, Villa, and Sanchez-Palencia, 2019; Schneider *et al.*, 2021]. Measuring the dynamical and spatial evolution of these correlations could then allow for extracting the dispersion relation. In the case where the excitations behave as *free* quasiparticles, it has been shown that the 2D Fourier transform of the correlations at wavevector $\mathbf{k}$ is expected to oscillate as a function of the interaction time t at frequency $2\omega_{\mathbf{k}}$ [Frérot, Naldesi, and Roscilde, 2018; Menu and Roscilde, 2018; Villa, Despres, and Sanchez-Palencia, 2019; Villa *et al.*, 2020; Menu and Roscilde, 2023]. This theory result is the key mechanism of the quench spectroscopy method. Compared to the three-steps method described previously, it offers two advantages:

- To ensure that the quasiparticles remain free, we must prepare an initial state with a sufficiently low excitation density, such that particle-particle interactions are negligible during the dynamics. While this requirement constrains the choice of initial state, it is less restrictive than preparing the ground state, which is usually entangled and thus challenging to obtain. As we will see in this chapter, we can target a state with low excitation density by preparing the mean-field ground state. In contrast to the true ground state, the mean-field ground state is a product state, making it much easier to prepare.

- To extract the dispersion relation from the correlations, we only need to measure evolution of the system over timescales comparable to the typical time scale of the dynamics $tJ/(2\pi) \sim 1$. In contrast, the three-step method requires preparing the ground state, usually via an adiabatic process that necessitates much longer experimental times $tJ/(2\pi) \gg 1$ to maintain adiabaticity. This requires an relatively long coherence time of the experiment which is not necessary for quench spectroscopy experiments.

For all these reasons, demonstrating that we can experimentally measure the dispersion relation using quench spectroscopy could pave the way for similar measurements using various systems and platforms. Motivated by this potential, we apply this in our Rydberg platform and illustrate the method by measuring the dispersion relation of the dipolar XY model.

For a nearest neighbour XY model on square array, the dispersion relation can analytically calculated and has been found to be linear $\omega_{\mathbf{k}}^{\mathrm{AFM}} = \omega_{\mathbf{k}}^{\mathrm{FM}} \propto |\mathbf{k}|$ [Manousakis, 1991]. However, for the dipolar XY model, Hans Peter Büchler and his team predicted a different dispersion relation for the FM ground state [Peter *et al.*, 2012]. Due to the $1/r_{ij}^3$ tail of the FM dispersion is modified from a linear dispersion to a non-linear one $\omega_{\mathbf{k}}^{\mathrm{FM}} \propto \sqrt{|\mathbf{k}|}$ while the AFM dispersion remains linear. In this chapter, we apply a quench spectroscopy experiment to measure this modified FM dispersion relation. We also perform comparative measurement between the FM and AFM dispersion relation. This chapter is organized as follow: In the first section we give a brief reminder about the linear spin wave theory used to link the dispersion relation to the correlations we measure in the system. In the second part, we focus of the experimental realization of the quench spectroscopy experiments and on the extraction of the dispersion relation. This work has been realized in collaboration with Tommaso Roscilde's team in Lyon and Norman Yao's team at Harvard. These results have been published and more details can be found in [Chen *et al.*, 2023b].

8.1   Linear spin wave theory

The quench spectroscopy experiment can be described using the linear Spin Wave (SW) theory. It consists in mapping the dipolar XY on a Bosonic model via an Holstein-Primakoff transformations [Holstein and Primakoff, 1940; Vogl *et al.*, 2020]. We then perform a *Rotor/Spin wave* decomposition to isolate the spin wave contribution. These spin waves can then linearised using a Bogolyubov transformation to extract the dispersion relation. In this section, I will re-derive the main results of this the spin wave theory for an infinite size square array. The theory methods and the associated results that I will describe now, closely follow the works published by our theory colleagues in Lyon [Roscilde, Comparin, and Mezzacapo, 2023a,b].

8.1.1 Rotor/Spin wave decomposition

Holstein-Primakoff mapping. The first step consists in mapping the dipolar XY model onto a bosonic model using the Holstein-Primakoff (HP) transformation. Taking the y axis as quantization axis, this transformation reads:

$$
\begin{aligned}
\sigma_j^x &= \sqrt{1 - n_j}\, b_j + b_j^\dagger \sqrt{1 - n_j} \\
\sigma_j^y &= 1 - 2n_j \\
\sigma_j^z &= -i \left(\sqrt{1 - n_j}\, b_j + b_j^\dagger \sqrt{1 - n_j} \right),
\end{aligned}
\tag{8.1}
$$

with $b_j / b_j^\dagger$ the bosonic annihilation/creation operator and $n_j = b_j^\dagger b_j$ the number operator acting on site j. In this HP picture, the presence/absence of a boson on site j corresponds to the spin j being in $|\leftarrow_y\rangle / |\rightarrow_y\rangle$. Equation 8.1 are non linear but can be simplified by considering that the number of excitation in the system is relatively small $\langle n_j \rangle \ll 1$ [Vogl *et al.*, 2020]. The above equations thus become at 1$^{\text{st}}$ order in the number of particle:

$$
\begin{aligned}
\sigma_j^x &\approx b_j + b_j^\dagger \\
\sigma_j^y &\approx 1 - 2n_j \\
\sigma_j^z &\approx -i \left(b_j - b_j^\dagger \right).
\end{aligned}
\tag{8.2}
$$

We now inject this transformation in $\mathcal{H}_{\text{XY}} = \frac{\hbar}{2} \sum_{i<j} J_{ij} \left(\sigma_i^x \sigma_j^x + \sigma_i^y \sigma_j^y \right)$ with $J_{ij} = Ja^3/r_{ij}^3$ and only keep the quadratic terms. The dipolar XY model now reads:

$$
\begin{aligned}
\mathcal{H}_{\text{XY}} &\approx E_{\text{CSS}} + \mathcal{H}_2 \\
&\approx \frac{\hbar}{2} \sum_{i<j} J_{ij} + \hbar \sum_{i<j} J_{ij} \left[\left(b_i b_j + b_i^\dagger b_j + b_i b_j^\dagger + b_i^\dagger b_j^\dagger \right) - (n_i + n_j) \right],
\end{aligned}
\tag{8.3}
$$

with $E_{\text{CSS}} = \frac{\hbar}{2} \sum_{i<j} J_{ij}$ being the mean field energy. It corresponds to the energy of the vacuum state in terms of HP bosons and to a coherent spin state $|\text{CSS}_y\rangle = |\rightarrow_y \rightarrow_y \rightarrow_y \rightarrow_y \cdots\rangle$ in the spin picture. The Hamiltonian $\mathcal{H}_2$ describes quadratic fluctuations around the mean field.

Rotor/Spin wave decomposition. We now introduce the HP bosonic operators in momentum spaces:

$$b_j = \frac{1}{\sqrt{N}} \sum_{\mathbf{k}} e^{i\mathbf{k}\cdot\mathbf{r}_j/a} b_{\mathbf{k}} = \frac{b_0}{\sqrt{N}} + \frac{1}{\sqrt{N}} \sum_{\mathbf{k}\neq 0} e^{i\mathbf{k}\cdot\mathbf{r}_j/a} b_{\mathbf{k}}, \qquad (8.4)$$

with the wavevector $\mathbf{k}$ running over the Brillouin zone. Similarly, we define the Fourier transform of the dipolar interaction J_{ij}

$$J_{\mathbf{k}} = \frac{1}{N} \sum_{i\neq j} e^{i\mathbf{k}\cdot\mathbf{r}_{ij}/a} J_{ij} \text{ and } J_0 = \frac{1}{N} \sum_{i\neq j} J_{ij}. \qquad (8.5)$$

Combining Eq. 8.4 and Eq. 8.5 we re-express the quadratic Hamiltonian that now reads:

$$\mathcal{H}_2 = \hbar \sum_{\mathbf{k}} A_{\mathbf{k}} - \hbar \sum_{\mathbf{k}} \begin{pmatrix} b_{\mathbf{k}}^{\dagger} & b_{-\mathbf{k}} \end{pmatrix} \begin{pmatrix} A_{\mathbf{k}} & B_{\mathbf{k}} \\ B_{\mathbf{k}} & A_{\mathbf{k}} \end{pmatrix} \begin{pmatrix} b_{\mathbf{k}} \\ b_{-\mathbf{k}}^{\dagger} \end{pmatrix}, \qquad (8.6)$$

with $A_{\mathbf{k}} = \left(J_0 - J_{\mathbf{k}}/2\right)/2$ and $B_{\mathbf{k}} = -J_{\mathbf{k}}/4$. We now isolate the $\mathbf{k} = 0$ mode that will describe a *rotor* Hamiltonian (see below), from the $\mathbf{k} \neq 0$ modes that represent the spin waves. We first focus on the rotor part and re-write $\mathcal{H}_2$ only keeping the $\mathbf{k} = 0$ mode:

$$\mathcal{H}_2\rfloor_{\mathbf{k}=0} = \frac{\hbar J_0}{4} \left(1 + b_0^{\dagger} b_0 + b_0^{\dagger} b_0^{\dagger} - b_0^{\dagger} b_0 - b_0 b_0^{\dagger}\right). \qquad (8.7)$$

Combining Eq. 8.2 and Eq. 8.4 we can re-express the operator $J_z = \frac{1}{2} \sum_i \sigma_i^z$ in terms of HP bosonic operator and keep the $\mathbf{k} = 0$ mode:

$$J_z\rfloor_{\mathbf{k}=0} = \frac{-i\sqrt{N}}{2} \left(b_0 - b_0^{\dagger}\right), \qquad (8.8)$$

that we now inject in $\mathcal{H}_2\rfloor_{\mathbf{k}=0}$. We then obtain an OAT-like Hamiltonian:

$$\mathcal{H}_2\rfloor_{\mathbf{k}=0} = -\frac{\hbar J_0}{N} J_z^2\rfloor_{\mathbf{k}=0} + \frac{\hbar J_0}{4} = \mathcal{H}_{\text{rotor}} + \frac{\hbar J_0}{4}. \qquad (8.9)$$

The first term corresponds to a rotor for which we can define a momentum of inertia I_N:

$$\mathcal{H}_{\text{rotor}} = \frac{J_z^2\rfloor_{\mathbf{k}=0}}{2I_N} \text{ with } \frac{1}{2I_N} = -\frac{\hbar J_0}{N}, \qquad (8.10)$$

and thus recover the expression that we already introduced in the previous chapter (see Eq. 7.4). When the number of bosons in the $\mathbf{k} = 0$ mode is dominant (*i.e.* when $\langle b_0^{\dagger} b_0 \rangle \gg \langle b_{\mathbf{k}\neq 0}^{\dagger} b_{\mathbf{k}\neq 0} \rangle$), we get $J_z^2\rfloor_{\mathbf{k}=0} \approx J_z^2$ and thus, the rotor Hamiltonian becomes

an OAT model $\mathcal{H}_{\mathrm{XY}} \approx \mathcal{H}_{\mathrm{rotor}} \approx \hbar J_z^2/(2I_N)$ that drives the dynamics. In particular, as explained in the previous chapter (see Sec. 7.1.2), this rotor Hamiltonian is responsible for the formation of scalable spin squeezing when using the dipolar XY model. The second term $\hbar J_0/4$ in Eq. 8.9 correspond to an energy correction to apply on the mean field energy E_{CSS} to get the ground state energy of $\mathcal{H}_{\mathrm{rotor}}$. Its energy ground state reads: $E_{\mathrm{rotor}} = E_{\mathrm{CSS}} + \hbar J_0/4 = \hbar J_0\left(N+1\right)/4$.

We now move the study of the $\mathcal{H}_2\rfloor_{\mathbf{k}\neq 0}$ term that contains the spin waves and thus carries the information about the dispersion relation.

8.1.2 Linearisation of the spin wave excitations

In summary, the total dipolar XY model reads:

$$\mathcal{H}_{\mathrm{XY}} \approx E_{\mathrm{CSS}} + \mathcal{H}_2\rfloor_{\mathbf{k}=0} + \mathcal{H}_2\rfloor_{\mathbf{k}\neq 0} = E_{\mathrm{rotor}} + \mathcal{H}_{\mathrm{rotor}} + \mathcal{H}_{\mathrm{SW}}, \tag{8.11}$$

with $\mathcal{H}_{\mathrm{SW}} = \mathcal{H}_2\rfloor_{\mathbf{k}\neq 0}$ the spin wave Hamiltonian that reads:

$$\mathcal{H}_{\mathrm{SW}} = \hbar \sum_{\mathbf{k}\neq 0} A_{\mathbf{k}} - \hbar \sum_{\mathbf{k}\neq 0} \begin{pmatrix} b_{\mathbf{k}}^\dagger & b_{-\mathbf{k}} \end{pmatrix} \begin{pmatrix} A_{\mathbf{k}} & B_{\mathbf{k}} \\ B_{\mathbf{k}} & A_{\mathbf{k}} \end{pmatrix} \begin{pmatrix} b_{\mathbf{k}} \\ b_{-\mathbf{k}}^\dagger \end{pmatrix}. \tag{8.12}$$

Bogolyubov diagonalization. To diagonalize this spin-wave Hamiltonian, we apply the following Bogoliubov transformation (this transformation is only valid for systems with an infinite size or with periodic boundary conditions): $b_{\mathbf{k}} = u_{\mathbf{k}} a_{\mathbf{k}} - v_{\mathbf{k}} a_{-\mathbf{k}}^\dagger$ with $a_{\mathbf{k}}/a_{\mathbf{k}}^\dagger$ the bosonic annihilation/creation operator operating on boson called *magnons* [Jean-Paul Blaizot, 1985]. They represent the linearised excitations of the system. The coefficient $u_{\mathbf{k}}$ and $v_{\mathbf{k}}$ are calculated to be:

$$u_{\mathbf{k}} = \sqrt{\frac{1}{2}\left(\frac{A_{\mathbf{k}}}{\omega_{\mathbf{k}}} + 1\right)} \text{ and } v_{\mathbf{k}} = \mathrm{sign}(B_{\mathbf{k}})\sqrt{\frac{1}{2}\left(\frac{A_{\mathbf{k}}}{\omega_{\mathbf{k}}} - 1\right)}, \tag{8.13}$$

with $\omega_{\mathbf{k}}$ the dispersion relation of the magnon:

$$\omega_{\mathbf{k}} = \sqrt{A_{\mathbf{k}}^2 + B_{\mathbf{k}}^2} = J_0\sqrt{1 - J_{\mathbf{k}}/J_0}. \tag{8.14}$$
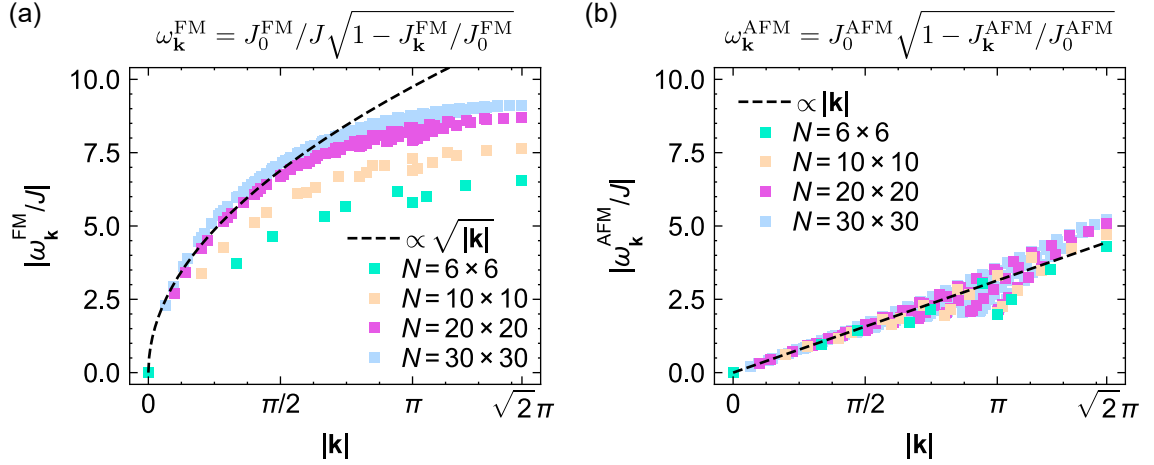
Figure 8.1: Calculations of the dispersion relations using the linear SW theory.
(a)/(b) For different system size N, we calculate the FM/AFM dispersion relations using
Eq. 8.16 and 8.17. The dashed curves represent a guide to the eye.

This transformation thus lead to the linearised form of the spin wave Hamiltonian:

$$\mathcal{H}_{\mathrm{SW}} = -2\hbar \sum_{\mathbf{k}\neq 0} \omega_{\mathbf{k}} a_{\mathbf{k}}^{\dagger} a_{\mathbf{k}} + \hbar \sum_{\mathbf{k}\neq 0} \left(A_{\mathbf{k}} - \omega_{\mathbf{k}} \right). \tag{8.15}$$

The first term of this Hamiltonian represents the energy of the linearised excitation with
$a_{\mathbf{k}}^{\dagger} a_{\mathbf{k}}$ the number of magnon in mode $\mathbf{k}$ and $\omega_{\mathbf{k}}$ their respective energies. The second
term represent an energy correction to apply to E_{CSS} to get the ground state energy
of $\mathcal{H}_{\mathrm{SW}}$. Its energy ground state corresponds to: $E_{\mathrm{SW}} = E_{\mathrm{CSS}} + \hbar \sum_{\mathbf{k}\neq 0} \left(A_{\mathbf{k}} - \omega_{\mathbf{k}} \right)$.

Dispersion relation. We now calculate the dispersion relation for the AFM and FM
state using Eq. 8.5 and 8.14. We first take $J < 0$ in which case, the ground state of
$\mathcal{H}_{\mathrm{XY}}$ on square array is the FM state $|\mathrm{FM}\rangle_{\mathrm{XY}}$ already discussed in Chapter 5.5. It has
been shown in [Frérot, Naldesi, and Roscilde, 2017] that by calculating the Fourier
transform of $J_{ij}^{\mathrm{FM}} = Ja^3/r_{ij}^3$ that we call $J_{\mathbf{k}}^{\mathrm{FM}}$, we can show that at short wavevector
$|\mathbf{k}| \ll 2\pi$:

$$\omega_{\mathbf{k}}^{\mathrm{FM}} = J_0^{\mathrm{FM}} \sqrt{1 - J_{\mathbf{k}}^{\mathrm{FM}}/J_0^{\mathrm{FM}}} \propto \sqrt{|\mathbf{k}|}, \tag{8.16}$$

with $J_0^{\mathrm{FM}} \approx 6.5J$. To calculate the dispersion relation of the AFM state on square
array, we apply a π rotation around the z-axis on half of the atoms in a staggered
configuration thus transforming the $\sigma_i^{x,y}$ operator into $(-1)^{(\mathbf{u}_x+\mathbf{u}_y)\cdot\mathbf{r}_{ij}/a}\sigma_i^{x,y}$. Under this
transformation, the $|\mathrm{AFM}\rangle_{\mathrm{XY}}$ state is the FM ground of a modified $\mathcal{H}_{\mathrm{XY}}$ Hamiltonian
with staggered coupling, $J_{ij}^{\mathrm{AFM}} = (-1)^{(\mathbf{u}_x+\mathbf{u}_y)\cdot\mathbf{r}_{ij}/a}Ja^3/r_{ij}^3$. We calculate its Fourier

transform $J_{\mathbf{k}}^{\text{AFM}}$ and show that for $|\mathbf{k}| \ll 2\pi$, the AFM dispersion relation reads:

$$\omega_{\mathbf{k}}^{\text{AFM}} = J_0^{\text{AFM}}\sqrt{1 - J_{\mathbf{k}}^{\text{AFM}}/J_0^{\text{AFM}}} \propto |\mathbf{k}|. \tag{8.17}$$

In Fig. 8.1 we compute the FM/AFM dispersion relation using Eq. 8.16 and 8.17 for various system sizes N. We observe that at low $|\mathbf{k}|$, as N increases ($N = 30 \times 30$ being the largest size I can compute with my laptop), the dispersion relations tend to be closer to the theory predictions $\propto \sqrt{|\mathbf{k}|}/\propto |\mathbf{k}|$ in the FM/AFM case.

Measuring the dispersion relations. To measure the dispersion relation, we first prepare the state in its mean field state. For the FM, it is a CSS state $|\text{CSS}_y\rangle = |\rightarrow_y \rightarrow_y \rightarrow_y \rightarrow_y \cdots\rangle$ (see Fig.8.2a) and for the AFM, it is a classical AFM state along y denoted $|\text{AFM}_y\rangle = |\rightarrow_y \leftarrow_y \rightarrow_y \leftarrow_y \cdots\rangle$) (see Fig.8.2). Then, we let these states freely evolve under the dipolar XY model $\mathcal{H}_{\text{XY}} = E_{\text{rotor}} + \mathcal{H}_{\text{rotor}} + \mathcal{H}_{\text{SW}}$ and assume that we measure, for all pair of atoms $\{i, j\}$ the two body connected correlation $\langle \sigma_i^z \sigma_j^z \rangle_{\text{c}}$ in the z-basis. We choose this particular basis to facilitate the measurement of the dispersion relation. As $\mathcal{H}_{\text{rotor}}$ is an all-to-all coupling Hamiltonian and commutes with J^z ($[\mathcal{H}_{\text{rotor}}, J_z] = 0$) and $\mathcal{H}_{\text{SW}}$ ($[\mathcal{H}_{\text{rotor}}, \mathcal{H}_{\text{SW}}] = 0$), the dynamics induced by $\mathcal{H}_{\text{rotor}}$ does not lead to formation of spin correlations in the z-basis. The z correlations are thus only produced by dynamics driven by the spin wave Hamiltonian $\mathcal{H}_{\text{SW}}$ that carries the information about the dispersion relation. Extracting the dispersion relation from correlations measured in an other basis would also be possible, but would be more complicated: an additional step in the analysis procedure would be required to separate the contribution to the correlations of $\mathcal{H}_{\text{SW}}$ from that of $\mathcal{H}_{\text{rotor}}$. From the $\langle \sigma_i^z \sigma_j^z \rangle_{\text{c}}$ measurements, we compute the time dependent structure factor:

$$S_{\mathbf{k}}^z(t) = \frac{1}{N} \sum_{i,j} e^{i\mathbf{k} \cdot \mathbf{r}_{ij}/a} \langle \sigma_i^z \sigma_j^z \rangle_{\text{c}}. \tag{8.18}$$

Using equation Eq. 8.2 and 8.4, we can rewrite the this operator in terms of bosonic operator:

$$S_{\mathbf{k}}^z(t) \approx \langle b_{\mathbf{k}} b_{\mathbf{k}} \rangle_{\text{c}} + \langle b_{-\mathbf{k}}^\dagger b_{\mathbf{k}}^\dagger \rangle_{\text{c}} - \langle b_{\mathbf{k}} b_{\mathbf{k}}^\dagger \rangle_{\text{c}} - \langle b_{-\mathbf{k}}^\dagger b_{-\mathbf{k}} \rangle_{\text{c}}. \tag{8.19}$$

On can then analytically calculate the expectation values for $S_{\mathbf{k}}^z(t)$ as a function of the interaction time t when the system is driven by the spin wave Hamiltonian $E_{\text{rotor}} + \mathcal{H}_{\text{rotor}} + \mathcal{H}_{\text{SW}}$ [Frérot, Naldesi, and Roscilde, 2018]. It takes a simple form that

reads:

$$S_{\mathbf{k}}^z(t) = C_{\mathbf{k}} + D_{\mathbf{k}} \cos(2\omega_{\mathbf{k}} t), \tag{8.20}$$

with $C_{\mathbf{k}} = 1 - J_{\mathbf{k}}/(2J_{\mathbf{0}})$ and $D_{\mathbf{k}} = J_{\mathbf{k}}/(2J_{\mathbf{0}})$. Measuring $S_{\mathbf{k}}^z(t)$ thus allows one to measure the dispersion relation in three different ways. We can: either extract the frequency at which $S_{\mathbf{k}}^z(t)$ oscillates to get $\omega_{\mathbf{k}}$, extract the amplitude or offset value of these oscillations to compute $\omega_{\mathbf{k}}$ via the following formulas:

$$\begin{aligned} \omega_{\mathbf{k}} &= J_0 \sqrt{2C_{\mathbf{k}} - 1} \\ \omega_{\mathbf{k}} &= J_0 \sqrt{1 - 2D_{\mathbf{k}}} \end{aligned} \tag{8.21}$$

These results form the basic principle of the quench spectroscopy experiment. They are only valid for an infinitely large array or for a finite size system with periodic boundary conditions. Extending this spin-wave analysis to finite size systems with open boundary conditions is not at all a trivial task However, our colleagues in Lyon demonstrated that at short times, when $|tJ/(2\pi)| \ll 1$, these results remain valid (see more details in [Chen *et al.*, 2023b]). We now have all the theory tools for this quench spectroscopy experiment and turn to its experimental realization.

8.2 Experimental measurement of the dispersion relation

All the data presented in this section have been obtained using a square array of $N = 10$ atoms. The experimental parameters are the same as for the previous chapter: $a = 15\,\mu\text{m}$, $J/(2\pi) = -0.25\,\text{MHz}$, $|\uparrow\rangle = \left|60S_{1/2}, m_J = 1/2\right\rangle$ and $|\downarrow\rangle = \left|60P_{3/2}, m_J = -1/2\right\rangle$.

8.2.1 Quench experiment

After having excited all the atoms in $|\uparrow\rangle$, we begin the quench spectroscopy experiment by initializing the system in a CSS state $|\text{CSS}_y\rangle$ or in a classical AFM state $|\text{AFM}_y\rangle$ pointing along y. To prepare $|\text{CSS}_y\rangle$, we apply a microwave $\pi/2$-pulse around x (see Fig.8.2c). To prepare $|\text{AFM}_y\rangle$, we first prepare a Néel state $|\uparrow\downarrow\uparrow\downarrow\cdots\rangle$ using a set of addressing beams and microwave pulses and following the procedure described in Sec. 3.2. We then apply a microwave $\pi/2$-pulse around x to rotate the spins and initialize the system in $|\text{AFM}_y\rangle$ (see Fig.8.2d). We then let the initial state
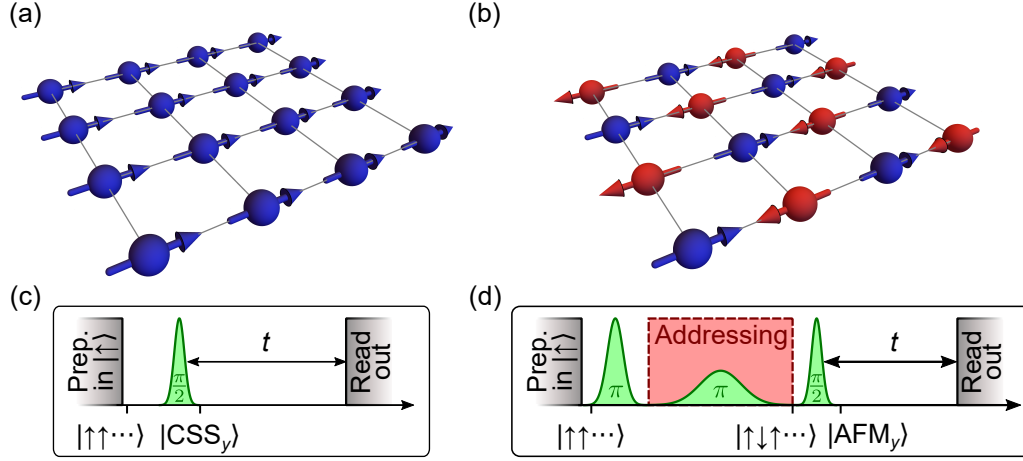
Figure 8.2: Experimental sequence for the quench spectroscopy. (a)/(b) Illustration on a 4 square array of the initial state at $t = 0$. to probe the FM/AFM dispersion relation. (c)/(d) Experimental sequence to measure the FM/AFM dispersion relation.
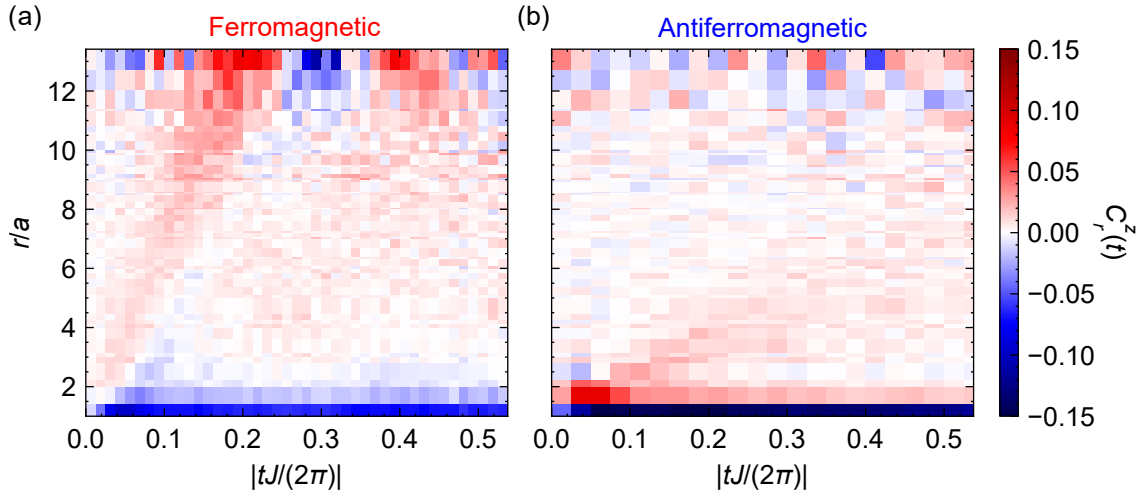

Figure 8.3: Spatial evolution of the z correlations as a function of time. (a)/(b) Averaged correlation C_r^z as a function of the interaction time t and the distance between the spins d/a for the FM/AFM state. The data shown in this figure has been taken with assembled arrays with at most three defects allowed.

evolves freely under the XY model, and measure its evolution as a function of the interacting time t.

From the measured spin correlations $\langle \sigma_i^z \sigma_j^z \rangle_c$, we compute the average correlation $C_r^z(t)$ as a function of the distance r between the spins (already defined in Eq. 5.9). Figure 8.3a and b show the experimental results as a function of t and r for the FM and AFM states. We observe that for both state, correlations build up at short distance and at short times and seem to propagate at long distances with time. We
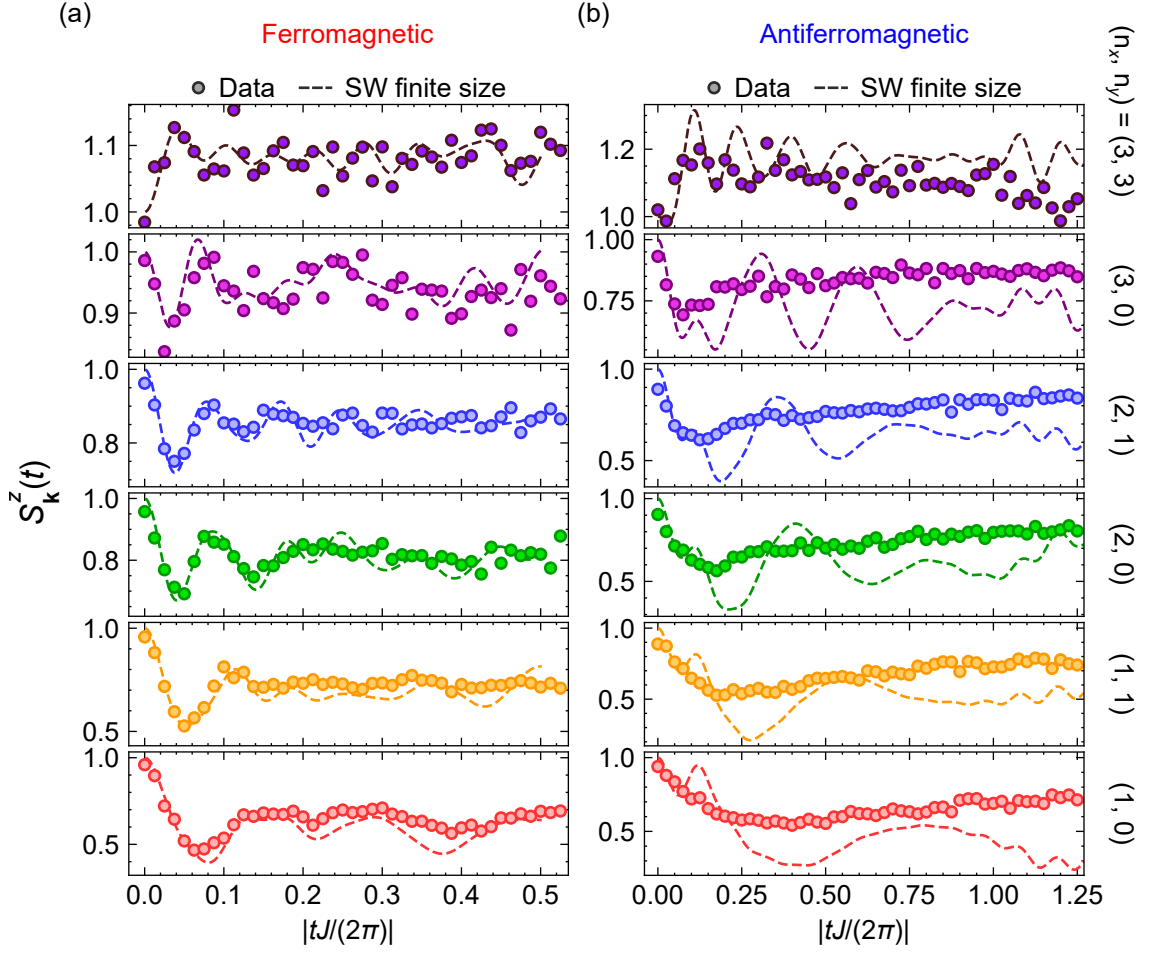
Figure 8.4: Time dependent structure factor. (a)/(b) Time evolution of the FM/AFM time-dependent structure factors $S_{\mathbf{k}}^z(z)$ (extracted from the data in Fig. 8.3) for different wave vectors $\mathbf{k} = \frac{2\pi}{\sqrt{N}}(n_x, n_y)$. The data shown in this figure has been taken with assembled arrays containing at most three defects.

also observe that the "speed" at which these correlations propagate differs for the FM and the AFM state suggesting a different dispersion relation.

We now turn to the measurement of the analysis of these z correlations to extract dispersion relation $\omega_{\mathbf{k}}^{\mathrm{FM/AFM}}$.

8.2.2 Extraction of the energy spectrum

Time-dependent structure factor. From the correlations, we calculate the time dependent structure factor $S_{\mathbf{k}}^z(t)$ for discrete values of the wave vector $\mathbf{k} \in \{k_x, k_y\} = \{n_x \frac{2\pi}{\sqrt{N}}, n_y \frac{2\pi}{\sqrt{N}}\}$ with $n_{x,y} \in \{\sqrt{N}/2 + 1, ..., \sqrt{N}/2\}$. Figure 8.4 shows some of these

$S_{\mathbf{k}}^z(t)$ curves for various values of $\{n_x, n_y\}$. For both the FM and AFM case, we observe that the $S_{\mathbf{k}}^z(t)$ curves do not follow a perfect sinusoidal function as predicted by the spin wave theory (see Eq. 8.21). In the FM case, we measure that for all wave vector $\mathbf{k}$, $S_{\mathbf{k}}^z(t)$ exhibits damped oscillations at small times. For some $\mathbf{k}$, we also observe a revival of these oscillations at long times. The AFM curves also seem to exhibit oscillations at small times but with a stronger damping compared to their FM counterpart with no visible revival of the oscillations at long times.

We identified three different physical processes that can explain the discrepancies between the measured $S_{\mathbf{k}}^z(t)$ curves and the ones predicted by the linear SW theory:

- **Finite size effects.** If the size of the array is not large enough, edge effects affect the dynamics of the system. In this case, spin waves of different wave vectors $\mathbf{k}$, and of different frequencies $\omega_{\mathbf{k}}$ are mixed. The $S_{\mathbf{k}}^z(t)$ curves would thus be the result of the sum of different sinusoidal curves oscillating at different frequencies, leading to an effective damping of the initial oscillation.

- **Particle-particle interaction.** If the number of excitations present in the system is too high, the approximations made in Eq. 8.2 break down, leading to extra terms in the XY Hamiltonian $\mathcal{H}_{\mathrm{XY}} = E_{\mathrm{rotor}} + \mathcal{H}_{\mathrm{rotor}} + \mathcal{H}_{\mathrm{SW}} + \mathcal{O}(b_j^3)$. These extra terms are non linear and correspond to interactions between the quasi-particles, which no longer behave as free quasiparticles and could result in damping of the $S_{\mathbf{k}}(t)$ oscillations. Furthermore, it can be shown that, due to the frustration induced by the AFM couplings, the number of particles is indeed higher in the AFM system, which could explain the stronger damping that we observe in the AFM case [Chen *et al.*, 2023b].

- **Experimental imperfections.** The damping that we observe could be induced by experimental imperfections and decoherence effects. Moreover, as preparing the initial state $|\mathrm{AFM}_y\rangle$ requires first creating a Néel state, which introduces more imperfections compared to preparing $|\mathrm{CSS}_y\rangle$, then, these additional imperfections may induce a stronger damping of the AFM oscillation compared to their FM counterparts which is consistent with the experimental observations.

To assess which physical process contribute the most, the team in Lyon calculated the result of the linear SW theory for a finite system size of $N = 10 \times 10$ spins (the details of these calculations can be found in the supplemental material of [Chen *et al.*, 2023b]). We compare these results (shown by dashed curves in Fig. 8.4) to the

experimental data. In the FM case, we observe relatively good agreements between the experimental results and the theoretical predictions indicating finite size effects play a significant role in the dynamics. However, the AFM data show a poor agreement with the finite size linear SW theory. For very early times $|tJ/(2\pi)| < 0.1$, the theoretical predictions match with the data, but for longer times, the theory predicts persistent oscillations that we do not observe experimentally. To assess the physical origins of this discrepancy, we repeated the experiments for small system sizes $N = 4 \times 4$ for which we can calculate the exact dynamics including the experimental imperfections (preparation and detection errors, Rydberg lifetimes and shot-to-shot positional disorder). The result indicate that experimental imperfections do not significantly alter the behavior of the $S_{\mathbf{k}}^z(t)$ oscillations (this analysis is not shown here but can be found in [Chen et al., 2023b]). We thus conclude that the damping of the $S_{\mathbf{k}}^z(t)$ oscillations in the AFM case observed in Fig. 8.4 is indeed intrinsic to the dynamics and can be at least partially attributed to interactions between the quasi-particles inducing non-linearities in the spin wave theory, an interesting result in itself.

Extracting the dispersion relations. To extract the FM/AFM dispersion relations, we fit each of these curves by a phenomenological damped cosine function defined as:

$$S_{\mathbf{k}}^z(t) = C_{\mathbf{k}}^{\text{fit}} + D_{\mathbf{k}}^{\text{fit}} \cos\big(2\omega_{\mathbf{k}}^{\text{fit}}t + \phi_{\mathbf{k}}^{\text{fit}}\big)e^{-t/\tau_{\mathbf{k}}^{\text{fit}}}, \tag{8.22}$$

with $C_{\mathbf{k}}^{\text{fit}}$, $D_{\mathbf{k}}^{\text{fit}}$, $\omega_{\mathbf{k}}^{\text{fit}}$, $\phi_{\mathbf{k}}^{\text{fit}}$ and τ^{fit} the fitting parameters. As shown in Fig. 8.5, to make sure the results are not biased by damping induced by the finite size effects or particle-particle interactions, we only fit the beginning of each $S_{\mathbf{k}}^z(t)$ curves where oscillations are still visible ($|tJ/(2\pi) < 0.2|$ for the FM and $|tJ/(2\pi) < 0.4|$ in the AFM case). From the fits, we extract the fitting parameters.

In Fig. 8.6a and b, we plot the extracted frequency $\omega_{\mathbf{k}}^{\text{fit}}$ as a function of $|\mathbf{k}|$. We compare these data to the SW theory calculation given by Eq. 8.16 and Eq. 8.17 for a system size of $N = 10 \times 10$ (yellow and purple square markers). In the FM case, we observe that the frequency $\omega_{\mathbf{k}}^{\text{fit}}$ increases non-linearly with $|\mathbf{k}|$, following a trend consistent with the theoretical predictions. Moreover, at low $|\mathbf{k}|$, we observe a good agreement between the measured frequencies and those predicted by the SW theory. At large wave vector $\mathbf{k}$, we observe a deviation between experiment and theory data. We attribute this discrepancy to finite size effects that modify the frequency $\omega_{\mathbf{k}}$ at large $|\mathbf{k}|$ (see [Chen et al., 2023b]). For the AFM case, we measure that $\omega_{\mathbf{k}}^{\text{fit}}$ increases
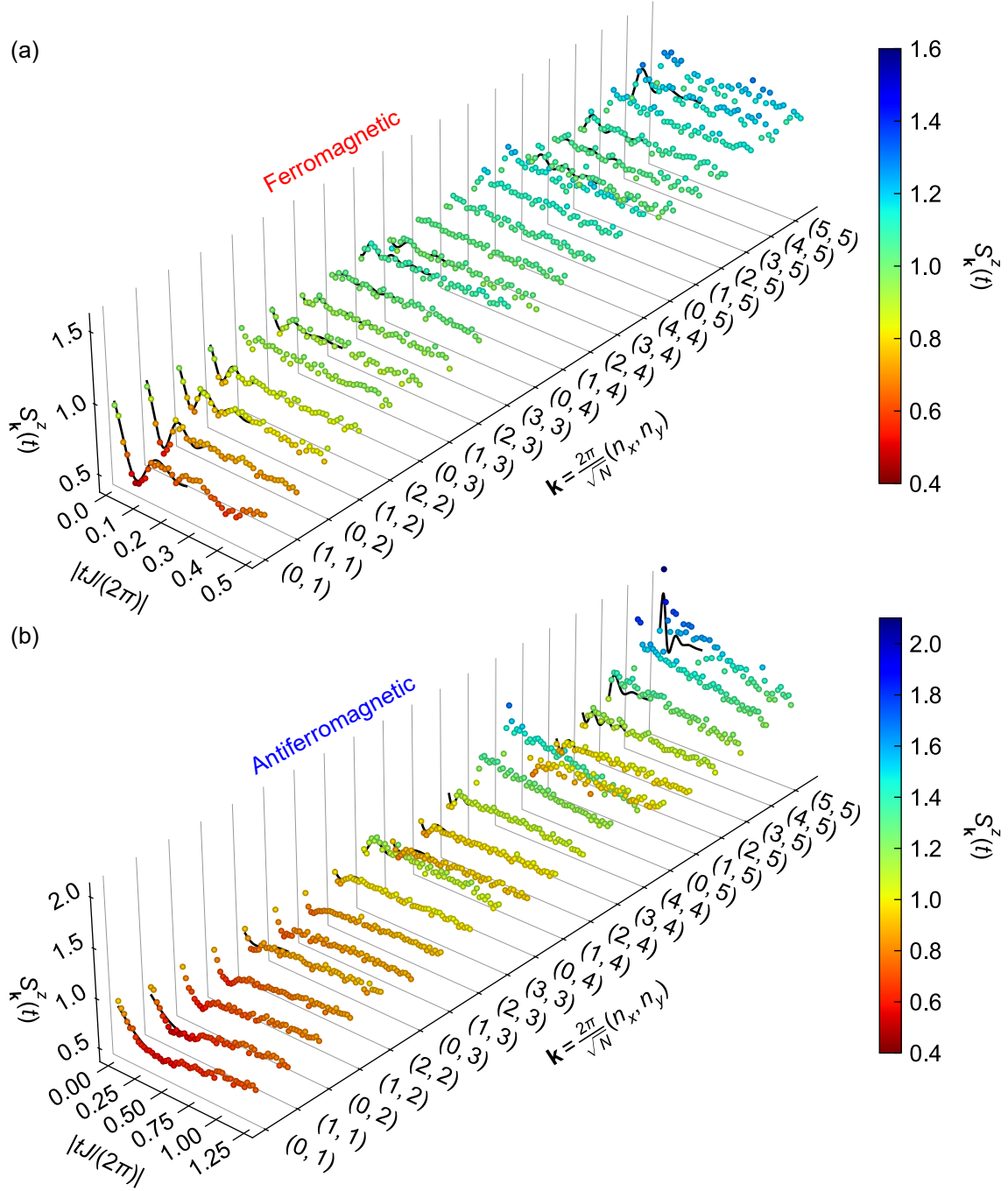
Figure 8.5: Full data sets for the time-dependent structure factor fitted by a cosine function. (a)/(b) Time evolution of the FM/AFM time-dependent structure factors $S_{\mathbf{k}}^z(z)$ (extracted from the data in Fig. 8.3) for different wave vectors $\mathbf{k} = \frac{2\pi}{\sqrt{N}}(n_x, n_y)$. Black solid lines: fit using a damped cosine function (see Eq. 8.22), we only fit the beginning of each curves with a time window of $|tJ/(2\pi) < 0.2|$ for the FM case and $|tJ/(2\pi) < 0.4|$ in the AFM one. The data shown in this figure have been taken with assembled arrays containing at most three defects.

Figure 8.6: Measurement of the dispersion relations. (a)/(b) Fitted frequency $\omega_{\mathbf{k}}^{\text{fit}}$ as a function of $|\mathbf{k}|$ for the FM/AFM case. Circle markers: experiment data. Square markers: SW theory calculation using 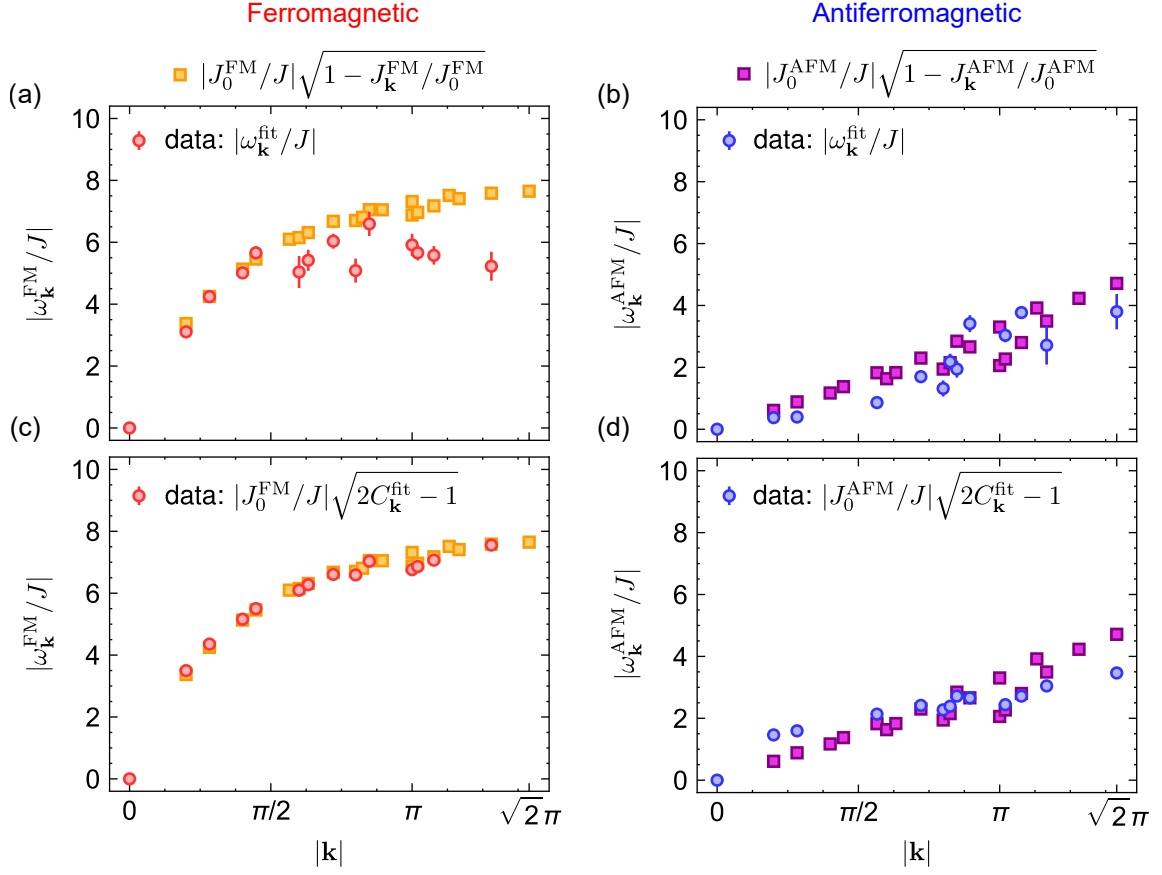Eq. 8.16 and Eq. 8.17 for a system size of $N = 10 \times 10$ (these are the same data points as the ones shown in Fig. 8.1). (c)/(d) Inferred frequencies from the fitted offset $\omega_{\mathbf{k}}^{\text{FM/AFM}} = J_0^{\text{FM/AFM}} \sqrt{2C_{\mathbf{k}}^{\text{fit}} - 1}$. The error bars represent the fit uncertainty of $\omega_{\mathbf{k}}^{\text{fit}}$ and $C_{\mathbf{k}}^{\text{fit}}$.

linearly with $|\mathbf{k}|$, which is also consistent with the theoretical predictions $\omega_{\mathbf{k}}^{\text{FM}} \propto |\mathbf{k}|$. Despite the $S_{\mathbf{k}}^z(t)$ curves being more strongly damped compared to the LSW theory, we also observe a relatively good agreement between theory and experiment.

We now focus the analysis on the amplitude $D_{\mathbf{k}}^{\text{fit}}$ and offset $C_{\mathbf{k}}^{\text{fit}}$ of each fit. Using Eq. 8.21, we compute the dispersion relations $\omega_{\mathbf{k}}$. As the fitted amplitudes $D_{\mathbf{k}}^{\text{fit}}$ are relatively noisy, we only focus of the offset terms and compute $\omega_{\mathbf{k}} = J_0 \sqrt{2C_{\mathbf{k}} - 1}$. Figure 8.6c and d show the inferred frequency as a function of $\sqrt{\mathbf{k}}$. For both FM and AFM, the data match the SW theory calculations and are in relatively good agreements with the fitted frequencies $\omega_{\mathbf{k}}^{\text{fit}}$.

These results confirm that the $1/r_{ij}^3$ tail of the dipolar XY interactions modifies

the properties of the low-lying excited FM/AFM states. It changes the excitation spectrum, thus altering the dispersion relation of the associated quasi-particles. In the FM case, the long range of the dipolar tail modifies the dispersion relation to be non-linear, while in the AFM case, it remains linear, characteristic of the effective short-range interactions induced by frustration.

8.3 Conclusion

In this chapter, I have presented a method called quench spectroscopy to measure the dispersion relation. This method consists in quenching the system to inject a finite density of excitations/quasi-particles and then measuring its dynamical evolution to extract the dispersion relation. Comparing the FM and AFM case, we confirm the theoretical prediction that dipolar ferromagnetic interactions modify the dispersion to be non-linear in the FM case. In the AFM case, the frustration resulting from the antiferromagnetic dipolar interactions leads to an effective cancellation of the long-range tail, recovering a linear dispersion relation (as in the case of finite-range interactions), which we also confirmed experimentally.

This quench spectroscopy procedure provides a more accessible way to measure the dispersion relation of a system. We believe it can be extend to characterize other systems using different spin Hamiltonians and implemented in other platforms.

Conclusion and outlook

In this manuscript, I have presented a few examples of quantum simulations of spin models based on arrays of single atoms excited in the Rydberg states. During my Ph.D., I have focused on the study of the dipolar XY model. I summarize here the main results and provide possible extensions of my work.

Implementation of the dipolar XY model. To implement the dipolar XY Hamiltonian, the spin states are encoded on two Rydberg states of opposite parities. This configuration couples the atoms via resonant dipole-dipole interactions, thereby realizing the dipolar XY model. When I joined the lab, experiments with approximately ten atoms ($N \sim 10$) had already been conducted using this model [de Léséleuc *et al.*, 2017; de Léséleuc *et al.*, 2019; Lienhard *et al.*, 2020]. Using the last upgrades installed by the former team to increase the number of atoms to a few hundreds and study the Ising model on large arrays [Scholl, 2021], we scaled up the number of atoms used in the quantum simulation of the XY model. Achieving this required addressing several limitations of the experimental setup.

- **Preparation and detection errors.** Many small improvements of the various manipulations of the atoms were made (see Chapter 2) to better excite/deexcite the atoms to/from the Rydberg states and improve microwave control of the spin states between the two Rydberg states. They allowed us to increase the preparation efficiency and minimize the detection errors.

- **Positional disorder.** The dipolar interaction strongly depends of the distance r between the atoms scaling as $\propto 1/r^3$. Therefore if the position of the atoms is not well controlled (static positional disorder) or vary from shot-to-shot (shot-to-shot positional disorder), it results in a disorder of the interatomic distances and, consequently, of the interaction energies. This disorder can destabilize the many-body system and prevent us from preparing or observing the phase we wish to characterize. We address this problem in two different ways. First we

upgraded the setup by performing Raman side band cooling to reduce the atomic temperature and, thus, the shot-to-shot positional disorder (see Chapter 2 and [Emperauger, 2025]). Second we started to investigate and study how to measure and correct the static positional disorder. We showed that based on the pairwise distances between the atoms, we can infer their position and thus correct it. We illustrated this method on a small system size, reducing the static positional disorder from $\sim 100\,\text{nm}$ to $\sim 20\,\text{nm}$ (see Chapter 4).

- **Local manipulation of the spins.** The spins can now be manipulated individually by using addressing beams inducing a local light shift on the target atoms (see Chapter 3). Historically, this method was used in the group to prepare one spin in one specific Rydberg state. During my Ph.D., we extended this method to arbitrary prepare any spins in $|\uparrow\rangle$ and the rest in $|\downarrow\rangle$. We can, for example, prepare Néel state $|\uparrow\downarrow\uparrow\downarrow\cdots\rangle$ of up to $N \sim 100$ atoms which turns out to be the starting point of many of our quantum simulation experiments of the XY models. We also showed that these local addressing beams allow us to perform arbitrary rotations on the atoms, enabling the measurement of exotic observables such as chirality and allow us to perform quantum state tomography.

We then performed two types of experiments. The first ones focuses of the preparation and characterization of the XY ground/highest energy state using various geometries. The second ones focuses of out-of-equilibrium state evolving under the dipolar XY model and leading to various interesting states.

Ground state physics of the dipolar XY model. We first studied the lowest /highest energy states of the XY model on 2D square arrays (see Chapter 5). Combining our ability to perform local rotations with an adiabatic procedure, we prepared these states and measured their properties in different bases. We showed that on any direction of the (x, y) plane, they exhibit complex ferromagnetic (FM) and antiferromagnetic (AFM) order. In particular, we assessed the role played by the relatively long-range tail of the dipolar interactions by measuring the averaged correlation along x as a function of the distance. We observed that, the AFM correlations decay faster with the distance than their FM counterpart. Then using partial quench experiments, we probed the $\{\delta, T\}$ phase diagram of the AFM/FM phase showing that the region for which the system exhibit an AFM order is smaller than the FM order region. These differences are induced by the dipolar tail of the interaction introducing frustration in

the AFM case and destabilizing its AFM order while it tends to stabilize the FM order.

Then, we moved to highly frustrated geometries. Theoretical works have predicted that the ground state of these systems could be an exotic phase of matter called spin liquids (Chapter 6). I presented our preliminary results on a $N = 114$ atoms in a Kagome array whose the ground state is expected to be a Dirac spin liquid. We showed that, in contrast with the ground state on square array, this state does not possess any magnetic order. Then we probed the response of the system to a local perturbation, and measured a signal consistent with Friedel oscillations which are the signature of a Dirac cone in the energy excitation spectrum. Further analyses are being made to better characterize the phase we prepared. Next, we moved to the chiral spin liquid, which is expected to be the ground state of the XY model using a breathing Kagome geometry. On a minimalistic system of two facing triangles, we prepared the ground state and measured the growth of chiral-chiral correlations between these triangles. This experiment illustrated the pairing mechanism of the chiralities between different triangles, which, in larger arrays, gives rise to a chiral spin liquid. This experiment represents the first step towards the realization and characterization of a chiral spin liquid.

Quench experiments.　We first demonstrated that, as predicted by recent theoretical works, the dipolar XY model can produce spin-squeezed states (see Chapter 7). These squeezed states are particularly interesting in the context of quantum metrology, as they can improve the sensitivity of measurements. We characterized this squeezing, showing that it is scalable, meaning that its metrological gain (squeezing parameter) increases with the system size. We also proposed different protocols that can be used for metrological applications.

Then we moved to the measurement of the XY dispersion relation. We used an alternative method called quench spectroscopy experiments (see Chapter 8). In contrast to "traditional methods", it offers the advantage that it does not require preparing the ground state of the system which can be challenging. It consists in initializing the system in an "easy to prepare" state whose energy is relatively close to its ground state energy, and let it freely evolves under the XY model. The linear theory then predicts that by measuring the dynamical evolution of the correlations, we can extract the dispersion relation. We applied the quench spectroscopy method to our system, and measured the dispersion relation of the dipolar XY model. Our results showed

a non linear dispersion relation $\omega_{\mathbf{k}}^{\mathrm{FM}} \propto \sqrt{|\mathbf{k}|}$ in the FM case while the AFM one in linear $\omega_{\mathbf{k}}^{\mathrm{AFM}} \propto |\mathbf{k}|$. These observations are consistent with the theory predictions. This method is relatively general and can thus be applied to other quantum simulator platforms exhibiting different Hamiltonians.

Outlook. We showed that Rydberg platforms are well suited to explore the dipolar XY model as it can be naturally implemented using Rydberg interactions. We performed experiments with hundreds of atoms which in many situations (*e.g.*, frustration induced by AFM couplings, out-of-equilibrium dynamics,...) exceed the number of spins that can be classically simulated. We demonstrated that the platform allows testing and verifying theory predictions: we highlighted how the dipolar tail of the interactions modifies the AFM/FM ground state properties, we showed that the dipolar XY model can generate scalable squeezing, and measure a linear/non-linear dispersion relation consistent for the AFM/FM case.

Future perspectives are envisioned for the experiments. First, on the setup, we identified and discussed a list of experimental imperfections (preparations and detection errors, positional disorder,...) that we believe can be addressed and minimized using technical solutions. We also discussed experimental upgrades that can be added to extend the versatility of the platform: allowing for example to prepare and readout any atoms in any arbitrary basis. We also wish to assemble larger arrays with more atoms. As we have seen, the size of array of $N \approx 100$ atoms is a limitation for the study of some many-body systems, for example, we suffer from edge effects when trying to the extract the dispersion relation $\omega_{\mathbf{k}}$ of the XY model (see Chapter 8). On the quantum simulation front, as explained, we started to explore exotic phases of matter such as spin liquids. Many other directions are also possible, we recently started to study the so called bosonic *t-J* model encoding the spin-1 states onto three different Rydberg states [Homeier *et al.*, 2024]. At the time of writing this manuscript, another setup is being build in order to hopefully solve theses technological challenges with getting more atoms.

Beyond the exploration of fundamental many-body physics problems, other applications are also possible. As we have seen, dipolar interactions can generate spin squeezed states. Metrological applications can then be thought. One could for example imagine to combine our ability to generate spin squeezed state with the natural high sensitivity of Rydberg states to electric fields to build quantum sensors based on Rydberg atoms. Other applications in quantum computing are also being developed,

recently, numerous companies such as QuEra® or Pasqal® emerged trying to build quantum computers based on Rydberg atoms [Henriet *et al.*, 2020].

Correcting the detection errors

In this Appendix we discuss the effects of the detection errors $\varepsilon_\uparrow/\varepsilon_\downarrow$ on the different observables that we measure. Due to the finite efficiency of each step in the readout sequence discussed in Sec. 2.3, an atom in $|\uparrow\rangle/|\downarrow\rangle$ has a small probability $\varepsilon_\uparrow/\varepsilon_\downarrow$ to be detected in $|\downarrow\rangle/|\uparrow\rangle$. The different observables that we measure (such as magnetization or correlation functions) can be corrected to account for these detection errors. We now describe this correction procedure, first for one atom and then for N atoms.

We denote $\mathbf{P}^i = (P_\uparrow^i, P_\downarrow^i)$ the probability to measure the atom i in $|\uparrow\rangle$ and $|\downarrow\rangle$. These raw probabilities are linked to their corresponding quantities $\tilde{\mathbf{P}}^i = (\tilde{P}_\uparrow^i, \tilde{P}_\downarrow^i)$ free from detection errors by $\mathbf{P}^i = M\tilde{\mathbf{P}}^i$, with M the detection error matrix:

$$M = \begin{pmatrix} 1 - \epsilon_\uparrow & \epsilon_\downarrow \\ \epsilon_\uparrow & 1 - \epsilon_\downarrow \end{pmatrix}. \tag{A.1}$$

To correct the raw data for detection errors we invert M and calculate $\tilde{\mathbf{P}}^i = M^{-1}\mathbf{P}^i$. We now extend this formula to N atoms. To do so, we now introduce $\mathbf{P} = (P_{\uparrow\cdots\uparrow}, P_{\uparrow\cdots\uparrow\downarrow}, \ldots, P_{\downarrow\cdots\downarrow})$ the probability to measure the N-atom in the 2^N different states $(|\uparrow\cdots\uparrow\rangle, |\uparrow\cdots\uparrow\downarrow\rangle, \ldots, |\uparrow\cdots\uparrow\downarrow\rangle)$. We also define the corresponding quantities $\tilde{\mathbf{P}}$ free from detection errors. Assuming that the detections are uncorrelated and remain of the same amplitude for each atoms, the formula now reads:

$$\mathbf{P} = \left(\bigotimes_{i=1}^{N} M \right) \tilde{\mathbf{P}}. \tag{A.2}$$

The matrix $\bigotimes_{i=1}^{N} M = M \otimes M \otimes \cdots \otimes M$ can be inverted to calculate $\tilde{\mathbf{P}}$.

Using the above formulas, we now explicitly calculate and analyse the effect of the detection errors on a few observables. For the rest of this appendix, for each observable value $\langle \mathcal{O} \rangle$, we will associate the corresponding value $\langle \tilde{\mathcal{O}} \rangle$ free from detection errors.

For an atom i, its magnetization reads:

$$\langle \sigma_i^{x,y,z} \rangle = (\varepsilon_\downarrow - \varepsilon_\uparrow) + (1 - \varepsilon_\downarrow - \varepsilon_\uparrow) \langle \tilde{\sigma}_i^{x,y,z} \rangle. \tag{A.3}$$

As $-1 \leqslant \langle \tilde{\sigma}_i^{x,y,z} \rangle \leqslant 1$, the above equations shows that the detection errors bound the measured values to $-1 + 2\varepsilon_\downarrow \leqslant \langle \sigma_i^{x,y,z} \rangle \leqslant 1 - 2\varepsilon_\uparrow$. This formula can be extended using any linear combination of $\langle \sigma_i^{x,y,z} \rangle$ with different atoms. For example, for the collective spin vector $\langle J_{x,y,z} \rangle = \frac{N}{2} \sum_i \langle \sigma_i^{x,y,z} \rangle$ we get:

$$\langle J_{x,y,z} \rangle = \frac{N}{2} (\varepsilon_\downarrow - \varepsilon_\uparrow) + (1 - \varepsilon_\downarrow - \varepsilon_\uparrow) \langle \tilde{J}_{x,y,z} \rangle. \tag{A.4}$$

We now consider a two body correlation function between two different atoms i and j (with $i \neq j$). At first order in $\varepsilon_{\uparrow,\downarrow}$, the formula reads:

$$\langle \sigma_i^{x,y,z} \sigma_j^{x,y,z} \rangle \approx (1 - 2\varepsilon_\downarrow - 2\varepsilon_\uparrow) \langle \tilde{\sigma}_i^{x,y,z} \tilde{\sigma}_j^{x,y,z} \rangle + (\varepsilon_\downarrow - \varepsilon_\uparrow) \left(\langle \tilde{\sigma}_i^{x,y,z} \rangle + \langle \tilde{\sigma}_j^{x,y,z} \rangle \right). \tag{A.5}$$

Similarly, we can derive a similar formula for the two body connected correlations:

$$\langle \sigma_i^{x,y,z} \sigma_j^{x,y,z} \rangle_c = \langle \sigma_i^{x,y,z} \sigma_j^{x,y,z} \rangle - \langle \sigma_i^{x,y,z} \rangle \langle \sigma_j^{x,y,z} \rangle \approx (1 - 2\varepsilon_\downarrow - 2\varepsilon_\uparrow) \langle \tilde{\sigma}_i^{x,y,z} \tilde{\sigma}_j^{x,y,z} \rangle_c \tag{A.6}$$

Here, the effect of the detection errors on $\langle \sigma_i^{x,y,z} \sigma_j^{x,y,z} \rangle_c$, is to reduce the amplitude of the measurement correlations by a factor $(1 - 2\varepsilon_\downarrow - 2\varepsilon_\uparrow)$. We now turn to the variance of the spin operator $\mathrm{Var}\,(J_{x,y,z})$ which reads:

$$\begin{aligned} \mathrm{Var}\,(J_{x,y,z}) &= \langle J_{x,y,z}^{\,2} \rangle - \langle J_{x,y,z} \rangle^2 \\ &\approx (1 - 2\varepsilon_\downarrow - 2\varepsilon_\uparrow) \mathrm{Var}\left(\tilde{J}_{x,y,z} \right) \\ &\quad + \varepsilon_\downarrow \left(\frac{N}{2} - \langle \tilde{J}_{x,y,z} \rangle \right) + \varepsilon_\uparrow \left(\frac{N}{2} + \langle \tilde{J}_{x,y,z} \rangle \right). \end{aligned} \tag{A.7}$$

Assuming that the magnetization measured in the same basis is negligible $|\langle \tilde{J}_{x,y,z} \rangle| \ll N/2$, this expression can be simplified as the sum of two terms:

$$\mathrm{Var}\,(J_{x,y,z}) \approx (1 - 2\varepsilon_\downarrow - 2\varepsilon_\uparrow) \mathrm{Var}\left(\tilde{J}_{x,y,z} \right) + \frac{N}{2} (\varepsilon_\downarrow + \varepsilon_\uparrow). \tag{A.8}$$

The first term represent a reduction of the measured variance by a factor $(1 - 2\varepsilon_\downarrow - 2\varepsilon_\uparrow)$. The second term represent a lower bound of the minimum variance that we can

measure. Even in the case where $\text{Var}\left(\tilde{J}_{x,y,z}\right) = 0$, we would experimentally measure $\text{Var}\left(J_{x,y,z}\right) \approx \frac{N}{2}\left(\varepsilon_\downarrow + \varepsilon_\uparrow\right)$. This implies that the spin squeezing that we measure in Chapter 7 is ultimately limited by the detection errors. To correct the spin squeezing parameter ξ_R^2 for the detection errors (as mentioned in Sec. 7.1.2) we invert Eq. A.4 and A.8 to compute $\tilde{\xi}_\text{R}^2 = \text{Var}\left(\tilde{J}_{\theta^\star}\right)/\langle\tilde{J}_y\rangle^2$.

Bibliography

"Scientists make seven-bit quantum leap in computer research," (2000) [cited in page 24].

"12-qubits reached in quantum information quest," (2006) [cited in page 24].

"World's first 28 qubit quantum computer demonstrated online at supercomputing 2007 conference," (2007) [cited in page 24].

Acín, A., Bruß, D., Lewenstein, M., and Sanpera, A., *"Classification of mixed three-qubit states,"* Phys. Rev. Lett. **87**, 040401 (2001) [cited in page 87].

Altman, E., Brown, K. R., Carleo, G., Carr, L. D., Demler, E., Chin, C., DeMarco, B., Economou, S. E., Eriksson, M. A., Fu, K.-M. C., Greiner, M., Hazzard, K. R., Hulet, R. G., Kollár, A. J., Lev, B. L., Lukin, M. D., Ma, R., Mi, X., Misra, S., Monroe, C., Murch, K., Nazario, Z., Ni, K.-K., Potter, A. C., Roushan, P., Saffman, M., Schleier-Smith, M., Siddiqi, I., Simmonds, R., Singh, M., Spielman, I., Temme, K., Weiss, D. S., Vučković, J., Vuletić, V., Ye, J., and Zwierlein, M., *"Quantum simulators: Architectures and opportunities,"* PRX Quantum **2**, 017003 (2021) [cited in pages 15 and 21].

Andersen, T. I., Astrakhantsev, N., Karamlou, A., Berndtsson, J., Motruk, J., Szasz, A., Gross, J. A., Westerhout, T., Zhang, Y., Forati, E., Rossi, D., Kobrin, B., Paolo, A. D., Klots, A. R., Drozdov, I., Kurilovich, V. D., Petukhov, A., Ioffe, L. B., Elben, A., Rath, A., Vitale, V., Vermersch, B., Acharya, R., Beni, L. A., Anderson, K., Ansmann, M., Arute, F., Arya, K., Asfaw, A., Atalaya, J., Ballard, B., Bardin, J. C., Bengtsson, A., Bilmes, A., Bortoli, G., Bourassa, A., Bovaird, J., Brill, L., Broughton, M., Browne, D. A., Buchea, B., Buckley, B. B., Buell, D. A., Burger, T., Burkett, B., Bushnell, N., Cabrera, A., Campero, J., Chang, H.-S., Chen, Z., Chiaro, B., Claes, J., Cleland, A. Y., Cogan, J., Collins, R., Conner, P., Courtney, W., Crook, A. L., Das, S., Debroy, D. M., Lorenzo, L. D., Barba, A. D. T., Demura, S., Devoret, M., Donohoe, P., Dunsworth, A., Earle, C., Eickbusch, A., Elbag, A. M., Elzouka, M., Erickson, C., Faoro, L., Fatemi, R., Ferreira, V. S., Burgos, L. F., Fowler, A. G., Foxen, B., Ganjam, S., Gasca, R., Giang, W., Gidney, C., Gilboa, D.,

Giustina, M., Gosula, R., Dau, A. G., Graumann, D., Greene, A., Habegger, S., Hamilton, M. C., Hansen, M., Harrigan, M. P., Harrington, S. D., Heslin, S., Heu, P., Hill, G., Hoffmann, M. R., Huang, H.-Y., Huang, T., Huff, A., Huggins, W. J., Isakov, S. V., Jeffrey, E., Jiang, Z., Jones, C., Jordan, S., Joshi, C., Juhas, P., Kafri, D., Kang, H., Kechedzhi, K., Khaire, T., Khattar, T., Khezri, M., Kieferová, M., Kim, S., Kitaev, A., Klimov, P. V., Korotkov, A. N., Kostritsa, F., Kreikebaum, J. M., Landhuis, D., Langley, B. W., Laptev, P., Lau, K.-M., Guevel, L. L., Ledford, J., Lee, J., Lee, K., Lensky, Y. D., Lester, B. J., Li, W. Y., Lill, A. T., Liu, W., Livingston, W. P., Locharla, A., Lundahl, D., Lunt, A., Madhuk, S., Maloney, A., Mandrà, S., Martin, L. S., Martin, O., Martin, S., Maxfield, C., McClean, J. R., McEwen, M., Meeks, S., Miao, K. C., Mieszala, A., Molina, S., Montazeri, S., Morvan, A., Movassagh, R., Neill, C., Nersisyan, A., Newman, M., Nguyen, A., Nguyen, M., Ni, C.-H., Niu, M. Y., Oliver, W. D., Ottosson, K., Pizzuto, A., Potter, R., Pritchard, O., Pryadko, L. P., Quintana, C., Reagor, M. J., Rhodes, D. M., Roberts, G., Rocque, C., Rosenberg, E., Rubin, N. C., Saei, N., Sankaragomathi, K., Satzinger, K. J., Schurkus, H. F., Schuster, C., Shearn, M. J., Shorter, A., Shutty, N., Shvarts, V., Sivak, V., Skruzny, J., Small, S., Smith, W. C., Springer, S., Sterling, G., Suchard, J., Szalay, M., Sztein, A., Thor, D., Torres, A., Torunbalci, M. M., Vaishnav, A., Vdovichev, S., Villalonga, B., Heidweiller, C. V., Waltman, S., Wang, S. X., White, T., Wong, K., Woo, B. W., Xing, C., Yao, Z. J., Yeh, P., Ying, B., Yoo, J., Yosri, N., Young, G., Zalcman, A., Zhu, N., Zobrist, N., Neven, H., Babbush, R., Boixo, S., Hilton, J., Lucero, E., Megrant, A., Kelly, J., Chen, Y., Smelyanskiy, V., Vidal, G., Roushan, P., Lauchli, A. M., Abanin, D. A., and Mi, X., *"Thermalization and criticality on an analog-digital quantum simulator,"* (2024), arXiv:2405.17385 [quant-ph] [cited in page 21].

Anderson, P., *"Resonating valence bonds: A new kind of insulator?"* Materials Research Bulletin **8**, 153 (1973) [cited in pages 117 and 138].

Anderson, P. W., *"The resonating valence bond state in la2cuo4 and superconductivity,"* Science **235**, 1196 (1987) [cited in pages 112, 117, and 134].

Arute, F., Arya, K., Babbush, R., Bacon, D., Bardin, J. C., Barends, R., Biswas, R., Boixo, S., Brandao, F. G. S. L., Buell, D. A., Burkett, B., Chen, Y., Chen, Z., Chiaro, B., Collins, R., Courtney, W., Dunsworth, A., Farhi, E., Foxen, B., Fowler, A., Gidney, C., Giustina, M., Graff, R., Guerin, K., Habegger, S., Harrigan, M. P.,

Hartmann, M. J., Ho, A., Hoffmann, M., Huang, T., Humble, T. S., Isakov, S. V., Jeffrey, E., Jiang, Z., Kafri, D., Kechedzhi, K., Kelly, J., Klimov, P. V., Knysh, S., Korotkov, A., Kostritsa, F., Landhuis, D., Lindmark, M., Lucero, E., Lyakh, D., Mandrà, S., McClean, J. R., McEwen, M., Megrant, A., Mi, X., Michielsen, K., Mohseni, M., Mutus, J., Naaman, O., Neeley, M., Neill, C., Niu, M. Y., Ostby, E., Petukhov, A., Platt, J. C., Quintana, C., Rieffel, E. G., Roushan, P., Rubin, N. C., Sank, D., Satzinger, K. J., Smelyanskiy, V., Sung, K. J., Trevithick, M. D., Vainsencher, A., Villalonga, B., White, T., Yao, Z. J., Yeh, P., Zalcman, A., Neven, H., and Martinis, J. M., *"Quantum supremacy using a programmable superconducting processor,"* Nature **574**, 505 (2019) [cited in pages 16 and 24].

Ashkin, A., Dziedzic, J. M., Bjorkholm, J. E., and Chu, S., *"Observation of a single-beam gradient force optical trap for dielectric particles,"* Optics Letters **11**, 288 (1986) [cited in page 13].

Aspect, A., Grangier, P., and Roger, G., *"Experimental realization of Einstein-Podolsky-Rosen-Bohm gedankenexperiment: A new violation of Bell's inequalities,"* Physical Review Letters **49**, 91 (1982) [cited in page 13].

Atala, M., Aidelsburger, M., Barreiro, J. T., Abanin, D., Kitagawa, T., Demler, E., and Bloch, I., *"Direct measurement of the zak phase in topological bloch bands,"* Nature Physics **9**, 795 (2013) [cited in page 20].

Auerbach, A., Interacting Electrons and Quantum Magnetism (Springer-Verlag, 1994) [cited in page 143].

Bakr, W. S., Gillen, J. I., Peng, A., Fölling, S., and Greiner, M., *"A quantum gas microscope for detecting single atoms in a hubbard-regime optical lattice,"* Nature **462**, 74 (2009) [cited in page 19].

Balasubramanian, G., Chan, I. Y., Kolesov, R., Al-Hmoud, M., Tisler, J., Shin, C., Kim, C., Wojcik, A., Hemmer, P. R., Krueger, A., Hanke, T., Leitenstorfer, A., Bratschitsch, R., Jelezko, F., and Wrachtrup, J., *"Nanoscale imaging magnetometry with diamond spins under ambient conditions,"* Nature **455**, 648 (2008) [cited in page 14].

Balents, L., *"Spin liquids in frustrated magnets,"* Nature **464**, 199 (2010) [cited in pages 133 and 138].

Ballance, C. J., Harty, T. P., Linke, N. M., Sepiol, M. A., and Lucas, D. M., *"High-fidelity quantum logic gates using trapped-ion hyperfine qubits,"* Phys. Rev. Lett. **117**, 060504 (2016) [cited in page 24].

Bao, Y., Yu, S. S., Anderegg, L., Chae, E., Ketterle, W., Ni, K.-K., and Doyle, J. M., *"Dipolar spin-exchange and entanglement between molecules in an optical tweezer array,"* Science **382**, 1138 (2023) [cited in page 158].

Bardeen, J., Cooper, L. N., and Schrieffer, J. R., *"Theory of superconductivity,"* Phys. Rev. **108**, 1175 (1957) [cited in page 15].

Barends, R., Kelly, J., Megrant, A., Veitia, A., Sank, D., Jeffrey, E., White, T. C., Mutus, J., Fowler, A. G., Campbell, B., Chen, Y., Chen, Z., Chiaro, B., Dunsworth, A., Neill, C., O'Malley, P., Roushan, P., Vainsencher, A., Wenner, J., Korotkov, A. N., Cleland, A. N., and Martinis, J. M., *"Superconducting quantum circuits at the surface code threshold for fault tolerance,"* Nature **508**, 500 (2014) [cited in page 24].

Barends, R., Lamata, L., Kelly, J., García-Álvarez, L., Fowler, A. G., Megrant, A., Jeffrey, E., White, T. C., Sank, D., Mutus, J. Y., Campbell, B., Chen, Y., Chen, Z., Chiaro, B., Dunsworth, A., Hoi, I.-C., Neill, C., O'Malley, P. J. J., Quintana, C., Roushan, P., Vainsencher, A., Wenner, J., Solano, E., and Martinis, J. M., *"Digital quantum simulation of fermionic models with a superconducting circuit,"* Nature Communications **6**, 7654 (2015) [cited in page 21].

Barends, R., Quintana, C. M., Petukhov, A. G., Chen, Y., Kafri, D., Kechedzhi, K., Collins, R., Naaman, O., Boixo, S., Arute, F., Arya, K., Buell, D., Burkett, B., Chen, Z., Chiaro, B., Dunsworth, A., Foxen, B., Fowler, A., Gidney, C., Giustina, M., Graff, R., Huang, T., Jeffrey, E., Kelly, J., Klimov, P. V., Kostritsa, F., Landhuis, D., Lucero, E., McEwen, M., Megrant, A., Mi, X., Mutus, J., Neeley, M., Neill, C., Ostby, E., Roushan, P., Sank, D., Satzinger, K. J., Vainsencher, A., White, T., Yao, J., Yeh, P., Zalcman, A., Neven, H., Smelyanskiy, V. N., and Martinis, J. M., *"Diabatic gates for frequency-tunable superconducting qubits,"* Phys. Rev. Lett. **123**, 210501 (2019) [cited in page 24].

Barredo, D., Lienhard, V., de Léséleuc, S., Lahaye, T., and Browaeys, A., *"Synthetic three-dimensional atomic structures assembled atom by atom,"* Nature **561**, 79 (2018) [cited in page 25].

Barredo, D., Lienhard, V., Scholl, P., de Léséleuc, S., Boulier, T., Browaeys, A., and Lahaye, T., *"Three-dimensional trapping of individual Rydberg atoms in ponderomotive bottle beam traps,"* Phys. Rev. Lett. **124**, 023201 (2020) [cited in pages 25 and 55].

Barredo, D., de Léséleuc, S., Lienhard, V., Lahaye, T., and Browaeys, A., *"An atom-by-atom assembler of defect-free arbitrary two-dimensional atomic arrays,"* Science **354**, 1021 (2016) [cited in pages 23, 24, 25, 37, and 38].

Barredo, D., Ravets, S., Labuhn, H., Béguin, L., Vernier, A., Nogrette, F., Lahaye, T., and Browaeys, A., *"Demonstration of a strong rydberg blockade in three-atom systems with anisotropic interactions,"* Phys. Rev. Lett. **112**, 183002 (2014) [cited in page 24].

Barry, J. F., Schloss, J. M., Bauch, E., Turner, M. J., Hart, C. A., Pham, L. M., and Walsworth, R. L., *"Sensitivity optimization for nv-diamond magnetometry,"* Rev. Mod. Phys. **92**, 015004 (2020) [cited in page 14].

Baskaran, G., *"Novel local symmetries and chiral-symmetry-broken phases in s=(1/2 triangular-lattice heisenberg model,"* Phys. Rev. Lett. **63**, 2524 (1989) [cited in page 146].

Baskaran, G., *"Five-fold way to new high tc superconductors,"* Pramana **73**, 61 (2009) [cited in page 112].

Baskaran, G., Zou, Z., and Anderson, P. W., *"The resonating valence bond state and high-tc superconductivity – a mean field theory,"* Solid State Communications **63**, 973 (1987) [cited in page 112].

Bastien, G., *"Quantum simulation with arrays of individual rydberg atoms: toward a new generation of quantum simulators,"* (2023), internship report - Master 2 QLMN (Université Paris-Saclay) [cited in page 96].

Beguin, L., Mesure de l' interaction de van der Waals entre deux atomes de Rydberg, Ph.D. thesis (2013), thèse de doctorat dirigée par Browaeys, Antoine Physique Palaiseau, Institut d'optique théorique et appliquée 2013 [cited in pages 32 and 33].

Bell, J. S., *"On the einstein podolsky rosen paradox,"* Physics Physique Fizika **1**, 195 (1964) [cited in page 13].

Benhelm, J., Kirchmair, G., Roos, C. F., and Blatt, R., *"Towards fault-tolerant quantum computing with trapped ions,"* Nature Physics **4**, 463 (2008) [cited in page 24].

Bennett, C. H., Bessette, F., Brassard, G., Salvail, L., and Smolin, J., *"Experimental quantum cryptography,"* Journal of Cryptology **5**, 3 (1992) [cited in page 14].

Bennett, C. H. and Wiesner, S. J., *"Communication via one- and two-particle operators on einstein-podolsky-rosen states,"* Phys. Rev. Lett. **69**, 2881 (1992) [cited in page 14].

Berezinsky, V. L., *"Destruction of long range order in one-dimensional and two-dimensional systems having a continuous symmetry group. I. Classical systems,"* Sov. Phys. JETP **32**, 493 (1971) [cited in page 128].

Bernien, H., Schwartz, S., Keesling, A., Levine, H., Omran, A., Pichler, H., Choi, S., Zibrov, A. S., Endres, M., Greiner, M., Vuletić, V., and Lukin, M. D., *"Probing many-body dynamics on a 51-atom quantum simulator,"* Nature **551**, 579 (2017) [cited in page 24].

Bintz, M., Liu, V. S., Hauschild, J., Khalifa, A., Chatterjee, S., Zaletel, M. P., and Yao, N. Y., *"Dirac spin liquid in quantum dipole arrays,"* (2024) [cited in pages 103, 135, 143, and 145].

Birkl, G. and Fortágh, J., *"Micro traps for quantum information processing and precision force sensing,"* Laser & Photonics Reviews **1**, 12 (2007) [cited in page 64].

Blatt, R. and Roos, C. F., *"Quantum simulations with trapped ions,"* Nature Physics **8**, 277 (2012) [cited in page 64].

Bloch, I., *"Ultracold quantum gases in optical lattices,"* Nature Physics **1**, 23 (2005) [cited in page 19].

Block, M., Ye, B., Roberts, B., Chern, S., Wu, W., Wang, Z., Pollet, L., Davis, E. J., Halperin, B. I., and Yao, N. Y., *"A Universal Theory of Spin Squeezing,"* (2023) [cited in pages 162 and 165].

Bornet, G., Emperauger, G., Chen, C., Machado, F., Chern, S., Leclerc, L., Gély, B., Chew, Y. T., Barredo, D., Lahaye, T., Yao, N. Y., and Browaeys, A., *"Enhancing a*

many-body dipolar rydberg tweezer array with arbitrary local controls," Phys. Rev. Lett. **132**, 263601 (2024) [cited in pages 77 and 146].

Bornet, G., Emperauger, G., Chen, C., Ye, B., Block, M., Bintz, M., Boyd, J. A., Barredo, D., Comparin, T., Mezzacapo, F., Roscilde, T., Lahaye, T., Yao, N. Y., and Browaeys, A., *"Scalable spin squeezing in a dipolar rydberg atom array,"* Nature **621**, 728 (2023) [cited in page 158].

Broholm, C., Cava, R. J., Kivelson, S. A., Nocera, D. G., Norman, M. R., and Senthil, T., *"Quantum spin liquids,"* Science **367**, eaay0668 (2020) [cited in page 133].

Browaeys, A. and Lahaye, T., *"Many-body physics with individually controlled rydberg atoms,"* Nature Physics **16**, 132 (2020) [cited in pages 25 and 26].

Brown, L. S. and Gabrielse, G., *"Geonium theory: Physics of a single electron or ion in a penning trap,"* Rev. Mod. Phys. **58**, 233 (1986) [cited in page 20].

Brown, M. O., Thiele, T., Kiehl, C., Hsu, T.-W., and Regal, C. A., *"Gray-molasses optical-tweezer loading: Controlling collisions for scaling atom-array assembly,"* Phys. Rev. X **9**, 011057 (2019) [cited in page 37].

Bruno, P., *"Absence of spontaneous magnetic order at nonzero temperature in one- and two-dimensional heisenberg and XY systems with long-range interactions,"* Phys. Rev. Lett. **87**, 137203 (2001) [cited in page 122].

Brydges, T., Elben, A., Jurcevic, P., Vermersch, B., Maier, C., Lanyon, B. P., Zoller, P., Blatt, R., and Roos, C. F., *"Probing rényi entanglement entropy via randomized measurements,"* Science **364**, 260 (2019) [cited in page 63].

Cai, J., Retzker, A., Jelezko, F., and Plenio, M. B., *"A large-scale quantum simulator on a diamond surface at room temperature,"* Nature Physics **9**, 168 (2013) [cited in page 158].

Cevolani, L., Despres, J., Carleo, G., Tagliacozzo, L., and Sanchez-Palencia, L., *"Universal scaling laws for correlation spreading in quantum systems with short- and long-range interactions,"* Phys. Rev. B **98**, 024302 (2018) [cited in page 180].

Chen, C., Bornet, G., Bintz, M., Emperauger, G., Leclerc, L., Liu, V. S., Scholl, P., Barredo, D., Hauschild, J., Chatterjee, S., Schuler, M., Läuchli, A. M., Zaletel, M.

P., Lahaye, T., Yao, N. Y., and Browaeys, A., *"Continuous symmetry breaking in a two-dimensional rydberg array,"* Nature **616**, 691 (2023a) [cited in pages 110, 129, 130, and 131].

Chen, C., Emperauger, G., Bornet, G., Caleca, F., Gély, B., Bintz, M., Chatterjee, S., Liu, V., Barredo, D., Yao, N. Y., Lahaye, T., Mezzacapo, F., Roscilde, T., and Browaeys, A., *"Spectroscopy of elementary excitations from quench dynamics in a dipolar xy rydberg simulator,"* (2023b) [cited in pages 181, 187, 190, and 191].

Chen, Y., Neill, C., Roushan, P., Leung, N., Fang, M., Barends, R., Kelly, J., Campbell, B., Chen, Z., Chiaro, B., Dunsworth, A., Jeffrey, E., Megrant, A., Mutus, J. Y., O'Malley, P. J. J., Quintana, C. M., Sank, D., Vainsencher, A., Wenner, J., White, T. C., Geller, M. R., Cleland, A. N., and Martinis, J. M., *"Qubit architecture with high coherence and fast tunable coupling,"* Phys. Rev. Lett. **113**, 220502 (2014) [cited in page 20].

Chow, J. M., Gambetta, J. M., Córcoles, A. D., Merkel, S. T., Smolin, J. A., Rigetti, C., Poletto, S., Keefe, G. A., Rothwell, M. B., Rozen, J. R., Ketchen, M. B., and Steffen, M., *"Universal quantum gate set approaching fault-tolerant thresholds with superconducting qubits,"* Phys. Rev. Lett. **109**, 060501 (2012) [cited in page 24].

Chuang, I. L., Gershenfeld, N., and Kubinec, M., *"Experimental implementation of fast quantum searching,"* Phys. Rev. Lett. **80**, 3408 (1998) [cited in page 24].

Cirac, J. I. and Zoller, P., *"Quantum computations with cold trapped ions,"* Phys. Rev. Lett. **74**, 4091 (1995) [cited in page 20].

Cline, R. A., Miller, J. D., Matthews, M. R., and Heinzen, D. J., *"Spin relaxation of optically trapped atoms by light scattering,"* Opt Lett **19**, 207 (1994) [cited in pages 48 and 49].

Colombo, S., Pedrozo-Peñafiel, E., Adiyatullin, A. F., Li, Z., Mendez, E., Shu, C., and Vuletić, V., *"Time-reversal-based quantum metrology with many-body entangled states,"* Nature Physics **18**, 925 (2022) [cited in page 175].

Comparin, T., Mezzacapo, F., and Roscilde, T., *"Multipartite entangled states in dipolar quantum simulators,"* Phys. Rev. Lett. **129**, 150503 (2022a) [cited in pages 158, 162, and 165].

Comparin, T., Mezzacapo, F., and Roscilde, T., *"Robust spin squeezing from the tower of states of u(1)-symmetric spin hamiltonians,"* Phys. Rev. A **105**, 022625 (2022b) [cited in page 168].

Comparin, T., Mezzacapo, F., Robert-de Saint-Vincent, M., and Roscilde, T., *"Scalable spin squeezing from spontaneous breaking of a continuous symmetry,"* Phys. Rev. Lett. **129**, 113201 (2022) [cited in pages 158, 162, and 174].

Conover, E., *"Google moves toward quantum supremacy with 72-qubit computer,"* (2018) [cited in page 24].

Dalmonte, M., Mirzaei, S. I., Muppalla, P. R., Marcos, D., Zoller, P., and Kirchmair, G., *"Realizing dipolar spin models with arrays of superconducting qubits,"* Phys. Rev. B **92**, 174507 (2015) [cited in page 158].

Darquié, B., Manipulation d'atomes dans des pièges dipolaires microscopiques et émission contrôlée de photons par un atome unique, Theses, Université Paris Sud - Paris XI (2005) [cited in page 33].

Davis, E., Bentsen, G., and Schleier-Smith, M., *"Approaching the heisenberg limit without single-particle detection,"* Phys. Rev. Lett. **116**, 053601 (2016) [cited in page 175].

Defenu, N., Donner, T., Macrì, T., Pagano, G., Ruffo, S., and Trombettoni, A., *"Long-range interacting quantum systems,"* Rev. Mod. Phys. **95**, 035002 (2023) [cited in pages 122 and 130].

Degen, C. L., Reinhard, F., and Cappellaro, P., *"Quantum sensing,"* Rev. Mod. Phys. **89**, 035002 (2017) [cited in page 14].

Dehmelt, H., *"Experiments with an isolated subatomic particle at rest,"* Rev. Mod. Phys. **62**, 525 (1990) [cited in page 13].

Deng, X.-L., Porras, D., and Cirac, J. I., *"Effective spin quantum phases in systems of trapped ions,"* Phys. Rev. A **72**, 063407 (2005) [cited in page 121].

Despres, J., Villa, L., and Sanchez-Palencia, L., *"Twofold correlation spreading in a strongly correlated lattice bose gas,"* Scientific Reports **9**, 4135 (2019) [cited in page 180].

Devoret, M. H. and Schoelkopf, R. J., *"Superconducting circuits for quantum information: An outlook,"* Science **339**, 1169 (2013) [cited in page 21].

Dey, S., *"Destabilization of u(1) dirac spin liquids on two-dimensional nonbipartite lattices by quenched disorder,"* Phys. Rev. B **102**, 235165 (2020) [cited in page 89].

DiCarlo, L., Chow, J. M., Gambetta, J. M., Bishop, L. S., Johnson, B. R., Schuster, D. I., Majer, J., Blais, A., Frunzio, L., Girvin, S. M., and Schoelkopf, R. J., *"Demonstration of two-qubit algorithms with a superconducting quantum processor,"* Nature **460**, 240 (2009) [cited in page 24].

Dicke, R. H., *"Coherence in spontaneous radiation processes,"* Phys. Rev. **93**, 99 (1954) [cited in page 117].

Dumitrescu, P. T., Bohnet, J. G., Gaebler, J. P., Hankin, A., Hayes, D., Kumar, A., Neyenhuis, B., Vasseur, R., and Potter, A. C., *"Dynamical topological phase realized in a trapped-ion quantum simulator,"* Nature **607**, 463 (2022) [cited in page 63].

Ebadi, S., Wang, T. T., Levine, H., Keesling, A., Semeghini, G., Omran, A., Bluvstein, D., Samajdar, R., Pichler, H., Ho, W. W., Choi, S., Sachdev, S., Greiner, M., Vuletić, V., and Lukin, M. D., *"Quantum phases of matter on a 256-atom programmable quantum simulator,"* Nature **595**, 227 (2021) [cited in pages 24 and 116].

Eibl, M., Kiesel, N., Bourennane, M., Kurtsiefer, C., and Weinfurter, H., *"Experimental realization of a three-qubit entangled w state,"* Phys. Rev. Lett. **92**, 077901 (2004) [cited in page 87].

Emperauger, G., Simulation quantique d'Hamiltoniens de spin à l'aide de matrices d'atomes de Rydberg individuels, Ph.D. thesis (2025), thèse de doctorat dirigée par Lahaye, Thierry Physique Palaiseau, Institut d'optique théorique et appliquée 2021 [cited in pages 43, 57, 114, 174, and 196].

Endres, M., Bernien, H., Keesling, A., Levine, H., Anschuetz, E. R., Krajenbrink, A., Senko, C., Vuletic, V., Greiner, M., and Lukin, M. D., *"Atom-by-atom assembly of defect-free one-dimensional cold atom arrays,"* Science **354**, 1024 (2016) [cited in pages 23 and 24].

Esslinger, T., *"Fermi-hubbard physics with atoms in an optical lattice,"* Annual Review of Condensed Matter Physics **1**, 129 (2010) [cited in pages 17 and 20].

Estève, J., Gross, C., Weller, A., Giovanazzi, S., and Oberthaler, M. K., *"Squeezing and entanglement in a bose-einstein condensate,"* Nature **455**, 1216 (2008) [cited in page 165].

Forster, D., Hydrodynamic Fluctuations, Broken Symmetry, And Correlation Functions, Advanced Books Classics (Taylor & Francis Limited (Sales), 2019) [cited in page 179].

Frérot, I., Naldesi, P., and Roscilde, T., *"Entanglement and fluctuations in the xxz model with power-law interactions,"* Phys. Rev. B **95**, 245111 (2017) [cited in page 185].

Frérot, I., Naldesi, P., and Roscilde, T., *"Multispeed prethermalization in quantum spin models with power-law decaying interactions,"* Phys. Rev. Lett. **120**, 050401 (2018) [cited in pages 180 and 186].

Fu, M., Imai, T., Han, T.-H., and Lee, Y. S., *"Evidence for a gapped spin-liquid ground state in a kagome Heisenberg antiferromagnet,"* Science **350**, 655 (2015) [cited in page 134].

Fukuhara, T., Schauß, P., Endres, M., Hild, S., Cheneau, M., Bloch, I., and Gross, C., *"Microscopic observation of magnon bound states and their dynamics,"* Nature **502**, 76 (2013) [cited in page 63].

Gaebler, J. P., Meier, A. M., Tan, T. R., Bowler, R., Lin, Y., Hanneke, D., Jost, J. D., Home, J. P., Knill, E., Leibfried, D., and Wineland, D. J., *"Randomized benchmarking of multiqubit gates,"* Phys. Rev. Lett. **108**, 260503 (2012) [cited in page 63].

Gaebler, J. P., Tan, T. R., Lin, Y., Wan, Y., Bowler, R., Keith, A. C., Glancy, S., Coakley, K., Knill, E., Leibfried, D., and Wineland, D. J., *"High-fidelity universal gate set for ^{9}Be$^+$ ion qubits,"* Phys. Rev. Lett. **117**, 060505 (2016) [cited in page 24].

Gaëtan, A., Miroshnychenko, Y., Wilk, T., Chotia, A., Viteau, M., Comparat, D., Pillet, P., Browaeys, A., and Grangier, P., *"Observation of collective excitation of two individual atoms in the rydberg blockade regime,"* Nature Physics **5**, 115 (2009) [cited in page 23].

Gallagher, T., *"Rydberg atoms,"* in Springer Handbook of Atomic, Molecular, and Optical Physics, edited by G. Drake (Springer New York, New York, NY, 2006) pp. 235–245 [cited in page 56].

Gambetta, J. M., Córcoles, A. D., Merkel, S. T., Johnson, B. R., Smolin, J. A., Chow, J. M., Ryan, C. A., Rigetti, C., Poletto, S., Ohki, T. A., Ketchen, M. B., and Steffen, M., *"Characterization of addressability by simultaneous randomized benchmarking,"* Phys. Rev. Lett. **109**, 240504 (2012) [cited in page 63].

Geier, S., Braemer, A., Braun, E., Müllenbach, M., Franz, T., Gärttner, M., Zürn, G., and Weidemüller, M., *"Time-reversal in a dipolar quantum many-body spin system,"* (2024) [cited in page 177].

Georgescu, I. M., Ashhab, S., and Nori, F., *"Quantum simulation,"* Review of Modern Physics **86**, 153 (2014) [cited in page 15].

Gerchberg, R. W. and Saxton, W. O., *"A practical algorithm for the determination of the phase from image and diffraction plane pictures,"* Optiik **35**, 237 (1972) [cited in page 35].

Giovannetti, V., Lloyd, S., and Maccone, L., *"Advances in quantum metrology,"* Nature Photonics **5**, 222 (2011) [cited in page 157].

Greenberger, D. M., Horne, M. A., and Zeilinger, A., *"Going beyond bell's theorem,"* in Bell's Theorem, Quantum Theory and Conceptions of the Universe, edited by M. Kafatos (Springer Netherlands, Dordrecht, 1989) pp. 69–72 [cited in page 168].

Greiner, M., Mandel, O., Esslinger, T., Hänsch, T. W., and Bloch, I., *"Quantum phase transition from a superfluid to a mott insulator in a gas of ultracold atoms,"* Nature **415**, 39 (2002) [cited in page 19].

Gross, C., *"Spin squeezing, entanglement and quantum metrology with bose–einstein condensates,"* Journal of Physics B: Atomic, Molecular and Optical Physics **45**, 103001 (2012) [cited in page 165].

Gühne, O., Hyllus, P., Bruss, D., Ekert, A., Lewenstein, M., Macchiavello, C., and Sanpera, A., *"Experimental detection of entanglement via witness operators and local measurements,"* Journal of Modern Optics **50**, 1079–1102 (2003) [cited in page 87].

Häffner, H., Hänsel, W., Roos, C. F., Benhelm, J., Chek-al kar, D., Chwalla, M., Körber, T., Rapol, U. D., Riebe, M., Schmidt, P. O., Becher, C., Gühne, O., Dür, W., and Blatt, R., *"Scalable multiparticle entanglement of trapped ions,"* Nature **438**, 643 (2005) [cited in page 24].

Han, T.-H., Helton, J. S., Chu, S., Nocera, D. G., Rodriguez-Rivera, J. A., Broholm, C., and Lee, Y. S., *"Fractionalized excitations in the spin-liquid state of a kagome-lattice antiferromagnet,"* Nature **492**, 406 (2012) [cited in page 134].

Haroche, S., *"Nobel lecture: Controlling photons in a box and exploring the quantum to classical boundary,"* Review of Modern Physics **85**, 1083 (2013) [cited in page 13].

Hastings, M. B., *"Dirac structure, rvb, and goldstone modes in the kagomé antiferromagnet,"* Phys. Rev. B **63**, 014413 (2000) [cited in page 134].

He, Y.-C., Sheng, D. N., and Chen, Y., *"Chiral spin liquid in a frustrated anisotropic kagome heisenberg model,"* Phys. Rev. Lett. **112**, 137202 (2014) [cited in page 146].

He, Y.-C., Zaletel, M. P., Oshikawa, M., and Pollmann, F., *"Signatures of dirac cones in a dmrg study of the kagome heisenberg model,"* Phys. Rev. X **7**, 031020 (2017) [cited in pages 134 and 143].

Henriet, L., Beguin, L., Signoles, A., Lahaye, T., Browaeys, A., Reymond, G.-O., and Jurczak, C., *"Quantum computing with neutral atoms,"* Quantum **4**, 327 (2020) [cited in page 199].

Hermele, M., Ran, Y., Lee, P. A., and Wen, X.-G., *"Properties of an algebraic spin liquid on the kagome lattice,"* Phys. Rev. B **77**, 224413 (2008) [cited in page 143].

Herrmann, N., Arya, D., Doherty, M. W., Mingare, A., Pillay, J. C., Preis, F., and Prestel, S., *"Quantum utility – definition and assessment of a practical quantum advantage,"* (2023), arXiv:2303.02138 [quant-ph] [cited in page 16].

Holland, C. M., Lu, Y., and Cheuk, L. W., *"On-demand entanglement of molecules in a reconfigurable optical tweezer array,"* Science **382**, 1143 (2023) [cited in page 158].

Holstein, T. and Primakoff, H., *"Field dependence of the intrinsic domain magnetization of a ferromagnet,"* Phys. Rev. **58**, 1098 (1940) [cited in page 181].

Homeier, L., Harris, T. J., Blatz, T., Geier, S., Hollerith, S., Schollwöck, U., Grusdt, F., and Bohrdt, A., *"Antiferromagnetic bosonic t-j models and their quantum simulation in tweezer arrays,"* Phys. Rev. Lett. **132**, 230401 (2024) [cited in page 198].

Hosten, O., Engelsen, N. J., Krishnakumar, R., and Kasevich, M. A., *"Measurement noise 100 times lower than the quantum-projection limit using entangled atoms,"* Nature **529**, 505 (2016) [cited in pages 14 and 157].

Houck, A. A., Türeci, H. E., and Koch, J., *"On-chip quantum simulation with superconducting circuits,"* Nature Physics **8**, 292 (2012) [cited in page 64].

Husimi, K., *"Some formal properties of the density matrix,"* Proceedings of the Physico-Mathematical Society of Japan. 3rd Series **22**, 264 (1940) [cited in page 160].

Impertro, A., Karch, S., Wienand, J. F., Huh, S., Schweizer, C., Bloch, I., and Aidelsburger, M., *"Local readout and control of current and kinetic energy operators in optical lattices,"* (2023) [cited in page 64].

Isenhower, L., Urban, E., Zhang, X. L., Gill, A. T., Henage, T., Johnson, T. A., Walker, T. G., and Saffman, M., *"Demonstration of a neutral atom controlled-not quantum gate,"* Phys. Rev. Lett. **104**, 010503 (2010) [cited in pages 23, 24, and 64].

Ising, E., *"Beitrag zur theorie des ferromagnetismus,"* Zeitschrift für Physik **31**, 253 (1925) [cited in page 18].

Jaksch, D., Cirac, J. I., Zoller, P., Rolston, S. L., Côté, R., and Lukin, M. D., *"Fast quantum gates for neutral atoms,"* Phys. Rev. Lett. **85**, 2208 (2000) [cited in page 22].

Jau, Y.-Y., Hankin, A. M., Keating, T., Deutsch, I. H., and Biedermann, G. W., *"Entangling atomic spins with a rydberg-dressed spin-flip blockade,"* Nature Physics **12**, 71 (2016) [cited in page 24].

Jean-Paul Blaizot, G. R., Quantum theory of finite systems (The MIT Press, 1985) [cited in page 184].

Jones, M. P. A., Beugnon, J., Gaëtan, A., Zhang, J., Messin, G., Browaeys, A., and Grangier, P., *"Fast quantum state control of a single trapped neutral atom,"* Phys. Rev. A **75**, 040301 (2007) [cited in page 64].

Kalmeyer, V. and Laughlin, R. B., *"Equivalence of the resonating-valence-bond and fractional quantum hall states,"* Phys. Rev. Lett. **59**, 2095 (1987) [cited in pages 134 and 146].

Keimer, B., Kivelson, S. A., Norman, M. R., Uchida, S., and Zaanen, J., *"From quantum matter to high-temperature superconductivity in copper oxides,"* Nature **518**, 179 (2015) [cited in page 15].

Kennedy, T., Lieb, E. H., and Shastry, B. S., *"The xy model has long-range order for all spins and all dimensions greater than one,"* in Statistical Mechanics: Selecta of Elliott H. Lieb, edited by B. Nachtergaele, J. P. Solovej, and J. Yngvason (Springer Berlin Heidelberg, Berlin, Heidelberg, 2004) pp. 327–329 [cited in page 121].

Kiesenhofer, D., Hainzer, H., Zhdanov, A., Holz, P. C., Bock, M., Ollikainen, T., and Roos, C. F., *"Controlling two-dimensional coulomb crystals of more than 100 ions in a monolithic radio-frequency trap,"* PRX Quantum **4**, 020317 (2023) [cited in page 20].

Kim, Y., Eddins, A., Anand, S., Wei, K. X., van den Berg, E., Rosenblatt, S., Nayfeh, H., Wu, Y., Zaletel, M., Temme, K., and Kandala, A., *"Evidence for the utility of quantum computing before fault tolerance,"* Nature **618**, 500 (2023) [cited in page 24].

Kitagawa, M. and Ueda, M., *"Squeezed spin states,"* Phys. Rev. A **47**, 5138 (1993) [cited in pages 158, 162, and 164].

Kjaergaard, M., Schwartz, M. E., Braumüller, J., Krantz, P., Wang, J. I.-J., Gustavsson, S., and Oliver, W. D., *"Superconducting qubits: Current state of play,"* Annual Review of Condensed Matter Physics **11**, 369 (2020) [cited in pages 21 and 64].

Klitzing, K. v., Dorda, G., and Pepper, M., *"New method for high-accuracy determination of the fine-structure constant based on quantized Hall resistance,"* Phys. Rev. Lett. **45**, 494 (1980) [cited in page 15].

Knill, E., Leibfried, D., Reichle, R., Britton, J., Blakestad, R. B., Jost, J. D., Langer, C., Ozeri, R., Seidelin, S., and Wineland, D. J., *"Randomized benchmarking of quantum gates,"* Phys. Rev. A **77**, 012307 (2008) [cited in page 63].

Koch, C. P., Boscain, U., Calarco, T., Dirr, G., Filipp, S., Glaser, S. J., Kosloff, R., Montangero, S., Schulte-Herbrüggen, T., Sugny, D., and Wilhelm, F. K., *"Quantum optimal control in quantum technologies. strategic report on current status, visions and goals for research in europe,"* EPJ Quantum Technology **9**, 19 (2022) [cited in page 24].

Kokail, C., Maier, C., van Bijnen, R., Brydges, T., Joshi, M. K., Jurcevic, P., Muschik, C. A., Silvi, P., Blatt, R., Roos, C. F., and Zoller, P., *"Self-verifying variational quantum simulation of lattice models,"* Nature **569**, 355 (2019) [cited in page 63].

Kosterlitz, J. M., *"The critical properties of the two-dimensional xy model,"* Journal of Physics C: Solid State Physics **7**, 1046 (1974) [cited in page 128].

Kosterlitz, J. M. and Thouless, D. J., *"Ordering, metastability and phase transitions in two-dimensional systems,"* Journal of Physics C: Solid State Physics **6**, 1181 (1973) [cited in page 128].

Krantz, P., Kjaergaard, M., Yan, F., Orlando, T. P., Gustavsson, S., and Oliver, W. D., *"A quantum engineer's guide to superconducting qubits,"* Applied Physics Reviews **6**, 021318 (2019) [cited in page 21].

Kubo, R., *"Generalized cumulant expansion method,"* Journal of the Physical Society of Japan **17**, 1100 (1962) [cited in pages 149 and 167].

Kunz, H. and Pfister, C. E., *"First order phase transition in the plane rotator ferromagnetic model in two dimensions,"* Communications in Mathematical Physics **46**, 245 (1976) [cited in page 129].

Labuhn, H., Rydberg excitation dynamics and correlations in arbitrary 2D arrays of single atoms, Theses, Université Paris Saclay (COmUE) (2016) [cited in page 66].

Labuhn, H., Barredo, D., Ravets, S., de Léséleuc, S., Macrì, T., Lahaye, T., and Browaeys, A., *"Tunable two-dimensional arrays of single rydberg atoms for realizing quantum ising models,"* Nature **534**, 667 (2016) [cited in pages 24 and 116].

Lai, Z., Zhang, S., Gou, Q., and Li, Y., *"Polarizabilities of rydberg states of rb atoms with n up to 140,"* Phys. Rev. A **98**, 052503 (2018) [cited in page 23].

Lanyon, B. P., Hempel, C., Nigg, D., Müller, M., Gerritsma, R., Zähringer, F., Schindler, P., Barreiro, J. T., Rambach, M., Kirchmair, G., Hennrich, M., Zoller, P., Blatt, R., and Roos, C. F., *"Universal digital quantum simulation with trapped ions,"* Science **334**, 57 (2011) [cited in page 20].

Lee, P. A., *"An end to the drought of quantum spin liquids,"* Science **321**, 1306 (2008) [cited in page 133].

Lee, P. A., Nagaosa, N., and Wen, X.-G., *"Doping a mott insulator: Physics of high-temperature superconductivity,"* Rev. Mod. Phys. **78**, 17 (2006) [cited in page 134].

Leibfried, D., DeMarco, B., Meyer, V., Lucas, D., Barrett, M., Britton, J., Itano, W. M., Jelenković, B., Langer, C., Rosenband, T., and Wineland, D. J., *"Experimental demonstration of a robust, high-fidelity geometric two ion-qubit phase gate,"* Nature **422**, 412 (2003) [cited in page 24].

de Léséleuc, S., Barredo, D., Lienhard, V., Browaeys, A., and Lahaye, T., *"Optical control of the resonant dipole-dipole interaction between rydberg atoms,"* Phys. Rev. Lett. **119**, 053202 (2017) [cited in pages 50, 55, and 195].

de Léséleuc, S., Barredo, D., Lienhard, V., Browaeys, A., and Lahaye, T., *"Analysis of imperfections in the coherent optical excitation of single atoms to rydberg states,"* Phys. Rev. A **97**, 053803 (2018) [cited in pages 24, 48, and 75].

Lesik, M., Plisson, T., Toraille, L., Renaud, J., Occelli, F., Schmidt, M., Salord, O., Delobbe, A., Debuisschert, T., Rondin, L., Loubeyre, P., and Roch, J.-F., *"Magnetic measurements on micrometer-sized samples under high pressure using designed nv centers,"* Science **366**, 1359 (2019) [cited in page 14].

Levine, H., Keesling, A., Omran, A., Bernien, H., Schwartz, S., Zibrov, A. S., Endres, M., Greiner, M., Vuletić, V., and Lukin, M. D., *"High-fidelity control and entanglement of rydberg-atom qubits,"* Phys. Rev. Lett. **121**, 123603 (2018) [cited in page 24].

Levine, H., Keesling, A., Semeghini, G., Omran, A., Wang, T. T., Ebadi, S., Bernien, H., Greiner, M., Vuletić, V., Pichler, H., and Lukin, M. D., *"Parallel implementation*

of high-fidelity multiqubit gates with neutral atoms," Phys. Rev. Lett. **123**, 170503 (2019) [cited in page 24].

Li, Z., null,, Colombo, S., Shu, C., Velez, G., Pilatowsky-Cameo, S., Schmied, R., Choi, S., Lukin, M., Pedrozo-Peñafiel, E., and Vuletić, V., "Improving metrology with quantum scrambling," Science **380**, 1381 (2023) [cited in page 175].

Lienhard, V., Physique quantique expérimentale à N corps dans des matrices d'atomes de Rydberg. Des modèles de spins à la matière topologique., Theses, Université Paris Saclay (COmUE) (2019) [cited in page 77].

Lienhard, V., Scholl, P., Weber, S., Barredo, D., de Léséleuc, S., Bai, R., Lang, N., Fleischhauer, M., Büchler, H. P., Lahaye, T., and Browaeys, A., "Realization of a density-dependent Peierls phase in a synthetic, spin-orbit coupled Rydberg system," Phys. Rev. X **10**, 021031 (2020) [cited in pages 55 and 195].

Lovesey, S., Theory of Neutron Scattering from Condensed Matter, International series of monographs on physics (Clarendon Press, 1986) [cited in page 179].

Lovesey, S. W., Condensed Matter Physics: Dynamic Correlations (Frontiers in Physics) (Benjamin-Cummings Publishing Company, 1980) [cited in page 179].

Ludlow, A. D., Boyd, M. M., Ye, J., Peik, E., and Schmidt, P. O., "Optical atomic clocks," Rev. Mod. Phys. **87**, 637 (2015) [cited in page 14].

Lukin, M. D., Fleischhauer, M., Cote, R., Duan, L. M., Jaksch, D., Cirac, J. I., and Zoller, P., "Dipole blockade and quantum information processing in mesoscopic atomic ensembles," Phys. Rev. Lett. **87**, 037901 (2001) [cited in page 22].

de Léséleuc, S., Quantum simulation of spin models with assembled arrays of Rydberg atoms, Ph.D. thesis (2021), thèse de doctorat dirigée par Lahaye, Thierry Physique Palaiseau, Institut d'optique théorique et appliquée 2018 [cited in pages 32 and 66].

de Léséleuc, S., Lienhard, V., Scholl, P., Barredo, D., Weber, S., Lang, N., Büchler, H. P., Lahaye, T., and Browaeys, A., "Observation of a symmetry-protected topological phase of interacting bosons with rydberg atoms," Science **365**, 775 (2019) [cited in page 195].

Löw, R., Weimer, H., Nipper, J., Balewski, J. B., Butscher, B., Büchler, H. P., and Pfau, T., "An experimental and theoretical guide to strongly interacting rydberg

gases," Journal of Physics B: Atomic, Molecular and Optical Physics **45**, 113001 (2012) [cited in page 22].

Ma, J., Wang, X., Sun, C., and Nori, F., *"Quantum spin squeezing,"* Physics Reports **509**, 89 (2011) [cited in page 158].

Madjarov, I. S., Cooper, A., Shaw, A. L., Covey, J. P., Schkolnik, V., Yoon, T. H., Williams, J. R., and Endres, M., *"An atomic-array optical clock with single-atom readout,"* Phys. Rev. X **9**, 041052 (2019) [cited in page 158].

Madjarov, I. S., Covey, J. P., Shaw, A. L., Choi, J., Kale, A., Cooper, A., Pichler, H., Schkolnik, V., Williams, J. R., and Endres, M., *"High-fidelity entanglement and detection of alkaline-earth rydberg atoms,"* Nature Physics **16**, 857 (2020) [cited in page 24].

Maller, K. M., Lichtman, M. T., Xia, T., Sun, Y., Piotrowicz, M. J., Carr, A. W., Isenhower, L., and Saffman, M., *"Rydberg-blockade controlled-not gate and entanglement in a two-dimensional array of neutral-atom qubits,"* Phys. Rev. A **92**, 022336 (2015) [cited in page 24].

Manetsch, H. J., Nomura, G., Bataille, E., Leung, K. H., Lv, X., and Endres, M., *"A tweezer array with 6100 highly coherent atomic qubits,"* (2024) [cited in page 24].

Manousakis, E., *"The spin-$\frac{1}{2}$ heisenberg antiferromagnet on a square lattice and its application to the cuprous oxides,"* Rev. Mod. Phys. **63**, 1 (1991) [cited in page 181].

Marx, R., Fahmy, A. F., Myers, J. M., Bermel, W., and Glaser, S. J., *"Approaching five-bit nmr quantum computing,"* Phys. Rev. A **62**, 012310 (2000) [cited in page 24].

Maze, J. R., Stanwix, P. L., Hodges, J. S., Hong, S., Taylor, J. M., Cappellaro, P., Jiang, L., Dutt, M. V. G., Togan, E., Zibrov, A. S., Yacoby, A., Walsworth, R. L., and Lukin, M. D., *"Nanoscale magnetic sensing with an individual electronic spin in diamond,"* Nature **455**, 644 (2008) [cited in page 14].

Mehlstäubler, T. E., *"Atomic clocks for geodesy,"* (2023) [cited in page 14].

Meng, Z. Y., Lang, T. C., Wessel, S., Assaad, F. F., and Muramatsu, A., *"Quantum spin liquid emerging in two-dimensional correlated dirac fermions,"* Nature **464**, 847 (2010) [cited in page 143].

Menu, R. and Roscilde, T., *"Quench dynamics of quantum spin models with flat bands of excitations,"* Phys. Rev. B **98**, 205145 (2018) [cited in page 180].

Menu, R. and Roscilde, T., *"Gaussian-state Ansatz for the non-equilibrium dynamics of quantum spin lattices,"* SciPost Phys. **14**, 151 (2023) [cited in page 180].

Mermin, N. D., *"Extreme quantum entanglement in a superposition of macroscopically distinct states,"* Phys. Rev. Lett. **65**, 1838 (1990) [cited in page 87].

Mermin, N. D. and Wagner, H., *"Absence of ferromagnetism or antiferromagnetism in one- or two-dimensional isotropic heisenberg models,"* Phys. Rev. Lett. **17**, 1133 (1966) [cited in pages 15, 110, and 122].

Messio, L., Bernu, B., and Lhuillier, C., *"Kagome antiferromagnet: A chiral topological spin liquid?"* Phys. Rev. Lett. **108**, 207204 (2012) [cited in page 146].

Metcalf, H. J. and van der Straten, P., Laser Cooling and Trapping (Springer-Verlag, New York, 1999) [cited in page 32].

Miller, J. D., Cline, R. A., and Heinzen, D. J., *"Far-off-resonance optical trapping of atoms,"* Phys. Rev. A **47**, R4567 (1993) [cited in page 48].

Mitra, A., *"Quantum quench dynamics,"* Annual Review of Condensed Matter Physics **9**, 245 (2018) [cited in page 180].

Monroe, C., Campbell, W. C., Duan, L.-M., Gong, Z.-X., Gorshkov, A. V., Hess, P. W., Islam, R., Kim, K., Linke, N. M., Pagano, G., Richerme, P., Senko, C., and Yao, N. Y., *"Programmable quantum simulations of spin systems with trapped ions,"* Rev. Mod. Phys. **93**, 025001 (2021) [cited in pages 64 and 158].

Monz, T., Schindler, P., Barreiro, J. T., Chwalla, M., Nigg, D., Coish, W. A., Harlander, M., Hänsel, W., Hennrich, M., and Blatt, R., *"14-qubit entanglement: Creation and coherence,"* Phys. Rev. Lett. **106**, 130506 (2011) [cited in pages 20 and 24].

Mucherino, A., Lavor, C., Liberti, L., and Maculan, N., Distance Geometry: Theory, Methods, and Applications, SpringerLink : Bücher (Springer New York, 2012) [cited in pages 92 and 93].

Muessel, W., Strobel, H., Linnemann, D., Zibold, T., Juliá-Díaz, B., and Oberthaler, M. K., *"Twist-and-turn spin squeezing in bose-einstein condensates,"* Phys. Rev. A **92**, 023603 (2015) [cited in page 171].

Nakamura, Y., Pashkin, Y. A., and Tsai, J. S., *"Coherent control of macroscopic quantum states in a single-cooper-pair box,"* Nature **398**, 786 (1999) [cited in page 20].

Neeley, M., Bialczak, R. C., Lenander, M., Lucero, E., Mariantoni, M., O'Connell, A. D., Sank, D., Wang, H., Weides, M., Wenner, J., Yin, Y., Yamamoto, T., Cleland, A. N., and Martinis, J. M., *"Generation of three-qubit entangled states using superconducting phase qubits,"* Nature **467**, 570 (2010) [cited in page 87].

Norcia, M. A., Kim, H., Cairncross, W. B., Stone, M., Ryou, A., Jaffe, M., Brown, M. O., Barnes, K., Battaglino, P., Bohdanowicz, T. C., Brown, A., Cassella, K., Chen, C. A., Coxe, R., Crow, D., Epstein, J., Griger, C., Halperin, E., Hummel, F., Jones, A. M. W., Kindem, J. M., King, J., Kotru, K., Lauigan, J., Li, M., Lu, M., Megidish, E., Marjanovic, J., McDonald, M., Mittiga, T., Muniz, J. A., Narayanaswami, S., Nishiguchi, C., Paule, T., Pawlak, K. A., Peng, L. S., Pudenz, K. L., Perez, D. R., Smull, A., Stack, D., Urbanek, M., van de Veerdonk, R. J. M., Vendeiro, Z., Wadleigh, L., Wilkason, T., Wu, T. Y., Xie, X., Zalys-Geller, E., Zhang, X., and Bloom, B. J., *"Iterative assembly of ^{171}yb atom arrays with cavity-enhanced optical lattices,"* (2024) [cited in page 24].

Norman Yao's team in Harvard,, *"Chiral spin liquids in quantum dipole arrays,"* Paper in preparation [cited in pages 148 and 149].

Novoselov, K. S., Jiang, D., Schedin, F., Booth, T. J., Khotkevich, V. V., Morozov, S. V., and Geim, A. K., *"Two-dimensional atomic crystals,"* Proceedings of the National Academy of Sciences **102**, 10451 (2005) [cited in page 15].

Paul, W., *"Electromagnetic traps for charged and neutral particles,"* Rev. Mod. Phys. **62**, 531 (1990) [cited in pages 13 and 20].

Pedrozo-Peñafiel, E., Colombo, S., Shu, C., Adiyatullin, A. F., Li, Z., Mendez, E., Braverman, B., Kawasaki, A., Akamatsu, D., Xiao, Y., and Vuletić, V., *"Entanglement on an optical atomic-clock transition,"* Nature **588**, 414 (2020) [cited in pages 14 and 158].

Perciavalle, F., Rossini, D., Haug, T., Morsch, O., and Amico, L., *"Controlled flow of excitations in a ring-shaped network of rydberg atoms,"* Phys. Rev. A **108**, 023305 (2023) [cited in page 77].

Perlin, M. A., Qu, C., and Rey, A. M., *"Spin squeezing with short-range spin-exchange interactions,"* Phys. Rev. Lett. **125**, 223401 (2020) [cited in pages 158 and 162].

Peter, D., Müller, S., Wessel, S., and Büchler, H. P., *"Anomalous behavior of spin systems with dipolar interactions,"* Phys. Rev. Lett. **109**, 025303 (2012) [cited in pages 110, 121, and 181].

Pezzè, L., Smerzi, A., Oberthaler, M. K., Schmied, R., and Treutlein, P., *"Quantum metrology with nonclassical states of atomic ensembles,"* Rev. Mod. Phys. **90**, 035005 (2018) [cited in pages 158, 164, and 169].

Phillips, W. D., *"Nobel lecture: Laser cooling and trapping of neutral atoms,"* Review of Modern Physics **70**, 721 (1998) [cited in page 13].

Pichard, G., Lim, D., Bloch, E., Vaneecloo, J., Bourachot, L., Both, G.-J., Mériaux, G., Dutartre, S., Hostein, R., Paris, J., Ximenez, B., Signoles, A., Browaeys, A., Lahaye, T., and Dreon, D., *"Rearrangement of single atoms in a 2000-site optical tweezers array at cryogenic temperatures,"* (2024) [cited in page 24].

Preskill, J., *"Quantum computing and the entanglement frontier,"* (2012), arXiv:1203.5813 [quant-ph] [cited in page 16].

Ran, Y., Hermele, M., Lee, P. A., and Wen, X.-G., *"Projected-wave-function study of the spin-1/2 heisenberg model on the kagomé lattice,"* Phys. Rev. Lett. **98**, 117205 (2007) [cited in page 134].

Reif, F., Fundamentals of Statistical and Thermal Physics (Waveland Press, 2009) [cited in page 15].

Robinson, J. M., Miklos, M., Tso, Y. M., Kennedy, C. J., Bothwell, T., Kedar, D., Thompson, J. K., and Ye, J., *"Direct comparison of two spin squeezed optical clocks below the quantum projection noise limit,"* arxiv.2211.08621 (2022), 10.48550/ARXIV.2211.08621 [cited in pages 14 and 158].

Roscilde, T., Comparin, T., and Mezzacapo, F., *"Entangling dynamics from effective rotor–spin-wave separation in u(1)-symmetric quantum spin models,"* Phys. Rev. Lett. **131**, 160403 (2023a) [cited in page 181].

Roscilde, T., Comparin, T., and Mezzacapo, F., *"Rotor/spin-wave theory for quantum spin models with u(1) symmetry,"* Phys. Rev. B **108**, 155130 (2023b) [cited in pages 163 and 181].

Rosenberg, E., Andersen, T. I., Samajdar, R., Petukhov, A., Hoke, J. C., Abanin, D., Bengtsson, A., Drozdov, I. K., Erickson, C., Klimov, P. V., Mi, X., Morvan, A., Neeley, M., Neill, C., Acharya, R., Allen, R., Anderson, K., Ansmann, M., Arute, F., Arya, K., Asfaw, A., Atalaya, J., Bardin, J. C., Bilmes, A., Bortoli, G., Bourassa, A., Bovaird, J., Brill, L., Broughton, M., Buckley, B. B., Buell, D. A., Burger, T., Burkett, B., Bushnell, N., Campero, J., Chang, H.-S., Chen, Z., Chiaro, B., Chik, D., Cogan, J., Collins, R., Conner, P., Courtney, W., Crook, A. L., Curtin, B., Debroy, D. M., Barba, A. D. T., Demura, S., Paolo, A. D., Dunsworth, A., Earle, C., Faoro, L., Farhi, E., Fatemi, R., Ferreira, V. S., Burgos, L. F., Forati, E., Fowler, A. G., Foxen, B., Garcia, G., Genois, E., Giang, W., Gidney, C., Gilboa, D., Giustina, M., Gosula, R., Dau, A. G., Gross, J. A., Habegger, S., Hamilton, M. C., Hansen, M., Harrigan, M. P., Harrington, S. D., Heu, P., Hill, G., Hoffmann, M. R., Hong, S., Huang, T., Huff, A., Huggins, W. J., Ioffe, L. B., Isakov, S. V., Iveland, J., Jeffrey, E., Jiang, Z., Jones, C., Juhas, P., Kafri, D., Khattar, T., Khezri, M., Kieferová, M., Kim, S., Kitaev, A., Klots, A. R., Korotkov, A. N., Kostritsa, F., Kreikebaum, J. M., Landhuis, D., Laptev, P., Lau, K.-M., Laws, L., Lee, J., Lee, K. W., Lensky, Y. D., Lester, B. J., Lill, A. T., Liu, W., Locharla, A., Mandrà, S., Martin, O., Martin, S., McClean, J. R., McEwen, M., Meeks, S., Miao, K. C., Mieszala, A., Montazeri, S., Movassagh, R., Mruczkiewicz, W., Nersisyan, A., Newman, M., Ng, J. H., Nguyen, A., Nguyen, M., Niu, M. Y., O' Brien, T. E., Omonije, S., Opremcak, A., Potter, R., Pryadko, L. P., Quintana, C., Rhodes, D. M., Rocque, C., Rubin, N. C., Saei, N., Sank, D., Sankaragomathi, K., Satzinger, K. J., Schurkus, H. F., Schuster, C., Shearn, M. J., Shorter, A., Shutty, N., Shvarts, V., Sivak, V., Skruzny, J., Smith, W. C., Somma, R. D., Sterling, G., Strain, D., Szalay, M., Thor, D., Torres, A., Vidal, G., Villalonga, B., Heidweiller, C. V., White, T., Woo, B. W. K., Xing, C., Yao, Z. J., Yeh, P., Yoo, J., Young, G., Zalcman, A., Zhang, Y., Zhu, N., Zobrist, N., Neven, H., Babbush, R., Bacon, D., Boixo, S., Hilton, J., Lucero, E., Megrant, A., Kelly, J., Chen, Y., Smelyanskiy, V., Khemani, V., Gopalakrishnan, S., Prosen, T., and Roushan, P., *"Dynamics of magnetization at infinite temperature in a heisenberg spin chain,"* Science **384**, 48 (2024) [cited in page 21].

Ross, I., A Primer on Pontryagin's Principle in Optimal Control (Collegiate Publishers,

2015) [cited in page 49].

Roushan, P., Neill, C., Megrant, A., Chen, Y., Babbush, R., Barends, R., Campbell, B., Chen, Z., Chiaro, B., Dunsworth, A., Fowler, A., Jeffrey, E., Kelly, J., Lucero, E., Mutus, J., O'Malley, P. J. J., Neeley, M., Quintana, C., Sank, D., Vainsencher, A., Wenner, J., White, T., Kapit, E., Neven, H., and Martinis, J., *"Chiral ground-state currents of interacting photons in a synthetic magnetic field,"* Nature Physics **13**, 146 (2017) [cited in pages 63 and 83].

Ruttley, D. K., Guttridge, A., Hepworth, T. R., and Cornish, S. L., *"Enhanced quantum control of individual ultracold molecules using optical tweezer arrays,"* (2024) [cited in pages 64 and 77].

Ryzhov, V. N., Tareyeva, E. E., Fomin, Y. D., and Tsiok, E. N., *"Berezinskii–kosterlitz–thouless transition and two-dimensional melting*,"* Physics-Uspekhi **60**, 857 (2017) [cited in page 128].

Sackett, C. A., Kielpinski, D., King, B. E., Langer, C., Meyer, V., Myatt, C. J., Rowe, M., Turchette, Q. A., Itano, W. M., Wineland, D. J., and Monroe, C., *"Experimental entanglement of four particles,"* Nature **404**, 256 (2000) [cited in page 24].

Salathé, Y., Mondal, M., Oppliger, M., Heinsoo, J., Kurpiers, P., Potočnik, A., Mezzacapo, A., Las Heras, U., Lamata, L., Solano, E., Filipp, S., and Wallraff, A., *"Digital quantum simulation of spin models with circuit quantum electrodynamics,"* Phys. Rev. X **5**, 021027 (2015) [cited in page 21].

Satzinger, K. J., Liu, Y.-J., Smith, A., Knapp, C., Newman, M., Jones, C., Chen, Z., Quintana, C., Mi, X., Dunsworth, A., Gidney, C., Aleiner, I., Arute, F., Arya, K., Atalaya, J., Babbush, R., Bardin, J. C., Barends, R., Basso, J., Bengtsson, A., Bilmes, A., Broughton, M., Buckley, B. B., Buell, D. A., Burkett, B., Bushnell, N., Chiaro, B., Collins, R., Courtney, W., Demura, S., Derk, A. R., Eppens, D., Erickson, C., Faoro, L., Farhi, E., Fowler, A. G., Foxen, B., Giustina, M., Greene, A., Gross, J. A., Harrigan, M. P., Harrington, S. D., Hilton, J., Hong, S., Huang, T., Huggins, W. J., Ioffe, L. B., Isakov, S. V., Jeffrey, E., Jiang, Z., Kafri, D., Kechedzhi, K., Khattar, T., Kim, S., Klimov, P. V., Korotkov, A. N., Kostritsa, F., Landhuis, D., Laptev, P., Locharla, A., Lucero, E., Martin, O., McClean, J. R., McEwen, M., Miao, K. C., Mohseni, M., Montazeri, S., Mruczkiewicz, W., Mutus, J., Naaman, O., Neeley, M., Neill, C., Niu, M. Y., O'Brien, T. E., Opremcak, A.,

Pató, B., Petukhov, A., Rubin, N. C., Sank, D., Shvarts, V., Strain, D., Szalay, M., Villalonga, B., White, T. C., Yao, Z., Yeh, P., Yoo, J., Zalcman, A., Neven, H., Boixo, S., Megrant, A., Chen, Y., Kelly, J., Smelyanskiy, V., Kitaev, A., Knap, M., Pollmann, F., and Roushan, P., *"Realizing topologically ordered states on a quantum processor,"* Science **374**, 1237 (2021) [cited in page 134].

Savary, L. and Balents, L., *"Quantum spin liquids: a review,"* Reports on Progress in Physics **80**, 016502 (2016) [cited in pages 133, 141, and 143].

Schäffner, D., Preuschoff, T., Ristok, S., Brozio, L., Schlosser, M., Giessen, H., and Birkl, G., *"Arrays of individually controllable optical tweezers based on 3D-printed microlens arrays,"* Opt. Express **28**, 8640 (2020) [cited in page 35].

Schauss, P., *"Quantum simulation of transverse ising models with rydberg atoms,"* Quantum Science and Technology **3**, 023001 (2018) [cited in page 116].

Schlosser, N., Reymond, G., Protsenko, I., and Grangier, P., *"Sub-poissonian loading of single atoms in a microscopic dipole trap,"* Nature **411**, 1024 (2001) [cited in pages 23 and 34].

Schneider, J. T., Despres, J., Thomson, S. J., Tagliacozzo, L., and Sanchez-Palencia, L., *"Spreading of correlations and entanglement in the long-range transverse ising chain,"* Phys. Rev. Res. **3**, L012022 (2021) [cited in page 180].

Scholl, P., Quantum simulation of spin models with large arrays of Rydberg atoms, Ph.D. thesis (2021), thèse de doctorat dirigée par Browaeys, Antoine Physique Palaiseau, Institut d'optique théorique et appliquée 2021 [cited in pages 32, 38, 44, 45, 46, 57, 98, and 195].

Scholl, P., Schuler, M., Williams, H. J., Eberharter, A. A., Barredo, D., Schymik, K.-N., Lienhard, V., Henry, L.-P., Lang, T. C., Lahaye, T., Läuchli, A. M., and Browaeys, A., *"Quantum simulation of 2d antiferromagnets with hundreds of rydberg atoms,"* Nature **595**, 233 (2021) [cited in pages 24 and 116].

Scholl, P., Shaw, A. L., Tsai, R. B.-S., Finkelstein, R., Choi, J., and Endres, M., *"Erasure conversion in a high-fidelity rydberg quantum simulator,"* (2023), arXiv:2305.03406 [quant-ph] [cited in pages 24 and 25].

Schymik, K.-N., Scaling-up the Tweezer Platform - Trapping Arrays of Single Atoms in a Cryogenic Environment, Theses, Université Paris-Saclay (2022) [cited in page 34].

Schymik, K.-N., Lienhard, V., Barredo, D., Scholl, P., Williams, H., Browaeys, A., and Lahaye, T., *"Enhanced atom-by-atom assembly of arbitrary tweezer arrays,"* Phys. Rev. A **102**, 063107 (2020) [cited in page 38].

Schymik, K.-N., Pancaldi, S., Nogrette, F., Barredo, D., Paris, J., Browaeys, A., and Lahaye, T., *"Single atoms with 6000-second trapping lifetimes in optical-tweezer arrays at cryogenic temperatures,"* Phys. Rev. Appl. **16**, 034013 (2021) [cited in page 13].

Schymik, K.-N., Ximenez, B., Bloch, E., Dreon, D., Signoles, A., Nogrette, F., Barredo, D., Browaeys, A., and Lahaye, T., *"In situ equalization of single-atom loading in large-scale optical tweezer arrays,"* Phys. Rev. A **106**, 022611 (2022) [cited in page 24].

Seifert, U. F. P., Willsher, J., Drescher, M., Pollmann, F., and Knolle, J., *"Spin-peierls instability of the u(1) dirac spin liquid,"* (2023) [cited in page 89].

Semeghini, G., Levine, H., Keesling, A., Ebadi, S., Wang, T. T., Bluvstein, D., Verresen, R., Pichler, H., Kalinowski, M., Samajdar, R., Omran, A., Sachdev, S., Vishwanath, A., Greiner, M., Vuletić, V., and Lukin, M. D., *"Probing topological spin liquids on a programmable quantum simulator,"* Science **374**, 1242 (2021) [cited in page 134].

Shor, P., *"Algorithms for quantum computation: discrete logarithms and factoring,"* Proceedings 35th Annual Symposium on Foundations of Computer Science, , 124 (1994) [cited in page 16].

Sobota, J. A., He, Y., and Shen, Z.-X., *"Angle-resolved photoemission studies of quantum materials,"* Rev. Mod. Phys. **93**, 025006 (2021) [cited in page 179].

Sorelli, G., Gessner, M., Smerzi, A., and Pezzè, L., *"Fast and optimal generation of entanglement in bosonic josephson junctions,"* Phys. Rev. A **99**, 022329 (2019) [cited in page 171].

Sørensen, A. S., Altman, E., Gullans, M., Porto, J. V., Lukin, M. D., and Demler, E., *"Adiabatic preparation of many-body states in optical lattices,"* Phys. Rev. A **81**, 061603 (2010) [cited in page 70].

Sørensen, A. S. and Mølmer, K., *"Entanglement and extreme spin squeezing,"* Phys. Rev. Lett. **86**, 4431 (2001) [cited in page 165].

Steffen, M., Ansmann, M., Bialczak, R. C., Katz, N., Lucero, E., McDermott, R., Neeley, M., Weig, E. M., Cleland, A. N., and Martinis, J. M., *"Measurement of the entanglement of two superconducting qubits via state tomography,"* Science **313**, 1423 (2006) [cited in page 24].

Swingle, B., Bentsen, G., Schleier-Smith, M., and Hayden, P., *"Measuring the scrambling of quantum information,"* Phys. Rev. A **94**, 040302 (2016) [cited in page 175].

Takeda, K., Noiri, A., Nakajima, T., Yoneda, J., Kobayashi, T., and Tarucha, S., *"Quantum tomography of an entangled three-qubit state in silicon,"* Nature Nanotechnology **16**, 965 (2021) [cited in page 86].

Tarruell, L. and Sanchez-Palencia, L., *"Quantum simulation of the hubbard model with ultracold fermions in optical lattices,"* Comptes Rendus Physique **19**, 365 (2018), quantum simulation / Simulation quantique [cited in pages 17 and 20].

Thomson, A. and Sachdev, S., *"Quantum electrodynamics in 2+1 dimensions with quenched disorder: Quantum critical states with interactions and disorder,"* Phys. Rev. B **95**, 235146 (2017) [cited in page 89].

Tóth, G., Knapp, C., Gühne, O., and Briegel, H. J., *"Spin squeezing and entanglement,"* Phys. Rev. A **79**, 042334 (2009) [cited in page 141].

Tse, M., Yu, H., Kijbunchoo, N., Fernandez-Galiana, A., Dupej, P., Barsotti, L., Blair, C. D., Brown, D. D., Dwyer, S. E., Effler, A., Evans, M., Fritschel, P., Frolov, V. V., Green, A. C., Mansell, G. L., Matichard, F., Mavalvala, N., McClelland, D. E., McCuller, L., McRae, T., Miller, J., Mullavey, A., Oelker, E., Phinney, I. Y., Sigg, D., Slagmolen, B. J. J., Vo, T., Ward, R. L., Whittle, C., Abbott, R., Adams, C., Adhikari, R. X., Ananyeva, A., Appert, S., Arai, K., Areeda, J. S., Asali, Y., Aston, S. M., Austin, C., Baer, A. M., Ball, M., Ballmer, S. W., Banagiri, S., Barker, D., Bartlett, J., Berger, B. K., Betzwieser, J., Bhattacharjee, D., Billingsley, G., Biscans, S., Blair, R. M., Bode, N., Booker, P., Bork, R., Bramley, A., Brooks, A. F., Buikema, A., Cahillane, C., Cannon, K. C., Chen, X., Ciobanu, A. A., Clara, F., Cooper, S. J., Corley, K. R., Countryman, S. T., Covas, P. B., Coyne, D. C., Datrier,

L. E. H., Davis, D., Di Fronzo, C., Driggers, J. C., Etzel, T., Evans, T. M., Feicht, J., Fulda, P., Fyffe, M., Giaime, J. A., Giardina, K. D., Godwin, P., Goetz, E., Gras, S., Gray, C., Gray, R., Gupta, A., Gustafson, E. K., Gustafson, R., Hanks, J., Hanson, J., Hardwick, T., Hasskew, R. K., Heintze, M. C., Helmling-Cornell, A. F., Holland, N. A., Jones, J. D., Kandhasamy, S., Karki, S., Kasprzack, M., Kawabe, K., King, P. J., Kissel, J. S., Kumar, R., Landry, M., Lane, B. B., Lantz, B., Laxen, M., Lecoeuche, Y. K., Leviton, J., Liu, J., Lormand, M., Lundgren, A. P., Macas, R., MacInnis, M., Macleod, D. M., Márka, S., Márka, Z., Martynov, D. V., Mason, K., Massinger, T. J., McCarthy, R., McCormick, S., McIver, J., Mendell, G., Merfeld, K., Merilh, E. L., Meylahn, F., Mistry, T., Mittleman, R., Moreno, G., Mow-Lowry, C. M., Mozzon, S., Nelson, T. J. N., Nguyen, P., Nuttall, L. K., Oberling, J., Oram, R. J., O'Reilly, B., Osthelder, C., Ottaway, D. J., Overmier, H., Palamos, J. R., Parker, W., Payne, E., Pele, A., Perez, C. J., Pirello, M., Radkins, H., Ramirez, K. E., Richardson, J. W., Riles, K., Robertson, N. A., Rollins, J. G., Romel, C. L., Romie, J. H., Ross, M. P., Ryan, K., Sadecki, T., Sanchez, E. J., Sanchez, L. E., Saravanan, T. R., Savage, R. L., Schaetzl, D., Schnabel, R., Schofield, R. M. S., Schwartz, E., Sellers, D., Shaffer, T. J., Smith, J. R., Soni, S., Sorazu, B., Spencer, A. P., Strain, K. A., Sun, L., Szczepańczyk, M. J., Thomas, M., Thomas, P., Thorne, K. A., Toland, K., Torrie, C. I., Traylor, G., Urban, A. L., Vajente, G., Valdes, G., Vander-Hyde, D. C., Veitch, P. J., Venkateswara, K., Venugopalan, G., Viets, A. D., Vorvick, C., Wade, M., Warner, J., Weaver, B., Weiss, R., Willke, B., Wipf, C. C., Xiao, L., Yamamoto, H., Yap, M. J., Yu, H., Zhang, L., Zucker, M. E., and Zweizig, J., *"Quantum-enhanced advanced ligo detectors in the era of gravitational-wave astronomy,"* Phys. Rev. Lett. **123**, 231107 (2019) [cited in pages 14 and 157].

Tsomokos, D. I., García-Ripoll, J. J., Cooper, N. R., and Pachos, J. K., *"Chiral entanglement in triangular lattice models,"* Phys. Rev. A **77**, 012106 (2008) [cited in pages 82 and 146].

Tuchendler, C., Lance, A. M., Browaeys, A., Sortais, Y. R. P., and Grangier, P., *"Energy distribution and cooling of a single atom in an optical tweezer,"* Phys. Rev. A **78**, 033425 (2008) [cited in page 42].

Tóth, G. and Mitchell, M. W., *"Generation of macroscopic singlet states in atomic ensembles,"* New Journal of Physics **12**, 053007 (2010) [cited in page 142].

Urban, E., Johnson, T. A., Henage, T., Isenhower, L., Yavuz, D. D., Walker, T. G.,

and Saffman, M., *"Observation of rydberg blockade between two atoms,"* Nature Physics **5**, 110 (2009) [cited in page 23].

Versini, L., El-Din, K. A., Mintert, F., and Mukherjee, R., *"Efficient estimation of quantum state k-designs with randomized measurements,"* (2023) [cited in page 77].

Villa, L., Despres, J., and Sanchez-Palencia, L., *"Unraveling the excitation spectrum of many-body systems from quantum quenches,"* Phys. Rev. A **100**, 063632 (2019) [cited in page 180].

Villa, L., Despres, J., Thomson, S. J., and Sanchez-Palencia, L., *"Local quench spectroscopy of many-body quantum systems,"* Phys. Rev. A **102**, 033337 (2020) [cited in page 180].

Vitanov, N. V., Rangelov, A. A., Shore, B. W., and Bergmann, K., *"Stimulated raman adiabatic passage in physics, chemistry, and beyond,"* Rev. Mod. Phys. **89**, 015006 (2017) [cited in page 45].

Vogl, M., Laurell, P., Zhang, H., Okamoto, S., and Fiete, G. A., *"Resummation of the holstein-primakoff expansion and differential equation approach to operator square roots,"* Phys. Rev. Res. **2**, 043243 (2020) [cited in pages 181 and 182].

Wallraff, A., Schuster, D. I., Blais, A., Frunzio, L., Huang, R.-. S., Majer, J., Kumar, S., Girvin, S. M., and Schoelkopf, R. J., *"Strong coupling of a single photon to a superconducting qubit using circuit quantum electrodynamics,"* Nature **431**, 162 (2004) [cited in page 20].

Wang, Y., Zhang, X., Corcovilos, T. A., Kumar, A., and Weiss, D. S., *"Coherent addressing of individual neutral atoms in a 3d optical lattice,"* Phys. Rev. Lett. **115**, 043003 (2015) [cited in page 20].

Wen, X. G., *"Gapless boundary excitations in the quantum hall states and in the chiral spin states,"* Phys. Rev. B **43**, 11025 (1991) [cited in page 146].

Wen, X. G., Wilczek, F., and Zee, A., *"Chiral spin states and superconductivity,"* Phys. Rev. B **39**, 11413 (1989) [cited in page 146].

Wietek, A., Schuler, M., and Läuchli, A. M., *"Studying continuous symmetry breaking using energy level spectroscopy,"* (2017) [cited in page 116].

Wilk, T., Gaëtan, A., Evellin, C., Wolters, J., Miroshnychenko, Y., Grangier, P., and Browaeys, A., *"Entanglement of two individual neutral atoms using rydberg blockade,"* Phys. Rev. Lett. **104**, 010502 (2010) [cited in pages 23 and 24].

Will, K., *"Ibm raises the bar with a 50-qubit quantum computer,"* (2017) [cited in page 24].

Wineland, D. J., Bollinger, J. J., Itano, W. M., and Heinzen, D. J., *"Squeezed atomic states and projection noise in spectroscopy,"* Phys. Rev. A **50**, 67 (1994) [cited in page 161].

Wineland, D. J., Bollinger, J. J., Itano, W. M., Moore, F. L., and Heinzen, D. J., *"Spin squeezing and reduced quantum noise in spectroscopy,"* Phys. Rev. A **46**, R6797 (1992) [cited in page 161].

Wineland, D. J., Dalibard, J., and Cohen-Tannoudji, C., *"Sisyphus cooling of a bound atom,"* J. Opt. Soc. Am. B **9**, 32 (1992) [cited in page 43].

Xia, T., Lichtman, M., Maller, K., Carr, A. W., Piotrowicz, M. J., Isenhower, L., and Saffman, M., *"Randomized benchmarking of single-qubit gates in a 2d array of neutral-atom qubits,"* Phys. Rev. Lett. **114**, 100503 (2015) [cited in page 64].

Xu, F., Ma, X., Zhang, Q., Lo, H.-K., and Pan, J.-W., *"Secure quantum key distribution with realistic devices,"* Rev. Mod. Phys. **92**, 025002 (2020) [cited in page 14].

Yan, B., Moses, S. A., Gadway, B., Covey, J. P., Hazzard, K. R. A., Rey, A. M., Jin, D. S., and Ye, J., *"Observation of dipolar spin-exchange interactions with lattice-confined polar molecules,"* Nature **501**, 521 (2013) [cited in pages 20, 64, and 158].

Yan, S., Huse, D. A., and White, S. R., *"Spin-liquid ground state of the s=1/2 kagome heisenberg antiferromagnet,"* Science **332**, 1173 (2011) [cited in page 134].

Yang, S.-J., Wang, X.-J., Bao, X.-H., and Pan, J.-W., *"An efficient quantum light–matter interface with sub-second lifetime,"* Nature Photonics **10**, 381 (2016) [cited in page 13].

Yao, N. Y., Zaletel, M. P., Stamper-Kurn, D. M., and Vishwanath, A., *"A quantum dipolar spin liquid,"* Nature Physics **14**, 405 (2018) [cited in pages 77 and 135].

Yavuz, D. D., Kulatunga, P. B., Urban, E., Johnson, T. A., Proite, N., Henage, T., Walker, T. G., and Saffman, M., *"Fast ground state manipulation of neutral atoms in microscopic optical traps,"* Phys. Rev. Lett. **96**, 063001 (2006) [cited in page 64].

Ye, J. and Zoller, P., *"Essay: Quantum sensing with atomic, molecular, and optical platforms for fundamental physics,"* Phys. Rev. Lett. **132**, 190001 (2024) [cited in page 14].

Yin, J., Cao, Y., Li, Y.-H., Liao, S.-K., Zhang, L., Ren, J.-G., Cai, W.-Q., Liu, W.-Y., Li, B., Dai, H., Li, G.-B., Lu, Q.-M., Gong, Y.-H., Xu, Y., Li, S.-L., Li, F.-Z., Yin, Y.-Y., Jiang, Z.-Q., Li, M., Jia, J.-J., Ren, G., He, D., Zhou, Y.-L., Zhang, X.-X., Wang, N., Chang, X., Zhu, Z.-C., Liu, N.-L., Chen, Y.-A., Lu, C.-Y., Shu, R., Peng, C.-Z., Wang, J.-Y., and Pan, J.-W., *"Satellite-based entanglement distribution over 1200 kilometers,"* Science **356**, 1140 (2017) [cited in page 14].

Young, A. W., Eckner, W. J., Milner, W. R., Kedar, D., Norcia, M. A., Oelker, E., Schine, N., Ye, J., and Kaufman, A. M., *"Half-minute-scale atomic coherence and high relative stability in a tweezer clock,"* Nature **588**, 408 (2020) [cited in page 158].

Young, J. T., Muleady, S. R., Perlin, M. A., Kaufman, A. M., and Rey, A. M., *"Enhancing spin squeezing using soft-core interactions,"* Phys. Rev. Res. **5**, L012033 (2023) [cited in page 158].

Zekavat, R. and Buehrer, R., Handbook of Position Location: Theory, Practice, and Advances, IEEE Series on Digital & Mobile Communication (Wiley, 2019) [cited in page 92].

Zhang, J., Pagano, G., Hess, P. W., Kyprianidis, A., Becker, P., Kaplan, H., Gorshkov, A. V., Gong, Z.-X., and Monroe, C., *"Observation of a many-body dynamical phase transition with a 53-qubit quantum simulator,"* Nature **551**, 601 (2017) [cited in page 24].

Zhou, Y., Kanoda, K., and Ng, T.-K., *"Quantum spin liquid states,"* Rev. Mod. Phys. **89**, 025003 (2017) [cited in page 138].

Zhou, Y. L., Ortner, M., and Rabl, P., *"Long-range and frustrated spin-spin interactions in crystals of cold polar molecules,"* Phys. Rev. A **84**, 052332 (2011) [cited in pages 20 and 64].

Zhu, W., Chen, X., He, Y.-C., and Witczak-Krempa, W., *"Entanglement signatures of emergent dirac fermions: Kagome spin liquid and quantum criticality,"* Science Advances **4**, eaat5535 (2018) [cited in pages 134 and 143].

Zimmerman, M. L., Littman, M. G., Kash, M. M., and Kleppner, D., *"Stark structure of the rydberg states of alkali-metal atoms,"* Phys. Rev. A **20**, 2251 (1979) [cited in page 53].

Title : Quantum simulation of the dipolar XY model using arrays of Rydberg atoms

Keywords : Rydberg atom, Quantum simulation, Optical tweezer, Spin model

Abstract : During my four years of Ph.D., I have focused on the implementation of the dipolar XY spin model using a Rydberg atom-based quantum simulator where the atoms are coupled by resonant Rydberg-Rydberg dipole interactions. We use our ability to address individual atoms in the arrays to first adiabatically prepare and study the properties of the 2D square dipolar XY ground state which exhibit non-trivial antiferromagnetic and ferroma- gnetic order. We then show that the dipolar XY model can produce scalable spin-squeezing states interesting for metrological purposes. Finally, we perform quench spectroscopy experiments to probe the dispersion relation of the XY magnets, in the AFM and FM case. Our studies can be generalized to any system exhibiting dipolar interaction, such as ultra-cold molecules, magnetic atoms or solid-state spin defects.

Titre : Simulation quantique du modèle XY dipolaire en utilisant des matrices d'atomes de Rydberg

Mots clés : Atome de Rydberg, Simulation quantique, Pince optique, Modèle de spin

Résumé : Au cours de mes quatre années de thèse, je me suis concentré sur l'étude du modèle de spin XY dipolaire à l'aide d'un simulateur quan- tique basé sur des atomes de Rydberg, couplés par des interactions dipolaires Rydberg-Rydberg réso- nantes (voir figure). Nous avons exploité notre ca- pacité à adresser individuellement les atomes pour préparer de manière adiabatique et étudier les pro- priétés de l'état fondamental de réseaux carrés bi- dimensionnels (2D) du modèle XY dipolaire, qui présente un ordre antiferromagnétique et ferroma- gnétique complexe. De plus, nous avons démon- tré que le modèle XY dipolaire peut produire des états dits de "spin-squeezing", qui sont particuliè- rement intéressants dans le domaine de la métrolo- gie quantique pour améliorer la sensibilité des me- sures. Nous avons caractérisé ces états, montrant que leur gain métrologique (paramètre de "squee- zing") augmente avec la taille du système. Enfin, nous avons appliqué une méthode de spectroscopie hors équilibre appelée "quench spectroscopy" pour mesurer la relation de dispersion du modèle XY dans les cas antiferromagnétique et ferromagné- tique. Nos études peuvent être généralisées à tout système présentant des interactions dipolaires, tels que les molécules ultra-froides, les atomes magné- tiques ou les défauts de spin dans les solides.